

# PhD Thesis

presented by

**Ashok Kumar VERMA**

Improvement of the planetary  
ephemerides using spacecraft  
navigation data and its application to  
fundamental physics

directed by Agnes Fienga

19<sup>th</sup> September 2013

## Jury :

Président :	Veronique Dehant	ROB, Belgium
Rapporteurs :	Gilles Metris	OCA, France
	Richard Biancale	CNES, France
Examineurs :	Jacques Laskar	IMCCE, France
	Luciano Iess	University of Rome, Italy
	Veronique Dehant	ROB, Belgium
	Jose Lages	UFC, France
Directeur:	Agnes Fienga	OCA, France



## Acknowledgements

Foremost, I would like to express my sincere gratitude to my advisor Dr. Agnes Fienga for the continuous support of my Ph.D study and research, for her patience, motivation, enthusiasm, and immense knowledge. Her guidance helped me in all the time of research, and writing of scientific papers and this thesis. I could not have imagined having a better advisor and mentor for my Ph.D study.

I would like to acknowledge the financial support of the French Space Agency (CNES) and Region Franche-Comte. Part of this thesis was made using the GINS software; I would like to acknowledge CNES, who provided us access to this software. I am also grateful to J.C Marty (CNES) and P. Rosenbatt (Royal Observatory of Belgium) for their support in handling the GINS software.

I would also like to thanks Observatoire de Besancon, UTINAM for providing me a library and computer facilities of the lab to pursue this study. I am grateful to all respective faculties, staff and colleagues of the lab for their direct and indirect contributions to made my stay fruitful and pleasant.

Needless to say, my Besancon years would not have been as much fun without the company of my friends, Arvind Rajpurohit, Eric Grux and Andre Martins. Without their support and love, I could not have imagined my successful stay at Besancon. And at last but not least, I am happy that the distance to my family and my friends back home has remained purely geographical. I wish to thank my family for their love and support which provided my inspiration and was my driving force. I owe them everything and wish I could show them just how much I love and appreciate them.

---



## Abstract

The planetary ephemerides play a crucial role for spacecraft navigation, mission planning, reduction and analysis of the most precise astronomical observations. The construction of such ephemerides is highly constrained by the tracking observations, in particular range, of the space probes collected by the tracking stations on the Earth. The present planetary ephemerides (DE, INPOP, EPM) are mainly based on such observations. However, the data used by the planetary ephemerides are not the direct raw tracking data, but measurements deduced after the analysis of raw data made by the space agencies and the access to such processed measurements remains difficult in terms of availability.

The goal of the thesis is to use archives of past and present space missions data independently from the space agencies, and to provide data analysis tools for the improvement of the planetary ephemerides INPOP, as well as to use improved ephemerides to perform tests of physics such as general relativity, solar corona studies, etc.

The first part of the study deals with the analysis of the Mars Global Surveyor (MGS) tracking data as an academic case for understanding. The CNES orbit determination software GINS was used for such analysis. The tracking observations containing one-, two-, and three-way Doppler and two-way range are then used to reconstruct MGS orbit precisely and obtained results are consistent with those published in the literature. As a supplementary exploitation of MGS, we derived the solar corona model and estimated the average electron density along the line of sight separately for slow and fast wind regions. Estimated electron densities are comparable with the one found in the literature. Fitting the planetary ephemerides, including additional data which were corrected for the solar corona perturbations, noticeably improves the extrapolation capability of the planetary ephemerides and the estimation of the asteroid masses ([Verma et al., 2013](#)).

The second part of the thesis deals with the complete analysis of the MESSENGER tracking data. This analysis improved the Mercury ephemeris up to two order of magnitude compared to any latest ephemerides. Such high precision ephemeris, INPOP13a, is then used to perform general relativity tests of PPN-formalism. Our estimations of PPN parameters ( $\beta$  and  $\gamma$ ) are the most stringent than previous results ([Verma et al., 2014](#)).

---



## Résumé

Les éphémérides planétaires jouent un rôle crucial pour la navigation des missions spatiales actuelles et la mise en place des missions futures ainsi que la réduction et l'analyse des observations astronomiques les plus précises. La construction de ces éphémérides est fortement contrainte par les observations de suivi des sondes spatiales collectées par les stations de suivi sur la Terre. Les éphémérides planétaires actuelles (DE, INPOP, EPM) sont principalement basées sur ces observations. Toutefois, les données utilisées par les éphémérides planétaires ne sont pas issues directement des données brutes du suivi, mais elles dépendent de mesures déduites après l'analyse des données brutes. Ces analyses sont faites par les agences spatiales et leur accès demeure difficile en terme de disponibilité.

L'objectif de la thèse est d'utiliser des archives de données de missions spatiales passées et présentes et de fournir des outils d'analyse de données pour l'amélioration de l'éphéméride planétaire INPOP, ainsi que pour une meilleure utilisation des éphémérides pour effectuer des tests de la physique tels que la relativité générale, les études de la couronne solaire, etc.

La première partie de l'étude porte sur l'analyse des données de suivi de la sonde Mars Global Surveyor (MGS) prise comme un cas d'école pour la compréhension de l'observable. Le logiciel du CNES pour la détermination d'orbite GINS a été utilisé pour une cette analyse. Les résultats obtenus sont cohérents avec ceux publiés dans la littérature. Comme exploitation supplémentaire des données MGS, nous avons étudié des modèles de couronne solaire et estimé la densité moyenne d'électrons le long de la ligne de visée séparément pour les zones de vents solaires lents et rapides. Les densités électroniques estimées sont comparables à celles que l'on trouve dans la littérature par d'autres techniques. L'ajout dans l'ajustement des éphémérides planétaires des données qui ont été corrigées pour les perturbations de plasma solaire, améliore sensiblement la capacité d'extrapolation des éphémérides planétaires et l'estimation des masses d'astéroïdes (Verma et al., 2013).

La deuxième partie de la thèse traite de l'analyse complète des données de suivi d'une sonde actuellement en orbite autour de Mercure, Messenger. Cette analyse a amélioré les éphémérides de Mercure jusqu'à deux ordres de grandeur par rapport à toutes les dernières éphémérides. La nouvelle éphéméride de haute précision, INPOP13a, est ensuite utilisée pour effectuer des tests de la relativité générale via le formalisme PPN. Nos estimations des paramètres PPN ( $\gamma$  et  $\beta$ ) donnent de plus fortes contraintes que les résultats antérieurs (Verma et al., 2014).

---





---

# Contents

<b>Contents</b>	<b>12</b>
<b>List of figures</b>	<b>16</b>
<b>List of tables</b>	<b>18</b>
<b>Acronyms</b>	<b>19</b>
<b>1. Introduction</b>	<b>1</b>
1.1. Introduction to planetary ephemerides . . . . .	1
1.2. INPOP . . . . .	3
1.2.1. INPOP construction . . . . .	3
1.2.2. INPOP evolution . . . . .	5
1.3. Importances of the direct analysis of radioscience data for INPOP . . . . .	8
<b>2. The radioscience observables and their computation</b>	<b>13</b>
2.1. Introduction . . . . .	13
2.2. The radioscience experiments . . . . .	14
2.2.1. Planetary atmosphere . . . . .	15
2.2.2. Planetary gravity . . . . .	15
2.2.3. Solar corona . . . . .	16
2.2.4. Celestial mechanics . . . . .	17
2.3. Radiometric data . . . . .	18
2.3.1. ODF contents . . . . .	18
2.3.1.1. Group 1 . . . . .	18
2.3.1.2. Group 2 . . . . .	19
2.3.1.3. Group 3 . . . . .	19
2.3.1.3.1. Time-tags . . . . .	19
2.3.1.3.2. Format IDs . . . . .	19
2.3.1.3.3. Observables . . . . .	20
2.3.1.4. Group 4 . . . . .	23
2.3.1.4.1. Ramp tables . . . . .	24
2.3.1.5. Group 5 . . . . .	25
2.3.1.6. Group 6 . . . . .	25
2.3.1.7. Group 7 . . . . .	25
2.4. Observation Model . . . . .	25

---

---

2.4.1.	Time scales . . . . .	26
2.4.1.1.	Universal Time (UT or UT1) . . . . .	26
2.4.1.2.	Coordinated Universal Time (UTC) . . . . .	26
2.4.1.3.	International Atomic Time (TAI) . . . . .	27
2.4.1.4.	Terrestrial Time (TT) . . . . .	28
2.4.1.5.	Barycentric Dynamical Time (TDB) . . . . .	28
2.4.2.	Light time solution . . . . .	30
2.4.2.1.	Time conversion . . . . .	31
2.4.2.2.	Down-leg $\tau_U$ computation . . . . .	31
2.4.2.3.	Up-leg $\tau_U$ computation . . . . .	33
2.4.2.4.	Light time corrections, $\delta\tau_D$ and $\delta\tau_U$ . . . . .	33
2.4.2.4.1.	Relativistic correction $\delta\tau_{RC}$ . . . . .	33
2.4.2.4.2.	Solar Corona correction $\delta\tau_{SC}$ . . . . .	34
2.4.2.4.3.	Media corrections $\delta\tau_{MC}$ . . . . .	34
2.4.2.5.	Total light time delay . . . . .	35
2.4.2.5.1.	Round-trip delay . . . . .	35
2.4.2.5.2.	One-way delay . . . . .	35
2.4.3.	Doppler and range observables . . . . .	36
2.4.3.1.	Two-way ( $F_2$ ) and Three-way ( $F_3$ ) Doppler . . . . .	37
2.4.3.1.1.	Ramped . . . . .	37
2.4.3.1.2.	Unramped . . . . .	39
2.4.3.2.	One-way ( $F_1$ ) Doppler . . . . .	40
2.4.3.3.	Two-way ( $\rho_{2,3}$ ) Range . . . . .	41
2.5.	GINs: orbit determination software . . . . .	43
2.5.1.	Dynamic model . . . . .	44
2.5.1.1.	Gravitational forces . . . . .	44
2.5.1.1.1.	Gravitational potential . . . . .	45
2.5.1.1.2.	Solid planetary tides . . . . .	46
2.5.1.1.3.	Sun, Moon and planets perturbation . . . . .	47
2.5.1.1.4.	General relativity . . . . .	48
2.5.1.2.	Non-Gravitational forces . . . . .	49
2.5.1.2.1.	Solar radiation pressure . . . . .	50
2.5.1.2.2.	Atmospheric drag and lift . . . . .	51
2.5.1.2.3.	Thermal radiation . . . . .	53
2.5.1.2.4.	Albedo and infrared radiation . . . . .	54
2.5.1.2.5.	Motor burn . . . . .	55
2.5.2.	Variational equations . . . . .	56
2.5.3.	Parameter estimation . . . . .	57
<b>3.</b>	<b>Mars Global Surveyor: Radioscience data analysis</b>	<b>61</b>
3.1.	Introduction . . . . .	61
3.2.	Mission overview . . . . .	62
3.2.1.	Mission design . . . . .	62
3.2.2.	Spacecraft geometry . . . . .	63
3.2.3.	Radioscience data . . . . .	65

---

---

3.3.	Orbit determination . . . . .	66
3.3.1.	Data processing and dynamic modeling . . . . .	67
3.3.2.	Solve-for parameters . . . . .	68
3.4.	Orbit computation results . . . . .	69
3.4.1.	Acceleration budget . . . . .	69
3.4.2.	Doppler and range postfit residuals . . . . .	71
3.4.3.	Orbit overlap . . . . .	73
3.4.4.	Estimated parameters . . . . .	74
3.4.4.1.	$F_S$ and $F_D$ scale factors . . . . .	74
3.4.4.2.	DSN station position and ephemeris bias . . . . .	75
3.5.	Supplementary investigations . . . . .	77
3.5.1.	GINS solution vs JPL Light time solutions . . . . .	77
3.5.2.	<i>Box-Wing</i> macro-model vs <i>Spherical</i> macro-model . . . . .	79
3.6.	Conclusion and prospectives . . . . .	82
<b>4.</b>	<b>Solar corona correction of radio signals and its application to planetary ephemeris</b>	<b>85</b>
4.1.	Introduction . . . . .	85
4.2.	The solar cycle . . . . .	86
4.2.1.	Magnetic field of the Sun . . . . .	86
4.2.2.	Sunspots . . . . .	88
4.2.3.	Solar maxima . . . . .	88
4.2.4.	Solar minima . . . . .	88
4.3.	The solar wind . . . . .	89
4.3.1.	Fast solar wind . . . . .	89
4.3.2.	Slow solar wind . . . . .	90
4.4.	Radio signal perturbation . . . . .	91
4.5.	Solar corona correction of radio signals and its application to planetary ephemeris	92
4.6.	Conclusion . . . . .	98
4.7.	<a href="#">Verma et al. (2013)</a> . . . . .	98
<b>5.</b>	<b>Improvement of the planetary ephemeris and test of general relativity with MESSENGER</b>	<b>117</b>
5.1.	Introduction . . . . .	117
5.2.	MESSENGER data analysis . . . . .	119
5.2.1.	Mission design . . . . .	119
5.2.2.	Spacecraft geometry . . . . .	120
5.2.3.	Radioscience data . . . . .	122
5.2.4.	Dynamical modeling and orbit determination processes . . . . .	122
5.3.	Orbit determination . . . . .	124
5.3.1.	Acceleration budget . . . . .	124
5.3.2.	Significance of MESSENGER observation for INPOP . . . . .	126
5.3.3.	Evolution of INPOP with the accuracy of MESSENGER orbit . . . . .	128
5.3.3.1.	Case I: First guess orbit for Messenger and INPOP12a . . . . .	129
5.3.3.1.1.	Description . . . . .	129
5.3.3.1.2.	Results . . . . .	130

---

---

5.3.3.2.	Case II: New Mercury orientation model and INPOP12b . . .	130
5.3.3.2.1.	Description . . . . .	130
5.3.3.2.2.	Results . . . . .	132
5.3.3.3.	Case III: Group delay and INPOP12c . . . . .	134
5.3.3.3.1.	Description . . . . .	134
5.3.3.3.2.	Results . . . . .	135
5.3.3.4.	Case IV: New gravity field HgM002 and INPOP12d . . . . .	135
5.3.3.4.1.	Description . . . . .	135
5.3.3.4.2.	Results . . . . .	136
5.3.3.5.	Case V: Extension of the mission and INPOP13a . . . . .	138
5.3.3.5.1.	Description . . . . .	138
5.3.3.5.2.	Results . . . . .	138
5.3.3.5.3.	Comparisons . . . . .	140
5.3.3.5.4.	INPOP13a ephemeris . . . . .	141
5.4.	<a href="#">Verma et al. (2014)</a> . . . . .	142
<b>6.</b>	<b>General conclusions</b>	<b>157</b>
	<b>Publications</b>	<b>161</b>
	<b>Bibliographie</b>	<b>171</b>

---

---

## List of Figures

1.1.	Schematic diagram for the procedure of the INPOP construction. . . . .	4
1.2.	Percentage contribution of the data in the INPOP construction. . . . .	5
1.3.	Percentage contribution of each data type used in the construction INPOP series (Fienga, 2011). . . . .	6
1.4.	Extrapolation capability of the planetary ephemerides: INPOP08 (Fienga et al., 2008), INPOP10a (Fienga et al., 2011a), and INPOP10b (Fienga et al., 2011b). . . . .	8
2.1.	Two- or three-way radio wave propagation between a spacecraft and Deep Space Network (DSN) station. . . . .	14
2.2.	Radio wave bending when the spacecraft is occulted by the planet and the signal propagates through the atmosphere and ionosphere of the planet. . . . .	15
2.3.	Mars gravity field derived from Mariner 9, Viking 1&2 and Mars Global Surveyor (MGS) spacecraft (Pätzold et al., 2004). . . . .	16
2.4.	Electron density distribution with respect to minimum distance of the line of sight (MDLOS) from Sun (Verma et al., 2013). Black: profile derived from Bird et al. (1996); and Red: profile derived from Guhathakurta et al. (1996) . . .	17
2.5.	One-, Two-, and three-way Doppler observables of the MGS spacecraft. . . . .	23
2.6.	Two way range observables of the MGS spacecraft. . . . .	23
2.7.	Ramped frequency $f_o$ and frequency rate $\dot{f}$ measured for MGS spacecraft. . . . .	24
2.8.	Transformation between the time scales. . . . .	26
2.9.	Time history of the $\Delta UT1$ since 1962. These values of $\Delta UT1$ are extracted from EOP file. . . . .	27
2.10.	Time history of the $\Delta TAI$ since 1973. . . . .	28
2.11.	Panels: (a) transformations of various coordinate time scales, (b) time history of TT - TDB. . . . .	29
2.12.	Geometric sketch of the vectors involved in the computation of the light time solution, where $C$ is the solar system barycentric; $E$ is the Earth geocenter; and $B$ is the center of the central body. . . . .	32
2.13.	Relativistic and solar corona corrections to light time solution (expressed in seconds): (a) for MGS, (b) for MESSENGER. . . . .	35
2.14.	Round-trip light time solution of MGS (panel $a$ ) and MESSENGER (panel $b$ ) spacecraft, computed from the Eq. 2.33. . . . .	36
2.15.	The technique used for computing the integration of Eq. 2.40. $W$ is the precision width of the interval of the integration, and $t_{start}$ and $t_{end}$ is the start and end times of the ramp table (see Section 2.4.3.1). . . . .	39

---

---

2.16. The process of the spacecraft orbit determination. . . . .	43
2.17. A simple geometric <i>macro-model</i> of the spacecraft. . . . .	50
3.1. Summary of MGS mission phases from launch to mapping period ( <a href="#">Albee et al., 2001</a> ). . . . .	63
3.2. View of the MGS spacecraft ( <a href="#">Albee et al., 2001</a> ). . . . .	64
3.3. Pole-to-Pole tracking of the MGS spacecraft during mapping period ( <a href="#">Tyler et al., 2001</a> ). . . . .	66
3.4. Gravitational and non-gravitational accelerations acting on the MGS spacecraft. See text for the explanation of each column. . . . .	70
3.5. Quality of the MGS orbit in terms of rms values of the postfit residuals for each one-day data-arc: (a) one-way Doppler given in millihertz (1-way: 1 mHz = 0.035 mm/s = speed of light / X-band frequency); (b) two- and three-way Doppler given in millihertz (2/3-way: 1 mHz = 0.0178 mm/s = 0.5×speed of light / X-band frequency); and (c) two-way range given in meter. The peaks and gaps in residuals correspond to solar conjunction periods of MGS. . . . .	71
3.6. Orbit overlap differences for the entire mapping period of MGS mission for the (a) radial direction, (b) along-track direction, and (c) cross-track or normal to the orbit plane. . . . .	73
3.7. Scale factors: a) atmospheric drag and b) solar radiation pressure. . . . .	74
3.8. The continental map of DSN stations. <i>Image credit: NASA</i> . . . . .	75
3.9. Distance bias estimated for each data-arc and for each participating station: a) station position bias and b) range bias corrections to the INPOP10b ephemeris. . . . .	76
3.10. Range bias comparison between GINS solution and Light time solution using INPOP10b ephemeris: (a) range bias computed from the JPL light time solution, (b) range bias corresponding to the GINS solution, (c) difference between the GINS and JPL light time solutions. . . . .	78
3.11. Evolution of the orbit change with respect to number of days in the data -arc and with the number of iterations. Panels of the figure are corresponding to a) Iteration-01 and b) Iterations-10. The green, red, and black colors in the figure are corresponding to 2-, 8-, and 15-days data-arc respectively. . . . .	79
3.12. Difference between <i>Box-Wing</i> and <i>Spherical</i> macro-models: (a) Doppler root mean square (rms) residuals, (b) range rms residuals, and (c) range bias. . . . .	80
3.13. Non-gravitational accelerations and scale factors estimated using <i>Box-Wing</i> macro-model (Black) and <i>Spherical</i> macro-model (Red). . . . .	81
4.1. Approximated global coronal magnetic field structure for the beginnings of years correspond to solar maximum: (a) 1992 and (b) 2002. The photospheric radial field strength is represented by the greyscale, with white/black indicating positive/negative polarity. Green/red field lines represent open fields of positive/negative polarity and blue lines represent closed fields. These figures have been extracted from <a href="#">Petrie (2013)</a> . . . . .	87
4.2. The solar sunspot cycle <sup>2</sup> , since 1955 to present. Figure shows the variation of an average monthly sunspot numbers with time. . . . .	87

---

4.3.	Approximated global coronal magnetic field structure for the beginnings of years: (a) 2008, solar minimum and (b) 2002, solar maximum. The photospheric radial field strength is represented by the greyscale, with white/black indicating positive/negative polarity. Green/red field lines represent open fields of positive/negative polarity and blue lines represent closed fields. These figures have been extracted from the <a href="#">Petrie (2013)</a> . . . . .	89
4.4.	Synoptic source surface maps of solar wind speeds, in the Carrington rotation number versus latitude for 1990 and 1996, which approximately correspond to the cycle 22 maximum ( <i>panel a</i> ) and 22/23 minimum ( <i>panel b</i> ), respectively. The dark solid line represents the neutral magnetic line. These figures have been extracted from the <a href="#">Tokumar et al. (2010)</a> . . . . .	90
4.5.	Flow chart describing the procedure involved in the derivation of solar corona model, electron density computations and further improvement of the planetary ephemeris. The abbreviations used in the flow chart are: POD: Precise Orbit Determination; SA: Solar Activity; SW : Solar Wind S.W : Slow Wind; F.W : Fast Wind; ED : Electron Density; PFR : PostFit Residuals . . . . .	93
4.6.	An average electron density distribution at $20R_{\odot}$ during different phases of solar activities and for different states of solar wind. Higher number of sunspots correspond to maximum phase of solar activity, while smaller number correspond to minimum phase. . . . .	95
5.1.	Summary of MESSENGER's entire trajectory from launch to mapping period ( <a href="#">McAdams et al., 2007</a> ). . . . .	119
5.2.	MESSENGER spacecraft geometry ( <a href="#">Vaughan et al., 2006</a> ). . . . .	120
5.3.	Gravitational and non-gravitational accelerations acting on the MESSENGER spacecraft. The empirical accelerations correspond to maneuvers and accelerations due to atmospheric drag were not computed for MESSENGER (see Section 5.2.4). . . . .	125
5.4.	MESSENGER orbit: (a) prime phase (June 24, 2011) (b) extended phase (June 24, 2012). . . . .	127
5.5.	Schematic diagram of the evolution of planetary ephemeris from INPOP10e to INPOP13a with the improvement of M <small>ER</small> cury Surface, Space Environment, G <small>E</small> ochemistry, and R <small>ANG</small> ing (MESSENGER) orbit. OM: Orientation Model; GM: Gravity Model; TD : Transponder Delay; RS : Radioscience OD S/W : Orbit Determination software; PE S/W : Planetary Ephemeris software (*) Prime mission; (**) prime+extended mission. . . . .	128
5.6.	Case 1: (a) rms values of the postfit two- and three-way Doppler residuals for each one-day data-arc, (b) rms values of the postfit two-way range residuals for each one-day data-arc, (c) range bias (prefit) correspond to INPOP10e, (d) range bias (postfit) correspond to newly fitted INPOP12a ephemeris, and (e) difference in the Mercury-Earth geometric distances between INPOP10e and INPOP12a ephemerides. The indicated area are intervals of time corresponding to Mariner 10 and MESSENGER observations. . . . .	132

---

5.7.	An example for the change of MESSENGER orbit characteristics due to <a href="#">Margot (2009)</a> Mercury orientation model. The differences are plotted with respect to IAU 1996 Mercury orientation model. . . . .	133
5.8.	Case II: (a) rms values of the postfit two- and three-way Doppler residuals for each one-day data-arc, (b) rms values of the postfit two-way range residuals for each one-day data-arc, (c) range bias (prefit) correspond to INPOP12a, (d) range bias (postfit) correspond to newly fitted INPOP12b ephemeris, and (e) difference in the Mercury-Earth geometric distances between INPOP12a and INPOP12b ephemerides. The indicated area are intervals of time corresponding to Mariner 10 and MESSENGER observations. . . . .	134
5.9.	Case III: (a) rms values of the postfit two- and three-way Doppler residuals for each one-day data-arc, (b) rms values of the postfit two-way range residuals for each one-day data-arc, (c) range bias (prefit) correspond to INPOP12b, (d) range bias (postfit) correspond to newly fitted INPOP12c ephemeris, and (e) difference in the Mercury-Earth geometric distances between INPOP12b and INPOP12c ephemerides. The indicated area are intervals of time corresponding to Mariner 10 and MESSENGER observations. . . . .	136
5.10.	Case IV: (a) rms values of the postfit two- and three-way Doppler residuals for each one-day data-arc, (b) rms values of the postfit two-way range residuals for each one-day data-arc, (c) range bias (prefit) correspond to INPOP12c, (d) range bias (postfit) correspond to newly fitted INPOP12d ephemeris, and (e) difference in the Mercury-Earth geometric distances between INPOP12c and INPOP12d ephemerides. The indicated area are intervals of time corresponding to Mariner 10 and MESSENGER observations. . . . .	137
5.11.	Case V: (a) rms values of the postfit two- and three-way Doppler residuals for each one-day data-arc, (b) rms values of the postfit two-way range residuals for each one-day data-arc, (c) range bias (prefit) correspond to INPOP12d, (d) range bias (postfit) correspond to newly fitted INPOP13a ephemeris, and (e) difference in the Mercury-Earth geometric distances between INPOP12d and INPOP13a ephemerides. The indicated area are intervals of time corresponding to Mariner 10 and MESSENGER observations. . . . .	139
5.12.	Mean and rms values of the postfit Doppler and range residuals, estimated for each data-arc. . . . .	140
5.13.	MESSENGER one-way range residuals obtained with INPOP13a, INPOP10a and DE423. . . . .	141

---



---

## List of Tables

1.1.	Solve-for parameters for different ephemerides. The parameters which are not modeled are denoted by $\mathcal{X}$ . The parameters that are fixed during orbit computations are denoted by $F$ , while fitted parameters are marked as $\checkmark$ , (Fienga, 2011) . . . . .	7
1.2.	Sources for the processed spacecraft and lander missions data sets, used for the construction of INPOP. . . . .	9
2.1.	Constants dependent upon transmitter or exciter band . . . . .	20
2.2.	Spacecraft transponder ratio $M_2$ ( $M_{2r}$ ) . . . . .	21
2.3.	Downlink frequency multiplier $C_2$ . . . . .	22
2.4.	Constant $C_{range}$ required for converting second to range units. . . . .	42
3.1.	MGS spacecraft macro-model characteristics (Marty, 2011) . . . . .	65
3.2.	Year wise summary of the Doppler and range tracking data used for orbit solution. . . . .	66
3.3.	Comparison of postfit Doppler and range residuals, and overlapped periods, between different authors. . . . .	72
4.1.	Electron densities estimated from different models at $20R_{\odot}$ and at $215R_{\odot}$ (1AU). . . . .	96
4.2.	Statistics of the range bias before and after solar corona corrections. . . . .	97
5.1.	MESSENGER spacecraft <i>macro-model</i> characteristics (Vaughan et al., 2002). . . . .	122
5.2.	Summary of the Doppler and range tracking data used for orbit determination. . . . .	124
5.3.	An average magnitude of MESSENGER accelerations estimated during prime and extended phase of the mission. . . . .	127
5.4.	Recommended values for the direction of the north pole of rotation and the prime meridian of the Mercury, 1996 (Davies et al., 1996). . . . .	129
5.5.	Statistics of the residuals obtained for Case I, i) postfit Doppler and range residuals, ii) prefit (INPOP10e) and postfit (INPOP12a) range bias. . . . .	131
5.6.	Recommended model for the orientation of Mercury (Margot, 2009). . . . .	131
5.7.	Statistics of the residuals obtained for Case II, i) postfit Doppler and range residuals, ii) prefit (INPOP12a) and postfit (INPOP12b) range bias. . . . .	133
5.8.	Statistics of the residuals obtained for Case III, i) postfit Doppler and range residuals, ii) prefit (INPOP12b) and postfit (INPOP12c) range bias. . . . .	135
5.9.	Statistics of the residuals obtained for Case IV, i) postfit Doppler and range residuals, ii) prefit (INPOP12c) and postfit (INPOP12d) range bias. . . . .	137

---

5.10. Statistics of the residuals obtained for Case V , i) postfit Doppler and range residuals, ii) prefit (INPOP12d) and postfit (INPOP13a) range bias. . . . .	139
5.11. Comparisons of postfit residuals between different authors. . . . .	141

---

---

## Acronyms

AMD	. . . . .	angular momentum wheel desaturation
BVE	. . . . .	block 5 exciter
BVLS	. . . . .	Bounded Variable Least Squares
BW <sub>mm</sub>	. . . . .	Box-Wing macro-model
CME	. . . . .	coronal mass ejections
CNES	. . . . .	Centre National d'Etudes Spatiales
COI	. . . . .	center of integration
DSMs	. . . . .	deep-space maneuvers
DSN	. . . . .	Deep Space Network
EOP	. . . . .	Earth Orientation Parameters
EPM	. . . . .	Ephemerides of Planets and the Moon
ESA	. . . . .	European Space Agency
Gaia	. . . . .	Global Astrometric Interferometer for Astrophysics
GINS	. . . . .	“Géodésie par Intégrations Numériques Simultanées”
GR	. . . . .	general relativity
HEF	. . . . .	high efficiency
HGA	. . . . .	high gain antenna
IAU	. . . . .	International Astronomical Union
IERS	. . . . .	International Earth Rotation and Reference Systems Service
IMF	. . . . .	Interplanetary Magnetic Field

---

INPOP	“Intégrateur Numérique Planétaire de l’Observatoire de Paris”
ITRF	International Terrestrial Reference Frame
JPL	Jet Propulsion Laboratory
LLR	Lunar Laser Ranging
LOS	line of sight
MDLOS	minimum distance of the line of sight
MDM	Momentum Dump Maneuver
MESSENGER	MErcury Surface, Space Environment, GEochemistry, and Ranging
MEX	Mars Express
MGS	Mars Global Surveyor
MMNAV	Multimission Navigation
MNL	Magnetic Neutral Line
MOI	Mars orbit insertion
NAIF	Navigation and Ancillary Information Facility
NASA	National Aeronautics and Space Administration
OCM	Orbit Correction Maneuver
ODF	Orbit Data File
ODP	Orbit Determination Program
ODY	Odyssey
PDS	Planetary Data System
PPN	Parameterized Post-Newtonian
RMDCT	Radio Metric Data Conditioning Team
rms	root mean square
SEP	Sun-Earth-Probe
SP <sub>mm</sub>	Spherical macro-model

---

---

TAI . . . . .	.International Atomic Time
TCB . . . . .	.Barycentric Coordinate Time
TCG . . . . .	.Geocentric Coordinate Time
TCMs . . . . .	.trajectory-correction maneuvers
TDB . . . . .	.Barycentric Dynamical Time
TT . . . . .	.Terrestrial Time
UT1 . . . . .	.Universal Time
UTC . . . . .	.Coordinated Universal Time
VEX . . . . .	.Venus Express
WSO . . . . .	.Wilcox Solar Observatory

---



# Chapter 1

## Introduction

### 1.1 Introduction to planetary ephemerides

The word *ephemeris* originated from the Greek language “*εφημερος*”. The planetary ephemeris gives the positions and velocities of major bodies of the solar system at a given epoch. Historically, positions (right ascension and declination) were given as printed tables of values, at regular intervals of date and time. Nowadays, the modern ephemerides are often computed electronically from mathematical models of the motion.

Before 1960's, analytical models were used for describing the state of the solar system bodies as a function of time. At that time only optical angular measurements of solar system bodies were available. In 1964 radar measurements of the terrestrial planets have been measured. These measurements significantly improved the knowledge of the position of the objects in space. The first laser ranges to the lunar corner cube retroreflectors were then obtained in 1969 ([Newhall et al., 1983](#)). With the developments of these techniques, a group at MIT, had initiated such an ephemeris program as a support of solar system observations and resulting scientific analyses. The first modern ephemerides, deduced from radar and optical observations, were then developed at MIT ([Ash et al., 1967](#)). The achieved precision in the measurements, and the improvement in the dynamics of the solar system objects, gave an opportunities to tests the theory of general relativity (GR) ([Shapiro, 1964](#)).

In the late 1970's, the first numerically integrated planetary ephemerides were built by Jet Propulsion Laboratory (JPL), so called DE96 ([Standish et al., 1976](#)). There have been many versions of the JPL DE ephemerides, from the 1960s through the present. With the beginning of the Space Age, space probes began their journeys resulting in a revolution in knowledge that is still continuing. These ephemerides have then served for spacecraft navigation, mission planning, reduction and analysis of the most precise of astronomical observations. Number of efforts were then also devoted for testing the GR using astrometric and radiometric observations ([Anderson et al., 1976, 1978](#)).

---

Improvements in the planetary ephemerides occurred simultaneously with the evolution of the space missions and the navigation of the probes. Navigation observations were included for the first time in the construction of DE102 ephemeris (Newhall et al., 1983). In this ephemeris, planet orbit were constrained by the Viking range measurements along with entire historical astronomical observations. Such addition of the Viking range measurements improved the Mars position by more than 4 order of magnitude and JPL becomes the only source of development of high precision planetary ephemerides. In the 1970's and early 1980's, a lot of work was done in the astronomical community to update the astronomical almanacs all around the world. Four major types of observations (optical measurements, radar ranging, spacecraft ranging, and lunar laser ranging) were then included in the adjustment of the ephemeris DE200 (Standish, 1990). This ephemeris becomes a worldwide standard for several decades. In the late 1990s, a new series of the JPL ephemerides were introduced. In particular, DE405 (Standish, 1998), which covers the period between 1600 to 2200, was widely used for the spacecraft navigation and data analysis. DE423 (Folkner, 2010) is the most recent documented ephemeris produced by the JPL.

However, almost from a decade, the European Space Agency (ESA) is very active in the development of interplanetary missions in collaboration with the National Aeronautics and Space Administration (NASA). These missions include: Giotto for the study of the comets Halley; Ulysses for charting the poles of the Sun; Huygens for Titan; Rosetta for comet; Mars Express (MEX) for Mars; Venus Express (VEX) for Venus; Global Astrometric Interferometer for Astrophysics (Gaia) for space astrometry; BepiColombo for Mercury (future mission); JUICE for Jupiter (future mission); etc. With the new era of European interplanetary missions, the "Intégrateur Numérique Planétaire de l'Observatoire de Paris" (INPOP) project was initiated in 2003 to build the first European planetary ephemerides independently from the JPL. INPOP has then evolved over the years and the first official release was made on 2008, so-called INPOP06 (Fienga et al., 2008). Currently several versions of INPOP are available to the users: INPOP06 (Fienga et al., 2008); INPOP08 (Fienga et al., 2009); INPOP10a (Fienga et al., 2011a); INPOP10b (Fienga et al., 2011b); and INPOP10e (Fienga et al., 2013). INPOP10a was the first planetary ephemerides solving for the mass of the Sun ( $GM_{\odot}$ ) for a given fixed value of Astronomical Unit (AU). Since INPOP10a, new estimations of the Sun mass together with the oblateness of the Sun ( $J2_{\odot}$ ) are regularly obtained. With the website [www.imcce.fr/inpop](http://www.imcce.fr/inpop), these ephemerides are freely distributed to the users. With this users can have access to positions and velocities of the major planets of our solar system and of the moon, the libration angles of the moon but also to the differences between the terrestrial time TT (time scale used to date the observations) and the barycentric times TDB or TCB (time scale used in the equations of motion).

With such gradual improvement, INPOP has become an international reference for space navigation. INPOP is the official ephemerides used for the Gaia mission navigation and the analysis of the Gaia observations. INPOP10e (Fienga et al., 2013) is the latest ephemerides delivered by the INPOP team to support this mission. Moreover, the INPOP team is also involved in the preparation of the Bepi-Colombo and the JUICE missions. The brief description of the INPOP construction and its evolution are given in Section 1.2.

---



Moreover, in addition to DE and INPOP ephemerides, there is one more numerical ephemerides which were developed at the Institute of Applied Astronomy of the Russian Academy of Sciences, called Ephemerides of Planets and the Moon (EPM). These ephemerides are based upon the same modeling as the JPL DE ephemeris. Their of the EPM ephemerides, the most recent are EPM2004 (Pitjeva, 2005), EPM2008 (Pitjeva, 2010), and EPM2011 (Pitjeva and Pitjev, 2013). The EPM2004 ephemerides were constructed over the 1880-2020 time interval in the TDB time scale. In this ephemerides GM of all planets, the Sun, the Moon and value of Earth-Moon mass ratio correspond to DE405 (Standish, 1998), while for EPM2008 these values are close to DE421 (Folkner et al., 2008).

## 1.2 INPOP

The construction of independent planetary ephemerides is a crucial point for the strategy of space development in Europe. As mentioned before, JPL ephemerides were used as a reference for spacecraft navigation of the US and the European missions. With the delivery of INPOP the situation has changed. Since 2006, a completely autonomous planetary ephemerides has been built in Europe and became an international reference for space navigation and for scientific research in the dynamics of the Solar System objects and in fundamental physics.

### 1.2.1 INPOP construction

INPOP numerically integrates the equations of motion of the major bodies of our solar system including about 300 asteroids about the solar system barycenter and of the motion and rotation of the Moon about the Earth. Figure 1.1 shows the systematic diagram for the procedure of the INPOP construction. The brief descriptions of this procedure is described as follows:

- The dynamic model of INPOP follows the recommendations of the International Astronomical Union (IAU) in terms of compatibility between time scales, Terrestrial Time (TT) and Barycentric Dynamical Time (TDB), and metric in the relativistic equations of motion. It is developed in the Parameterized Post-Newtonian (PPN) framework, and includes the solar oblateness, the perturbations induced by the major asteroids (about 300) as well as the tidal effects of the Earth and Moon. The trajectories of the major bodies are obtained by the numerical integration of a differential equation of first order,  $Y' = F(t, Y(t))$ , where  $Y$  is the parameter that describes the state vectors of the system (position/velocity of the bodies, their orientations) (Manche, 2011). Prior knowledge of these parameters at epoch zero ( $t_0$ , usually J2000) are then used to initiate the integrations with the method of Adams (Hairer et al., 1987). Detailed descriptions of the INPOP dynamic modeling are given in the Fienga et al. (2008) and Manche (2011).
- The numerical integration produces a file of positions and velocities (state vectors) of the

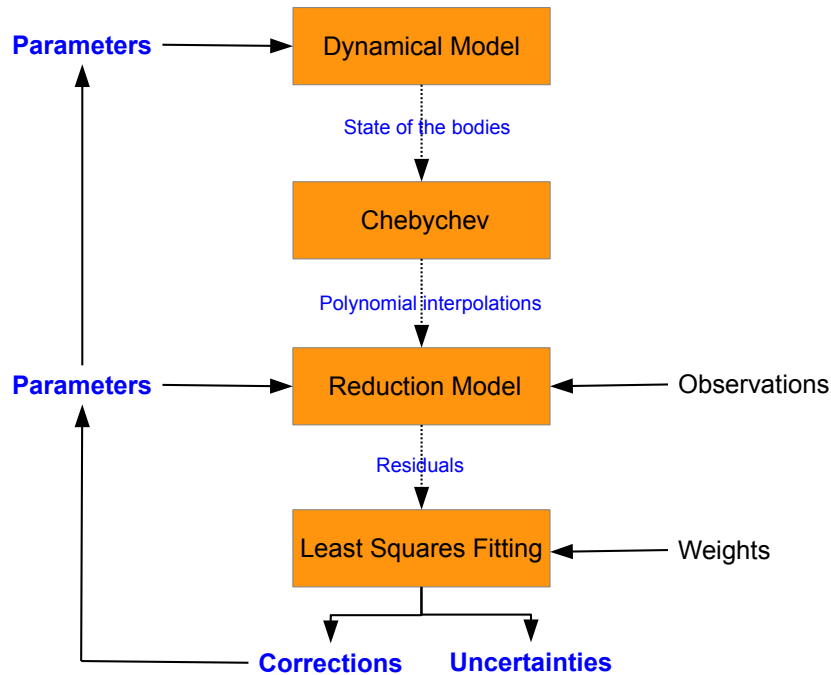


Figure 1.1: Schematic diagram for the procedure of the INPOP construction.

solar system bodies at each time step of the integration. The step size of 0.055 days is usually chosen to minimize the roundoff error. Each component of the state vectors of the solar system bodies relative to the solar system barycenter and the Moon relative to the Earth are then represented by an  $N$ th-degree expansion in Chebyshev polynomials (see [Newhall \(1989\)](#) for more details). Interpolation of these polynomials gives the access of the state vectors at any given epoch.

- Interpolated solutions of the state vectors are then used to reduce the observations. There are several types of observations that are used for the construction of planetary ephemerides ([Fienga et al., 2008](#)): direct radar observations of the planet surface (Venus, Mercury and Mars), spacecraft tracking data (radar ranging, ranging and VLBI), optical observations (transit, photographic plates and CCD observations for outer planets), and Lunar Laser Ranging (LLR) for Moon. The observations and the parameters associated with the data reduction are then induced in the data reduction models (see Figure 1.1). Description of such models can be found in [Fienga et al. \(2008\)](#). Figure 1.2 shows the contributions in percentage of the different types of data used for constraining the recent series of INPOP. More than 136,000 planetary observations are involved in this process. From Figure 1.2 one can noticed that, nowadays, planetary ephemerides are mainly driven by the spacecraft data. However, old astrometric data are still important especially for a better knowledge of outer planet orbits for which few or no spacecraft data are available (see Section 1.2.2 for more details).

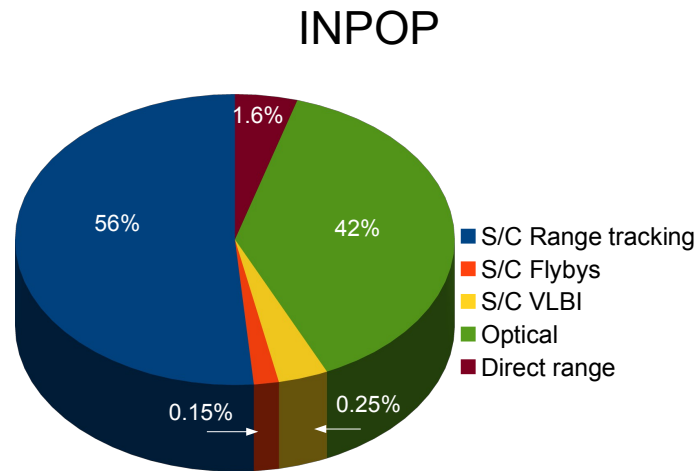


Figure 1.2: Percentage contribution of the data in the INPOP construction.

- Data reduction process allows to compute the differences obtained between the observations and its calculation from the planetary solution, called residuals (observation-calculation). The same program can also calculate the matrix of partial derivatives with respect to the parameters that required to be adjusted.
- The residuals and the matrix of partial derivatives are then used to adjust the parameters, associated with dynamic models and data reduction models, using least squares techniques. In addition, the file containing the weights, assigned to each observation, is also used to assist the parameter fitting. Usually, almost 400 parameters are estimated during the orbit fitting. About 70 parameters related to the Moon orbit and rotation initial conditions are fitted iteratively with the planetary parameters (Manche et al., 2010; Manche, 2011). The objective of the parameter fitting is to minimize the residuals using an iterative process. In this process, newly estimated parameters at  $i^{th}$  iteration are then feedback to the dynamical and reduction model for initiating the  $i^{th} + 1$  iteration.

### 1.2.2 INPOP evolution

As stated previously, since 2006, INPOP has become an international reference for space navigation and for scientific research in the dynamics of the solar system objects and in fundamental physics. Since then several versions of the INPOP have been delivered. The Figure 1.3 shows the evolution of the INPOP ephemerides from INPOP06 (Fienga et al., 2008) to INPOP10a (Fienga et al., 2011a) and Table 1.1 gives the solve-for parameters for these ephemerides.

INPOP06 was the first version of the INPOP series, published in 2008. As one can noticed, INPOP06 was mainly driven by optical observations of outer planets and Mars tracking data,

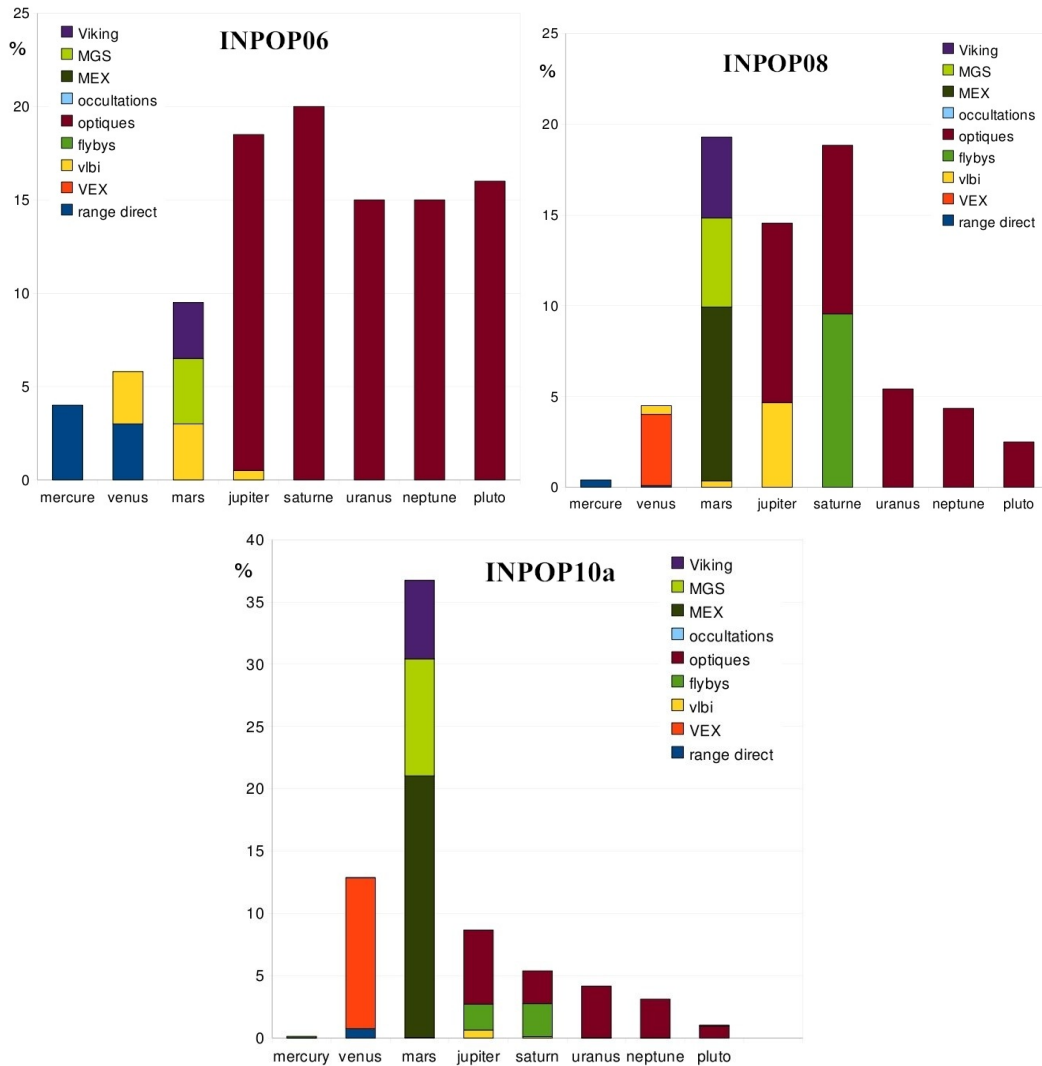


Figure 1.3: Percentage contribution of each data type used in the construction INPOP series (Fienga, 2011).

and solved for 63 parameters. The choice of the estimated parameters and the methods are very similar to DE405 (see Fienga et al. (2008) and Table 1.1).

Thanks to new collaborations with ESA, VEX and MEX navigation data have been introduced in INPOP since INPOP08 (Fienga et al., 2009). As a result, estimation of Earth-Venus and Earth-Mars distances, based on VEX and MEX data, were improved by a factor 42 and 6, respectively, compared to INPOP06.

With the availability of more and more processed range data, it was then possible to improve the accuracy of INPOP ephemerides significantly. Consequently, as one can see on Figure 1.3, INPOP10a is mainly driven by Mars spacecraft tracking and by the VEX tracking data. The Mercury, Jupiter, and Saturn positions deduced from several flybys were also included

Table 1.1: Solve-for parameters for different ephemerides. The parameters which are not modeled are denoted by  $\times$ . The parameters that are fixed during orbit computations are denoted by  $F$ , while fitted parameters are marked as  $\checkmark$ , (Fienga, 2011)

Contents	Parameters	INPOP06	INPOP08	INPOP10a	INPOP10b	INPOP10e
Asteroids	fitted masses	5	34	145	120	79
	fixed masses	0	5	16	71	73
	asteroid ring	$\checkmark$	$F$	$F$	$\checkmark$	$\checkmark$
	densities	295	261	$\times$	$\times$	$\times$
Constants	AU	$F$	$\checkmark$	$F$	$F$	$F$
	EMRAT	$F$	$\checkmark$	$\checkmark$	$F$	$\checkmark$
	$GM_{\odot}$	$F$	$F$	$\checkmark$	$\checkmark$	$\checkmark$
	$J2_{\odot}$	$\checkmark$	$\checkmark$	$\checkmark$	$F$	$\checkmark$
Time	end of the fit	2005.5	2008.5	2010.0	2010.0	2010.0
Total	fitted parameters	63	83	202	177	137

in the INPOP10a adjustment. Since INPOP10a, the Bounded Variable Least Squares (BVLS) algorithm (Lawson and Hanson, 1995; Stark and Parker, 1995) is used for the adjustment of parameters, especially for the mass of the asteroids. Compared to the previous versions, significant improvements were noticed in the postfit residuals and in the fitted parameters. The detailed description of these ephemerides and its comparisons are given in Fienga (2011).

Nowadays, modern planetary ephemerides are being more and more spacecraft dependent. However, the accuracy of the planetary ephemerides is characterized by the extrapolation capability. Such capability of the ephemerides is very important for mission design and analysis. In INPOP10b therefore, the efforts were mainly devoted to improve the extrapolation capabilities of the INPOP ephemeris. On Figure 1.4 are plotted the one-way Earth-Mars distances residuals estimated with INPOP08, INPOP10a, and INPOP10b ephemerides. The plotted MEX data were not included in the fit of the planetary ephemerides, hence represent the extrapolated postfit residuals. By adding more informations on asteroid masses estimated (see Table 1.1) with other techniques (close-encounters between two asteroids, or between a spacecraft and an asteroid), INPOP10b has improved its extrapolation on the Mars-Earth distances of about a factor of 10 compared to INPOP10a. Furthermore, Figure 1.4 also demonstrates that, it is crucial to input regularly new tracking data in order to keep the extrapolation capabilities of the planetary ephemerides below 20 meters after 2 years of extrapolation, especially for Mars.

INPOP10e is the latest INPOP version developed for the Gaia mission. Compared to previous versions, new sophisticated procedures related to the asteroid mass determinations have been implemented: BVLS have been associated with a-priori sigma estimators (Kuchynka,

2010; Fienga et al., 2011b) and solar plasma corrections (see Chapter 4 and Verma et al. (2013)). In addition to INPOP10b data, very recent Uranus observations and the positions of Pluto deduced from Hubble Space Telescope have been also added in the construction of INPOP10e. This ephemerides further used for the analysis of the MESSENGER spacecraft radioscience data for the planetary orbits (see Chapter 5).

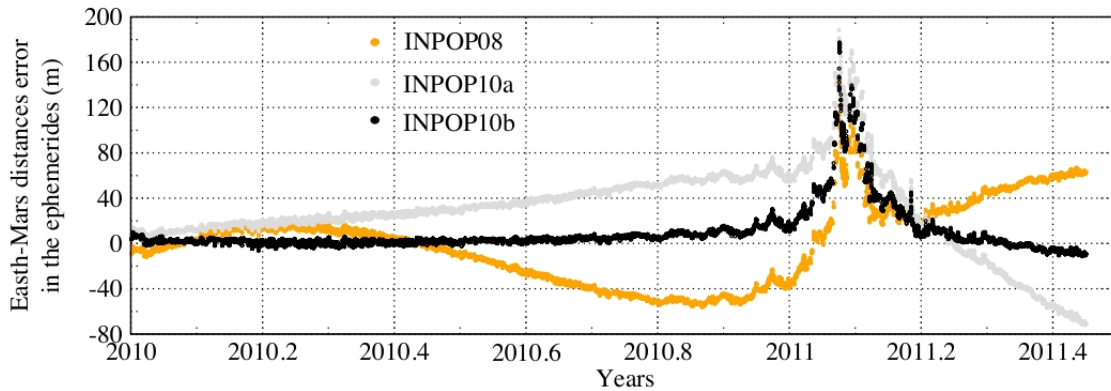


Figure 1.4: Extrapolation capability of the planetary ephemerides: INPOP08 (Fienga et al., 2008), INPOP10a (Fienga et al., 2011a), and INPOP10b (Fienga et al., 2011b).

### 1.3 Importances of the direct analysis of radioscience data for INPOP

In the Figure 1.2, is given the distribution of the data samples used for the construction of the INPOP planetary ephemerides. The dependency of the planetary ephemerides on the range observations of the robotic space missions (56%) is obvious and will increase with the continuous addition of spacecraft and lander data like MESSENGER, Opportunity etc. However, the range observations used by the planetary ephemerides are not the direct raw tracking data, but measurements (also called range bias) deduced after the analysis of raw data (Doppler and Range) using orbit determination softwares.

Until recently, space agencies (NASA and ESA) were the only source for the access of such processed range measurements to construct INPOP. Thanks to the PDS server<sup>1</sup>, it is now possible to download the raw tracking observations of space missions such as MGS and MESSENGER and to use them independently for the computations of precise probe orbits and biases for planetary ephemeris construction. Furthermore, flybys of planets by spacecraft are also a good source of information. Owing to the vicinity of the spacecraft and its accurate tracking during this crucial phase of the mission, it is possible to deduce very accurate positions of the planet as the spacecraft pass by. For gaseous planets, this type of observations is the major

<sup>1</sup><http://pds-geosciences.wustl.edu/>

constraint on their orbits (flybys of Jupiter, Neptune, and Saturn, mainly). Even if they are not numerous (less than 0.5% of the data sample), they provide 50% of the constraints brought to outer planet orbits.

Table 1.2: Sources for the processed spacecraft and lander missions data sets, used for the construction of INPOP.

Type	Mission	Planet	Data source
Orbiter	VEX	Venus	ESA
	MGS	Mars	JPL/CNES/PDS
	MEX	Mars	ESA/ROB
	ODY	Mars	JPL
Flyby	Mariner 10	Mercury	JPL
	MESSENGER	Mercury	JPL/PDS
	Pioneer 10 & 11	Jupiter	JPL
	Voyager 1 & 2	Jupiter	JPL
	Ulysses	Jupiter	JPL
	Cassini	Jupiter	JPL
	Voyager 2	Uranus	JPL
	Voyager 2	Neptune	JPL
Lander	Viking	Mars	JPL
	pathfinder	Mars	JPL

The goal of the thesis is therefore to analyze the radioscience data independently (see Chapter 2) and then to improve INPOP. High precision ephemerides are then used for performing tests of physics such as solar corona studies (see Chapter 4) and tests of GR through the PPN formalism (see Chapter 5). In this thesis, such analysis has been performed with entire Mars Global Surveyor (MGS) (see Chapter 3) and MESSENGER (see Chapter 5) radioscience data using Centre National d'Etudes Spatiales (CNES) orbit determination software "Géodésie par Intégrations Numériques Simultanées" (GINS). Key aspects of this thesis are:

- To make INPOP independent from the space agencies and to deliver most up-to-date high accurate ephemerides to the users.
- To maintain consistency between spacecraft orbit and planet orbit constructions.
- To perform for the first time studies of the solar corona with the ephemerides. The solar corona model derived from the range bias are then used to correct the solar corona perturbations and for the construction of INPOP ephemerides (Verma et al., 2013).
- To analyze the entire MESSENGER radioscience data corresponding to the mapping phase, make INPOP the first ephemerides in the world with the high precision Mercury orbit INPOP13a of about  $-0.4 \pm 8.4$  meters (Verma et al., 2014).

- To perform one of the most sensitive GR tests of PPN-formalism based on the Mercury improved ephemerides. Estimated PPN parameters ( $\beta$  and  $\gamma$ ) are most stringent than previous results ([Verma et al., 2014](#)).

Furthermore, the scientific progress in planetary ephemerides, radio science data modeling and orbit determinations will allow the INPOP team to better advance in the interpretation of the space data. This will propel INPOP at the forefront of planetary ephemerides and the future ephemerides will be in competition with other ephemerides (DE ephemerides from the US for instance), which yields a better security on their validity and integrity from the checking and comparison of the series between them.

The outline of the thesis is as follows:

In Chapter 2, the inherent characteristics of the radioscience data are introduced. The contents of the Orbit Determination File (ODF) that are used to measure the spacecraft motion are described. The definitions and the formulations used to index the observations and describe the spacecraft motion are given. The formulations associated with the modeling of the observables, that include precise light time solution, one-, two-, and three-way Doppler shift and two-way range, are discussed. Finally, the modeling of gravitational and non-gravitational forces used in the GINS software to describe the spacecraft motion are also discussed briefly.

In Chapter 3, the analysis of the radioscience data of the MGS mission has been chosen as an academic case to test our understanding of the raw radiometric data and their analysis with GINS. Data processing and dynamic modeling used to reconstruct the MGS orbit are discussed. Results obtained during the orbit computation are then compared with the estimations found in the literature. Finally, a supplementary test, that addresses the impact of the macro-model on the orbit reconstruction, and the comparison between the GINS solution and the JPL light time solution are also discussed. These results have been published in the *Astronomy & Astrophysics* journal, [Verma et al. \(2013\)](#).

In Chapter 4, we address issues of radio signal perturbations during the period of superior solar conjunctions of the spacecraft. Brief characteristics of the solar magnetic field, solar activity, and solar wind are given. The complete description of the solar corona models that have been derived from the range measurements of the MGS, MEX, and VEX spacecraft are discussed in details. The solar corona correction of radio signals and its impact on planetary ephemeris and on the estimation of asteroid masses is also discussed. All results corresponding to this study were published in *Astronomy & Astrophysics* journal, [Verma et al. \(2013\)](#).

In Chapter 5, we analyze one and half year of radioscience data of the MESSENGER mission using GINS software. Data processing and dynamic modeling used to reconstruct the MESSENGER orbit are discussed. We also discussed the construction of the first high precision Mercury ephemeris INPOP13a using the results obtained with the MESSENGER orbit determination. Finally, GR tests of PPN formalism using updated MESSENGER and Mer-

---



cury ephemerides are discussed. All these results are published in Astronomy & Astrophysics journal, [Verma et al. \(2014\)](#).

In Chapter 6, we summarize the achieved goal followed by the conclusions and perspectives of the thesis.

---



## Chapter 2

# The radioscience observables and their computation

### 2.1 Introduction

The radioscience study is the branch of science which usually consider the phenomena associated with radio wave generation and propagation. In space, these radio signals could be originated from natural sources (for example: pulsars) or from artificial sources such as spacecraft. If the source of these signals is natural, then study is referred to radio astronomy. Usually the objective of radio astronomy is to perform a study of the generation and of the process of propagation of the signal.

However, if the source of the radio signals is artificial satellite, then the radioscience experiment are usually related to the phenomena that occurred along the line of sight (LOS) which affect the radio waves propagation. Small changes in phase or amplitude (or both) of the radio signals, when propagating between spacecraft and the Deep Space Network (DSN) station on Earth, allow us to study, celestial mechanics, planetary atmosphere, solar corona, planetary ephemeris, planetary gravity field, test of GR, etc.

The figure 2.1 represents the schematic diagram of the communication between a spacecraft and the DSN stations. These DSN stations are used primarily for the uplink transmission of signal and downlink reception of spacecraft data. The uplink is first transmitted by the transmitter from the DSN station at time  $t_1$ . These signals are received by the spacecraft antenna which is typically a few meter in size. The received signals are then transmitted back (downlink) by the transponder to the DSN station at bouncing time  $t_2$ . The spacecraft transponder multiplies the uplink frequency by a transponder ratio so that downlink frequency is coherently related to the uplink frequency. The transmitted signals (downlink) are then received by the receiver at DSN station at time  $t_3$ .

---

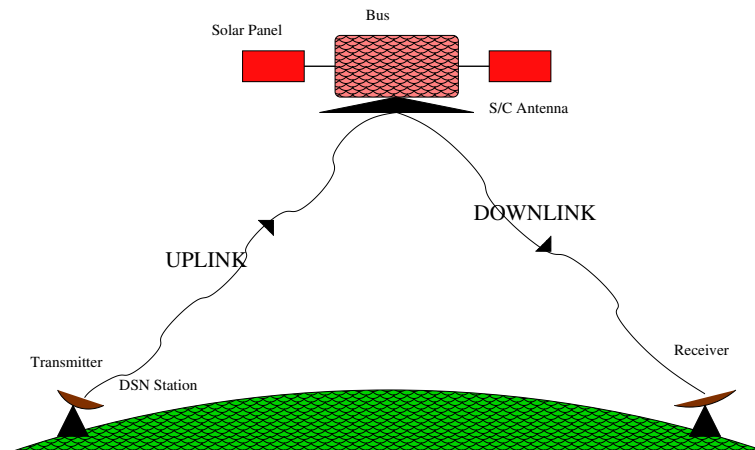


Figure 2.1: Two- or three-way radio wave propagation between a spacecraft and Deep Space Network (DSN) station.

While tracking the spacecraft, the Doppler shift is routinely measured in the frequency of the signal at the receiving DSN station. The Doppler shift, which represents the change in the received signal frequency from the transmitted signal, may be caused by the spacecraft orbit around the planet, Earth revolution around the Sun, Earth rotation, atmospheric perturbations etc. Doppler observables, which are collected at the receiving station, are the average values of this Doppler shift over a period of time called count interval. These collected radiometric data could be one-, two-, or three-way Doppler and range observations. Time delay in terms of distance is represented by range observable and rate of change of this distance is called Doppler observables. When the DSN stations on Earth only receive a downlink signal from a spacecraft, the communication is called one-way. The observables are called two-way if the transmitted and received antennas are the same, and three-way observables if they are different. An example of two- or three-way communication is shown in Figure 2.1).

## 2.2 The radioscience experiments

The radioscience experiments are used for study the planetary environment and its physical state. Such experiments already have been performed and tested with early flight planetary missions. For example, Voyager (Eshleman et al., 1977; Tyler et al., 1981, 1986), Ulysses (Bird et al., 1994; Pätzold et al., 1995), Marine 10 (Howard et al., 1974), Mars Global Surveyor (Tyler et al., 2001; Konopliv et al., 2006; Marty et al., 2009), Mars Express (Pätzold et al., 2004). Brief description of these investigation are discussed below.

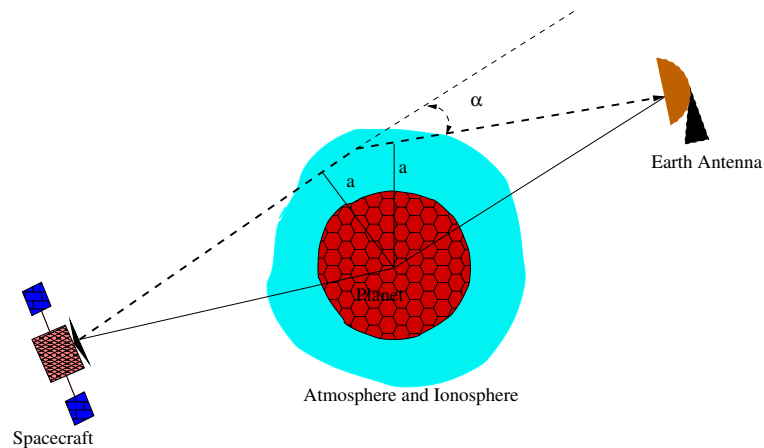


Figure 2.2: Radio wave bending when the spacecraft is occulted by the planet and the signal propagates through the atmosphere and ionosphere of the planet.

### 2.2.1 Planetary atmosphere

In order to study planetary environment, the spacecraft orbit can be arranged such that the spacecraft passes behind the orbiting planet as seen from the DSN stations. This phenomenon is known as occultation. Just before, the spacecraft is hidden by the planetary disc, signals sent between the spacecraft and the ground station will travel through the atmosphere and ionosphere of the planet. The refraction in the atmosphere and ionosphere bends the LOS, as shown in Figure 2.2. This bending will produce a phase and frequency shift in the received signal. Analysis of this shift can then account for investigating the atmospheric and ionospheric properties of the planet.

Measurements of the Doppler shift on a spacecraft coherent downlink determine the LOS component of the spacecraft velocity. These Doppler and range measurements are then also useful to compute the precise orbit of the spacecraft. The geometry between the spacecraft and the Earth station are then useful to determine the refraction or bending angle,  $\alpha$ , as shown in Figure 2.2. The ray asymptotes,  $a$  (see Figure 2.2), and the bending angle,  $\alpha$ , can be used to estimate the refraction profile of the atmosphere and ionosphere (Fjeldbo et al., 1971). This refractivity could be then interpreted in terms of pressure and temperature by assuming the hydrostatic equilibrium (Pätzold et al., 2004).

### 2.2.2 Planetary gravity

The accurate determination of the spacecraft orbit requires a precise knowledge of the gravity field and its temporal variations of the planet. Such variations in the gravity field are associated with the high and low concentration of the mass below and at the surface of the planet. They cause the slight change in the speed of the spacecraft relative to the ground station on Earth and

induced small shift in the receiving frequency. After removing the Doppler shift induced by the planetary motion, spacecraft orbital motion, atmospheric friction, solar wind, it is then possible to compute the spacecraft acceleration or deceleration induced by the gravity field of the planet.

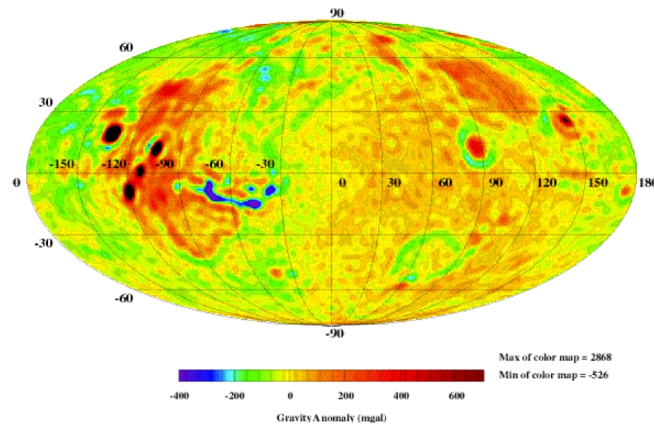


Figure 2.3: Mars gravity field derived from Mariner 9, Viking 1&2 and Mars Global Surveyor (MGS) spacecraft (Pätzold et al., 2004).

Gravity field mapping requires the spacecraft downlink carries signal coherent with a highly stable uplink from the Earth station. The two-way radio tracking of these signals provides an accurate measurement of spacecraft velocity along the LOS to the tracking station on Earth. Figure 2.3 represents an example of the gravity field mapping of the Mars surface using such radio tracking signals of Mariner 9, Viking 1&2 and Mars Global Surveyor (MGS) spacecraft (Pätzold et al., 2004). This mapping was derived from the gravity field model (Kaula, 1966), developed up to degree and order 75. The strong positive anomalies shown in Figure 2.3 correspond to the regions of highest elevation on the Mars surface. The low circular orbiter, such as MGS, allows to mapping an accurate and complete gravity field of the planet. However, the highly eccentric orbiter, such as Mars Express (MEX) or MESSENGER, is not best suitable for investigating the global map of the gravity field of orbiting planet.

### 2.2.3 Solar corona

When the LOS passes close to the sun as seen from the Earth and all three bodies (Planet, Sun and Earth) approximately lies in the straight line, then such geometric configuration is called solar conjunction. During conjunction periods, strong turbulent and ionized gases of corona region severely degrade the radio wave signals when propagating between spacecraft and Earth tracking stations. Such degradations cause a delay and a greater dispersion of the radio signals. The group and phase delays induced by the Sun activity are directly proportional to the total electron contents along the LOS and inversely with the square of carrier radio wave frequency.

By analyzing spacecraft radio waves which are directly intercepted by solar plasma, it is then possible to study the corona density distribution, the solar wind region and the corona

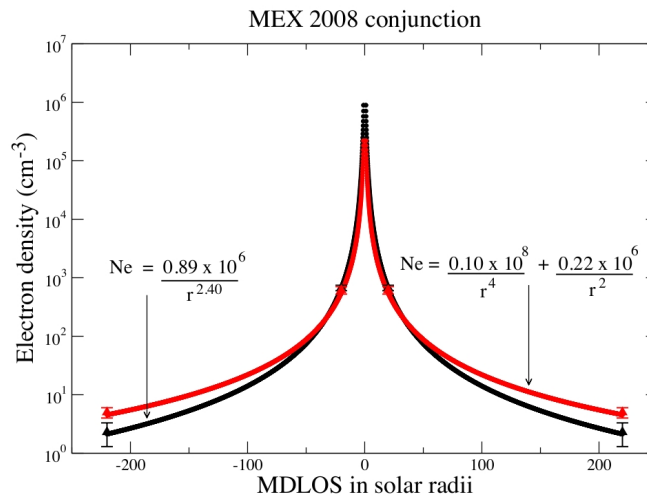


Figure 2.4: Electron density distribution with respect to minimum distance of the line of sight (MDLOS) from Sun (Verma et al., 2013). Black: profile derived from Bird et al. (1996); and Red: profile derived from Guhathakurta et al. (1996)

mass ejection. Two viable methods which are generally used for performing these studies are (Muhleman and Anderson, 1981): (1) direct *in situ* measurements of the electron density, speed, and energies of the electron and photons (2) analysis of a single and dual frequency time delay data acquired from interplanetary spacecraft. The second method which corresponds to radio-science experiment has been already tested using radiometric data acquired at the time of solar conjunctions from interplanetary spacecraft (Muhleman et al., 1977; Anderson et al., 1987b; Guhathakurta and Holzer, 1994; Bird et al., 1994, 1996).

Figure 2.4 represents an example of corona density distribution computed from the Mars Express (MEX) radiometric data acquired at the time minimum solar cycle, 2008 (Verma et al., 2013). These electronic profiles of the density can be derived by computing the time or phase delay due to the solar corona. Computed time delay is then fitted over the radiometric data in order to estimate the solar corona model parameters and consequentially the electron density. The detailed analysis of the radio-science solar corona experiment is discussed in Chapter 4.

## 2.2.4 Celestial mechanics

As discussed in Chapter 1, the radio-science data are also useful to estimate an accurate position and velocity of the planets, and other solar system parameters from the dynamic modeling of the planetary motion, called planetary ephemerides. Accurate planetary ephemerides are necessary for the spacecraft mission design, orbitography and to perform fundamental tests of physics. However, radio-science data are not directly imposed into the planetary ephemeris

software, they are instead first analyzed by the spacecraft orbit determination software. Range bias, which present the systematic error in the geometric position of the planet as seen from the Earth, can be estimated while computing the orbit of the spacecraft. These rang bias impose strong constraints on the orbits of the planet, as well as on other solar system parameters. In consequence, such data not only allow the construction of an accurate planetary ephemeris, they also contribute significantly to our knowledge of parameters such as asteroid masses. A detailed description of such analysis using MGS, and MESSENGER spacecraft radiometric data is discussed in Chapters 3, and 5, respectively.

## 2.3 Radiometric data

The radiometric data which are produced by the NASA DSN Multimission Navigation (MM-NAV) Radio Metric Data Conditioning Team (RMDCT) is called Orbit Data File (ODF)<sup>1</sup>. These ODF are used to determine the spacecraft trajectories, gravity field affecting them, and radio propagation conditions. Each ODF is in standard JPL binary format and consists of many 36-byte logical records, which falls into 7 primary groups. In this work, we have developed an independent software to extract the contents of these ODFs. This software reads the binary ODF and writes the contents in specific format, called GINS format. GINS is the orbit determination software, independently developed at the CNES (see Section 2.5).

### 2.3.1 ODF contents

The ODF contains several groups of informations. An ODF usually contains most groups, but may not have all. The format of such groups are given in [Kwok \(2000\)](#). The brief description of the contents of these groups is given below.

#### 2.3.1.1 Group 1

- This group is usually a first group among the several records. It identifies the spacecraft ID, the file creation time, the hardware, and the software associated with the ODF. This group also provides the information about the reference date and time for ODF time-tags. Currently the ODF data time-tags are referenced to Earth Mean Equatorial equinox of 1950 (EME-50).

---

<sup>1</sup><http://geo.pds.nasa.gov/>

---



### 2.3.1.2 Group 2

- This group is usually a second group among the several groups records. It contains the string character that some time used to identify the contents of the data record, such as, TIMETAG, OBSRVBL, FREQ, ANCILLARY-DATA.

### 2.3.1.3 Group 3

- This is the third group that usually contains majority of the data included in the ODF. According to the data categories, the description of this group is given below.

#### 2.3.1.3.1 Time-tags

- **Observable time:** First in this category is the Doppler and range observable time  $TT$  measured at the receiving station. Observable time  $TT$  corresponds to the time at the midpoint of the count interval,  $T_c$ . The integer and the fractional part of this time-tag ( $TT$ ) is given separately in ODF. The integer part is measured from 0 hours UTC on 1 January 1950, whereas the fractional part is given in milliseconds.
- **Count interval:** Doppler observables are derived from the change in the Doppler cycle count. The time period on which these counts are accumulated is called count interval or compression time  $T_c$ . Typically count times have a duration of tens of seconds to a few thousand of seconds. For example, count time could be between 1-10  $s$  when the spacecraft is near a planet or roughly 1000  $s$  for interplanetary cruise.
- **Station delay:** This gives the information corresponding to the downlink and uplink delay at the receiving and at the transmitting station respectively. It is given in nanosecond in the ODF.

#### 2.3.1.3.2 Format IDs

- **Spacecraft ID:** It identifies the spacecraft ID which corresponds to ODF data. For example: 94 for MGS
  - **Data type ID:** As mentioned before, the radiometric data could be one-, two-, and three-way Doppler and two-way range. The ODF provides a specific ID associated with these data set. For example: 11, 12, and 13 integers give in ODF correspond to one-, two-, and three-way Doppler respectively, whereas 37 stands for two-way range.
-

- **Station ID:** This is an integer that gives the receiving and transmitting stations ID that are associated with the time period covered by the ODF. The transmitting station ID is set to zero, if the date type is one-way Doppler.
- **Band ID:** It identifies the uplink (at transmitting station), downlink (at receiving station), and exciter band (at receiving station) ID. The ID of these bands are set to 1, 2, and 3 for S, X, and Ka band.
- **Date Validity ID:** It is the quality indicator of the data. It set to zero for a good quality of data and set to one for a bad data.

### 2.3.1.3.3 Observables

- **Reference frequency:** It is the frequency measured at the reception time  $t_3$  at the receiving station in UTC (see Section 2.4.1). This frequency can be constant or ramped. However, the given reference frequency in the ODF could be a reference oscillator frequency  $f_q$ , or a transmitter frequency  $f_T$ , or a Doppler reference frequency  $f_{REF}$ . The computed values of Doppler observables are directly affected by the  $f_{REF}$ . Hence, the computation of the  $f_{REF}$  from the reference oscillator frequency  $f_q$ , or from the transmitter frequency  $f_T$  is discussed below.

- (i) When the given frequency in the ODF is  $f_q$ , then it is needed to first compute the transmitter frequency, which is given by (Moyer, 2003):

$$f_T(t) = T_3 \times f_q(t) + T_4 \quad (2.1)$$

where  $T_3$  and  $T_4$  are the transmitter-band dependent constants as given in Table 2.1. From Eq. 2.1, one can compute the transmitter frequency at the receiving station and at the transmitting station by replacing the time  $t$  to  $t_3$  and  $t_1$  respectively. Thus, the  $f_{REF}$  at reception time can be calculated by multiplying the spacecraft transponder ratio with  $f_T$ :

$$f_{REF}(t_3) = M_{2R} \times f_T(t_3) \quad (2.2)$$

Table 2.1: Constants dependent upon transmitter or exciter band

Band	Transmitter Band			
	$T_1$	$T_2$	$T_3$	$T_4$ (Hz)
S	240	221	96	0
X	240	749	32	$6.5 \times 10^9$
Ku	142	153	1000	$-7.0 \times 10^9$
Ka	14	15	1000	$1.0 \times 10^{10}$

Table 2.2: Spacecraft transponder ratio  $M_2$  ( $M_{2R}$ )

Uplink (Exciter) band	Downlink band		
	S	X	Ka
S	$\frac{240}{221}$	$\frac{880}{221}$	$\frac{3344}{221}$
X	$\frac{240}{749}$	$\frac{880}{749}$	$\frac{3344}{749}$
Ka	$\frac{240}{3599}$	$\frac{880}{3599}$	$\frac{3344}{3599}$

where  $M_{2R}$  is the spacecraft transponder ratio (see Table 2.2). It is the function of the exciter band at the transmitting station and of the downlink band at the receiving station. Whereas,  $M_2$  given in Table 2.2 is the function of uplink band at the transmitting station and the downlink band at the receiving station. Hence, the corresponding frequency  $f(t_1)$  at the transmission time  $t_1$  can be calculated by,

$$f(t_1) = M_2 \times f_T(t_1) \quad (2.3)$$

In Eqs. 2.2 and 2.3,  $f_T(t_3)$  and  $f_T(t_1)$  can be calculated from the Eq. 2.1. If the given value of  $f_q$  in the ODF is ramped then  $f_q$  is calculated through ramp-table (see Group 4).

- (ii) When the transmitter frequency at reception time  $f_T(t_3)$  is given in the ODF, then Eq. 2.2 can be used to compute the  $f_{REF}$ . The given  $f_T(t_3)$  could be the constant or ramped. The ramped  $f_T(t_3)$  can be calculated from the ramped table. However, when the spacecraft is the transmitter (one-way Doppler), then  $f_T$  is given by (Moyer, 2003):

$$f_T(t) = C_2 \times f_{S/C} \quad (2.4)$$

where  $C_2$  is the downlink frequency multiplier. Table 2.3 shows the standard DSN values of the  $C_2$  for S, X, and Ka downlink bands for the data point.  $f_{S/C}$  is the spacecraft transmitter frequency which is given by (Moyer, 2003):

$$f_{S/C} = f_{T_0} + \Delta f_{T_0} + f_{T_1}(t - t_0) + f_{T_2}(t - t_0)^2 \quad (2.5)$$

where  $f_{T_0}$  is the nominal value of  $f_{S/C}$  and give in ODF.  $\Delta f_{T_0}$ ,  $f_{T_1}$ , and  $f_{T_2}$  are the solve-for quadratic coefficients used to represent the departure of  $f_{S/C}$ . The quadratic coefficients are specified by time block with start time  $t_0$ .

- (iii) Finally, the given frequency in the ODF could be a constant value of  $f_{REF}$ . This value is usually constant for a given pass.

- **Doppler observable:** Doppler observables are derived from the change in the Doppler cycle count  $N(t_3)$ , which accumulates during the compression time  $T_c$  at the receiving station. These observables in the ODF are defined as follows:

$$\text{Observable} = \left( \frac{B}{|B|} \right) \times \left[ \left( \frac{N_j - N_i}{t_j - t_i} \right) - |F_b \times K + B| \right] \quad (2.6)$$

Table 2.3: Downlink frequency multiplier  $C_2$ 

Multiplier	Downlink Band		
	S	X	Ka
$C_2$	1	$\frac{880}{230}$	$\frac{3344}{240}$

where:

- B = Bias placed on receiver
- $N_i$  = Doppler count at time  $t_i$
- $N_j$  = Doppler count at time  $t_j$
- $t_i$  = start time of interval
- $t_j$  = end time of interval
- $F_b$  = frequency bias
- K = 1 for S-band receivers
- = 11/3 for X-band receivers
- = 176/27 for Ku-band receivers
- = 209/15 for Ka-band receivers

$$F_b = (X_1/X_2) \times (X_3 \times f_R + X_4) - f_{s/c} + R_3 \quad \text{for 1 - way Doppler} \quad (2.7)$$

$$F_b = (X_1/X_2) \times (X_3 \times f_{qR} + X_4) - (T_1/T_2) \times (T_3 \times f_{qT} + T_4) \quad \text{for 2/3 - way Doppler} \quad (2.8)$$

$$T_c = t_j - t_i \quad \text{compression time} \quad (2.9)$$

where:

- $f_{qR}$  = Receiver oscillator frequency at time  $t_3$
- $f_{s/c}$  = Spacecraft (beacon) frequency
- $f_{qT}$  = Transmitter oscillator frequency at time  $t_1$
- $R_3$  = 0 for all receiving bands
- $T_1$  to  $T_4$  = Transmitters band (Table 2.1)
- $X_1$  to  $X_4$  = Exciter band ( same value as transmitter band, Table 2.1)

Figure 2.5 shows an example of two and three way Doppler observables extracted from the MGS ODF.

- **Range observable:** Range observables are obtained from the ranging machine at the receiving station. These range observables are measured in range units (see Section 2.4.3) and defined in ODF as follows:

$$\text{Observable} = R - C + Z - S \quad (2.10)$$

where:

- R = range measurement
- C = station delay calibration
- Z = Z-height correction
- S = spacecraft delay

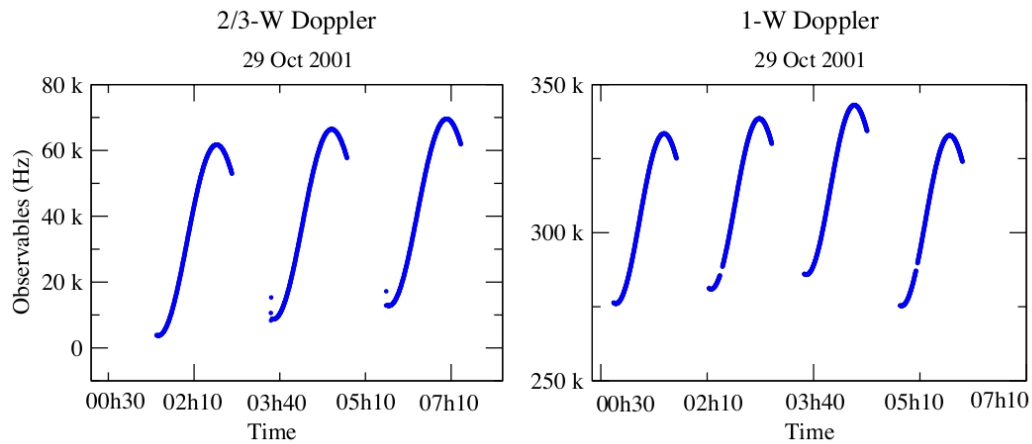


Figure 2.5: One-, Two-, and three-way Doppler observables of the MGS spacecraft.

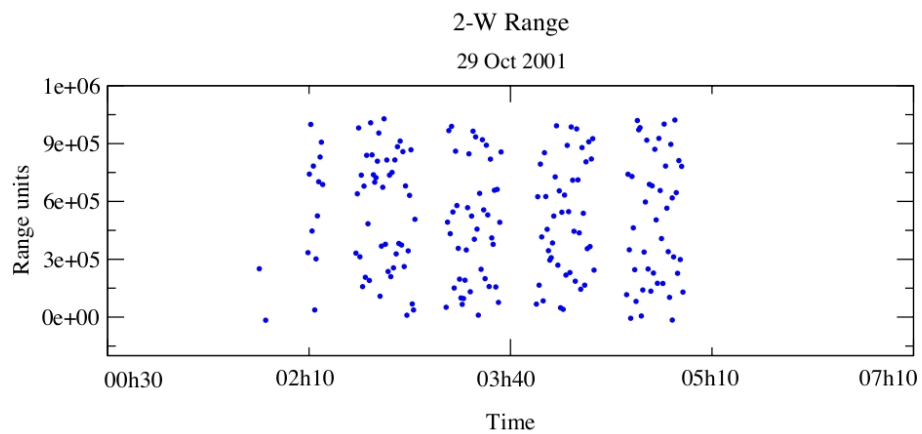


Figure 2.6: Two way range observables of the MGS spacecraft.

Figure 2.6 shows an example of two way range observables extracted from the MGS's ODF.

#### 2.3.1.4 Group 4

- Ramp groups are usually the fourth of several groups of record in ODF. This group contains the information about the tuning of the receiver or transmitter on the Earth station. Ramping is a technique to achieve better quality communication with spacecraft when its velocity varies with respect to ground stations and it has been implemented at the DSN. There is usually one ramp group for each DSN station. The contents of this group and the procedure to calculate the ramped transmitter frequency  $f_T(t)$  is described below.

### 2.3.1.4.1 Ramp tables

As mentioned in Group 3, the reference frequency given in ODF can be a constant or ramped. When the given frequency is ramped then the reference frequency is computed through the ramp table. The ramp table contains the start UTC time  $t_o$ , end UTC time  $t_f$ , the values of ramped frequency  $f_o$  at the start time  $t_o$ , the constant time derivative of frequency (ramp rate)  $\dot{f}$ , and the tracking station. The ramp table can be specified as the reference oscillator frequency  $f_q(t)$  or the transmitter frequency  $f_T(t)$ . However, Eq. 2.1 can be used to convert reference oscillator frequency  $f_q(t)$  into the transmitter frequency  $f_T(t)$ . The ramped frequency can be then calculated by:

$$f_T(t) = f_o + \dot{f}(t - t_o) \quad (2.11)$$

where  $t$  is the interpolation time. For Doppler observables, the ramp table for the receiving station gives the ramped transmitter frequency  $f_T(t)$  as a function of time. This ramped frequency or a constant value of  $f_T(t)$  at the receiving station can be then used to calculate the Doppler reference frequency  $f_{REF}(t_3)$  at receiving station using Eq. 2.2.

The Figure 2.7 shows an example of the ramped frequency  $f_o$  and the ramp rate  $\dot{f}$  plotted over the start time  $t_o$  of the ramp table. These ramp informations are extracted from the MGS ODF.

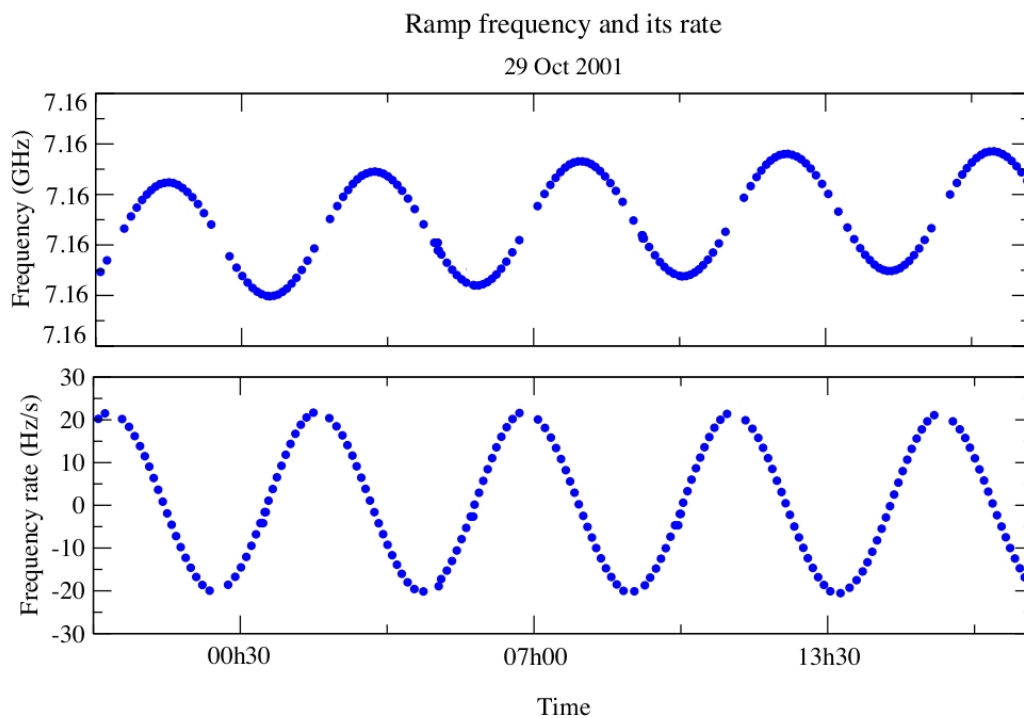


Figure 2.7: Ramped frequency  $f_o$  and frequency rate  $\dot{f}$  measured for MGS spacecraft.

### 2.3.1.5 Group 5

- This is a clock offset group. It is usually the fifth of several groups of record in ODF. It contains information on clock offsets at DSN stations contributing to the ODF. This group may be omitted from the ODF and used only with VLBI data. It contains the start and end time of the clock offset which is measured from 0 hours UTC on 1 January 1950. It also includes the DSN station ID and the correspond clock offset given in nanoseconds. The informations of this group are generally not useful for the radioscience studies.

### 2.3.1.6 Group 6

- This group is usually not include in the ODF and omitted all the time.

### 2.3.1.7 Group 7

- It is a data summary group which contains summary information on contents of the ODF, such as, the first and last date of the data sample, total number of samples, used transmitting and receiving stations, band ID, and the type of data available in the ODF. This group is optional and may be omitted from the ODF.

## 2.4 Observation Model

For given spacecraft radiometric data obtained by the DSN are described in Section 2.3. These data record for each data point contains ID information which is necessary to unambiguously identify the data point and the observed value of the observable (see Group 3 of Section 2.3.1). In order to better understand these radiometric data and to estimate the precise orbit of the spacecraft, it is then necessary to compute the observables.

The computation of the observables requires the time and frequency information of the transmitted frequencies at the transmitter. The various time scales and their transformations used for these computation are described in Section 2.4.1. Using the time scale transformations, the reception time  $t_3$  and the transmission time  $t_1$  can be then derived from the light-time delay described in the Section 2.4.2. Using these informations it is then possible to compute the Doppler and range observables as described in Section 2.4.3.

---

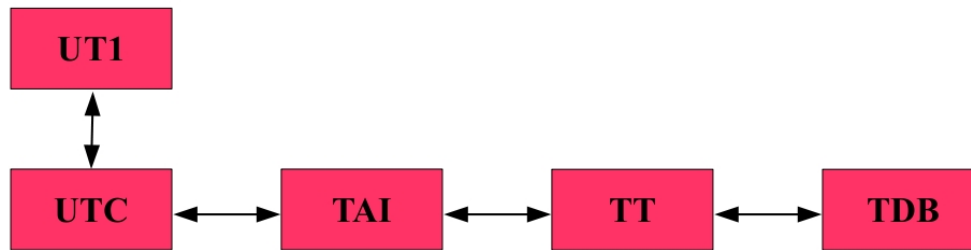


Figure 2.8: Transformation between the time scales.

### 2.4.1 Time scales

As described in Group 3 of Section 2.3.1, the given time in the ODF is measured in UTC from 0 hours, 1 January 1950. However, the orbital computations of the celestial body and the artificial satellite are described in TDB. Therefore, it is necessary to transform the given UTC time into TDB. The transformation between these time scales is give in Figure 2.8.

#### 2.4.1.1 Universal Time (UT or UT1)

UT1 (or UT) is the modern equivalent of mean solar time. It is defined through the relationship with the Earth rotation angle (formerly through sidereal time), which is the Greenwich hour angle of the mean equinox of date, measured in the true equator of date. Owing the Earth rotation rate which is slightly irregular for geophysical reasons and is gradually decreasing, the UT1 is not uniform. Hence, this makes Universal Time (UT1) unsuitable for use as a time scale in physics applications.

#### 2.4.1.2 Coordinated Universal Time (UTC)

Coordinated Universal Time (UTC) is the basis of civilian time which is the standard time for 0° longitude along the Greenwich meridian. Since January 1, 1972, UTC is given in unit of SI seconds and has been derived from the International Atomic Time (TAI). UTC is close to UT1 and maintained within 0.90 second of the observed UT1 by adding a positive or negative leap second to UTC. Figure 2.9 shows the time history of the  $\Delta UT1$  since 1962, which can be defined as the time scale difference between UT1 and UTC:

$$\Delta UT1 = UT1 - UTC \quad (2.12)$$



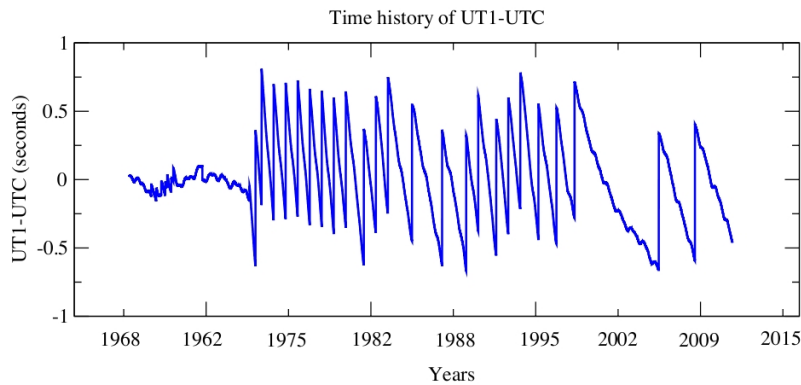


Figure 2.9: Time history of the  $\Delta UT1$  since 1962. These values of  $\Delta UT1$  are extracted from EOP file.

The  $\Delta UT1$  can be extracted from the Earth Orientation Parameters (EOP)<sup>2</sup> file and at any given time,  $\Delta UT1$  can be obtained by interpolating this file.

### 2.4.1.3 International Atomic Time (TAI)

The International Atomic Time (TAI) is measured in the unit of SI second and defined the duration of 9,192,631,770 periods of the radiation corresponding to the transition between the two hyperfine levels of the ground state of the caesium 133 atom (Moyer, 2003). TAI is a laboratory time scale, independent of astronomical phenomena apart from having been synchronized to solar time. TAI is obtained from a worldwide system of synchronized atomic clocks. It is calculated as a weighted average of times obtained from the individual clocks, and corrections are applied for known effects.

TAI is ahead of UTC by an integer number of seconds. The Figure 2.10 shows the time history of the difference between TAI and UTC time scales  $\Delta TAI$  since 1973. The value of the  $\Delta TAI$  can be extracted from the International Earth Rotation and Reference Systems Service (IERS)<sup>3</sup> and it given by

$$\Delta TAI = TAI - UTC \quad (2.13)$$

<sup>2</sup><http://www.iers.org/IERS/EN/DataProducts/EarthOrientationData>

<sup>3</sup><http://www.iers.org/>

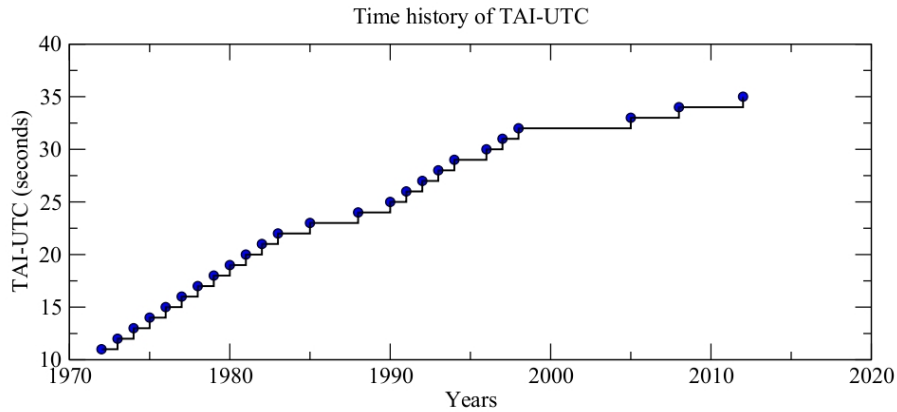


Figure 2.10: Time history of the  $\Delta$ TAI since 1973.

#### 2.4.1.4 Terrestrial Time (TT)

TT is the theoretical time scale for clocks at sea-level. In a modern astronomical time standard, it defined by the IAU as a measurement time for astronomical observations made from the surface of the Earth. TT runs parallel to the atomic timescale TAI and it is ahead of TAI by a certain number of seconds which is given as

$$TT - TAI = 32.184s \quad (2.14)$$

From Figure 2.8 and from Eqs. 2.13 and 2.14, one can transform the time scale from UTC to TT or from TT to UTC.

#### 2.4.1.5 Barycentric Dynamical Time (TDB)

TT and Geocentric Coordinate Time (TCG) are the geocenter time scales to be used in the vicinity of the Earth, while Barycentric Coordinate Time (TCB) and TDB are the solar system barycentric time scales to be used for planetary ephemerides or interplanetary spacecraft navigation. Transformation between these time scales are plotted in Figure 2.11.

The geocentric coordinate time, TCG, is appropriate for theoretical studies of geocentric ephemerides and differ from the TT by a constant rate with linear transformation (McCarthy and Petit, 2004):

$$TCG - TT = L_G \times (JD - T_0) \times 86400 \quad (2.15)$$

where  $L_G = 6.969290134 \times 10^{-10}$ ,  $T_0 = 2443144.5003725$ , and JD is TAI measured in Julian days.  $T_0$  is JD at 1977 January 1, 00h 00m 00s TAI. The time-scale used in the ephemerides of planetary spacecraft, as well as that of solar system bodies, is the barycentric dynamical time,

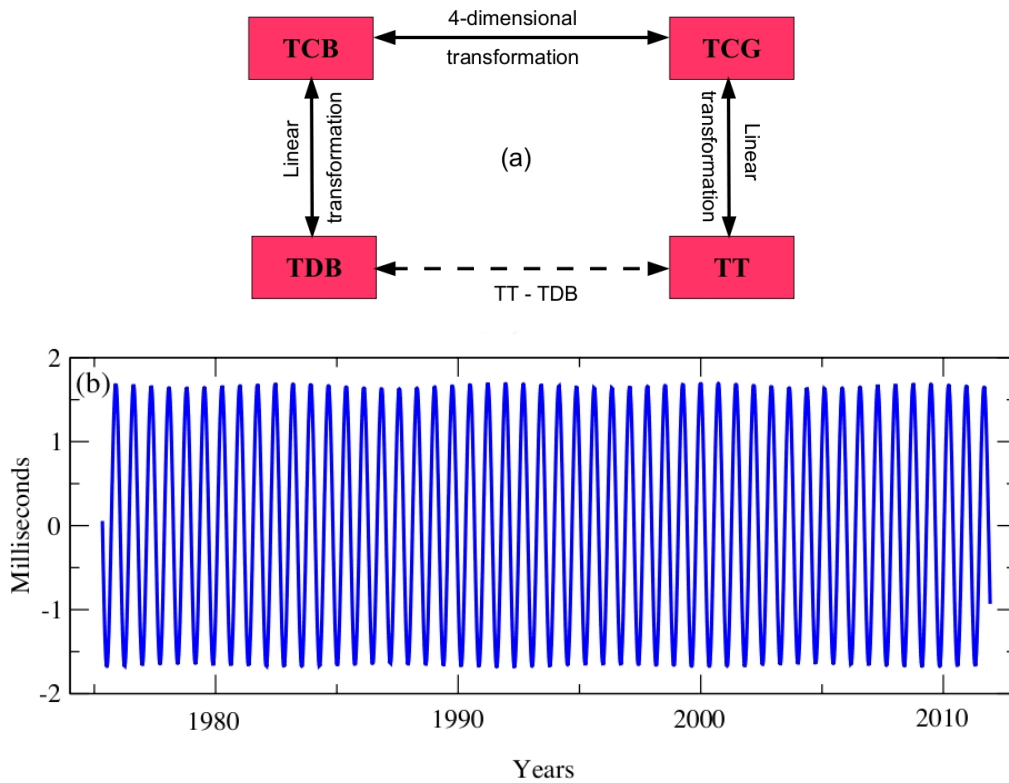


Figure 2.11: Panels: (a) transformations of various coordinate time scales, (b) time history of TT - TDB.

TDB, a scaled version of the barycentric coordinate time, TCB, (the time coordinate of the IAU space-time metric BCRS) (Klioner, 2008). The TDB stays close to TT ( $< 2\text{ms}$ , see panel *b* of Figure 2.11) on the average by suppressing a drift in TCB due to the combined effect of the terrestrial observer orbital speed and the gravitational potential from the Sun and planets by applying a linear transformation (McCarthy and Petit, 2004):

$$\text{TCB} - \text{TDB} = L_B(\text{JD} - T_0) \times 86400 - \text{TDB}_0 \quad (2.16)$$

where  $T_0 = 2443144.5003725$ ,  $L_B = 1.550519768 \times 10^{-8}$ ,  $\text{TDB}_0 = -6.55 \times 10^5$  s, and JD is the TCB Julian date which is  $T_0$  for the event 1977 January 1, 00h 00m 00s TAI.

The barycentric coordinate time, TCB, is appropriate for applications where the observer is imagined to be stationary in the solar system so that the gravitational potential of the solar system vanishes at their location and is at rest relative to the solar system barycenter (Klioner, 2008). The transformation from TCG to TCB thus takes account of the orbital speed of the geocenter and the gravitational potential from the Sun and planets. The difference between TCG and TCB involves a full 4-dimensional GR transformation (McCarthy and Petit, 2004):

$$\text{TCB} - \text{TCG} = c^{-2} \left\{ \int_{t_0}^t \left[ \frac{v_e^2}{2} + U_{\text{ext}}(\vec{x}_e) \right] dt + \vec{v}_e \cdot (\vec{x} - \vec{x}_e) \right\} + O(c^{-4}) \quad (2.17)$$

where  $\vec{x}_e$  and  $\vec{v}_e$  are the barycentric position and velocity of the geocenter, the  $\vec{x}$  is the barycentric position of the observer and  $U_{\text{ext}}$  is the Newtonian potential of all of the solar system bodies apart from the Earth, evaluated at the geocenter. In this formula,  $t$  is TCB and  $t_0$  is chosen to be consistent with 1977 January 1, 00h 00m 00s TAI. The neglected terms,  $O(c^{-4})$ , are of order  $10^{-16}$  in rate for terrestrial observers.  $U_{\text{ext}}(\vec{x}_e)$  and  $\vec{v}_e$  are all ephemeris-dependent, and so the resulting TCB belongs to that particular ephemeris, and the term  $\vec{v}_e \cdot (\vec{x} - \vec{x}_e)$  is zero at the geocenter.

The all above set of Equations 2.15-2.17 are precisely modeled in INPOP. The numerical integration has been performed to obtain a realization of Equation 2.17 with a nanosecond accuracy (Fienga et al., 2009). The difference between TT-TDB therefore can be extracted at any time from the INPOP planetary ephemeris using the tool called calceph<sup>4</sup>. The spacecraft orbit determination software GINS (see Section 2.5), integrates the equations of motion in the specific coordinate time called, ephemeris time (ET). In GINS, this time is also referred to as TDB, as defined by Moyer (2003). As discrepancies between TT and TDB or ET are smaller than 2 ms (see panel *b* of Figure 2.11), the transformation between the time scales defined either in INPOP or GINS are analogous and show consistency between both software.

## 2.4.2 Light time solution

The light time solution is used to compute the one-way or round-trip light time of the signal propagating between the tracking station on the Earth and the spacecraft. In order to compute the Doppler and range observables, the first step is to obtain the light time solution. This solution can be modeled by computing the positions and velocities of the transmitter at the transmitting time  $t_1(\text{TDB})$ , spacecraft at the bouncing time  $t_2(\text{TDB})$  (for round-trip) or transmitting time  $t_2(\text{TDB})$  (for one-way), and receiver at the receiving time  $t_3(\text{TDB})$ .

For round-trip light time, spacecraft observations involve two tracking stations, a transmitter, and a receiver which may not be at the same location. Therefore, two light time solutions must be computed, one for up-leg of the signal (transmitter to spacecraft) and one for down-leg (spacecraft to receiver). However, one-way light time requires only single solution because the signal is transmitting by the spacecraft to the receiver. These solutions can be obtained in the Solar system barycenter space-time reference frame for a spacecraft located anywhere in the Solar system.

Since spacecraft observations are usually given at receiver time UTC (see section 2.3.1), the computation sequence therefore works backward in time: given the receiver time  $t_3(\text{UTC})$ ,

<sup>4</sup><http://www.imcce.fr/inpop/calceph/>

bouncing or transmitting time  $t_2(TDB)$  can be computed iteratively, and using this result, transmitter time  $t_1(UTC)$  is also computed iteratively. The total time delay for the round-trip signal is then computed by summing the two light time solutions (up-leg and down-leg).

The procedure for modeling the spacecraft light time solution can be divided in several steps as discussed below:

#### 2.4.2.1 Time conversion

- As discussed in the Section 2.3.1, the spacecraft observations are given in the receiver time  $t_3(UTC)$ . However, participants (transmitter, spacecraft, and receiver) state vectors (position and velocity) are must be computed in TDB. Thus, given receiver time  $t_3(UTC)$  can be transformed into receiver time  $t_3(TDB)$  as described in Section 2.4.1.

#### 2.4.2.2 Down-leg $\tau_U$ computation

- Figure 2.12 represents the schematic diagram of the vector relationship between the participants. From this figure, the Solar system barycentric C state vector  $r_3^C(t_3)$  of the Earth tracking station at receiver time  $t_3(TDB)$  can be calculated by,

$$r_3^C(t_3) = r_E^C(t_3) + r_3^E(t_3) \quad (2.18)$$

where superscript and subscript are correspond to the Solar system barycenter C and the Earth geocenter E. The vector  $r_E^C(t_3)$  is the state vectors of the Earth relative to Solar system barycenter C which can be obtained from the planetary ephemerides. The geocentric space-fixed state vectors  $r_3^E(t_3)$  of the Earth tracking station can be calculated using proper formulation which includes Earth precession, nutation, polar motion, plate motion, ocean loading, Earth tides, and plot tide. The detail of this formulation can be find in [Moyer \(2003\)](#).

- The transmission time  $t_2(TDB)$  and the corresponding state vectors of the spacecraft has to compute through the iterative process. In order to start the iterations, first approximation of transmission time  $t_2(TDB)$  can be taken as the reception time  $t_3(TDB)$ . Hence, using this approximation and the geometric relationship between the vectors as shown in Figure 2.12, one can compute the spacecraft state vectors relative to the Solar system barycenter  $r_2^C(t_2)$  using the spacecraft and planetary ephemerides. The approximated down-leg time delay  $\tau_D$  required by the signal to reach the spacecraft from the Earth receiving station can be then computed as,

$$r_2^C(t_2) = \left[ r_B^C(t_2) + r_2^B(t_2) \right]_{t_2=t_3} \quad (2.19)$$

$$\tau_D \approx \frac{1}{c} \left[ \left| r_2^C(t_2) - r_3^C(t_3) \right| \right]_{t_2=t_3} \quad (2.20)$$

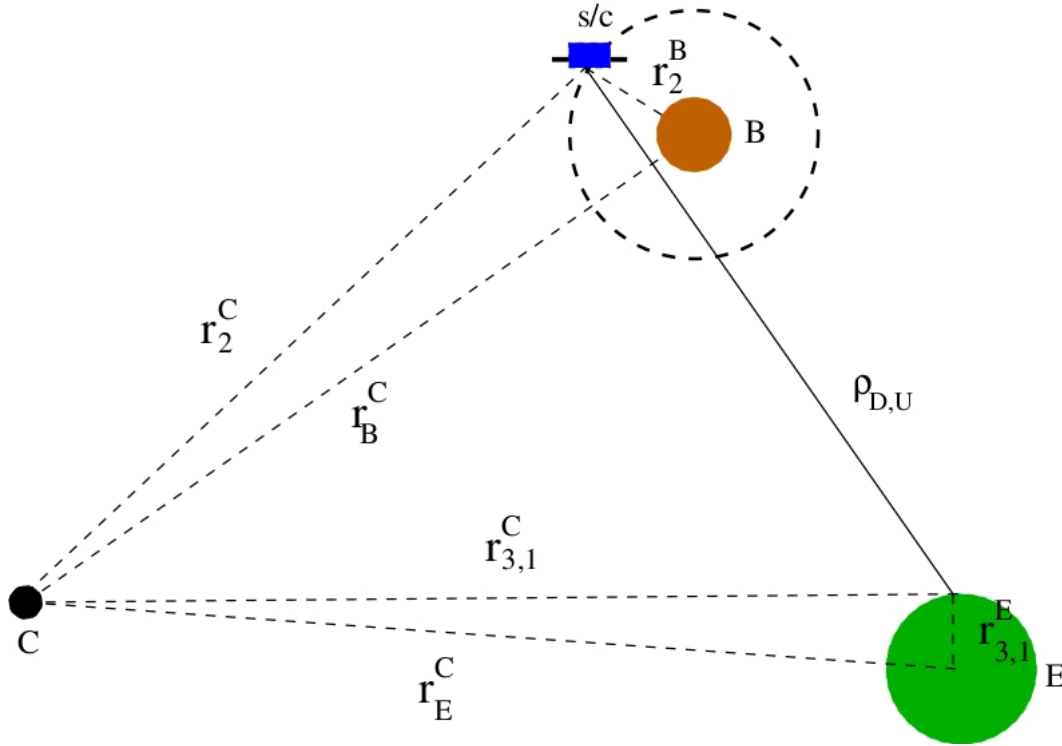


Figure 2.12: Geometric sketch of the vectors involved in the computation of the light time solution, where  $C$  is the solar system barycentric;  $E$  is the Earth geocenter; and  $B$  is the center of the central body.

where superscript  $B$  represents the central body of the orbiting spacecraft. The vector  $r_B^C(t_2)$  given in Eq. 2.19 is the state vector of the central body relative to the Solar system barycenter obtained from the planetary ephemerides. While,  $r_2^B(t_2)$  is the spacecraft state vectors relative to center of the central body computed from the spacecraft ephemerides. In Eq. 2.20,  $c$  is the speed of light and  $\tau_D$  is the down-leg time delay which can be computed through the Eqs. 2.19 and 2.18. An estimated value of the bouncing time  $t_2$  can be then computed as,

$$t_2 = t_3 - \tau_D \quad (2.21)$$

- Now using this result, we can then estimate the barycentric position of the spacecraft at bouncing time  $t_2$ . Hence, the down-leg vector  $\rho_D$  as shown in Figure 2.12 can be then obtained as,

$$\rho_D = r_2^C(t_2) - r_3^C(t_3) \quad (2.22)$$

The improved value of the down-leg time delay  $\tau_D$ , in seconds, can be then estimated as,

$$\tau_D = \frac{1}{c}(|\rho_D|) + \delta\tau_D \quad (2.23)$$

where  $\delta\tau_D$  is a down-leg light time corrections which includes the relativistic, solar corona, and media contributions to the propagation delay. Furthermore, Eqs. 2.21 to

2.23 need to iterate until the latest estimate of  $\tau_D$  differs from the previous estimate by some define value such as  $0.05\mu$ .

### 2.4.2.3 Up-leg $\tau_U$ computation

- For round-trip light time solution, next is to compute the up-leg time delay. A similar iterative procedure as used for down-leg solution can be used the up-leg solution. Up-leg time delay  $\tau_U$  which represents the time required for signal to travel between the spacecraft and the Earth transmitting station. In order to begin the iterations, first approximation can be assumed as,

$$\tau_U \approx \tau_D \quad (2.24)$$

Therefore, while using Eq. 2.24, approximated transmitting time  $t_1(TDB)$  can be then computed as,

$$t_1 = t_2 - \tau_U \quad (2.25)$$

- The barycentric state vectors of the transmitting station  $r_1^C(t_1)$  at transmitted time  $t_1(TDB)$  as shown in Figure 2.12 can be computed from Eq. 2.18 by replacing the 3 with 1, that is,

$$r_1^C(t_1) = r_E^C(t_1) + r_1^E(t_1) \quad (2.26)$$

Now, using Eq. 2.26, one can compute the up-leg state vector as give by,

$$\rho_U = r_2^C(t_2) - r_1^C(t_1) \quad (2.27)$$

where  $r_2^C(t_2)$  is the barycentric position of the spacecraft at bouncing time  $t_2(TDB)$  and can be calculated from Eq. 2.19. Finally, the new estimation of the up-leg time delay  $\tau_U$ , in seconds, is given by,

$$\tau_U = \frac{1}{c}(|\rho_U|) + \delta\tau_U \quad (2.28)$$

where  $\delta\tau_U$  is the up-leg light time correction analogous to  $\delta\tau_D$  of Eq. 2.23. Eqs. 2.25 to 2.28 are then need to iterative until the convergence is achieved.

### 2.4.2.4 Light time corrections, $\delta\tau_D$ and $\delta\tau_U$

#### 2.4.2.4.1 Relativistic correction $\delta\tau_{RC}$

Electromagnetic signals that are traveling between the spacecraft and the Earth tracking encounters light time delay when it passes close to the massive celestial bodies. This effects is known as *Shapiro delay* or gravitational time delay (Shapiro, 1964). Such time delays are caused by the bending of the light path which increase the travailing path of the signal. Hence,

relativistic time delays caused by the gravitational attraction of the bodies can be expressed, in seconds, as (Shapiro, 1964; Moyer, 2003),

$$\begin{aligned} \delta\tau_{RC_U} = & \frac{(1 + \gamma) \mu_S}{c^3} \ln \left[ \frac{r_1^S + r_2^S + r_{12}^S + \frac{(1+\gamma) \mu_S}{c^2}}{r_1^S + r_2^S - r_{12}^S + \frac{(1+\gamma) \mu_S}{c^2}} \right] \\ & + \sum_{B=1}^{10} \frac{(1 + \gamma) \mu_B}{c^3} \ln \left[ \frac{r_1^B + r_2^B + r_{12}^B}{r_1^S + r_2^S - r_{12}^S} \right] \end{aligned} \quad (2.29)$$

where superscript  $S$  and  $B$  correspond to the Sun and the celestial body.  $r_1$ ,  $r_2$ , and  $r_{12}$  are the distance between the spacecraft and the Sun  $S$  (or celestial body  $B$ ), the Earth station and the Sun  $S$  (or celestial body  $B$ ), and the spacecraft and the Earth station, respectively. The  $\mu_S$  and  $\mu_B$  are the gravitational constant of the Sun and the celestial body, respectively.

For round-trip signal, Eq. 2.29 represents the relativistic time delay  $\delta\tau_{RC_U}$  relative to the up-leg of the signal. The corresponding down-leg relativistic time delay  $\delta\tau_{RC_D}$  can be calculate using the same equation by replacing the 1 with 2 and 2 with 3. Hence, the total relativistic time delay, in seconds, during the round-trip of the signal can be given as,

$$\delta\tau_{RC} = \delta\tau_{RC_U} + \delta\tau_{RC_D} \quad (2.30)$$

#### 2.4.2.4.2 Solar Corona correction $\delta\tau_{SC}$

As mentioned in Section 2.2.3, solar corona severely degrades the radio wave signals when propagating between spacecraft and Earth tracking stations. The delay owing to the solar corona are directly proportional to the total electron contents along the LOS and inversely with the square of carrier radio wave frequency. Solar corona model for computing such delays for each legs are described in Chapter 3. The total round-trip solar corona delay, in seconds, can be written as,

$$\delta\tau_{SC} = \delta\tau_{SC_U} + \delta\tau_{SC_D} \quad (2.31)$$

#### 2.4.2.4.3 Media corrections $\delta\tau_{MC}$

The media corrections consist of Earth's troposphere correction and the correction due to the charge particles of the Earth ionosphere. Such delays however relatively lesser compare to the relativistic and solar corona delays. The tropospheric model used for computing these corrections for each legs are discussed in Chao (1971); Moyer (2003). The total round-trip media correction, in seconds, can be written as,

$$\delta\tau_{MC} = \delta\tau_{MC_U} + \delta\tau_{MC_D} \quad (2.32)$$

Figure 2.13 shows an example of relativistic correction and solar corona correction to light time solution for MGS and MESSENGER spacecraft.



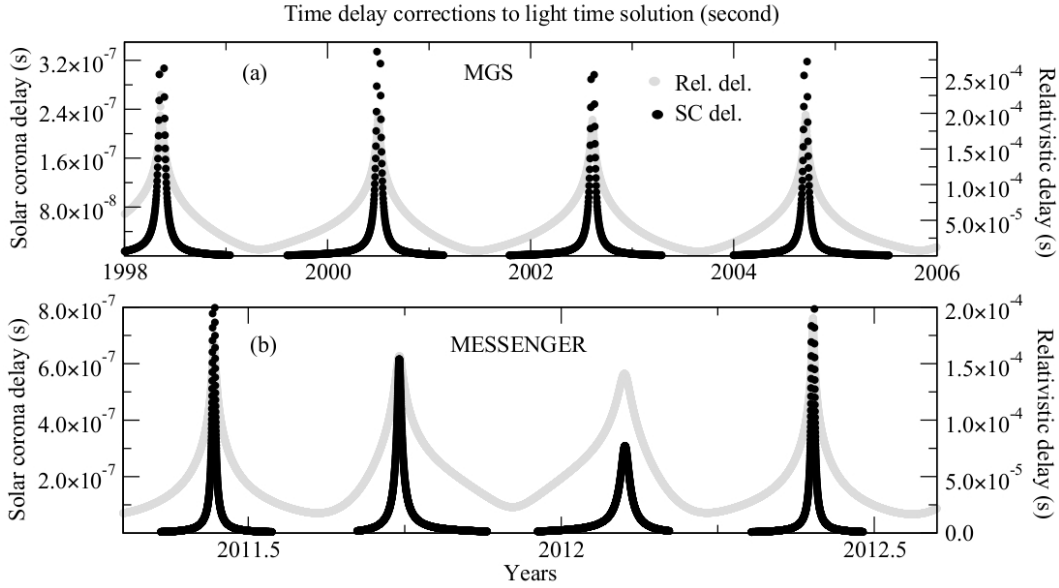


Figure 2.13: Relativistic and solar corona corrections to light time solution (expressed in seconds): (a) for MGS, (b) for MESSENGER.

### 2.4.2.5 Total light time delay

#### 2.4.2.5.1 Round-trip delay

The total round-trip delay is the sum of number of terms, that includes,

$$\begin{aligned}
 \rho = & (\tau_D + \tau_U) - (TDB - TAI)_{t_3} + (TDB - TAI)_{t_1} \\
 & - (TAI - UTC)_{t_3} + (TAI - UTC)_{t_1} \\
 & + \delta\rho_U + \delta\rho_D
 \end{aligned} \tag{2.33}$$

where quantities  $\delta\rho_D$  and  $\delta\rho_U$  are the downlink delay at receiver and uplink delay at transmitter (see Group 3 of Section 2.3.1), respectively. The time differences given in Eq. 2.33 can be obtained as described in Section 2.4.1, while  $\tau_D$  and  $\tau_U$  can be obtained from Eqs. 2.23 and 2.28 respectively. Figure 2.14 illustrates an example for the total round-trip time that required by the signal to travel from the transmitter to the spacecraft (up-leg) and then from the spacecraft to the receiver (down-leg). This time solution shown in Figure 2.14 corresponds to MGS (panel a) and MESSENGER (panel b) spacecraft.

#### 2.4.2.5.2 One-way delay

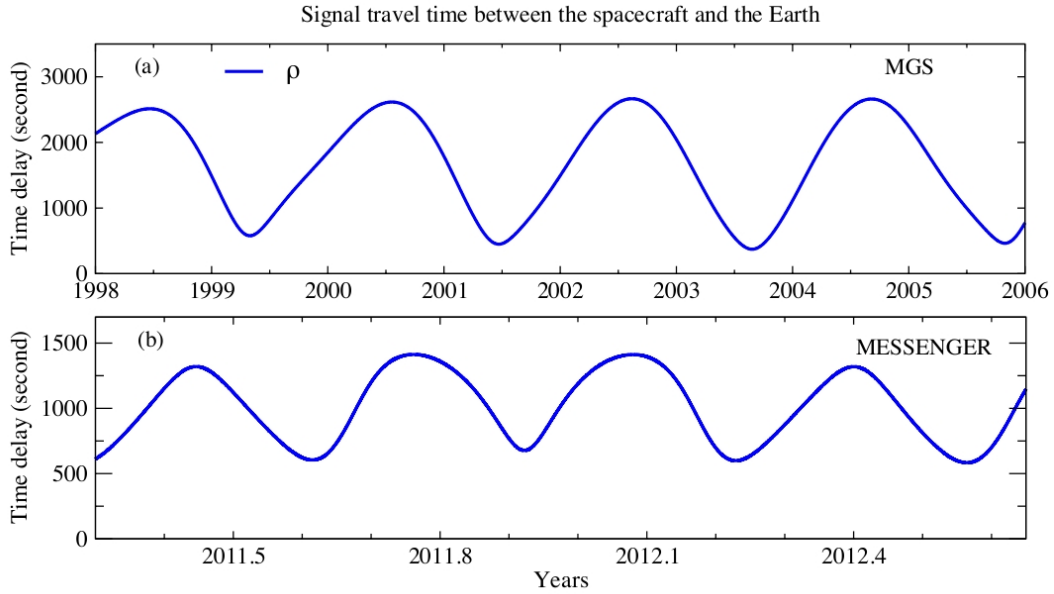


Figure 2.14: Round-trip light time solution of MGS (panel *a*) and MESSENGER (panel *b*) spacecraft, computed from the Eq. 2.33.

One-way light, in seconds, which is used to calculate the one-way Doppler observables can be calculated as,

$$\hat{\rho}_1 = \rho_1 + (\text{TDB} - \text{TAI})_{t_2} \quad (2.34)$$

where  $\rho_1$  is the difference between reception time  $t_3(\text{UTC})$  and the spacecraft transmitter time  $t_2(\text{TDB})$ .

### 2.4.3 Doppler and range observables

The radiometric data obtained by the Earth tracking station (DSN) usually consists of three kind of measurements (one-way Doppler, two/three-way Doppler, and two-way range). The detail description of these measurements and other contents of the ODF that are useful for recognize the data are described in Section 2.3.1. Observation model which computes the observations requires the time history of the transmitted frequency at the transmitter. Such time history which contains transmitter time  $t_1(\text{UTC})$  and receiver time  $t_3(\text{UTC})$ , can be obtained as described in Section 2.4.2. The corresponding transmitter frequency which can be obtained from the different forms of given frequency in ODF is described in Group 3 of Section 2.3.1.

One of the most important aspect of precise orbit determination of the spacecraft is to compute the observables. These observables require spacecraft ephemerides which can be constructed from the dynamic modeling (see Section 2.5). An observation model accounts the propagation of signal and allows to compute the frequency change between received and transmitted signal, also called *Doppler shift*. The difference between observed (given in ODF) and

computed values, also called residuals, are then used to adjust the dynamic model along with observation model for accounting the discrepancy in the models.

This section contains the formulations for computing the one-way Doppler, two/three-way Doppler, and two-way range observables. These formulations are based on Moyer (2003). The motivation for developing an observation model is to have a better understanding of the radiometric data. However, for precise computation, such as for MGS (see Chapter 3) and for MESSENGER (see Chapter 5), GINS orbit determination model (see Section 2.5) has been used. Moreover, GINS observation model is also based on Moyer (2003) formulations and the brief overview of the GINS dynamic model is described in Section 2.5.

### 2.4.3.1 Two-way ( $F_2$ ) and Three-way ( $F_3$ ) Doppler

#### 2.4.3.1.1 Ramped

Doppler observable can be derived from the difference between the number of cycles received by a receiving station and the number of cycles produced by a fixed or ramped known reference frequency  $f_{REF}$ , during a specific count interval  $T_c$ . The given observables time-tag  $TT$  in the ODF is the mid-point of the count interval  $T_c$  (see Group 3 of Section 2.3.1). To compute these observables (Eq. 2.40), it is thus necessary to obtain the starting time  $t_{3_s}(UTC)$  and the ending time  $t_{3_e}(UTC)$  of the count interval, which is given in seconds by

$$t_{3_s}(UTC) = TT - \frac{1}{2} T_c \quad (2.35)$$

$$t_{3_e}(UTC) = TT + \frac{1}{2} T_c \quad (2.36)$$

where  $TT$  and  $T_c$  can be extracted from the ODF. Using Eqs. 2.35 and 2.36 the corresponding transmitting starting time  $t_{1_s}(UTC)$  and ending time  $t_{1_e}(UTC)$ , in seconds, can be obtained from light time solution (see Section 2.4.2), that is,

$$t_{1_s}(UTC) = t_{3_s}(UTC) - \rho_s \quad (2.37)$$

$$t_{1_e}(UTC) = t_{3_e}(UTC) - \rho_e \quad (2.38)$$

where  $\rho_s$  and  $\rho_e$  is the round-trip light time computed from Eq. 2.33. Similarly, the corresponding start and end TDB at the receiving station and at the transmission station, which are required for the light time solution, can be computed as described in Section 2.4.1.

Using the time recorded history of the transmitters, the two-way Doppler  $F_2$  and three-way Doppler  $F_3$  can be computed as the difference in the total accumulation of the Doppler cycles, which is given as, in Hz,

$$F_{2,3} = \frac{1}{T_c} \left[ \int_{t_{3s}}^{t_{3e}} f_{REF}(t_3) dt_3 - \int_{t_{1s}}^{t_{1e}} f(t_1) dt_1 \right] \quad (2.39)$$

where  $f_{REF}(t_3)$  and  $f(t_1)$  can be computed from the Eqs. 2.2 and 2.3. The all time scales given in Eq. 2.39 correspond to UTC. Now by substituting Eqs. 2.2 and 2.3 into Eq. 2.39 gives, in Hz:

$$F_{2,3} = \frac{M_{2R}}{T_c} \int_{t_{3s}}^{t_{3e}} f_T(t_3) dt_3 - \frac{M_2}{T_c} \int_{t_{1s}}^{t_{1e}} f_T(t_1) dt_1 \quad (2.40)$$

where  $M_{2R}$  and  $M_2$  are the spacecraft turnaround ratio which is given in Table 2.2. The transmitter frequency  $f_T(t_1)$  at the transmitting station on Earth is ramped and can be obtained from the ramped table using Eq. 2.11. However, the transmitter frequency  $f_T(t_3)$  at receiving station can be fixed or ramped. If it is ramped then it can be obtained from the ramped table using Eq. 2.11 and for fixed, Eq. 2.40 can be re-written as, in Hz:

$$F_{2,3} = M_{2R} f_T(t_3) - \frac{M_2}{T_c} \int_{t_{1s}}^{t_{1e}} f_T(t_1) dt_1 \quad (2.41)$$

In order to compute the observables, it is necessary to solve the integrations given in Eq. 2.40. Let us assume that,  $W$  is the precision width of the interval of the integration, in seconds, which is  $T_c$  for reception interval and  $T_c^T$  for the transmission interval, and can be expressed as, in seconds:

$$T_c^T = t_{1e} - t_{1s} \quad (2.42)$$

Furthermore, let  $t_s$  be the starting time of the interval of integration which is  $t_{3s}(UTC)$  for the reception and  $t_{1s}(UTC)$  for the transmission. Similarly corresponding end time can be denoted as  $t_e$ . Each ramp of the ramp table given in the ODF is specified by the start time  $t_0$  and end time  $t_f$  for each participating Earth stations (see Group 3 of Section 2.3.1). The interval of the integration can be covered by one or more ramps (let say  $n$  ramps). Figure 2.15 illustrates the above assumptions and the technique used for computing the integration of Eq. 2.40. In Figure 2.15,  $t_{start}$  and  $t_{end}$  is the starting and ending time of the ramp table respectively. Now using Figure 2.15 and above made assumptions, one can compute the observables as follows:

1. Compute the transmitter frequency at the start time  $t_s$  of the integration using the first ramp (see Figure 2.15) transmitter frequency. It can be achieved by using the Eq. 2.11. Therefore, the new transmitter frequency can be given as, in Hz:

$$f_0(t_s) = f_0(t_0) + \dot{f}(t_s - t_0) \quad (2.43)$$

where  $\dot{f}$  is the corresponding frequency rate of first ramp expressed in Hz/s.

2. If the interval of integration  $W$  contains the two or more ramp as shown in Figure 2.15, then calculates the width of each ramp  $i$  except the last ramp:

$$W_i = t_f - t_0 \quad (2.44)$$

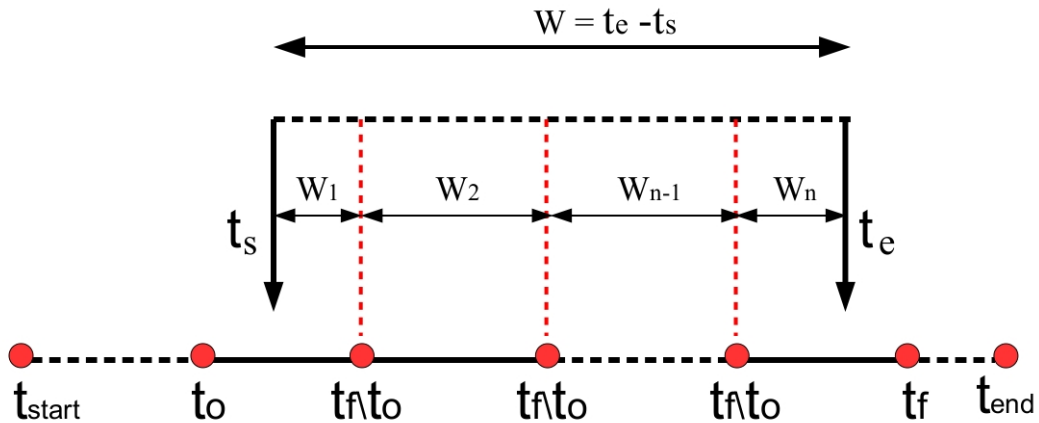


Figure 2.15: The technique used for computing the integration of Eq. 2.40.  $W$  is the precision width of the interval of the integration, and  $t_{start}$  and  $t_{end}$  is the start and end times of the ramp table (see Section 2.4.3.1).

where  $t_f$  and  $t_0$  are the start and end times, in seconds, of each ramp (see Figure 2.15). Last ramp precision width  $W_n$  therefore computed as:

$$W_n = W - \sum_{i=1}^{n-1} W_i \quad (2.45)$$

If the interval of the integration  $W$  only contains the single ramp ( $n=1$ ), then the precision width is given as:

$$W_{n=1} = W \quad (2.46)$$

3. Calculate the average of the transmitter frequency  $f_i$  for each ramp, in Hz:

$$f_i = f_0 + \frac{1}{2} \dot{f} W_i \quad (2.47)$$

where  $f_0$  is the transmitter frequency at the each start time  $t_s$  of the ramp (see Figure 2.15) and  $\dot{f}$  is the corresponding frequency rate. Ramp width  $W_i$  for each ramp can be obtained from Eq. 2.44.

4. The integral of the transmission frequency over the reception of transmission interval  $W$  can be then obtained as:

$$\int_{t_s}^{t_e} f_T(t) dt = \sum_{i=1}^n f_i W_i \quad \text{cycles} \quad (2.48)$$

#### 2.4.3.1.2 Unramped

As mentioned earlier, the given transmitter frequency can be constant or ramped. If it is constant, then it corresponds to the unramped transmitter frequency. Let us consider that, during an interval  $dt_1$ ,  $dn$  cycles of the constant transmitter frequency  $f_T(t_1)$  are transmitted. During the corresponding reception interval  $dt_3$ , receiving station on Earth received  $M_2 dn$  cycles, where  $M_2$  is the spacecraft turnaround ration (see Table 2.2). Therefore, the total accumulation of the constant Doppler cycles is given as, in Hz:

$$F_{2,3} = \frac{M_2 f_T(t_1)}{T_c} \left[ \int_{t_{3s}}^{t_{3e}} dt_3 - \int_{t_{1s}}^{t_{1e}} dt_1 \right] \quad (2.49)$$

where  $t_{3s}$  and  $t_{3e}$  are the start and end times of the reception time-tag  $TT$  which can be computed from Eqs. 2.35 and 2.36 respectively. Similarly  $t_{1s}$  and  $t_{1e}$  are the corresponding transmitting times which can be computed from Eqs. 2.37 and 2.38 respectively. All the time given in Eq. 2.49 are in UTC.

Now evaluating Eq. 2.49:

$$F_{2,3} = \frac{M_2 f_T(t_1)}{T_c} \left\{ [t_{3e} - t_{1e}] - [t_{3s} - t_{1s}] \right\} \quad (2.50)$$

Eq. 2.50 can be used to calculate the computed values of unramped two-way  $F_2$  and three-way  $F_3$  Doppler observables, in Hz.

### 2.4.3.2 One-way ( $F_1$ ) Doppler

When the radio signal is continuously transmitted from the spacecraft and received by the DSN station on Earth, then the observables are referred to one-way. These observations are always unramped and can be modeled as, in Hz, (Moyer, 2003):

$$F_1 = C_2 f_{T_0} - \frac{1}{T_c} \int_{t_{2s}(TAI)}^{t_{2e}(TAI)} \left[ f_T(t_2) \right] dt_2(TAI) \quad (2.51)$$

where  $C_2$  is the downlink frequency multiplier given in Table 2.3.  $f_{T_0}$  is the nominal value of spacecraft transmitter frequency  $f_{S/C}$  (Eq. 2.5).  $f_T(t_2)$  is the transmitter frequency at the spacecraft at transmission time  $t_2(TAI)$ , given by Eq. 2.4.

Now by substituting Eqs. 2.4 and 2.5 in Eq. 2.51, the one-way Doppler observables can be written as, in Hz:

$$F_1 = C_2 f_{T_0} - \frac{C_2}{T_c} \int_{t_{2s}(TAI)}^{t_{2e}(TAI)} \left[ f_{T_0} + \Delta f_{T_0} + f_{T_1}(t_2 - t_0) + f_{T_2}(t_2 - t_0)^2 \right] dt_2(TAI) \quad (2.52)$$

As one can see in Eq. 2.52, the terms containing the coefficients  $f_{T_1}$  and  $f_{T_2}$  are functions of the spacecraft transmission time  $t_2(TAI)$ . Hence, the upper limit  $t_{2_e}(TAI)$  and lower limit  $t_{2_s}(TAI)$  of the integration are only required to evaluate these terms. Since these terms ( $< 2\text{ms}$ ) are small, the limits of the integration can be replaced with the corresponding values in coordinate time TDB (Moyer, 2003). These coordinate times,  $t_{2_e}(TDB)$  and  $t_{2_s}(TDB)$ , can be obtained from the light time solution (see down-leg computation of Section 2.4.2).

Now by evaluating the integral of Eq. 2.52 using the above approximation it comes (Moyer, 2003), in Hz:

$$F_1 = C_2 f_{T_0} \frac{(\rho_{1_e} - \rho_{1_s} + \Delta)}{T_c} - C_2 \left\{ \Delta f_{T_0} + f_{T_1}(t_{2_m} - t_0) + f_{T_2}(t_{2_m} - t_0)^2 + \frac{f_{T_2}(T'_c)^2}{12} \right\} \frac{T'_c}{T_c} \quad (2.53)$$

where  $\rho_{1_e}$  and  $\rho_{1_s}$  are the one-way light times at the end and at the start of the Doppler count interval  $T_c$  at the receiver. These one-way light times and the time bias  $\Delta$ , expressed in seconds, are given by:

$$\rho_{1_e} = t_{3_e}(\text{UTC}) - t_{2_e}(\text{TDB}) \quad (2.54)$$

$$\rho_{1_s} = t_{3_s}(\text{UTC}) - t_{2_s}(\text{TDB}) \quad (2.55)$$

$$\Delta = (\text{TDB} - \text{TAI})_{t_{2_e}} - (\text{TDB} - \text{TAI})_{t_{2_s}} \quad (2.56)$$

The quadratic coefficients  $\Delta f_{T_0}$ ,  $f_{T_1}$ , and  $f_{T_2}$  given in Eq. 2.53 are specified by time block with start a time  $t_0$ . In Eq. 2.53,  $T'_c$  is the transmission interval at the spacecraft and  $t_{2_m}$  is the average of the TDB values of the epochs at the start and end of the transmission interval at the spacecraft. These can expressed as, in seconds:

$$T'_c = T_c - (\rho_{1_e} - \rho_{1_s} + \Delta) \quad (2.57)$$

$$t_{2_m} = \frac{t_{2_e}(\text{TDB}) + t_{2_s}(\text{TDB})}{2} \quad (2.58)$$

### 2.4.3.3 Two-way ( $\rho_{2,3}$ ) Range

In addition to Doppler data, ODF also contains the range data as described in section 2.3.1. These data sets usually are not included in the orbit determination process. However, processing of range data along with orbit determination are extremely useful for the improvement of the planetary ephemerides. This section will give the formulation for computing the two-way ramp range observables.

The range observables given in ODF are uniquely given in the range units. The conversion factor  $F$  required to convert seconds into range units is a function of the transmitter signal

Table 2.4: Constant  $C_{range}$  required for converting second to range units.

Type	$C_{range}$	
S-Band	$\frac{1}{2}$	a: for uplink X-band at a 34-m mount high efficiency (HEF) antenna.
X-Band <sup>a</sup> , HEF	$\frac{11}{75}$	b: for uplink X-band at any tracking station that as a block 5 exciter (BVE).
X-Band <sup>b</sup> , BVE	$\frac{221}{1496}$	

frequency  $f_T$  and a constant fraction depending on the uplink band (Moyer, 2003). The integral of  $F dt$  at the transmitting station gives the change in the phase of the transmitted ranging pulse (uniquely coded in range units) at its transmission time. When the spacecraft receives the ranging pulse, it returns the pulse on its downlink. The time needed by the spacecraft to turn the pulse around within its electronics is called transponder delay which is different for each spacecraft. When the pulse is received at the Earth station, the actual light time is determined including the light time delay corrections described in section 2.4.2. In addition it also includes the delays due to the transmitter and receiver electronics at the Earth station and the delay in the spacecraft transponder.

The equation for calculating the conversion factor  $F$  at the transmitting or receiving station on Earth is a function of the uplink band at the station. For S-, and X-band transmitter frequency  $f_T$ , is in range units/second:

$$F = C_{range} f_T \quad (2.59)$$

where,  $C_{range}$  is the band based constant given in Table 2.4. The classification of uplink X-band antennas, which may either be mounted as high efficiency (HEF) or as block 5 exciter (BVE), can be obtained from the ODF. The equation for calculating the computed value of 2-way ramped range observable is given by (Moyer, 2003), in modulo  $M$  expressed range units,

$$\rho_2 = \int_{t_1(UTC)}^{t_3(UTC)} F(t) dt \quad (2.60)$$

where  $t_3(UTC)$  is the reception time at the receiving station and  $t_1(UTC)$  is the transmission time at the transmitting station. The conversion factor  $F(t)$  can be calculated from Eq. 2.59 for the corresponding band. Modulo  $M$  is the length of the ranging pulse in range units and it is calculated from:

$$M = 2^{n+6} \quad (2.61)$$

where  $n$  is the component number of the lowest frequency ranging component. The number  $n$  can be obtained from the ODF. The integral of Eq. 2.60 can be evaluated using the same technique as described for two- and three-way ramped Doppler.

The transmitting time  $t_1(UTC)$  given in Eq. 2.60 can be obtained from the light time solution as described in Section 2.4.2. Now by substituting Eq. 2.59 in Eq. 2.60, it will give the time



integral of ramped transmitted frequency  $f_T(t)$ . This integral can be then evaluated by using the algorithms given for Eq. 2.40 by replacing  $t_{3_e}$  or  $t_{1_e}$  with  $t_3$  and  $t_{3_s}$  or  $t_{1_s}$  with  $t_1$ .

## 2.5 GINS: orbit determination software

An accurate orbit determination of the orbiting spacecraft involves an estimation of the positions and velocities of the spacecraft from a sequence of observations, which are functions of the spacecraft position, and velocity. This can be accomplished by integrating the equations of motion, starting from an initial epoch to produce predicted observations. In practice, the initial state (position and velocity) of the spacecraft is never known exactly. However, some physical constants and parameters of the forces (gravitational and non-gravitational) which are required to integrate the equations of motion, are known approximately. Such limit of the knowledge of the motion, would deviate the predicted motion of the spacecraft from the actual motion. The precision of orbit determination results therefore depends on the error in spacecraft dynamic model. To absorb this error, the components of the spacecraft state (position and velocity,

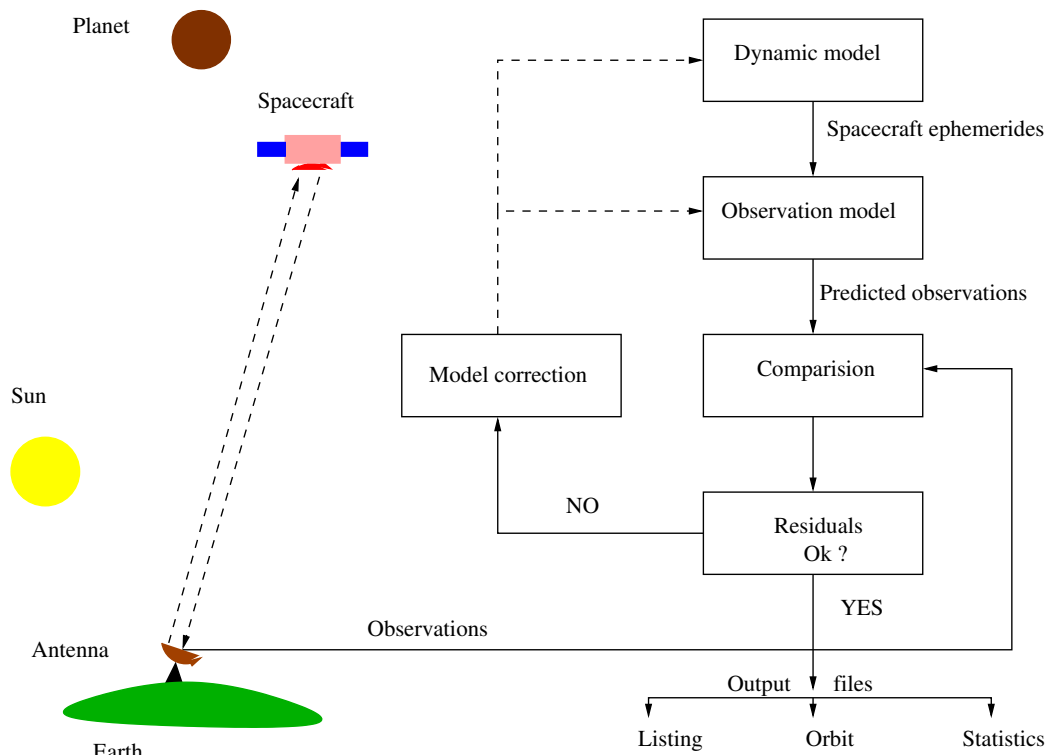


Figure 2.16: The process of the spacecraft orbit determination.

estimated force, and measurement model parameters) at the initial epoch are then re-estimated by comparison to observations in order to minimize the observation residuals (observation - computation). The adjustment of the parameters can be achieved by using iterative least-square

techniques. Hence, it can be summarized that, for the precise orbit determination, one needs a dynamic model which describes the forces acting on the spacecraft, a observational model which is a function of observed parameters and spacecraft state vector, and a least-squares estimation algorithm used to obtain the estimates.

The flow chart of orbit determination based on dynamic model in the frame of GINS software is given Figure 2.16. GINS is an orbit determination software developed by the CNES. This software was initially developed for the Earth orbiting spacecraft and then further developed for the interplanetary spacecraft. GINS numerically integrates the equations of motion and the associated variational equations, and simultaneously retrieves the physical parameters of the force model using an iterative least-squares technique. From Figure 2.16, one can see that, the first step of the orbit determination is to compute the spacecraft ephemerides from the dynamic model of the spacecraft motion. The section 2.5.1 gives a brief description of such dynamic model used in the GINS software for planetary spacecraft. After computing the spacecraft ephemerides, the next step is to predict the observations from the observation model. The formulation associated with the observation model, which may consist to one-, two-, and three-way Doppler and range observables, is described in Section 2.4.3. Finally, the difference between observed and computed observables gives the residuals, which describe the precision in the computations. These residuals are then used to adjust the dynamic and observation models by computing the solve-for parameters using least square techniques described in Section 2.5.3. If the residuals meet the convergence criteria then it produce a three files output: a listing containing the estimated solve-for parameters, an ephemeris of the orbit containing the spacecraft state vectors and its acceleration at each time step of the numerical integration, and statistics of the residuals. The detailed description of GINS software algorithms are given in the [igsac-cnes webpage](http://igsac-cnes.org)<sup>5</sup>.

## 2.5.1 Dynamic model

The dynamic model which consists of equations of motion can be described in an inertial frame as follows:

$$\ddot{\vec{r}} = \vec{a}_g + \vec{a}_{ng} \quad (2.62)$$

where  $\vec{r}$  is the position vector between the center of mass of the spacecraft and the planet,  $\vec{a}_g$  is the sum of gravitational forces acting on the spacecraft, and  $\vec{a}_{ng}$  is the sum of non-gravitational forces acting on the spacecraft.

### 2.5.1.1 Gravitational forces

When the spacecraft is orbiting the planet then the primary force acting of the spacecraft is the force of gravity, specifically, the gravitational attraction of the orbiting planet. However, there

<sup>5</sup>[http://igsac-cnes.cls.fr/documents/gins/GINS\\_Doc\\_Algo\\_V4.html](http://igsac-cnes.cls.fr/documents/gins/GINS_Doc_Algo_V4.html)

are other gravitational forces also which significantly affect the motion of the spacecraft. All these forces can be expressed as:

$$\vec{a}_g = \vec{P}_{pot} + \vec{P}_{tid} + \vec{P}_n + \vec{P}_{rel} \quad (2.63)$$

where

$$\vec{P}_{pot} = \text{perturbation due to the gravitational potential of the planet}$$

$$\vec{P}_{rel} = \text{perturbation due to solid planetary tides}$$

$$\vec{P}_n = \text{perturbation due to the Sun, Moon and planets}$$

$$\vec{P}_{rel} = \text{perturbation due to GR}$$

### 2.5.1.1.1 Gravitational potential

The perturbing forces acting on the spacecraft due to the gravitational attraction of the orbiting planet can be expressed as the gradient of the potential,  $U$ , which satisfies the Laplace equation,  $\nabla^2 U = 0$ , that is:

$$\vec{P}_{pot} = \nabla U \quad (2.64)$$

where  $U$  is the potential due to the solid-body mass distribution. It is generally expressed in terms of a spherical harmonic expansion in a reference system fixed with respect to the planet (Kaula, 1966):

$$U = \frac{GM}{r} + \frac{GM}{r} \sum_{l=0}^L \sum_{m=0}^l \left(\frac{R}{r}\right)^l P_{lm}(\sin \phi) \left(C_{lm} \cos(m\lambda) + S_{lm} \sin(m\lambda)\right) \quad (2.65)$$

where

$$GM = \text{the gravitational constant of the planet}$$

$$P_{lm}(\sin \phi) = \text{the Legendre function of degree } l \text{ and order } m$$

$$C_{lm}, S_{lm} = \text{the dimensionless spherical harmonic coefficients of}$$

degree  $l$  and order  $m$

$R$  = the mean equatorial radius of the planet

$r, \phi, \lambda$  = the spherical coordinates of the spacecraft in a reference system fixed with respect to the planet

$L$  = the maximum number of degree and order

In practice, Eq. 2.65 is usually represented by the normalized spherical harmonic coefficients ( $\bar{C}_{lm}, \bar{S}_{lm}$ ) and normalized Legendre function  $\bar{P}_{lm}$ . The normalized coefficients are much more uniform in magnitude than the unnormalized coefficients. These normalized coefficients are defined by:

$$\begin{Bmatrix} \bar{C}_{lm} \\ \bar{S}_{lm} \end{Bmatrix} = \sqrt{\frac{(l+m)!}{(2-\delta_{0m})(2l+1)(l-m)!}} \begin{Bmatrix} C_{lm} \\ S_{lm} \end{Bmatrix} \quad (2.66)$$

and

$$\bar{P}_{lm} = \sqrt{\frac{(2-\delta_{0m})(2l+1)(l-m)!}{(l+m)!}} P_{lm} \quad (2.67)$$

If one assumes that the reference system origin coincides with center of mass of the planet, then summation of Eq. 2.65 starts from degree ( $l$ ) 2 or  $\bar{C}_{10} = \bar{C}_{11} = \bar{S}_{10} = 0$ .

### 2.5.1.1.2 Solid planetary tides

Since the planet is a non-rigid elastic body, its mass distribution and the shape will be changed under the gravitational attraction of the perturbing bodies. Tides deformations of a planet or natural satellite caused by periodic variations of the local gravity acceleration as the planet or satellite rotates and revolves in the gravity field of a perturbing bodies. Tidal disturbances of a planet are primarily caused by the sun and by its satellites. The temporal variation of the free space geopotential induced from solid planet tides can be expressed as a change in the external geopotential by the following expression (Wahr, 1981; Dow, 1988)

$$\vec{a}_{\text{tid}} = \nabla(\Delta U_{\text{tid}}) \quad (2.68)$$

where,

$$\Delta U_{\text{tid}} = \frac{GM}{R^2} \sum_{l=2}^3 \sum_{m=0}^1 \sum_{k(l,m)} H_k e^{i(\Theta_k + \lambda_k)} k_k^0 \left[ \left( \frac{R}{r} \right)^{l+1} Y_m^l(\phi, \lambda) + k_k^+ \left( \frac{R}{r} \right)^{l+3} Y_m^{l+2}(\phi, \lambda) \right] \quad (2.69)$$

$$Y_m^l(\phi, \lambda) = (-1)^m \sqrt{\frac{(2l+1)(l-m)!}{4\pi(l+m)!}} P_{lm}(\sin \phi) e^{im\lambda} \quad (2.70)$$

$P_{lm}(\sin \phi)$  = the unnormalized associated Legendre function of degree  $l$  and order  $m$

$H_k$  = the frequency dependent tidal amplitude in meters

$\Theta_k, \chi_k$  = Doodson argument and phase correction for constituent  $k$   
 ( $\chi_k = 0$ , if  $l - m$  is even;  $\chi_k = \pi/2$ , if  $l - m$  is odd)

$k_k^0, k_k^+$  = Love numbers for tidal constituent  $k$

$r, \phi, \lambda$  = geocentric body-fixed coordinates of the satellite

$k(l, m)$  = each combination of  $l, m$  has a unique list of tidal frequencies,  $k$ , to sum over

### 2.5.1.1.3 Sun, Moon and planets perturbation

The gravitational perturbations of the Sun, Moon and other planets can be modeled with sufficient accuracy using point mass approximations. In the inertial coordinate system of the center of integration (COI), the N-body accelerations can be expressed as:

$$\vec{P}_n = \sum_i GM_i \left[ \frac{\vec{r}_{ic}}{r_{ic}^3} - \frac{\vec{r}_{ip}}{r_{ip}^3} \right] \quad (2.71)$$

where

$GM_i$  = gravitational constant of body  $i$

$r_{ic}$  = position of body  $i$  relative to COI

$r_{ip}$  = position of spacecraft relative of body  $i$

The gravitational constant  $GM$  and the position of body  $i$  can be obtained from the planetary ephemerides (Standish, 1998; Fienga et al., 2009, 2011a).

#### 2.5.1.1.4 General relativity

When the massless particle moves in the field of one massive body then relativistic perturbative acceleration can be given as:

$$\begin{aligned} \vec{P}_{\text{rel}} = & \frac{GM_c}{c^2 r^3} \left[ \left( (2\beta + 2\gamma) \frac{GM_c}{r} - \gamma(\dot{\vec{r}} \cdot \dot{\vec{r}}) \right) \vec{r} + (2 + 2\gamma) (\vec{r} \cdot \dot{\vec{r}}) \dot{\vec{r}} \right] \\ & + 2(\vec{\Omega} \times \dot{\vec{r}}) \\ & + L(1 + \gamma) \frac{GM_c}{c^2 r^3} \left[ \frac{3}{r^2} (\vec{r} \times \dot{\vec{r}}) (\vec{r} \cdot \vec{J}) + (\dot{\vec{r}} \times \vec{J}) \right] \end{aligned} \quad (2.72)$$

where

$$\vec{\Omega} \approx \left( \frac{1 + \gamma}{2} \right) \dot{\vec{R}}_{cs} \times \left[ \frac{-GM_s \vec{R}_{cs}}{c^2 R_{cs}^3} \right]$$

$GM_c$  = gravitational constant of the COI

$GM_s$  = gravitational constant of Sun

$\vec{r}, \dot{\vec{r}}$  = position and velocity vectors of the spacecraft relative to the COI

$\vec{R}_{cs}, \dot{\vec{R}}_{cs}$  = position and velocity vectors of the Sun relative to the COI

$\vec{J}$  = the COI angular momentum per unit mass

$L$  = the Lense-Thirring parameter

$\gamma, \beta$  = the parameterized post-Newtonian (PPN) parameters

The first term of Eq. 2.72 is the Schwarzschild motion (Huang et al., 1990) and describes the main effect on the spacecraft orbit with the precession of perigee. The second term of Eq. 2.72 is the effect of geodesic precession, which results in a precession of the orbit plane (Bertotti et al., 1987). The last term of Eq. 2.72 is the Lense-Thirring precession (Ciufolini, 1986).

### 2.5.1.2 Non-Gravitational forces

Computation of the spacecraft trajectory which relies on radio tracking is limited by the uncertainty on the spacecraft non-gravitational acceleration. There are several non-gravitational forces acting on a spacecraft, many of which must be taken into account in order to achieve high accuracy in the orbit determination. Such non-gravitational forces acting on the spacecraft can be expressed as:

$$\vec{a}_{ng} = \vec{P}_{sr} + \vec{P}_{cd} + \vec{P}_{th} + \vec{P}_{rad} + \vec{P}_{mb} \quad (2.73)$$

where

$\vec{P}_{sr}$  = perturbations due to the solar radiation pressure

$\vec{P}_{cd}$  = perturbations due to the atmospheric drag

$\vec{P}_{th}$  = perturbations due to the thermal radiation

$\vec{P}_{rad}$  = perturbations due to the albedo and infrared radiation

$\vec{P}_{mb}$  = perturbations due to the motor burn

Since the surface forces depend on the shape and orientation of the spacecraft, the force models are therefore spacecraft dependent. The *Box – Wing* model of the spacecraft so-called

---

*macro-model* (Marshall, 1992) is usually used for the modeling of non-gravitational perturbations. In the *macro-model*, the spacecraft main body and the solar panel are represented by a simple geometric model, a box and a wing, and the non-gravitational forces are then computed for each surface and summed over the surfaces. An example of simple *macro-model* is shown in Figure 3.1.

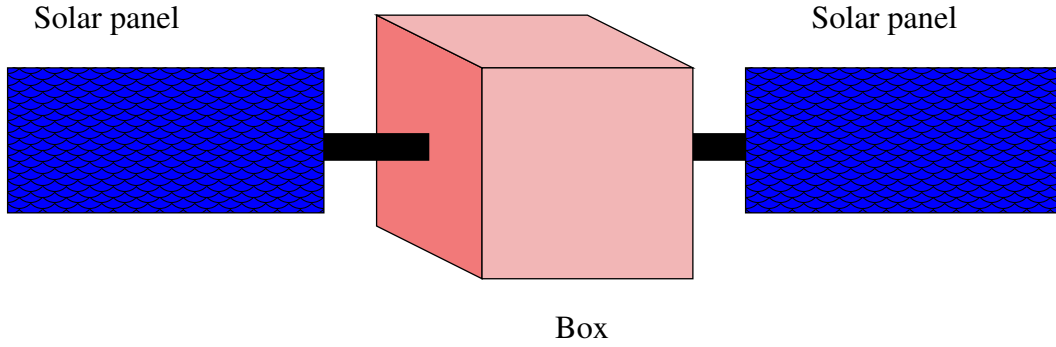


Figure 2.17: A simple geometric *macro-model* of the spacecraft.

### 2.5.1.2.1 Solar radiation pressure

A spacecraft that is exposed to solar radiation experiences a small force that arise owing to the exchange of momentum between solar photons and the spacecraft, as solar photons are absorbed or reflected by the spacecraft. This force can be significant in magnitude in the vicinity of the Earth, at  $\sim 1$  AU from the Sun, especially when considering spacecraft with a large surface area, such as those with large solar panels or antennas. The solar radiation acceleration experiences by the spacecraft *macro-model* can be computed as (Milani et al., 1987):

$$\vec{P}_{sr} = -P \frac{F_S \nu}{m} \sum_{i=1}^n A_i \cos \theta_i \left[ 2 \left( \frac{K_{D_i}}{3} + K_{S_i} \cos \theta_i \right) \hat{n}_i + (1 - K_{S_i}) \hat{s} \right] \quad (2.74)$$

where

$P$  = the momentum flux due to the Sun

$F_S$  = solar radiation pressure scale factor (priori = 1)

$\nu$  = the eclipse factor (0 for full shadow, 1 for full Sun)



$m$  = mass of the spacecraft

$A_i$  = surface area of the  $i$ -th plate

$\theta_i$  = angle between surface normal and spacecraft-Sun vector for  $i$ -th plate

$\hat{n}_i$  = surface normal unit vector for  $i$ -th plate

$\hat{s}$  = spacecraft-Sun unit vector

$K_{D_i}$  = specular reflectivity for  $i$ -th plate

$K_{S_i}$  = diffusive reflectivity for  $i$ -th plate

$n$  = total number of plates in the model

Typically materials used for the construction of the spacecraft, specular reflectivity  $K_D$  and diffusive reflectivity  $K_S$  coefficients lies in the range from 0.2 to 0.9 ([van der Ha and Modi, 1977](#)).

#### 2.5.1.2.2 Atmospheric drag and lift

When a spacecraft is in the vicinity of a planetary body then low altitude spacecraft may experience non-gravitational perturbation due to the atmosphere of planet. This atmospheric perturbation on the spacecraft is negligible if the planet does contain an atmosphere ( for example, the Mercury and the Moon). The accurate modeling of this aerodynamic force requires the knowledge of the physical properties of the atmosphere, especially the density of the upper atmosphere.

A spacecraft of arbitrary shape moving with velocity  $\vec{v}$  in an atmosphere of density  $\rho$  will experience both lift and drag forces. However, the lift forces are very small as compared to the drag forces. These drag forces are directed opposite to the velocity of the spacecraft motion with respect to the atmospheric flux, hence decelerating the spacecraft. The drag and lift force can be model as:

$$\vec{P}_{cd} = -\frac{1}{2} \rho \left[ F_D \sum_{i=1}^n C_{D_i} \frac{A_i}{m} (\vec{v}_r \cdot \vec{n}_i) \cdot \vec{v}_r \right]$$

$$+F_D \sum_{i=1}^n C_{L_i} \frac{A_i}{m} (\vec{v}_r \cdot \vec{n}_i) \vec{v}_r \quad (2.75)$$

where

$\rho$  = the atmospheric density

$\vec{v}_r$  = the spacecraft velocity relative to the atmosphere

$m$  = mass of the spacecraft

$n$  = total number of spacecraft faces directly expose to atmosphere

$\vec{n}_i$  = the unit vector normal to the face  $i$

$A_i$  = the cross-sectional area of the  $i$ -th face

$C_{D_i}$  = the aerodynamic drag coefficient of the  $i$ -th face

$C_{L_i}$  = the aerodynamic lift coefficient of the  $i$ -th face

$F_D$  = drag force scale factor (priori = 1)

Density models for the upper atmosphere are partly empirical and based on the laws of static equilibrium distribution. There are a number of empirical atmospheric density models used for computing the atmospheric density. These include the Jacchia 71 (Jacchia, 1977), the Drag Temperature Model (DTM) (Barlier et al., 1978), NRLMSISE-00 (Hedin et al., 1996).

The relative velocity  $\vec{v}_r$  of the spacecraft with respect to the atmosphere depends on the complex atmospheric dynamics. However, a reasonable approximation of the relative velocity is obtained with the assumption that the atmosphere co-rotates with the planet. Therefore, using this assumption relative velocity can be expressed as:

$$\vec{v}_r = \vec{v} - \vec{\omega} \times \vec{r} \quad (2.76)$$

where,  $\vec{v}$  is the spacecraft velocity,  $\vec{r}$  is the spacecraft position from the COI, and  $\vec{\omega}$  is the angular velocity of the planet.

### 2.5.1.2.3 Thermal radiation

The surface temperature of a spacecraft is affected by exterior flows received from the Sun and the planet. Since the temperatures of the spacecraft surface are not uniform, there exists a force due to a net thermal radiation imbalance. This perturbation depends on the shape, the thermal property, the pattern of thermal dumping, the orbit characteristics, and the thermal environment of the spacecraft as a whole. The perturbation due to thermal radiation can be model as (Afonso et al., 1989):

$$\vec{P}_{th} = -\frac{2\sigma}{3c} \sum_{i=1}^n \frac{A_i}{m} \varepsilon_i T_i^4 \vec{n}_i \quad (2.77)$$

where

$\sigma$  = the Stefan-Boltzmann constant

$c$  = the speed of light

$m$  = mass of the spacecraft

$n$  = total number of spacecraft faces

$\vec{n}_i$  = the unit vector normal to the  $i$ -th face

$A_i$  = the cross-sectional area of the  $i$ -th face

$T_i$  = the temperature of the  $i$ -th face

$\varepsilon_i$  = the emissivity coefficient of the  $i$ -th face

### 2.5.1.2.4 Albedo and infrared radiation

In addition to the direct solar radiation pressure, the radiation emitted by the planet leads to a small pressure on the spacecraft. Such radiations can have two components, that is short-wave albedo and longwave infrared. In both cases the acceleration on the spacecraft decreases slightly with the altitude due to the inverse square law of the emitted radiation pressure. This perturbation can be model as:

#### (i) Albedo radiation

$$\vec{P}_{\text{rad}} = \frac{P}{\pi} \sum_{i=1}^n \frac{A_i}{m} \sum_{i=1}^n \rho_a \frac{(\vec{s} \cdot \vec{dS})(\vec{u} \cdot \vec{dS})}{D^2} \vec{\beta}_i \quad (2.78)$$

#### (ii) Infrared radiation

$$\vec{P}_{\text{rad}} = \frac{P}{\pi} \sum_{i=1}^n \frac{A_i}{m} \sum_{i=1}^n \frac{e}{4} \frac{(\vec{u} \cdot \vec{dS})}{D^2} \vec{\beta}_i \quad (2.79)$$

where

$P$  = the momentum flux due to the Sun ( $4,5605 \times 10^{-6}$ )

$\vec{s}$  = the unit vector in the direction COI-Sun

$\vec{dS}$  = the unit vector normal to the surface element of the orbiting planet

$\vec{n}$  = the planet-spacecraft unit vector in the direction of surface element

$D$  = distance between the surface element of planet and the spacecraft

$\rho_a$  = albedo relative to the surface element

$e$  = emissivity relative to the surface element

$m$  = mass of the spacecraft

$n$  = total number of spacecraft faces

$\vec{n}_i$  = the unit vector normal to the  $i$ -th face

$A_i$  = the cross-sectional area of the  $i$ -th face

$\vec{\beta}_i$  = reflectivity vector of the  $i$ -th face

$\vec{\beta}_i$  = reflectivity infrared vector of the  $i$ -th face

#### 2.5.1.2.5 Motor burn

The acceleration of the spacecraft due to a motor burn can be represented by (Moyer, 1971):

$$\vec{P}_{mb} = aU \left[ u(t - T_0) + u(t - T_f) \right] \quad (2.80)$$

where,

$a$  = magnitude of  $\vec{P}_{mb}$

$U$  = unit vector in direction of  $\vec{P}_{mb}$

$T_0$  = effective start time of motor

$T_f$  = effective end time of motor

$T_f$  = epoch in TDB

$u(t - T_0)$  = 1 for  $t \geq T_0$  and 0 for  $t < T_0$ , when  $T_0 \rightarrow T_f$

The acceleration magnitude  $a$  is given by (Moyer, 1971):

$$a = \frac{F(t)}{m(t)} C = \frac{F_0 + F_1 \bar{t} + F_2 \bar{t}^2 + F_3 \bar{t}^3 + F_4 \bar{t}^4}{m_0 + \dot{M}_0 \bar{t} + \frac{1}{2} \dot{M}_1 \bar{t}^2 + \frac{1}{3} \dot{M}_2 \bar{t}^3 + \frac{1}{4} \dot{M}_3 \bar{t}^4} C \quad (2.81)$$

where,

$F(t)$  = magnitude of thrust at time  $t$ . The polynomial coefficients of  $F(t)$  is solve-for paramerts

$$\bar{t} = t - T_0$$

$m(t)$  = spacecraft mass at time  $t$

$\dot{M}_n$  = polynomial coefficients of propellant mass flow rate at time  $t$

$C$  = 0.001 for  $F$  in newtons and  $m$  in  $kg$

## 2.5.2 Variational equations

Variational equations are the way to describe the variations in the spacecraft state with respect to the solve-for parameters. These equations are always linear and solved simultaneously with the equations of motion. Let the differential equations of motion is given by:

$$\frac{d^2 \vec{r}}{dt^2} = \vec{F}(\vec{r}, \dot{\vec{r}}, t, \vec{\varepsilon}) \quad (2.82)$$

where  $\vec{r}$  and  $\dot{\vec{r}}$  are the state vector of the spacecraft relative to COI.  $\vec{\varepsilon}$  is the vector of solve-for parameter (such as, initial conditions, drag coefficient, solar radiation pressure coefficient, gravity harmonics, etc). The variational equations can be then written as:

$$\frac{d^2}{dt^2} \left( \frac{\partial \vec{r}}{\partial \vec{\varepsilon}} \right) = \frac{\partial \vec{F}}{\partial \vec{r}} \cdot \frac{\partial \vec{r}}{\partial \vec{\varepsilon}} + \frac{\partial \vec{F}}{\partial \dot{\vec{r}}} \cdot \frac{\partial \dot{\vec{r}}}{\partial \vec{\varepsilon}} + \frac{\partial \vec{F}}{\partial \vec{\varepsilon}} \quad (2.83)$$

with, at  $t = t_0$

- if  $\vec{\varepsilon}$  is the parameter of the dynamical equations ( $\vec{\varepsilon}_d$ ), then:

$$\frac{\partial \vec{r}}{\partial \vec{\varepsilon}_d} = \frac{\partial \dot{\vec{r}}}{\partial \vec{\varepsilon}_d} = 0 \quad (2.84)$$

- if  $\vec{\varepsilon}$  is the initial state vectors ( $\vec{\varepsilon}_0$ ), then:

$$\frac{\partial \vec{r}}{\partial \vec{\varepsilon}_0} = \begin{bmatrix} \frac{\partial x_0}{\partial \varepsilon_0^1} & \cdots & \cdots & \frac{\partial x_0}{\partial \varepsilon_0^6} \\ \vdots & \vdots & \vdots & \vdots \\ \frac{\partial z_0}{\partial \varepsilon_0^1} & \cdots & \cdots & \frac{\partial z_0}{\partial \varepsilon_0^6} \end{bmatrix} \quad (2.85)$$

$$\frac{\partial \dot{\vec{r}}}{\partial \vec{\varepsilon}_0} = \begin{bmatrix} \frac{\partial \dot{x}_0}{\partial \varepsilon_0^1} & \cdots & \cdots & \frac{\partial \dot{x}_0}{\partial \varepsilon_0^6} \\ \vdots & \vdots & \vdots & \vdots \\ \frac{\partial \dot{z}_0}{\partial \varepsilon_0^1} & \cdots & \cdots & \frac{\partial \dot{z}_0}{\partial \varepsilon_0^6} \end{bmatrix} \quad (2.86)$$

The matrices  $\partial \vec{F} / \partial \vec{r}$  and  $\partial \vec{F} / \partial \dot{\vec{r}}$  in Eq. 2.83 are evaluated in terms of corresponding solutions of the nonlinear equations of motion, and likewise the vector  $\partial \vec{F} / \partial \vec{\varepsilon}$ . These variational equations can be solved simultaneously with the nonlinear equations of motion using cowell<sup>6</sup> numerical integrator.

### 2.5.3 Parameter estimation

One of the most important task in the orbit determination is to estimate the solve-for parameters. To do so, the least-square technique has been used in the GINS software to estimate such parameters. The objective of the least-square is to adjust the solve-for parameters of a model function to best fit the data set. These parameters are then refined iteratively by using the values that are obtained by successive approximation. The brief description of least-square technique is described below.

Let  $\vec{\varepsilon}$  is the vector of  $p$  number of solve-for parameters and  $k$  is the iteration number. Therefore, the solve-for parameters can be given as:

$$\vec{\varepsilon}^{k+1} = \vec{\varepsilon}^k + \Delta \vec{\varepsilon} \quad (2.87)$$

where  $\Delta \vec{\varepsilon}$  is the correction in the adjusted solve-for parameter. By using first-order linearized approximation of a Taylor series expansion about  $\vec{\varepsilon}^k$ :

$$Q_c(\vec{\varepsilon}) = Q_c^k(\vec{\varepsilon}) + \sum_{i=1}^p \frac{\partial Q_c^k(\vec{\varepsilon})}{\partial \varepsilon_i} \Delta \varepsilon_i \quad (2.88)$$

---

<sup>6</sup>[http://igsac-cnes.cls.fr/documents/gins/Integration\\_Numerique/Integration\\_numerique.pdf](http://igsac-cnes.cls.fr/documents/gins/Integration_Numerique/Integration_numerique.pdf)

---

where  $Q_c$  is the theoretical values computed from the models which is a function of solve-for parameters  $\vec{\varepsilon}$ . If,  $Q_o$  defines the real observations, then the residuals (observation - computation) can be given as:

$$\begin{aligned} r &= Q_o - Q_c \\ &= Q_o - Q_c^k(\vec{\varepsilon}) + \sum_{i=1}^p \frac{\partial Q_c^k(\vec{\varepsilon})}{\partial \varepsilon_i} \Delta \varepsilon_i \\ &= \Delta Q - \sum_{i=1}^p \frac{\partial Q_c^k(\vec{\varepsilon})}{\partial \varepsilon_i} \Delta \varepsilon_i \end{aligned} \quad (2.89)$$

If  $m$  be the number of observations, then first and second terms Eq. 2.89 can be written as:

$$\vec{\Delta Q} = \begin{bmatrix} \Delta Q_1 \\ \vdots \\ \vdots \\ \Delta Q_m \end{bmatrix} = B \quad (2.90)$$

$$\frac{\partial \vec{Q}_c^k}{\partial \vec{\varepsilon}} \Delta \vec{\varepsilon} = \begin{bmatrix} \frac{\partial Q_{c_1}^k}{\partial \varepsilon_1} & \cdots & \cdots & \frac{\partial Q_{c_1}^k}{\partial \varepsilon_p} \\ \vdots & \cdots & \cdots & \vdots \\ \vdots & \cdots & \cdots & \vdots \\ \frac{\partial Q_{c_m}^k}{\partial \varepsilon_1} & \cdots & \cdots & \frac{\partial Q_{c_m}^k}{\partial \varepsilon_p} \end{bmatrix} \cdot \begin{bmatrix} \Delta \varepsilon_1 \\ \vdots \\ \vdots \\ \Delta \varepsilon_p \end{bmatrix} = A \cdot \Delta \vec{\varepsilon} \quad (2.91)$$

In order to estimate the best solve-for parameters, according to least-square technique, sum  $S$  of the square of the residuals should be minimum. Where sum  $S$  is given by:

$$S = \sum_{j=1}^m (B_j - A_j \cdot \Delta \vec{\varepsilon})^2 \quad (2.92)$$

where  $B_j$  is the  $j^{\text{th}}$  value of  $B$  and  $A_j$  is the  $j^{\text{th}}$  row of matrix  $A$ . For weighted least-square, the expression of sum  $S$  is given as:

$$S = \sum_{j=1}^m W_j \cdot (B_j - A_j \cdot \Delta \vec{\varepsilon})^2 \quad (2.93)$$

where  $W_j$  is the  $j^{\text{th}}$  value of diagonal weight matrix  $W$ , which is given by:

$$W = \begin{bmatrix} W_1 & & 0 \\ & \cdot & \\ 0 & & W_m \end{bmatrix} \quad (2.94)$$



In order to achieve the minimum square of the sum  $S$  of the residuals, the gradient of  $S$  with respect of solve-for parameter should equal to zero. Which is given as:

$$\begin{aligned} \mathbf{A}^T \cdot \mathbf{W} \cdot (\mathbf{B} - \mathbf{A} \cdot \Delta\boldsymbol{\varepsilon}) &= 0 \\ \mathbf{A}^T \cdot \mathbf{W} \cdot \mathbf{A} \cdot \Delta\boldsymbol{\varepsilon} &= \mathbf{A}^T \cdot \mathbf{W} \cdot \mathbf{B} \end{aligned} \quad (2.95)$$

For example, if  $\mathbf{W}$  is the identity matrix and number of solve-for parameters  $P$  equal to 2, then Eq. 2.95 can be written as:

$$\begin{bmatrix} \sum_{j=1}^m \left( \frac{\partial Q_{c_j}}{\partial \varepsilon_1} \right)^2 & \sum_{j=1}^m \left( \frac{\partial Q_{c_j}}{\partial \varepsilon_1} \right) \cdot \left( \frac{\partial Q_{c_j}}{\partial \varepsilon_2} \right) \\ \sum_{j=1}^m \left( \frac{\partial Q_{c_j}}{\partial \varepsilon_1} \right) \cdot \left( \frac{\partial Q_{c_j}}{\partial \varepsilon_2} \right) & \sum_{j=1}^m \left( \frac{\partial Q_{c_j}}{\partial \varepsilon_2} \right)^2 \end{bmatrix} \cdot \begin{bmatrix} \Delta\varepsilon_1 \\ \Delta\varepsilon_2 \end{bmatrix} = \begin{bmatrix} \sum_{j=1}^m \Delta Q \cdot \left( \frac{\partial Q_{c_j}}{\partial \varepsilon_1} \right) \\ \sum_{j=1}^m \Delta Q \cdot \left( \frac{\partial Q_{c_j}}{\partial \varepsilon_2} \right) \end{bmatrix} \quad (2.96)$$

The computed value of the observations  $Q_c$  can be calculated from the state vectors of the spacecraft and the position of the stations at time of measurement (see Section 2.4.3). The gradient of the  $Q_c$  with respect to the solve-for parameters  $\boldsymbol{\varepsilon}$  given in Eq. 2.96 can be written as:

$$\frac{\partial \vec{Q}_{c_j}}{\partial \boldsymbol{\varepsilon}} = \frac{\partial \vec{Q}_{c_j}}{\partial \vec{r}} \cdot \frac{\partial \vec{r}}{\partial \boldsymbol{\varepsilon}} + \frac{\partial \vec{Q}_{c_j}}{\partial \vec{r}'} \cdot \frac{\partial \vec{r}'}{\partial \boldsymbol{\varepsilon}} \quad (2.97)$$

In Eq. 2.97,  $\vec{r}$  and  $\vec{r}'$ , and  $\partial \vec{r} / \partial \boldsymbol{\varepsilon}$  and  $\partial \vec{r}' / \partial \boldsymbol{\varepsilon}$ , can be computed from the numerical integration of equations of motion and variational equations (Eqs. 2.85 and 2.86) respectively. Whereas,  $\partial \vec{Q}_{c_j} / \partial \vec{r}$  and  $\partial \vec{Q}_{c_j} / \partial \vec{r}'$  can be computed analytically.

The steps used for estimating the solve-for parameters are (see Figure 2.16):

- to provide initial conditions and planetary ephemerides to the dynamical model,
- integrate numerically the equations of motion (Eq. 2.62) along with the variational equations (Eq. 2.83) in order to calculate the state vectors of the spacecraft and the partial derivative of the state vector with respect to solve-for parameters (Eqs. 2.85 and 2.86),
- to calculate the theoretical observations  $Q_c$  using the formulation given in section 2.4.3,
- to calculate the partial derivative of the theoretical observations with respect to solve-for parameters and then to compute the residuals (Eq. 2.89),
- to calculate the normal matrix and its inverse and then to calculate the corrections in the solve-for parameters (Eq. 2.95),

- these correction are then used to refine the parameters using iterative processes (Eq. 2.87) until the residuals have met the specified convergence criterion.
-

## Chapter 3

# Mars Global Surveyor: Radioscience data analysis

### 3.1 Introduction

Mars is the most explored terrestrial planet in the solar system. Many space missions have been attempted to Mars than to any other place in the solar system except the Moon. These missions include flyby missions (Mariner, Rosetta), orbiter missions (Mars Global Surveyor, Mars Odyssey, Mars Express, Mars Reconnaissance Orbiter ), and lander missions (Viking, Mars Exploration Rovers, Mars Science Laboratory). Obtaining scientific information is the primary reason for launching and operating such deep-space missions. Usually, science objectives of such missions involve: high resolution imaging of the planet surface, studies of the gravity and topography, studies of the atmosphere and the interior of the Mars, studies of biological, geological, and geochemical processes, etc. To achieve the mission objectives, some of these investigations are performed by using a dedicate science instrument aboard the spacecraft, which measure a particular physical phenomenon, for example:

- The thermal emission spectrometer: is used to measure the infrared spectrum of energy emitted by the planet. This information is used to study the composition of rock, soil, atmospheric dust, clouds, etc.
- The orbital laser altimeter: is used to measure the time, takes for a transmitted laser beam to reach the surface, reflect, and return. This information provides the topographic maps of Mars.
- The magnetometer: is used to determine a magnetic field, and its strength and orientation.

On the other hand, some objectives are undertaken as opportunities arise to take advantage of a spacecraft special capabilities or unique location or other circumstance. For example:

---

- With the radioscience experiment, which measures the Doppler shift of radio signals, it is then possible to determine the gravity field by computing the change in the speed of the spacecraft, associated with the high and low concentration of the mass below and at the surface of the Mars. Moreover, unique location such as spacecraft occultation allows the radio signals pass through the Martian atmosphere on their way to Earth. Hence, perturbations in the signals induced by the atmosphere allows to derive the atmospheric and ionospheric characteristics of the Mars. Brief description of such investigations are discussed in Chapter 2.

This chapter deals with the radioscience data analyses to precisely construct the MGS orbit. Such analyses has been already performed by several authors, such as [Yuan et al. \(2001\)](#); [Lemoine et al. \(2001\)](#); [Konopliv et al. \(2006\)](#); [Marty et al. \(2009\)](#). We have therefore chosen MGS as an academic case to test our understanding of the raw radiometric data (ODF, see Chapter 2) and their analysis with GINS by comparing our results with the one found in the above literature. Moreover, these analyses also allowed us to derive solar corona model and to perform corona physic studies. Derivation of such models and their application to planetary ephemerides are discussed in Chapter 4 and in [Verma et al. \(2013\)](#).

The outline of this chapter is as follows: in the Section 3.2 an overview of the MGS mission is discussed. Data processing and dynamic modeling used for the orbit construction is described in the Section 3.3. Results obtained during the orbit computation and their comparison with the estimations found in the literature are discussed in the Section 3.4. The supplementary tests, which include: (a) comparison between the GINS solution and the JPL light time solution, and (b) the impact of the *macro-model* on the orbit reconstruction, are discussed in Section 3.5. Conclusion and perspectives of these results are reported in Section 3.6.

## 3.2 Mission overview

### 3.2.1 Mission design

MGS was a NASA's space mission to Mars. It was launched from the Cape Canaveral Air Station in Florida on 7<sup>th</sup> November 1996 aboard a Delta II rocket. The MGS began its Mars orbit insertion on 12<sup>th</sup> September 1997. Figure 3.1 illustrates the summary of the MGS mission from launch to the Mars orbit insertion (MOI) in an elliptical orbit, the initial areobraking period, the science-phase period, the aerobraking resumption, and mapping in the circular orbit ([Albee et al., 2001](#)).

The MOI represents an extremely crucial maneuver, because any failure would result in a fly-by mission. The MOI slows down the spacecraft and allows Mars to capture the probe into an elliptical orbit. Near the point of closest approach on spacecraft in-bound trajectory, the main engines fired for approximately 20 to 25 minutes to slow down the spacecraft. This

---

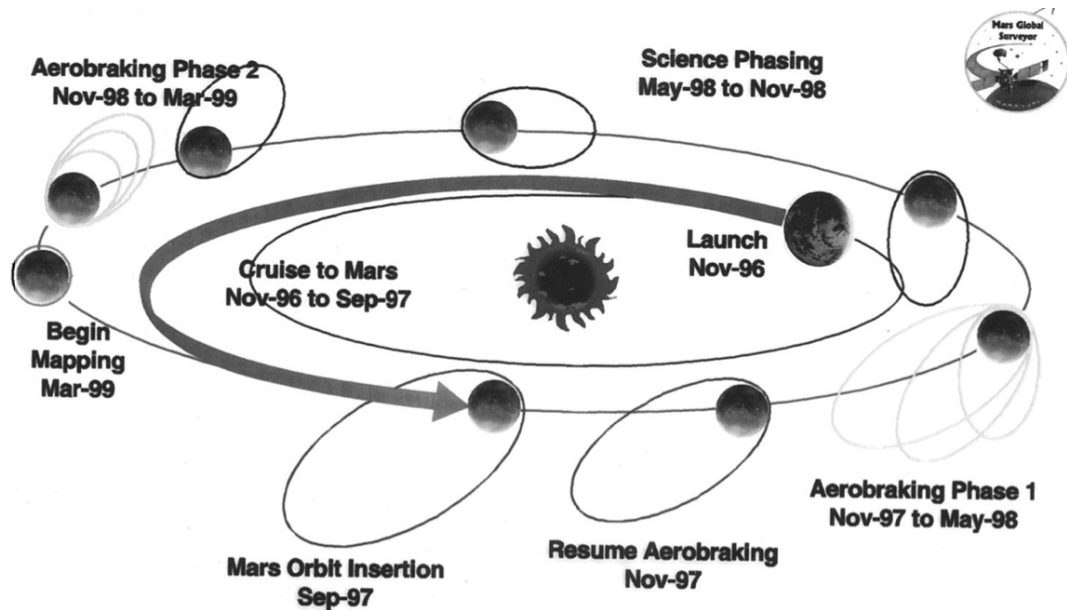


Figure 3.1: Summary of MGS mission phases from launch to mapping period (Albee et al., 2001).

burn allowed the spacecraft to run off of the hyperbolic approach trajectory and to approach the planet onto a highly elliptical orbit. Initially, the MGS orbit had a periapsis of 262 km above the northern hemisphere, and an apoapsis of 54,026 km above the southern hemisphere and took 45 hours to complete one orbit.

In order to attain the mapping orbit, MGS spacecraft was designed to facilitate the use of aerobraking. Aerobraking is the utilization of atmospheric drag on the spacecraft to reduce the energy of the orbit. The friction caused by the passage of the spacecraft through the atmosphere provides a velocity change at periapsis, which results in the lowering of the apoapsis altitude. After almost sixteen months of orbit insertion, the aerobraking events were utilized to convert the elliptical orbit into an almost circular 2-hour low altitude sun synchronous polar orbit with an average altitude of 378 km. Thus, MGS started its low altitude mapping orbital phase in March 1999 and lost communication with the ground station on 2<sup>nd</sup> November 2006.

### 3.2.2 Spacecraft geometry

MGS was designed to carry science payloads to Mars, to maintain proper pointing and orbit as a three-axis stabilized platform for acquiring mapping data and return to the Earth.

In order to meet the strength mass requirements, the spacecraft structure was constructed of lightweight composite materials. It was divided into four sub-assemblies (Figure 3.2, extracted from Albee et al. (2001)):

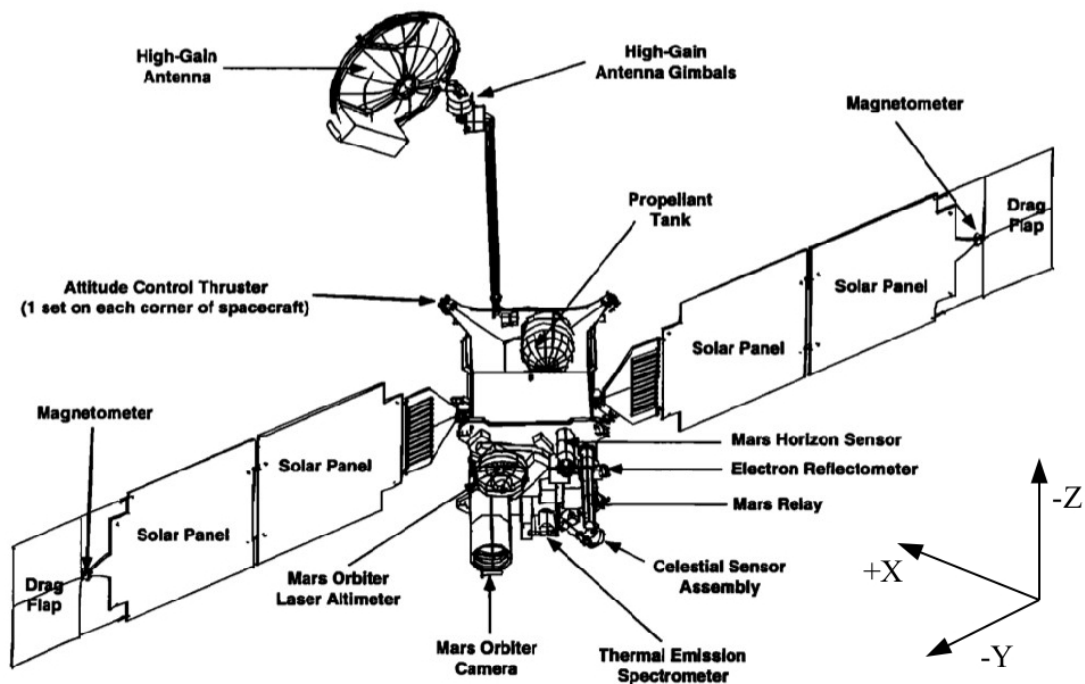


Figure 3.2: View of the MGS spacecraft (Albee et al., 2001).

- Equipment module:** it houses the avionics system and the science instruments. MGS carried six on-board instruments, that are Magnetometer/Electron Reflectometer, Mars orbiter camera, Mars orbiter laser altimeter, Mars relay, Thermal Emissions Spectrometer, and ultra-stable oscillator. All science instruments are bolted to the nadir equipment deck, mounted above the equipment module on the +Z panel.
- Propulsion module:** it serves as the adapter between the launch vehicle and contains the propellant tanks, main engines, and attitude control thrusters. This module bolts beneath the equipment module on the -Z panel.
- Solar arrays:** two solar arrays provide power for the MGS spacecraft. Each array mounts close to the top of the propulsion module on the +Y and -Y panels, near the interface between the propulsion and equipment modules. Rectangular shaped, metal drag *flaps* mounted onto the ends of both arrays. These *flaps* were only used to increase the total surface area of the array structure to increase the spacecraft's ballistic coefficient during aerobraking.
- High Gain Antenna:** a parabolic high gain antenna (HGA) structure was also bolt to the outside of the propulsion module. It was used to make high rate communication with the Earth. When fully deployed, the 1.5 meter diameter HGA sits at the end of a 2.0 meter long boom, mounted to the +X panel of the propulsion module.

Table 3.1: MGS spacecraft macro-model characteristics (Marty, 2011)

Spacecraft body	Components	Area (m <sup>2</sup> )	Diffuse ref	Specular ref.
Solar Arrays	Composite (front)	7.85	0.049	0.198
	Composite (back)	7.85	0.079	0.282
Spacecraft Bus	+X, -X	3.30	0.130	0.520
	+Y, -Y	3.56	0.130	0.520
	+Z, -Z	2.31	0.130	0.520
HGA	+X	1.94	0.100	0.400

As described in Chapter 2 (Section 2.5.1), the precise computation of the spacecraft trajectory relies on the non-gravitational accelerations that are acting in the spacecraft. These non-gravitational forces depend on the shape, size, surface properties, and orientations of the spacecraft. Thus, an accurate spacecraft geometry is an essential information for modeling such forces precisely. The characteristics of the MGS macro-model are given in Table 3.1 (Lemoine et al., 1999).

### 3.2.3 Radioscience data

MGS is the first operational planetary mission to employ exclusively X-band technology for radioscience observations, tracking, and spacecraft command and communication (Tyler et al., 2001). The radioscience instrument used for this purpose is the spacecraft telecommunications subsystem, augmented by an ultra-stable oscillator, and the normal MGS transmitter and receiver. The ultra-stable oscillator typically have frequency stabilities on the order of  $1 \times 10^{-13}$  for time intervals of 1 to 100 seconds (Cash et al., 2008). The oscillator provides the reference frequency for the radioscience experiments and operates on the X-band 7164.624 MHz uplink and 8416.368 MHz downlink frequency. The radioscience data are then collected by the DSN and consist of one-way Doppler, two- and three-way ramped Doppler, and two-way range observations (see Chapter 2 for full details of radioscience data).

Figure 5.2.3 illustrates the MGS tracking strategy during the mapping period for sharing the orbit between: i) the occultation studies when MGS was near the limb of the planet, and ii) the gravity studies during the MGS Earth side pass (Tyler et al., 2001). Pole-to-Pole two- and three-way Doppler observations provide the primary information of Mars gravity field. Whereas, one-way Doppler observations obtained during the occultation period provide an information about the Martian atmosphere and ionosphere. Table 3.2 gives the summary of the data coverage obtained during the mapping period and used to construct the MGS orbit.

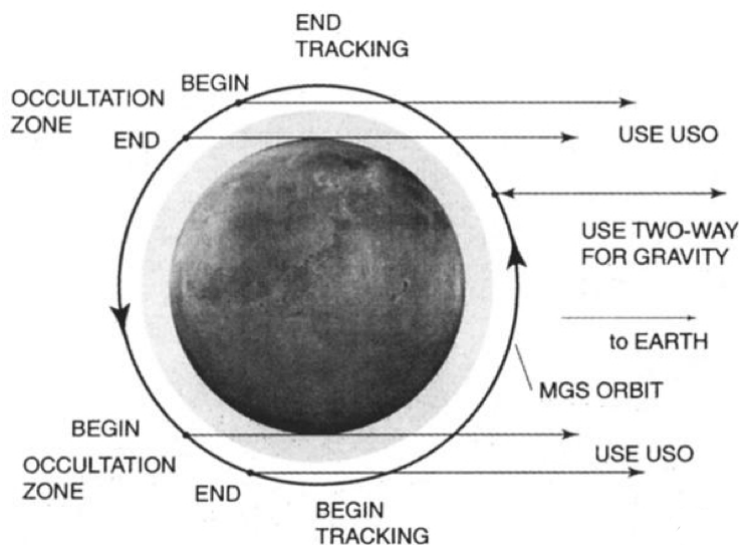


Figure 3.3: Pole-to-Pole tracking of the MGS spacecraft during mapping period (Tyler et al., 2001).

Table 3.2: Year wise summary of the Doppler and range tracking data used for orbit solution.

Year	Number of 1-way Dop.	Number of 2-way Dop.	Number of 3-way Dop.	Number of Range	Number of Ramp
1999	133,188	1,060,416	120,931	46,277	202,188
2000	1,472,366	536,142	74,950	5,192	192,992
2001	1,389,279	877,315	86,482	54,582	192,624
2002	1,772,226	641,729	86,984	30,533	203,309
2003	937,566	552,073	64,260	21,784	155,255
2004	660,020	446,934	52,836	17,022	78,991
2005	205,832	98,130	2,028	6,200	23,626
2006	1,105,734	452,655	33,486	23,148	120,846

### 3.3 Orbit determination

We have used Doppler- and range-tracking observations to compute the MGS orbits precisely. However as stated before, this computation was mainly performed as an academic case to understand the dynamic model and the radiometric data. With this computation, we were then able to compare our results with those obtained by Yuan et al. (2001); Lemoine et al. (2001); Konopliv et al. (2006); Marty et al. (2009) (see Section 3.4.2). Tests were also performed and reported in Section 3.11, in order to understand the sensitivity of the data processing with the



accuracy of non-gravitational forces by assuming different shapes of MGS macro-model.

### 3.3.1 Data processing and dynamic modeling

The radioscience observations, used for computing the MGS orbit, are available on the NASA Planetary Data System (PDS) Geoscience website<sup>1</sup>. These observations are analyzed with the help of the GINS software. As described in Section 2.5 of Chapter 2, GINS numerically integrates the equations of motion (Eqs. 2.62) and the associated variational equations (Eqs. 2.83). It simultaneously retrieves the physical parameters of the force model using an iterative least-squares technique (see Section 2.5.3). The modeling of the MGS orbit includes gravitational and non-gravitational forces that are acting on the spacecraft (see Section 2.5.1). In addition to these forces, third body perturbations due to Phobos and Deimos are also included.

The data processing and the dynamic modeling are done as follows:

- In order to have access to the planet positions and velocities, planetary ephemeris has been used for both measurements and force models (e.g, DE405, INPOP10b).
- The Mars geopotential is modeled in terms of spherical harmonic. This model is given by Eq. 2.65 as described in section 2.5.1. Fully normalized spherical harmonic coefficients of MGS95J solution<sup>2</sup> has been used. MGS95J is a 95x95 spherical harmonics model which was derived from 6 years of MGS tracking data plus 3 years of measurements on the Mars Odyssey (ODY) spacecraft (Konopliv et al., 2006).
- The rotation model which defines the orientation of the Mars is taken from the Konopliv et al. (2006).
- Earth kinematics and polar motion effects are taken according to the IERS standards (McCarthy and Petit, 2003).
- The Phobos and Deimos ephemerides are taken as developed by Lainey et al. (2007).
- The complex geometry of the spacecraft is treated as a combination of flat plates arrange in the shape of box, with attached solar arrays and drag flaps, and attached HGA. This *Box-Wing* model includes six plates for the spacecraft bus, four plates to represent the front and back side of the +Y and -Y solar arrays, and a parabolic HGA. The surface area and reflectivity of this macro-model are given in Table 3.1. Moreover, in addition to this macro-model, a *Spherical* macro-model has been also used to reconstruct the MGS orbit and to understand the impact of macro-model over the orbit reconstruction (see Section 3.5).

---

<sup>1</sup><http://geo.pds.nasa.gov/missions/mgs/rsraw.html>

<sup>2</sup>[http://pds-geosciences.wustl.edu/mgs/mgs-m-rss-5-sdp-v1/mors\\_1033/sha/](http://pds-geosciences.wustl.edu/mgs/mgs-m-rss-5-sdp-v1/mors_1033/sha/)

---

- Using such configurations of the MGS *macro-models*, solar radiation pressure (Eq. 2.74), atmospheric drag (Eq. 2.75), and Mars radiation pressure (Eqs. 2.78 and 2.79) forces are computed separately for each plate and HGA. Vectorial sum of all these components are then compute to calculate the total force acting on the spacecraft.
- In addition to the macro-model characteristics, orientations of the spacecraft are also taken in account. The attitude of spacecraft, and of its articulated panels and antenna in inertial frame are defined in terms of quaternions. These quaternions are extracted from the SPICE Navigation and Ancillary Information Facility (NAIF) C-Kernels<sup>3</sup>.
- MGS periodically fires its thruster to desaturate the reactions wheels, which absorb angular momentum from disturbance torque acting on the spacecraft. Thus, empirical accelerations are modeled over the duration of each angular momentum wheel desaturation (AMD) event (Marty, 2011). Constant radial, along-track, and cross-track accelerations are applied over the duration of each AMD event, and are estimated as part of each orbit determination solution.
- The relativistic effects on the measurements and on the spacecraft dynamics are modeled based on the PPN formulation as described in Sections 2.4 and 2.5.1 of Chapter 2.
- The tropospheric delay corrections to the measurements are also included. Computation of this delay uses meteorological data (pressure, temperature and humidity) collected every half-hour at the DSN sites.

### 3.3.2 Solve-for parameters

For the orbit computation and for the parameter estimation, a multi-arc approach is used to get independent estimates of the MGS accelerations. In this method, orbital fits are obtained from short data-arcs of two days with two hours (approx. one orbital period of MGS) of overlapping period. The short day data-arcs are used to accounting the model imperfections (see Section 3.5) and overlapping period are used to estimate the quality of the spacecraft orbit determination by taking orbit overlap differences between two successive data-arcs (see Section 3.4). In order to account the effect of shortest wavelengths of Mars gravity field on the MGS motion, we integrate the equations of motion using the time-step of 20s. An iterative least-squares fit is then performed on the complete set of Doppler- and range-tracking data-arcs.

Solve-for parameters which have been estimated during the MGS orbit determination are:

- The initial state vector components at the epoch for each arc. Prior values of these vectors are taken from the SPICE NAIF kernels.

---

<sup>3</sup><http://naif.jpl.nasa.gov/naif/>

---

- Scale factor,  $F_D$ , for the drag force. One  $F_D$  per arc is computed for accounting mis-modeling of the drag force.
- Scale factor,  $F_S$ , for the solar radiation pressure force. One  $F_S$  per arc is also computed for accounting mis-modeling in the solar radiation pressure.
- Empirical delta accelerations, radial, along-track, and cross-track, are computed at the AMD epochs. The information of these epochs are given by [Marty \(2011\)](#).
- For each arc, one offset per DSN station for two or three-way Doppler measurements.
- One offset per arc for one-way Doppler measurements accounting for the ultra stable oscillator stability uncertainty.
- One bias per DSN station for accounting the uncertainties on the DSN antenna center position or the instrumental delays (such as the range group delay of the transponder)
- One range bias per arc for ranging measurements to account the systematic geometric positions error (ephemerides error) between the Earth and the Mars.

## 3.4 Orbit computation results

### 3.4.1 Acceleration budget

Accurate orbit determination of planetary spacecraft requires good knowledge of gravitational and non-gravitational forces which act on the spacecraft. These forces are precisely modeled in the GINS software as described in Chapter 2. Figure 3.4 illustrates an average of various accelerations experienced by the MGS spacecraft, that are:

- **Accelerations due to gravitational potential:** the first two columns of the Figure 3.4 represent the accelerations owing to the gravitational attraction of Mars. These are the most dominating forces that are acting on the MGS spacecraft.  $GM/r + J_2$  in Figure 3.4 represents the mean and zonal coefficients contribution in the accelerations, which are related to  $C_{lm}$  by the relation  $J_l = -C_{l,0}$ . However, *gravity* in the same figure represents the tesseral ( $l \neq m$ ) and sectoral ( $l = m$ ) coefficients contribution in the accelerations (see Eq. 2.65). An average acceleration for potentials  $GM/r + J_2$  and *gravity* is estimated as 3.0 and  $8.9 \times 10^{-4}$  m/s<sup>2</sup> respectively.
- **Accelerations due to third body attractions:** the third and fourth columns of the Figure 3.4 represent the accelerations owing to the Sun and the Moon, and planets-satellite attractions (see Eq. 2.71), respectively. The Sun-Moon attraction is the third most dominating gravitational acceleration, whereas planets-satellite causes a smaller perturbation in the MGS orbit. Average accelerations estimated for Sun-Moon and planets-satellite attractions are  $6.0 \times 10^{-8}$  and  $2.7 \times 10^{-12}$  m/s<sup>2</sup>, respectively.

## MGS acceleration budget

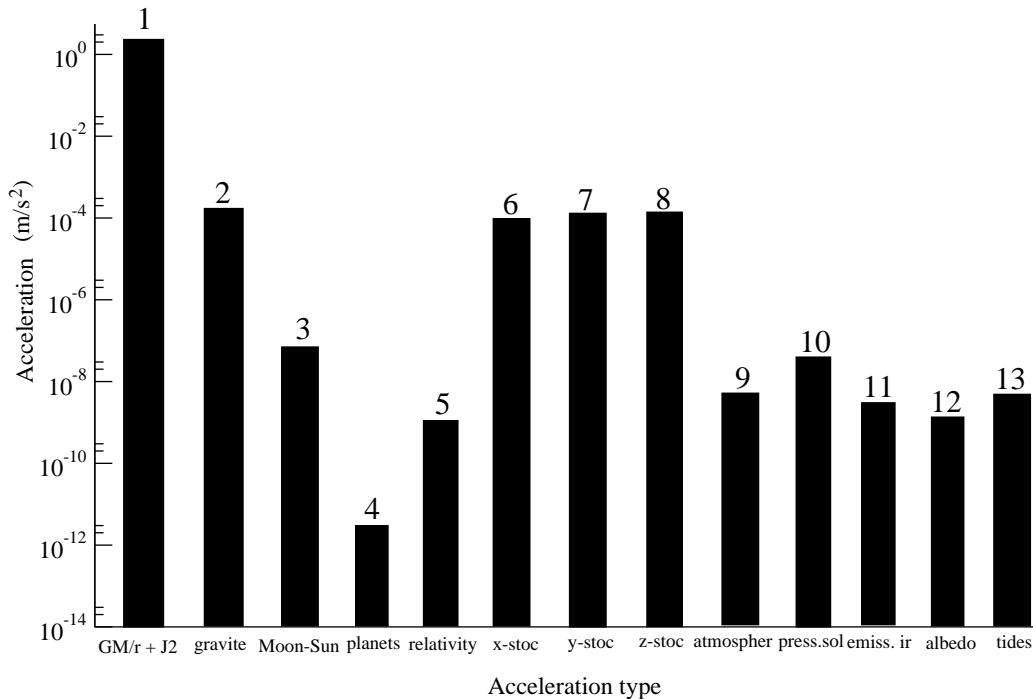


Figure 3.4: Gravitational and non-gravitational accelerations acting on the MGS spacecraft. See text for the explanation of each column.

- **Accelerations due to general relativity:** the fifth column of the Figure 3.4 represents the accelerations owing to the contribution of general relativity (see Eq. 2.72). An average value of this acceleration is estimated as  $1.1 \times 10^{-9} \text{ m/s}^2$ .
- **Accelerations due to maneuvers:** the sixth, seventh, and eighth columns of the Figure 3.4 represent empirical accelerations that are estimated over the duration of each AMD (see Eq. 2.80). Average value of radial (x-stoc), along-track (y-stoc), and cross-track (z-stoc) accelerations are estimated as  $1.0 \times 10^{-4}$ ,  $1.2 \times 10^{-4}$ , and  $1.8 \times 10^{-4} \text{ m/s}^2$  respectively.
- **Accelerations due to atmospheric drag:** the ninth column of the Figure 3.4 represents the acceleration owing to the resistance of the Mars atmosphere (see Eq. 2.75). It is one of the largest non-gravitational accelerations acting on the low altitude spacecraft. For MGS, an average value of this acceleration is estimated as  $4.8 \times 10^{-9} \text{ m/s}^2$ .
- **Accelerations due to solar radiation pressure:** the tenth column of the Figure 3.4 represents the acceleration due to the solar radiation pressure (see Eq. 2.74). It is the largest non-gravitational acceleration acting on the MGS spacecraft with an average value of  $4.5 \times 10^{-8} \text{ m/s}^2$ .

- **Accelerations due to Mars radiation:** the eleventh and twelfth columns represent the accelerations due to the Infra-Red radiation (see Eq. 2.79) and Albedo (see Eq. 2.78) of the Mars. These are the smallest non-gravitational accelerations acting on the MGS spacecraft with average values of  $1.1 \times 10^{-9}$  and  $3.0 \times 10^{-9}$  m/s<sup>2</sup> respectively.
- **Accelerations due to solid planetary tides:** the thirteen column represents the accelerations owing to the contribution of solid planetary tides (see Eq. 2.69). An average value of this acceleration is estimated as  $4.18 \times 10^{-9}$  m/s<sup>2</sup>.

### 3.4.2 Doppler and range postfit residuals

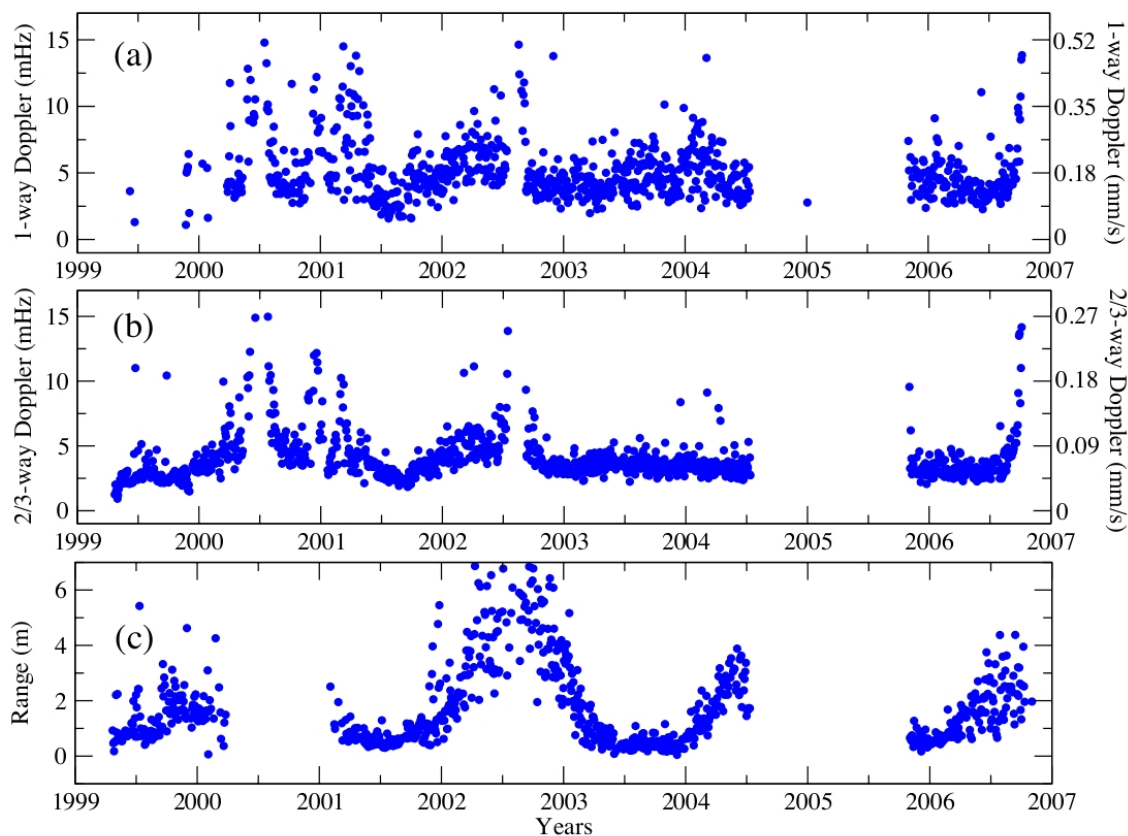


Figure 3.5: Quality of the MGS orbit in terms of rms values of the postfit residuals for each one-day data-arc: (a) one-way Doppler given in millihertz (1-way: 1 mHz = 0.035 mm/s = speed of light / X-band frequency); (b) two- and three-way Doppler given in millihertz (2/3-way: 1 mHz = 0.0178 mm/s = 0.5×speed of light / X-band frequency); and (c) two-way range given in meter. The peaks and gaps in residuals correspond to solar conjunction periods of MGS.

In general, the Doppler data are mainly used for the computation of spacecraft orbit. They are sensitive to the modeling of the spacecraft dynamics and provide strong constraints on the

orbit construction. However, range data are also used to assist the orbit computation. Unlike Doppler data, range data are more sensitive to the positions of the planet in the solar system and provide strong constraints to the planetary ephemerides.

Figure 3.5 illustrates the rms values of the Doppler- and range postfit residuals estimated for each data-arc. Doppler residuals represent the accuracy in the computation of Doppler shift and in the dynamic modeling of the MGS spacecraft, whereas range residuals represents the accuracy in the computation of range measurements. To plot, we did not consider 19% of the data-arcs during which: i) the Sun-Earth-Probe (SEP) angle  $<12^\circ$  and rms value of the postfit Doppler and range residuals are above 15mHz and 7 m respectively, and ii) the drag coefficients and solar radiation pressures have unrealistic values.

In Figure 3.5, the peaks and the gaps in the postfit residuals correspond to solar conjunction periods. Excluding these periods, the rms value of the postfit Doppler- and two- way range residuals for each data-arc is varying from 1.8 to 5.8 mHz<sup>4,5</sup> and 0.4 to 1.2m, respectively. These estimations are comparable with Yuan et al. (2001); Lemoine et al. (2001); Marty et al. (2009), see Table 3.3. The mean value of the estimated Doppler offset for each DSN station tracking pass is of the order of a few tenths of mHz, which is lower than the Doppler postfit residuals for each data-arc. This implies that there is no large offset in the modeling of the Doppler shift measurements at each tracking DSN station.

Table 3.3: Comparison of postfit Doppler and range residuals, and overlapped periods, between different authors.

Authors	Residuals <sup>a</sup>		Overlap <sup>b</sup>			
	Doppler (mHz)	Range (m)	R (m)	T (m)	N (m)	3D (m)
Yuan et al. (2001) <sup>c</sup>	3.4-4.9	-	1.6	2.5	10.6	-
Lemoine et al. (2001) <sup>c</sup>	3.4-5.6	-	1.5	2.55	8.75	-
Konopliv et al. (2006)	-	-	0.15	1.5	1.6	-
Marty et al. (2009)	2-5	0.5-1	-	-	-	2.1
This chapter	1.8-5.8	0.4-1.2	0.33±0.27*	2.5±2.1*	3.0±2*	2.7±2.0*

<sup>a</sup> range of the mean values estimated for each data-arc.

<sup>b</sup> mean value estimated for entire data.

<sup>c</sup> authors gave the values in mm/s, we therefore divided the values by a factor 0.0178 to obtain approximate values in mHz.

\* mean±1- $\sigma$  dispersion of the rms values

### 3.4.3 Orbit overlap

The quality of the orbit fits can also be investigated from the differences in MGS positions between overlapping data-arcs. Such investigations are shown in Figure 3.6, which represents the rms values of each overlap differences. These rms values correspond to the MGS position differences between successive two-days data-arcs over overlap duration of two-hours (one revolution of MGS around Mars). As one can see from Figure 3.6, the radial component of the orbit error is less scattered after September 2001. This is due to the reduce number of AMDs after this period. However, mean and  $1-\sigma$  values of the radial, along-track, and cross-track components of the orbit error are  $0.33\pm 0.27^6$ m,  $2.5\pm 2.1^6$ m, and  $3.0\pm^6$ m respectively. The comparison of these values with the estimations of other authors are presented in Table 3.3. As one can notice, statistics of our results are compatible within  $1-\sigma$  with the latest [Konopliv et al. \(2006\)](#); [Marty et al. \(2009\)](#). However, overlap differences estimated by [Yuan et al. \(2001\)](#); [Lemoine](#)

<sup>4</sup>1-way: 1 mHz = 0.035 mm/s = speed of light / X-band frequency

<sup>5</sup>2/3-way: 1 mHz = 0.0178 mm/s = 0.5×speed of light / X-band frequency

<sup>6</sup>mean± $1-\sigma$  dispersion of the rms values

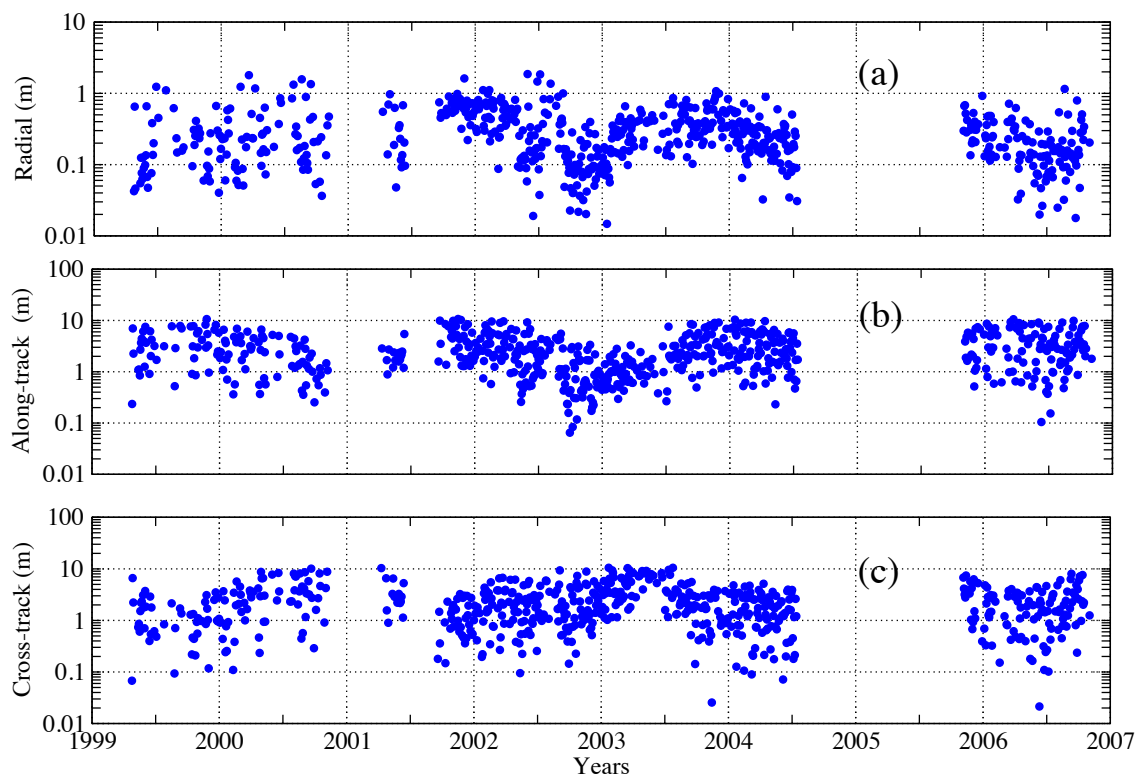


Figure 3.6: Orbit overlap differences for the entire mapping period of MGS mission for the (a) radial direction, (b) along-track direction, and (c) cross-track or normal to the orbit plane.

et al. (2001) are approximately  $\sim 3$  times higher in the normal direction and approximately  $\sim 5$  times higher in the radial-direction. It can be explained by the different gravity fields which were used for the computations. For example, Yuan et al. (2001) had used a spherical harmonics model developed upto degree and order 75, while Lemoine et al. (2001) updated the model upto degree and order 80. Moreover, both authors used only one year of mapping data for their computations. On the other hand, Konopliv et al. (2006); Marty et al. (2009) and on this chapter, the entire mapping period data since 1999 to the end of mission (late 2006) has been analyzed with  $95 \times 95$  spherical harmonics model. Because of the short circular orbit of the MGS, such high order tesseral ( $l \neq m$ ) and sectoral ( $l = m$ ) coefficients are important to model gravitation forces precisely.

### 3.4.4 Estimated parameters

#### 3.4.4.1 $F_S$ and $F_D$ scale factors

The Solar radiation pressure (Eqs. 2.74) and the atmospheric drag (Eqs. 2.75) are the most dominating non-gravitational forces that are acting on the MGS spacecraft. As mentioned earlier, these non-gravitational forces depend upon the characteristic of the spacecraft model (macro-model) and its orientation. Thus, in order to accounting the inaccuracy in the spacecraft modeling and its orientations, an overall scale factors ( $F_S$  and  $F_D$ ) are estimated for each data-arc. However, for an accurate modeling, one can expect these values approximately equal to one.

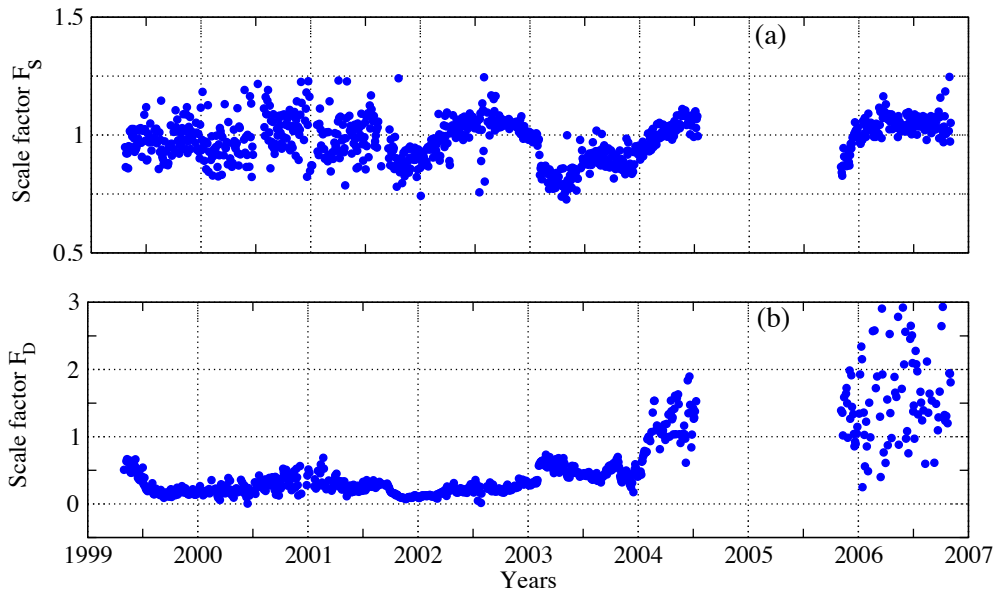


Figure 3.7: Scale factors: a) atmospheric drag and b) solar radiation pressure.



A priori values of  $1 \pm 1$  were adopted for computing the two coefficients. Figure 3.7 shows the variation with time of these coefficients. As one can see on the panel *a* of this figure, the computed values of the solar radiation pressure coefficient  $F_S$  stay around the nominal value. An average value of  $F_S$  is estimated as  $0.97 \pm 0.09$ .

However, the drag coefficient (panel *b* of same figure) stay rather below the nominal value up to the beginning of 2004, and then exhibit large variations which have been unexplained yet. An average value of  $F_D$  is estimated as  $0.50 \pm 0.40$ . This small value of  $F_D$  may be a sign of lack of decorrelation with other parameters, enhanced over this time period by the weakness of the solar activity and an inadequate parameterization of the solar flux effect in the DTM-Mars model (Marty et al., 2009).

### 3.4.4.2 DSN station position and ephemeris bias

To account for the uncertainties on the DSN antenna center position or in the instrumental delays, one bias per station is adjusted on the range measurements for each data-arc. For computing this bias, GINS used station coordinates that are given in the 2008 International Terrestrial Reference Frame (ITRF). These coordinates are then corrected from the continental drift, tides and then projected into an inertial frame through the EOP. The continental map of DSN stations is given in Figure 3.8

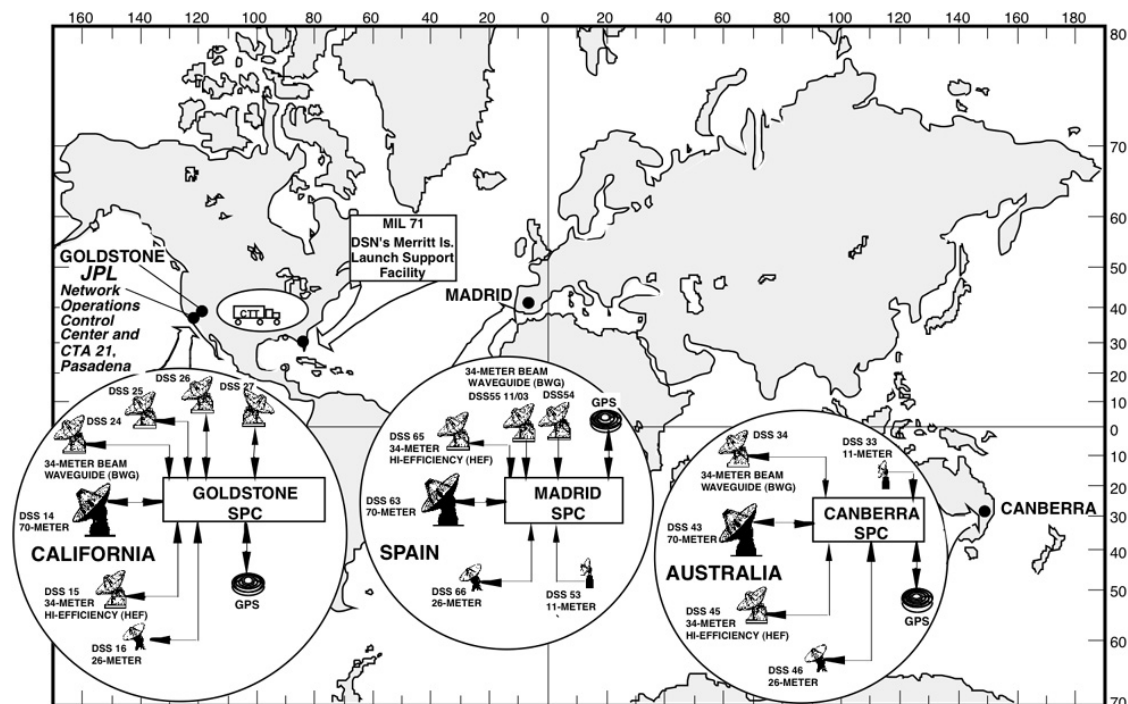


Figure 3.8: The continental map of DSN stations. *Image credit: NASA*

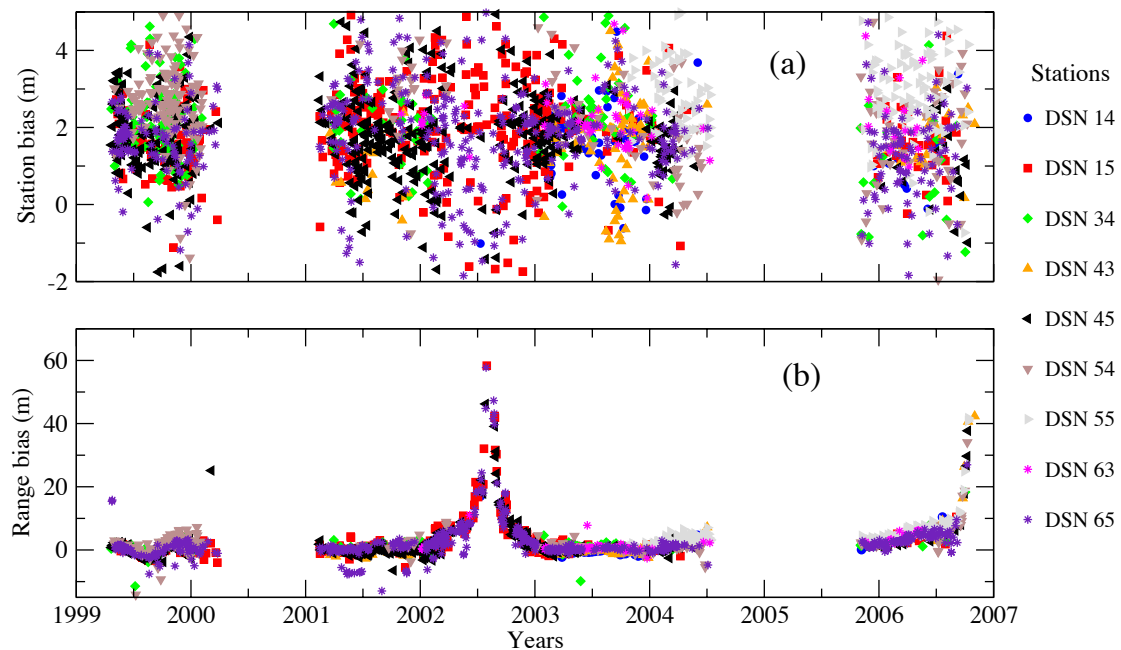


Figure 3.9: Distance bias estimated for each data-arc and for each participating station: a) station position bias and b) range bias corrections to the INPOP10b ephemeris.

The adjustment of the station bias has been done simultaneously with the orbit fit. It is done independently for each station which are participating in the data-arc. This adjustment then absorbs the error at each station like uncalibrated delay in the wires. The panel *a* of Figure 3.9 shows the variations with time of the computed station bias for each station. A mean and 1- $\sigma$  value of the station bias is estimated as  $2 \pm 1$  meter, which is compatible with the [Konopliv et al. \(2006\)](#).

In addition to the station bias, one ephemeris bias (so called range bias) is computed for each data-arc. The range bias represents the systematic error in the geometric positions between the Earth and Mars. Similar to the station bias, the range bias is also estimated from the range measurements of each data-arc. The panel *b* of Figure 3.9 shows the variations with time of the estimated range bias per station compared to distances estimated with INPOP10b ephemeris. The peaks and gaps shown in Figure 3.9 demonstrate the effect of the solar conjunction on the range bias.

Moreover, such estimation of range bias are very crucial for the construction of planetary ephemeris and also to perform solar corona studies ([Verma et al., 2013](#)). The complete description of solar corona investigations (that are performed with these range bias) and its impact on the planetary ephemeris and the asteroids mass determination are discussed in Chapter 4.

## 3.5 Supplementary investigations

### 3.5.1 GINS solution vs JPL Light time solutions

One of the important information brought by the radioscience analysis is the range bias measurements between the Earth and the planet. These measurements are important for the estimation of the planet orbit. However, the range measurement accuracy is limited by the calibration of the radio signal delays at the tracking antennas and by the accuracy of the spacecraft orbit reconstruction. In order to check the accuracy of our estimations of the range bias, we computed the range bias (separately from the GINS) from the light time data<sup>7</sup> provided by the JPL and compared them with the one obtained from the GINS.

The JPL data represent a round-trip light time for each range measurement of MGS spacecraft made by the DSN relative to Mars system barycenter. Unlike to the radioscience data, the light-time is a processed data from the JPL Orbit Determination Program (ODP). ODP estimated the MGS orbit from the Doppler tracking data and then measured the Mars position relative to an Earth station by adjusting the spacecraft range measurements for the position of the MGS relative to the Mars center-of-mass (Konopliv et al., 2006). In the ODP software, a calibration for the tropospheric and ionospheric path delay at the DSN stations has been applied based on calibration data specific to the time of each measurement. Moreover, a calibration for the electronic delay in the spacecraft transponder and a calibration for the DSN tracking station measured for each tracking pass are also applied in the ODP (Konopliv et al., 2006). However, no calibration or model for solar plasma has been applied for this JPL release of the MGS light-time.

In addition to MGS, JPL also provides light time data for Odyssey and MRO missions on an irregular time basis. In order to use these light time in the INPOP construction, we therefore modeled a precise light time solution (based on the algorithms given in Section 2.4.2 of Chapter 2) to compute the round-trip time delay from Earth station to planet barycenter (in this case Mars) using INPOP planetary ephemerides. Except solar corona, all corrections which introduced perturbations in the radio signal have been taken in account. With this configuration of light time solution, we are then able to analyze the effect of the solar corona over the ranging data. The solar corona model derived from this analysis is discussed in Chapter 4.

The range bias obtained from the light time solution using INPOP10b ephemeris are shown in panel *a* of Figure 3.10. Panel *b* of the same figure represents the range bias obtained from the GINS software. As one can see in Figure 3.10, both range bias show a similar behavior. The major difference between both solutions is the density of the data. JPL light time data sets are denser than the range bias obtained with GINS as this latest estimated one bias over each two days data-arc when the JPL provides one light time measurement for each range measurement. To plot the approximated differences between both range measurements, we computed an average values of the JPL light time solution over each two days. The differences

---

<sup>7</sup><http://iau-comm4.jpl.nasa.gov/plan-eph-data/>

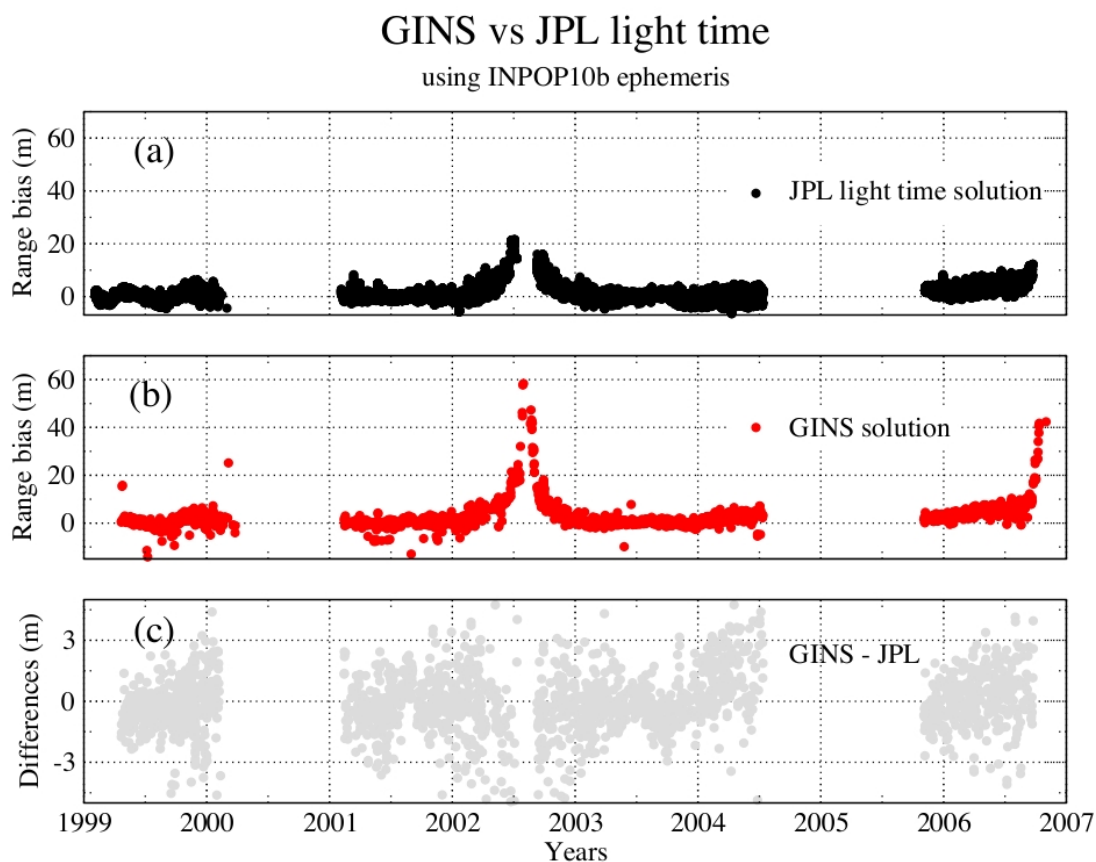


Figure 3.10: Range bias comparison between GINS solution and Light time solution using INPOP10b ephemeris: (a) range bias computed from the JPL light time solution, (b) range bias corresponding to the GINS solution, (c) difference between the GINS and JPL light time solutions.

between GINS range bias and averaged JPL light time are plotted in panel *c*. In this panel, one can notice meter-level fluctuations in the differences, especially during 2004. Such fluctuations may be explained, by the degradations in the computation of the atmospheric drag forces (see Figure 3.7 and Section 3.4.4.1), and by the different approaches and softwares that have been used for the analysis of the MGS radiometric data. Although, the average differences between both solutions was estimated as  $-0.08 \pm 1.2^8 \text{m}$ , which is less than the current accuracy of the planetary ephemerides.

<sup>8</sup>mean  $\pm 1\text{-}\sigma$  dispersion

### 3.5.2 *Box-Wing macro-model vs Spherical macro-model*

As mentioned earlier, non-gravitational forces which are acting on the spacecraft are function of spacecraft model characteristics. These forces are however not as important in amplitude as the gravitational forces as shown in Figure 3.4. Although, despite of their smaller contributions, these forces are extremely important for the precise computation of spacecraft orbit and the detection of geophysical signatures. However, in practice, the complete information of the spacecraft shape (also called macro-model) is either not precisely known or not publicly available. Therefore, the motivation of this study is to understand the impact of in-perfect macro-model over the spacecraft orbit and estimated parameters.

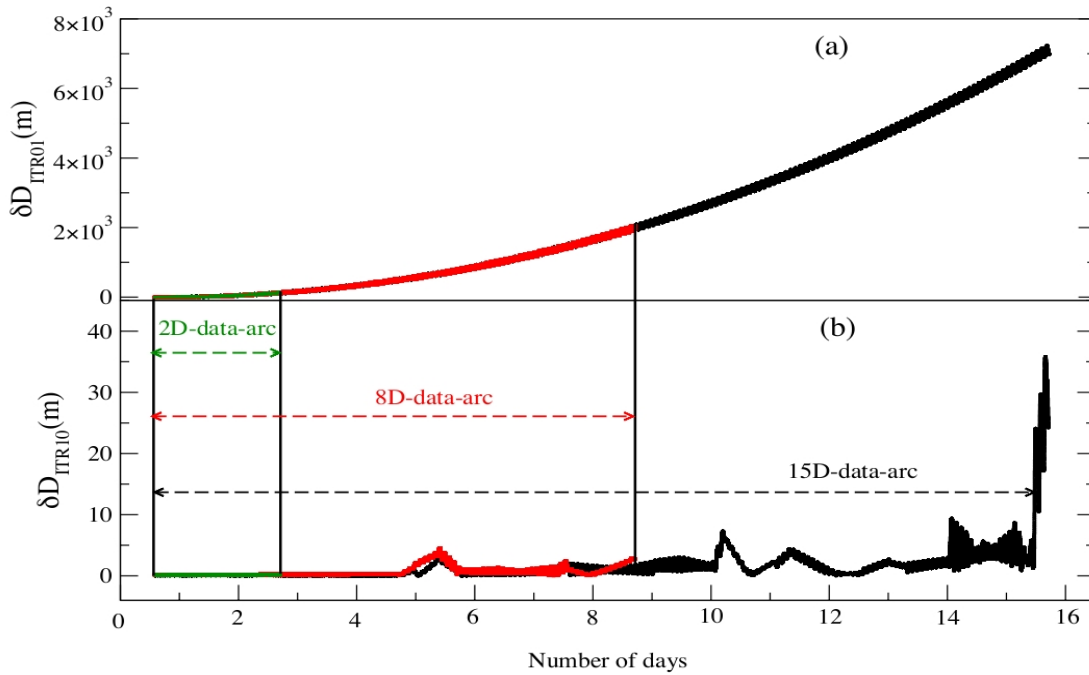


Figure 3.11: Evolution of the orbit change with respect to number of days in the data -arc and with the number of iterations. Panels of the figure are corresponding to a) Iteration-01 and b) Iterations-10. The green, red, and black colors in the figure are corresponding to 2-, 8-, and 15-days data-arc respectively.

To perform this test, we have chosen two kinds of macro-model representing the MGS spacecraft: 1) the *Box-Wing macro-model* ( $BW_{mm}$ ) and 2) the *Spherical macro-model* ( $SP_{mm}$ ). The characteristics of  $BW_{mm}$  are approximately close to the original one and are given in Table 3.1, whereas  $SP_{mm}$  represents the spherical shape macro-model whose characteristics have been chosen randomly. These two models allowed us to clearly distinguish the impact of the macro-model over the orbit determination and the related parameters.

The most common method to minimize the impact of unperfect spacecraft modeling is to shorten the data-arc. We therefore test the evolution of the orbit change with respect to length of the data-arc. Figure 3.11 illustrate such changes using 2- (green), 8- (red), and 15-days (black)

data-arcs. The panel *a* of this figure represents the differences,  $\delta D_{ITR01}$ , between the integrated orbits using  $BW_{mm}$  and  $SP_{mm}$ . These orbits were not fitted to the measurements. As one can see, without the orbit fit  $\delta D_{ITR01}$  is significantly propagating with time. Hence, for 2-, 8-, and 15-days data-arcs, the maximum differences in the orbits are found as 140m, 2000m, and 7200m respectively.

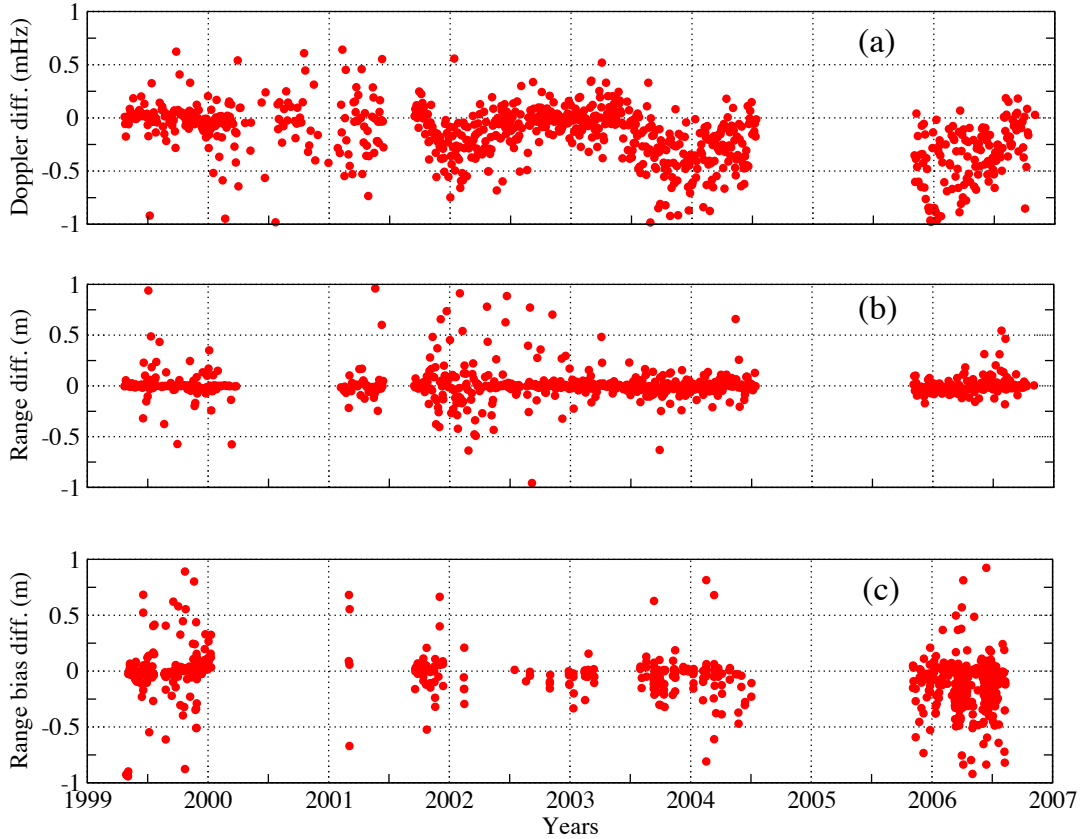


Figure 3.12: Difference between *Box-Wing* and *Spherical* macro-models: (a) Doppler rms residuals, (b) range rms residuals, and (c) range bias.

However, during the orbit determination, least-squares fitting of an orbit using an iterative process may absorb the orbit perturbation induced by the selection of macro-model. Hence, the panel *b* of Figure 3.11 demonstrates the differences in the orbits,  $\delta D_{ITR10}$ , after ten iterations. From this figure, one can see that, the value of  $\delta D_{ITR10}$  is significantly smaller than  $\delta D_{ITR01}$ . The maximum values of  $\delta D_{ITR10}$  for 2-, 8-, and 15-days data-arcs are found as 0.22m, 4.5m, and 36m respectively. In particular, for 2-days data-arc, the maximum value of  $\delta D_{ITR10}$  is less than the  $1-\sigma$  dispersion found in the overlap differences using  $BW_{mm}$  (see Section 3.4.2). Thus, short days data-arc would be the best choice for compensating the macro-model impact during the orbit determination. However, these statistics may vary during solar conjunction periods where most of the perturbations in the radio-signals and in the computed orbit are due to the solar corona.

Furthermore based on this analysis, using 2-days data-arc, we re-analyzed the entire MGS data to understand the impact of  $SP_{mm}$  on the forces (that are acting on the MGS spacecraft) and on the estimated parameters. This analysis has been done in the same way as for  $BW_{mm}$  (see Section 5.3).

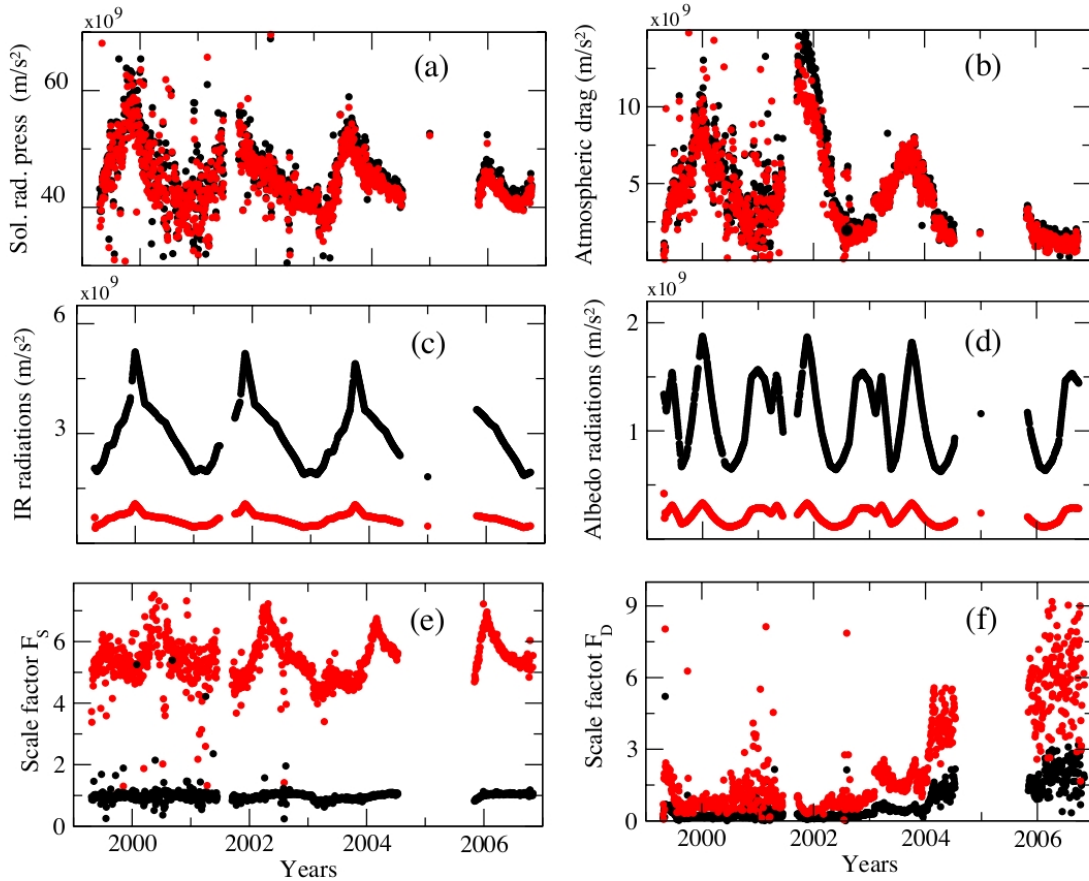


Figure 3.13: Non-gravitational accelerations and scale factors estimated using *Box-Wing* macro-model (Black) and *Spherical* macro-model (Red).

Figure 3.12 illustrates the differences in the residuals (Doppler and range) and the range bias that are obtained during the orbit determination using  $BW_{mm}$  and  $SP_{mm}$ . Average values of these differences are estimated as  $-0.16 \pm 0.26 \text{ mHz}$  ( $-2.8 \pm 4.5 \text{ } \mu\text{m/s}$ ),  $0.003 \pm 0.17 \text{ m}$ , and  $-0.0154 \pm 0.22 \text{ m}$  for Doppler residuals, range residuals, and range bias respectively. These differences are below  $1-\sigma$  of dispersion found for  $BW_{mm}$  (see Section 3.4.2).

Furthermore, as mentioned earlier, characteristics of the spacecraft model only influence the non-gravitational accelerations. These accelerations are changing with one macro-model to another (see Eqs. 2.74 to 2.79). We have computed the non-gravitational accelerations which are acting on the MGS spacecraft using  $BW_{mm}$  and  $SP_{mm}$ . Summary of these accelerations are plotted in Figure 3.13.

In this figure, black dots correspond to  $BW_{mm}$  and red dots correspond to  $SP_{mm}$ . As one

can see that, scale factor estimations for the solar radiation pressure  $F_S$  (panel *e*) and for the atmospheric drag  $F_D$  (panel *f*) are much higher for  $SP_{mm}$  than  $BW_{mm}$ . These scale-factors are estimated to account the mis-modeling in the corresponding accelerations. As a result, both  $BW_{mm}$  and  $SP_{mm}$  experienced approximately a similar accelerations due to the solar radiation pressure (panel *a*) and the atmospheric drag (panel *b*).

However, such scale factors have not been estimated for accelerations due to the Mars radiations (Infra-Red radiation (panel *c*) and Albedo (panel *d*)). Owing to the different physical properties of both *macro-models*, as expected,  $BW_{mm}$  experienced approximately five times greater Mars radiation accelerations than  $SP_{mm}$ . Due to the small contribution of these accelerations over the spacecraft motion, they did not bring much perturbations in the overall spacecraft orbit (Figure 3.11) and postfit residuals (Figure 3.12).

### 3.6 Conclusion and prospectives

The radioscience data analysis of the MGS spacecraft was chosen as an academic case to test our understanding of the raw radiometric data and their analysis with GINS by comparing our results with the literature. In this chapter, we have analyzed the entire radioscience data of Mars Global Surveyor since 1999 to 2006. This analysis has been done independently by using GINS orbit determination software. For accounting the non-gravitational forces precisely, a ten-plate with parabolic high gain antenna *Box-Wing* macro-model was used. In addition, orientations of the spacecraft and its articulated panels were also taken in account and modeled in terms of quaternions. Two-day data-arcs have been used to perform the numerical integration using updated 95×95 MGS95J Mars gravity model.

The estimated accuracy of the orbit and the parameters are consistent with the results found in the literature (Yuan et al. (2001); Lemoine et al. (2001); Konopliv et al. (2006); Marty et al. (2009), see Table 3.3). Moreover, we also compared range bias that were computed from our analysis with reduced light time data provided by JPL. An independent light time solution software has been developed to treat the JPL light time data. The range bias computed from both softwares are consistent with each other, and hence confirm the validity of our analysis with respect to JPL ODP software.

To understand the impact of the macro-model over the orbit perturbations and estimated parameters, we developed a new *Spherical* macro-model. We then re-analyzed the entire radioscience data and compared the outcomes with the one obtained from the *Box-Wing* macro-model. With this comparison, we confirmed that, in the absence of precise knowledge of the spacecraft characteristics, short data-arc can be preferable to accounting the mis-modeling in the spacecraft model without costing the orbit accuracy. However, this analysis may be not preferable for extracting an accurate geophysical signals from the Doppler measurements, such as the estimation of gravity field coefficients. In that case, an accurate modeling of the non-gravitational forces which depend upon the quality of macro-model are highly essential.



The part of these analysis, which consists of an accurate orbit determination of the MGS with *Box-Wing* macro-model, is published in [Verma et al. \(2013\)](#). Moreover as a prospective of these analysis, we performed solar physics studies using data acquired at the time of solar conjunction periods. The Chapter 4 deals with the deduction of a solar corona model from the range bias that are computed at the time of the solar conjunctions. This model is then used to correct the range bias from the solar corona perturbations and also to estimate the corresponding averaged electron densities. The corrected or improved range bias are then used for the construction of planetary ephemerides ([Verma et al., 2013](#)).

Furthermore, the hypothesis based on the supplementary tests of macro-model and the choice of data-arc, have been successfully used in Chapter 5 for the analysis of MESSENGER radioscience data and for the precise computations of MESSENGER orbit.

---



## Chapter 4

# Solar corona correction of radio signals and its application to planetary ephemeris

### 4.1 Introduction

The corona is a high temperature portion of the Sun outer atmosphere, beginning slightly above the visible surface and extending hundreds of thousands of kilometers, or further, into interplanetary space. It has a temperature of millions of degrees, but it is 10 billion times less dense than the atmosphere of the Earth at the sea level. The solar corona is the result of highly dense and strongly turbulent ionized gases that are ejected from the Sun. The particular combination of temperature and particle density in the corona leads to treat this ionized gas as a *plasma*. The term plasma represents the state of matter in which the neutral atoms are separated into charged components and with relatively strong electromagnetic forces between them.

In deep space navigation, the superior conjunction of a probe refers to the situation where the spacecraft, the Earth and the Sun lie in the same line with the spacecraft located on the opposite side of the sun with respect to the Earth. During this occasion, radio signals sent out by the spacecraft pass through the solar corona regions as they travel towards the Earth. Due to strongly turbulent and inhomogeneous plasma in the solar corona regions, radio frequency signals suffer severe degradation in their amplitude, frequency and phase.

The plasma effect on the radio signal propagation may change with the solar wind (slow or fast) and with the solar activity (minimum or maximum). Sections 4.2 and 4.3 give brief descriptions of these solar activity and solar wind characteristics, respectively. Moreover, the solar flares and coronal mass ejections (CME) events that cause the perturbation in the radio signals during the solar conjunction are described in Section 4.4. A brief description of solar corona correction of radio signals and its application to planetary ephemeris are given in Section 4.5. Conclusions of the analysis are then discussed in Section 4.6.

---

All results described in this chapter are published in the *Astronomy & Astrophysics* journal. We therefore represent Section 4.7 by [Verma et al. \(2013\)](#). This section gives the complete description of the solar corona model that has been derived from the range measurements of the MGS, MEX, and VEX, spacecraft. The improvement in the extrapolation capability of the planetary ephemeris and the estimation of the asteroid masses are also discussed in the same section.

## 4.2 The solar cycle

The amount of magnetic flux that rises up to the Sun surface varies with time in a cycle called the solar cycle, which also correspond to the periodic change in the Sun's activity (including changes in the levels of solar radiation and ejection of solar material) and appearance (sunspots, flares, etc). This cycle is sometimes referred to as the sunspot cycle which is associated with strong magnetic fields. According to the Sun activity and the appearance of sunspots, the extreme of the solar cycles can be defined as solar maximum or solar minimum. A brief description of these terminology are given below.

### 4.2.1 Magnetic field of the Sun

The Sun magnetic field is generated by the motion of conductive plasma inside the Sun. This motion is created through convection. The high temperatures of the Sun cause the positively charged ions and negatively charged electrons that make up its plasma to move around. Such movement of the plasma creates many complicated magnetic fields. Moreover, due to the unequal rotation of the Sun around its axis, the plasma near the poles rotates slower than the plasma at the equator causing twisting and stretching of magnetic fields. The twisted magnetic fields lead to the formation of Sunspots (see Section 4.2.2), prominences, and an active corona.

The Sun magnetic field is stronger near the poles and weaker at the equator. In addition to being complex, the magnetic lines actually extend far out into space and this distant extension of the magnetic field is called the Interplanetary Magnetic Field (IMF). Indeed, most of the structure of the Sun corona is shaped by the magnetic field which traps and contains the hot gases. As shown in Figure<sup>1</sup> 4.1, the basic shape of the Sun magnetic field is like the field of a simple bar magnet that connect opposite polarities. However, this basic field (also called a dipole field) is a much more complex series of local fields that vary over time, scattered all over the surface, and constantly changing their positions and strengths (closed field presented by blue lines on the same figure).

On Figure 4.1 one can notice that, the Sun magnetic field has flipped (open field presented by green and red lines) around the time of solar maximum (see Section 4.2.3). Eventually

---

<sup>1</sup>This figure has been extracted from the [Petrie \(2013\)](#) only for the demonstration purpose.

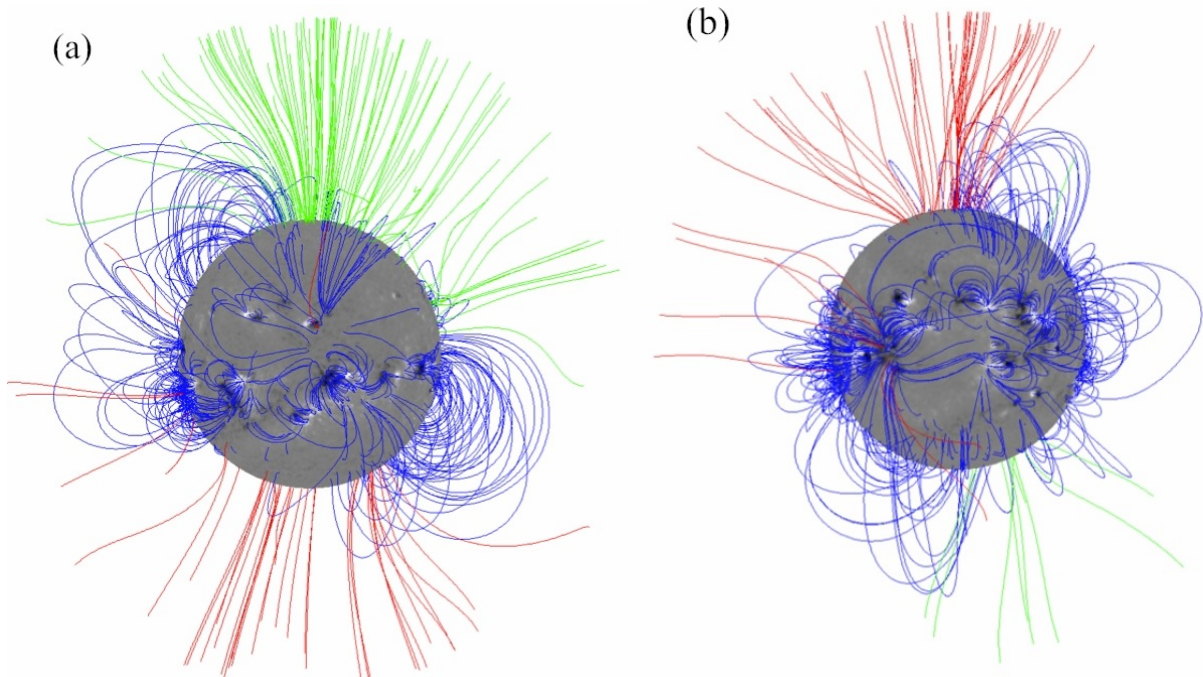


Figure 4.1: Approximated global coronal magnetic field structure for the beginnings of years correspond to solar maximum: (a) 1992 and (b) 2002. The photospheric radial field strength is represented by the greyscale, with white/black indicating positive/negative polarity. Green/red field lines represent open fields of positive/negative polarity and blue lines represent closed fields. These figures have been extracted from [Petrie \(2013\)](#).

after  $\sim 11$  years, at the peak of the sunspot cycle the magnetic poles exchange places, called *polarity reversal*. The winding process then starts over leading to another cycle of  $\sim 11$  years with another polarity reversal to return to the Sun to its original state. Thus, the solar magnetic field has a  $\sim 22$  years cycle to return to its original state.

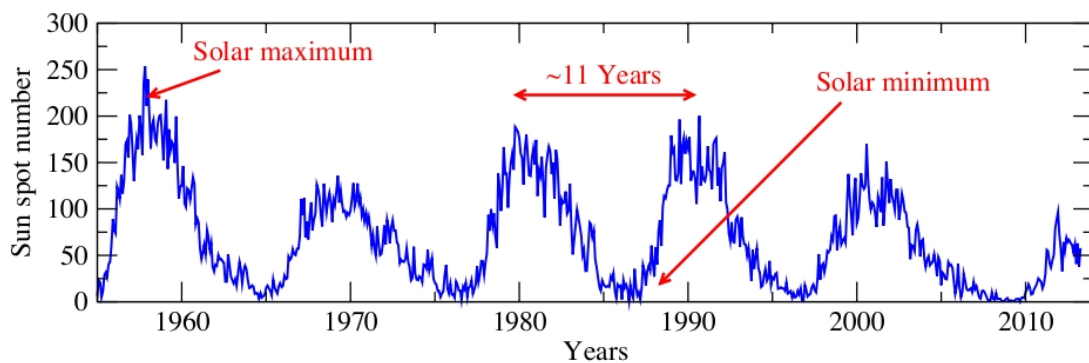


Figure 4.2: The solar sunspot cycle<sup>2</sup>, since 1955 to present. Figure shows the variation of an average monthly sunspot numbers with time.

### 4.2.2 Sunspots

Sunspots are regions where the solar magnetic fields are very strong and twisted. They are temporary phenomena on the photosphere of the Sun that appear visibly as dark spots and typically last for several days, although very large ones may live for several weeks (see [Ringnes \(1964\)](#) for age-frequency distribution of sunspot groups). In visible light, sunspots appear darker than their surroundings as they are relatively thousands of degrees cooler than an average temperature of solar surface. The quantity that measures the number of sunspots and the groups of sunspots present on the Sun surface is refereed as sunspot number. The number and location of sunspots change over time. An average monthly distribution of sunspot numbers<sup>2</sup> are plotted with respect to time in Figure 4.2. The peaks in this figure correspond to the highest solar activities and the cycle of these activities last approximately for 11 years on average.

### 4.2.3 Solar maxima

The solar maxima is the period of greatest solar activity in the ~11 years solar cycle (Figure 4.2). During a solar maximum, the solar surface is covered by relatively large active regions ([Leon and Jay, 2010](#)) and large numbers of sunspots appear on the Sun surface. At solar maximum, the Sun magnetic field lines are the most distorted due to the magnetic field on the solar equator rotating at a slightly faster than at the solar poles and causing more solar activity (see Figure 4.3). The magnetic field of the Sun approximates that of a dipole at high solar latitudes and reverse polarity during the peak of the sunspot cycle (see Figure 4.1).

### 4.2.4 Solar minima

In contrast to solar maximum, the solar minimum is the period of least solar activity in the ~11 year solar cycle (Figure 4.2). During this time the Sun is in line with its magnetic poles as it has completed an 180 degree reversal and then have less solar activity. Typically, the active regions that are present during this time, occur at high solar latitude (far from the equator) ([Leon and Jay, 2010](#)). During a solar minimum the Sun magnetic field, resembles that of an iron bar magnet, with great closed loops near the equator and open field lines near the poles (see Figure 4.3).

---

<sup>2</sup><http://www.sidc.be/sunspot-data/>

---

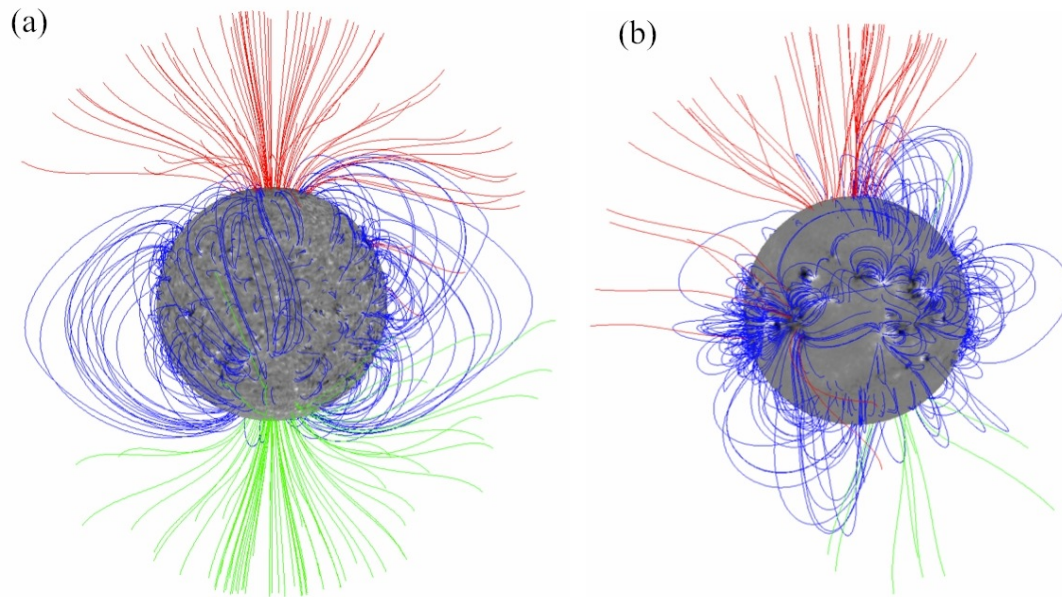


Figure 4.3: Approximated global coronal magnetic field structure for the beginnings of years: (a) 2008, solar minimum and (b) 2002, solar maximum. The photospheric radial field strength is represented by the greyscale, with white/black indicating positive/negative polarity. Green/red field lines represent open fields of positive/negative polarity and blue lines represent closed fields. These figures have been extracted from the [Petrie \(2013\)](#).

## 4.3 The solar wind

The solar wind is a stream of energized, charged particles, primarily electrons and protons, flowing outward from the Sun. The stream of particles varies in temperature and speed over time. Due to high temperature and kinetic energy these particles can escape the Sun gravity. Moreover, as described by [Kojima and Kakinuma \(1990\)](#), the large-scale solar wind structure is changing systematically with the phase of solar activity. The solar wind is divided into two components, respectively termed the slow solar wind and the fast solar wind.

### 4.3.1 Fast solar wind

The fast wind has been associated with open field lines extended from coronal holes. It is characterized by a low density, and a low mass flux. The fast solar wind has a typical velocity of  $\approx 750$  km/s, a temperature of  $\approx 8 \times 10^5$  K and it nearly matches the composition of the Sun photosphere ([Feldman et al., 2005](#)). The fast solar wind is thought to originate from coronal holes, which are the regions of open field lines in the Sun magnetic field ([Hassler et al., 1999](#)). In these regions the magnetic field lines are open to the interplanetary medium ([Zirker, 1977](#)), see Figure 4.3. The fast wind areas increase systematically as the solar activity diminishes,

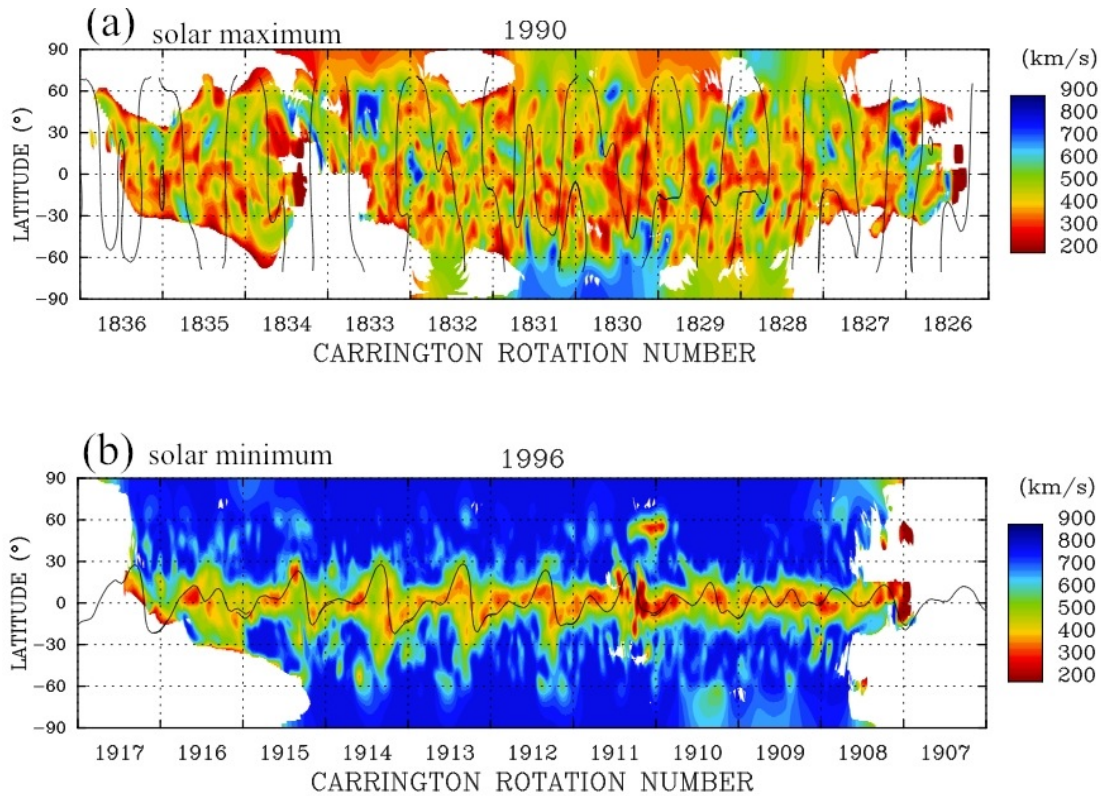


Figure 4.4: Synoptic source surface maps of solar wind speeds, in the Carrington rotation number versus latitude for 1990 and 1996, which approximately correspond to the cycle 22 maximum (*panel a*) and 22/23 minimum (*panel b*), respectively. The dark solid line represents the neutral magnetic line. These figures have been extracted from the Tokumaru et al. (2010).

reaching the maximum value at the minimum phase (Tokumaru et al., 2010). Figure<sup>3</sup> 4.4 shows an example of solar wind speed maps extracted from Tokumaru et al. (2010). From panel *b* one can see that, during a solar minimum, the high-to-mid latitude regions ( $\sim \pm 30^\circ$ ) were occupied with the fast wind. These regions however diminished or disappeared greatly during solar maximum (see panel *a*).

### 4.3.2 Slow solar wind

The slow wind has been associated with the most active coronal regions and mainly with closed magnetic structures (Schwenn, 1983), which cause its speed to be less than the fast solar wind. It is denser, and has a more complex structure, with turbulent regions and large-scale structures (Kallenrode, 2004). The slow wind has a velocity of about  $\approx 400$  km/s, a temperature of  $\approx 1.4$ - $1.6 \times 10^6$  K (Feldman et al., 2005). The slow solar wind appears to originate from a region

<sup>3</sup>This figure has been extracted from the Tokumaru et al. (2010) only for the demonstration purpose.



around the Sun equatorial belt that is known as the *streamer belt*. Coronal streamers extend outward from this region, carrying plasma from the interior along closed magnetic loops (Lang, 2000). However Bravo and Stewart (1997) suggest that coronal holes may also be the sources of slow winds, which could be emerging from the bordering. During solar maximum, the slow wind area increase systematically over the solar latitude and decrease as solar activity diminishes (Tokumaru et al., 2010). Figure 4.4 shows that, during solar minimum, the low latitude regions were dominated by the slow wind and became ubiquitous at all latitudes during the maximum.

## 4.4 Radio signal perturbation

The perturbation in the radio signals is one of the consequences of the solar corona. For a deep space probe, when the Sun directly intercepts the radio signals between the spacecraft and the Earth, it induces perturbations in the signals and degrades them enormously. However, such degradations give an opportunity to compute time delay induced by the solar plasma and to study its physical characteristics with the plasma parameter. The time delay indicates the extra time due to the presence of an ionized medium in the propagation path, and the plasma parameter is a measure of the number of particles in a volume (so called electron density) along the line of sight (LOS).

There could be a number of causes which degrade the radio signal during solar conjunctions. The solar flares and CME could be the most important events that occur in the solar corona and cause the degradation of signal. These events are often associated with the solar activity and can occur during both phases of Sun activity, solar maximum and solar minimum. During the low periods of the solar cycle, events are less frequent and generally confined to the Sun equatorial region, when during periods of high solar activity, events are much more frequent and may occur at any place on the Sun surface (see Figure 4.4). The brief characteristics of these events are given below:

- **Solar flare:** Sudden energy release in the solar atmosphere is called solar flare (Hudson et al., 1995). The enormous explosions of the Sun surface typically last for a few minutes and can release enormous amount of energy. The solar flares are known to be associated with the magnetic field structure of the Sun around the sunspots (Parker, 1963). If this structure becomes twisted and sheared then magnetic field lines can cross and reconnect with an explosive release of energy. This causes an eruption of gases on the solar surface, and extends hundreds of thousands of kilometers out from the surface of the Sun following the magnetic lines to form a solar flare. During the first stages of the solar flare, high velocity protons are ejected and travel at around a third the speed of light. The ejected material follows the arc of the magnetic lines and then returns to the Sun, although some material is ejected into outer space especially during the larger flares.
- **Coronal mass ejections:** They are another form of disturbance that can affect radio com-

munications. CME are the explosions in the Sun corona that cause huge bubbles of gas that are threaded with magnetic field lines, and the bubbles are ejected over the space during several hours. During the CME, the fluctuations of the Sun magnetic fields cause a release of huge quantities of matter and electromagnetic radiation into space above the Sun surface, either near the corona, or farther into the solar system, or even beyond. Such release of matter disrupts the steady flow of the solar wind producing a large increase in the flow. Unlike a solar flare, a CME doesn't produce intense light. But it does produce a magnetic shockwave which may interact with the Earth magnetic field.

Both events increase the level of solar radiation in the solar corona regions. During superior solar conjunctions, when radio signals interact with these radiations, then the signals suffer severe degradation and cause a time delay on ranging measurements and a phase advance on Doppler measurements. The magnitudes of these effects are inversely proportional to the square of the signal frequency and the radial distance (outward from the Sun) (Muhleman et al., 1977; Schwenn and Marsch, 1990, 1991; Guhathakurta and Holzer, 1994; Bird et al., 1994; Guhathakurta et al., 1996). Thus, solar corona effects on the radio signals are decreasing with increase in frequency and with distance from the Sun. Peaks in the Figures 3.5 and 3.9 (panel *b*) of Chapter 3 show an example of solar corona effects on Doppler and range measurements. The solar corona model deduce from the range measurements acquired at the time of solar conjunctions allowed us to compute time delay due to the presence of an ionized medium in the propagation path. One can then also estimate an average electron density along the line of sight (LOS).

## 4.5 Solar corona correction of radio signals and its application to planetary ephemeris

As described in sections 4.2 and 4.3, solar wind area and solar events are frequently changing with the solar activity. Hence, one can expect different distributions of charged particles in slow and fast wind regions (Schwenn, 2006). Therefore, it is necessary to identify if the region of the radio signal propagation is either affected by the slow wind or by the fast wind. In this section we investigated these regions and derived the characteristics of solar corona models and associated electron density distribution at different phases of solar activity (maximum and minimum) and at different solar wind states (slow and fast). The processed range data obtained after orbit determination have been used to derive the models and to estimate the time delay due to the solar corona. These estimations lead us to remove the solar corona perturbations from the range data. The corrected range data are then used for the construction of planetary ephemeris. This complementary range data noticeably improve the extrapolation capability of the planetary ephemeris and the estimation of the asteroid masses. All results corresponding to this study are published in the *Astronomy & Astrophysics* journal. In this section we gave the brief description of the steps used to derive the solar corona models. The outcomes of this study are given in Section 4.7 and followed by Verma et al. (2013).

---

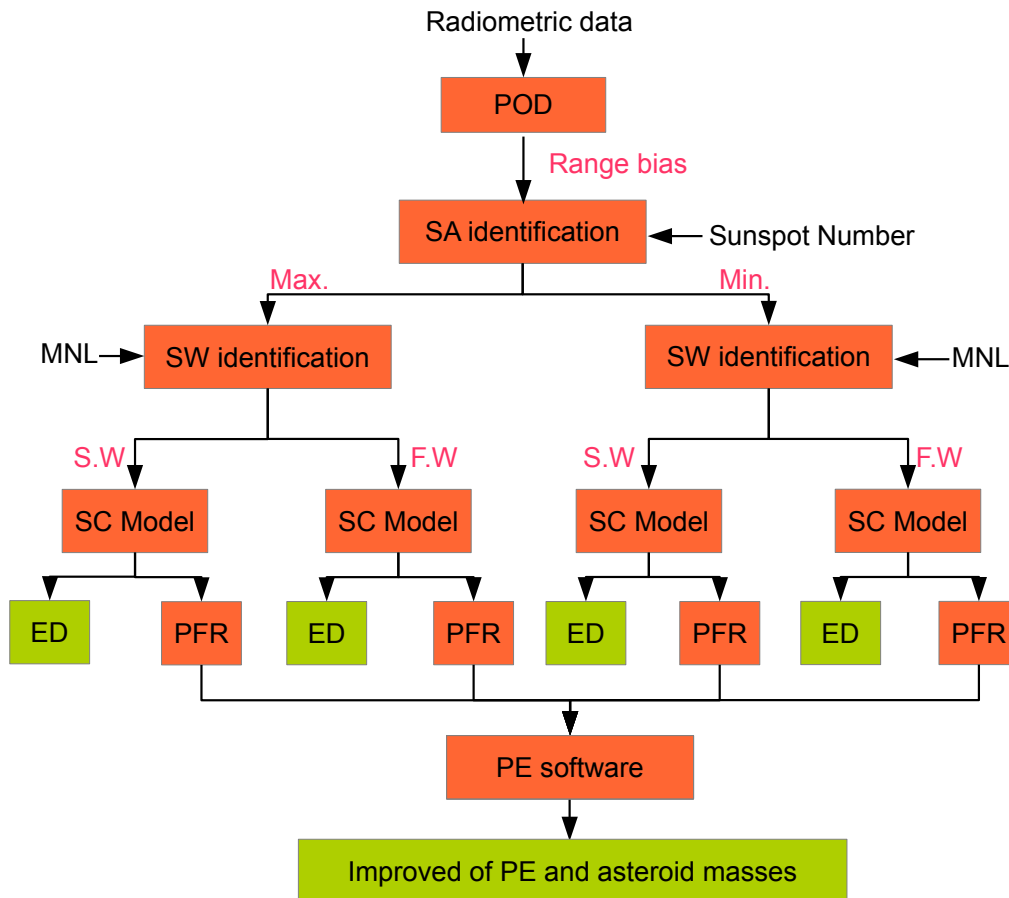


Figure 4.5: Flow chart describing the procedure involved in the derivation of solar corona model, electron density computations and further improvement of the planetary ephemeris. The abbreviations used in the flow chart are:

POD: Precise Orbit Determination; SA: Solar Activity; SW : Solar Wind

S.W : Slow Wind; F.W : Fast Wind; ED : Electron Density; PFR : PostFit Residuals

Figure 4.5 described the procedure used to perform this study, that are:

- Precise Orbit Determination:** The radiometric data of MGS, MEX, and VEX, consisting of two-way Doppler- and range measurements (see Chapter 2), have been used to perform this study. These data set are first analyzed by the orbit determination software to compute the spacecraft orbit precisely. Such analysis of the MGS radiometric data using GINS software have been performed in Chapter 3. However, for MEX, and VEX these analysis were performed by ESA navigation team. The range bias obtained from these computations were then provided by ESA, and we compared them to light-time delays computed with the INPOP10b, and the DE421 ephemerides. The brief description of MEX and VEX orbit accuracy and their estimation are given in [Fienga et al. \(2009\)](#) and in [Verma et al. \(2013\)](#) (see Section 4.7).
- Solar activity identifications:** As described in Section 4.2, unequal rotation of the Sun

causes twisting and stretching of the magnetic fields. The twisted magnetic fields leads to the formation of sunspots, prominences, and an active corona. Hence, as shown in Figure 4.2, larger (smaller) number of sunspots appeared on the Sun surface represents the maximum (minimum) solar activity. In June 2002, when the solar activity was maximum (see Figure 4.2), the MGS SEP angle remained below  $10^\circ$  for two months and went at minimum to  $3.325^\circ$ . MEX experienced superior conjunctions during the minimum phase of solar activities: October 2006, December 2008, and February 2011. During these time MEX SEP angle remained below  $10^\circ$  for two months. Similarly, the VEX SEP angle remained below  $8^\circ$  for two months during October 2006 and June 2008 (solar minima, see Figure 4.2). The peaks and gaps shown in Figure 2 of Section 4.7 demonstrate the effect of the solar conjunction on the estimated range bias for MGS, MEX, and VEX.

- **Solar wind identifications:** As shown in Figure 4.4, the distribution of the solar slow-, and fast-winds varies significantly with the solar activities. Hence, as described in Schwenn (2006), the electronic profiles are very different in slow- and fast-wind regions. MGS, and MEX and VEX experienced superior conjunctions during the solar maxima and minima, respectively. It is therefore necessary to identify if the region of the LOS is either affected by the slow-wind or by the fast-wind when passes through the solar corona regions. Such identification can be performed by locating the minimum distance of the line of sight (MDLOS) heliographic longitudes and latitudes with the maps of the solar corona magnetic field as provided by the Wilcox Solar Observatory (WSO)<sup>4</sup>. Magnetic Neutral Line (MNL), where the resultant magnetic field is zero, can be then used to define the limit of slow-, and fast-winds. We took limits of the slow solar wind regions as a belt of  $20^\circ$  above and below the MNL during the solar minima and  $\pm 70^\circ$  during solar maxima (You et al., 2007, 2012). The entire distributions of the LOS for all three spacecraft are given in Section 4.7.
- **Solar corona model:** From Figure 4.5 one can see that, the solar corona models have been derived separately for different types of solar winds (fast, slow), and for solar activity phases (minimum, maximum). As mentioned previously, interactions between radio signals and solar corona regions cause severe degradations in the signals and a time delay on ranging measurements. Such effects on the radio signals decrease with an increase in frequency and with distance from the Sun, and can be modeled by integrating the entire ray path from the Earth station ( $L_{Earth_s/n}$ ) to the spacecraft ( $L_{s/c}$ ) at a given epoch. This model is defined as:

$$\Delta\tau = \frac{1}{2cn_{cri}(f)} \times \int_{L_{Earth_s/n}}^{L_{s/c}} N_e(l) dL \quad (4.1)$$

$$n_{cri}(f) = 1.240 \times 10^4 \left( \frac{f}{1 \text{ MHz}} \right)^2 \text{ cm}^{-3} ,$$

where  $c$  is the speed of light,  $n_{cri}$  is the critical plasma density for the radio carrier frequency  $f$ , and  $N_e$  is an electron density in the unit of electrons per  $\text{cm}^3$  and is expressed as (Bird et al., 1996)

<sup>4</sup><http://wso.stanford.edu/>

$$N_e(l) = B \left( \frac{l}{R_\odot} \right)^{-\epsilon} \text{ cm}^{-3} . \quad (4.2)$$

where  $B$  and  $\epsilon$  are the real positive parameters to be determined from the data.  $R_\odot$  and  $l$  are the solar radius and radial distance in AU. The maximum contribution in the electron density occurs when  $l$  equals the MDLOS,  $p$ , from the Sun. At a given epoch, MDLOS is estimated from the planetary and spacecraft ephemerides. We also defined the impact factor  $r$  as the ration between MDLOS  $p$  and the solar radii ( $R_\odot$ ). The complete analytical solutions for computing the Equation 4.1 is given in Appendix A of Section 4.7. Moreover, in addition to [Bird et al. \(1996\)](#) corona model, we have also used [Guhathakurta et al. \(1996\)](#) corona model that added one or more terms to Equation 4.2, that is:

$$N_e(l) = A \left( \frac{l}{R_\odot} \right)^{-c} + B \left( \frac{l}{R_\odot} \right)^{-d} \text{ cm}^{-3} \quad (4.3)$$

with  $c \simeq 4$  and  $d = 2$ .

The parameters of Equations 4.2 and 4.3 are calculated using least-squares techniques. These parameters are obtained for various ranges of the MDLOS, from  $12R_\odot$  to  $215R_\odot$  for MGS,  $6R_\odot$  to  $152R_\odot$  for MEX, and from  $12R_\odot$  to  $154R_\odot$  for VEX. The fitting of the parameters were performed, for all available data acquired at the time of the solar conjunctions, for each spacecraft individually, and separately for fast- and slow-wind regions. The summary of estimated parameters for each spacecraft and for each solar wind region are given in Table 2 of Section 4.7).

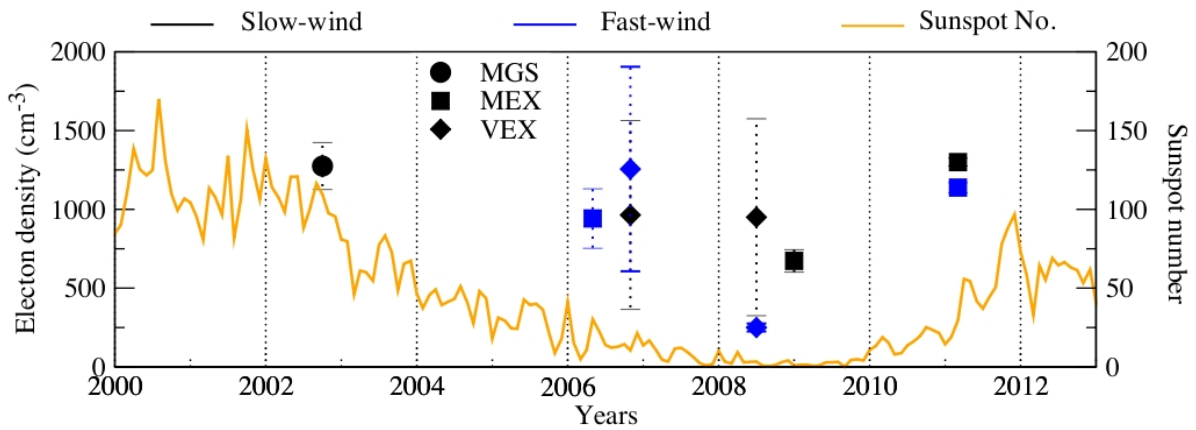


Figure 4.6: An average electron density distribution at  $20R_\odot$  during different phases of solar activities and for different states of solar wind. Higher number of sunspots correspond to maximum phase of solar activity, while smaller number correspond to minimum phase.

- (a) **Electron density:** The MGS experienced its superior conjunction in 2002 when the solar activity was maximum and the slow-wind region was spread at about  $\pm 70^\circ$  of heliolatitude ([Tokumaru et al., 2010](#)). Hence, MDLOS of the MGS exclusively

affected by the slow-wind region (see Figure 6 of Section 4.7). In contrast, MEX and VEX experienced their superior conjunctions during solar minima (2006, 2008, and 2011). During these periods, the slow-wind region was spread at about  $\pm 30^\circ$  of heliolatitude (Tokumaru et al., 2010). Owing to small slow-wind region, MDLOS of the MEX and VEX were affected by both slow-, and fast-wind regions (see Figure 4 of Section 4.7).

For an example, on Figure 4.6, are plotted the average electron densities obtained at  $20R_\odot$  for all three spacecraft, computed separately for fast- and slow-wind regions using Equation 4.2. These densities are then compared with the various models, as given in Table 4.1.

Table 4.1: Electron densities estimated from different models at  $20R_\odot$  and at  $215R_\odot$  (1AU).

Authors	Spacecraft	Solar activity	MDLOS	Ne @ $20R_\odot$ (el. $\text{cm}^{-3}$ )	Ne @ $215R_\odot$ (el. $\text{cm}^{-3}$ )
<a href="#">Leblanc et al. (1998)</a>	Wind	Min	1.3-215	847	7.2
<a href="#">Bougeret et al. (1984)</a>	Helios 1 and 2	Min/Max	65-215	890	6.14
<a href="#">Issautier et al. (1998)</a>	Ulysses	Min	327-497	307*	$2.65 \pm 0.5^*$
This chapter**	MEX06	Min	6-40	$942 \pm 189$	$2.3 \pm 0.9$
This chapter**	MEX08	Min	6-71	$673 \pm 72$	$2.3 \pm 1.3$
This chapter**	VEX08	Min	12-154	$950 \pm 625$	$3 \pm 2$
<a href="#">Muhleman et al. (1977)</a>	Mariner 6 and 7	Max.	5-100	$1231 \pm 64$	$9 \pm 3$
This chapter**	MGS	Max	12-215	$1275 \pm 150$	$11.0 \pm 1.5$
<a href="#">Bird et al. (1994)</a>	Ulysses	Max	5-42	$1700 \pm 100$	$4.7 \pm 0.415$
<a href="#">Anderson et al. (1987b)</a>	Voyager 2	Max	10-88	$6650 \pm 850$	$38 \pm 4$

\* Mean electron density corresponds to latitude  $\geq 40^\circ$

\*\* The values correspond to Table 2 of Section 4.7, [Verma et al. \(2013\)](#)

In Table 4.1, we provide the average electron density at  $20R_\odot$  and  $215R_\odot$ , based on the corresponding model parameters (if not given by the authors). Table 4.1 shows a wide range of the average electron densities, estimated at  $20R_\odot$  and  $215R_\odot$  during different phases of solar activity. As one can notice, our estimates of the average electron density are very close to the previous estimates, especially during solar minimum. The widest variations between our results and the earlier estimates were found during solar maxima and can be explained from the high variability of the solar corona during these periods.

Moreover, as one can notice on Figure 4.6 and Table 4.1, dispersions in the estimation of electron densities using VEX range data are relatively large compared to the MGS or MEX. This can be explained by the limitations in the VEX orbit determi-

nation (Fienga et al., 2009), which introduced bias in the estimation of the model parameters and consequently in the electron densities. The detailed analysis of these results are discussed in Section 4.7

- (b) **Postfit residuals:** In addition to electron density computations, one can also compute the light time delay due to the solar corona. This time delay can then be removed from the range bias to minimize the effect of solar corona. Statistics of the range bias before (prefit) and after (postfit) the correction of the solar corona perturbations are given in Table 4.2. From this table one can notice that, the estimated dispersions in the postfit range bias are one order of magnitude lower than the dispersions in the prefit range bias. It shows a good agreement between the model estimates and the range radiometric data. However, because of the degraded quality of VEX orbit (Fienga et al., 2009), the statistics of the VEX residuals are not as good as for the MGS and MEX.

Table 4.2: Statistics of the range bias before and after solar corona corrections.

S/C	Pre-fit		Post-fit	
	mean (m)	$\sigma$ (m)	mean (m)	$\sigma$ (m)
MGS, 2002	6.02	10.10	-0.16	2.89
MEX, 2006	42.03	39.30	0.85	9.06
MEX, 2008	16.00	20.35	-0.10	4.28
MEX, 2011	15.44	19.20	0.11	6.48
VEX, 2006	5.47	11.48	-0.74	6.72
VEX, 2008	3.48	11.48	-0.87	7.97

- **Planetary ephemerides improvements:** As described in Chapter 1, range bias data are very important for the construction of the planetary ephemerides. Usually, due to high uncertainties, the range bias affected by the solar corona perturbations ( $\sim 4$ -6 months of data) are not included in the construction of the planetary ephemerides. Thanks to the solar corona corrections, it was possible to use for the first time these range bias. To demonstrate the impact of these complementary data, corrected for the solar corona perturbations, we construct two ephemerides, INPOP10c and INPOP10d, both fitted over the same data set as was used for the construction of INPOP10b (see Chapter 1). INPOP10c was constructed without solar corona corrections while these corrections were included in the INPOP10d construction. These additional data represents  $\sim 8\%$  of whole data set used for the ephemeris construction.

In particular, the Mars orbit is affected by the belt of asteroids. The asteroid masses may cause a degradation in the estimates of the Mars orbit. Therefore by keeping more observations during solar conjunction intervals we have noticed the noticeable improvements in the extrapolation capability of the planetary ephemerides and the estimation of the asteroid masses. Table 5 of Section 4.7 gives such estimations of the asteroid masses. On Table

6 of Section 4.7, significantly improved masses, estimated with INPOP10d, are then compared with the one found in the literature and showed 80% better consistency with respect to INPOP10c. Moreover, MEX extrapolated residuals computed with INPOP10d show a better long-term behavior compared with INPOP10c with 30% less degraded residuals after two years of extrapolation. The complete analysis of these results are discussed in Section 4.7.

## 4.6 Conclusion

We have analyzed the large-scale structure of the corona electron density, since 2001 to 2011. This analysis has been done with the range bias data of the MGS, MEX, and VEX spacecraft acquired during solar conjunction periods. The parameters of the solar corona models are then deduced from these data. These parameters were estimated separately for each spacecraft at different phases of solar activity (maximum and minimum) and at different solar wind states (slow and fast). We compared our results with the previous estimations that were based on different techniques and different data sets. Our results are consistent, especially during solar minima, with estimations obtained by these different techniques. However, during the solar maxima, electron densities obtained with different methods or different spacecraft show weaker consistencies.

We have also demonstrated the impact of solar corona correction on the construction of planetary ephemerides. The supplementary data, corrected from the solar corona perturbations, allowed us to gain ~8% of whole data set. Such corrected data are then used for the first time in the construction of INPOP and induce a noticeable improvement in the estimation of the asteroid masses and a better long-term behavior of the ephemerides. In addition to these improvements, recent Uranus observations and positions of Pluto have been added to construct the latest INPOP10e ephemerides (Fienga et al., 2013). For the further improvement, INPOP10e is then used for the analysis of MESSENGER radioscience data (see Chapter 5).

As stated previously, all results described in this chapter are published in the *Astronomy & Astrophysics* journal. The Section 4.7 therefore represented by the Verma et al. (2013), which described the complete analysis of these results.

## 4.7 Verma et al. (2013)

---



# Electron density distribution and solar plasma correction of radio signals using MGS, MEX, and VEX spacecraft navigation data and its application to planetary ephemerides<sup>★</sup>

A. K. Verma<sup>1,2</sup>, A. Fienga<sup>1,3</sup>, J. Laskar<sup>3</sup>, K. Issautier<sup>4</sup>, H. Manche<sup>3</sup>, and M. Gastineau<sup>3</sup>

<sup>1</sup> Observatoire de Besançon, CNRS UMR6213, 41bis Av. de l'Observatoire, 25000 Besançon, France

<sup>2</sup> CNES, Toulouse, France

e-mail: ashok@obs-besancon.fr

<sup>3</sup> Astronomie et Systèmes Dynamiques, IMCCE-CNRS UMR 8028, 77 Av. Denfert-Rochereau, 75014 Paris, France

<sup>4</sup> LESIA, Observatoire de Paris, CNRS, UPMC, Université Paris Diderot, 5 place Jules Janssen, 92195 Meudon, France

Received 25 June 2012 / Accepted 19 December 2012

## ABSTRACT

The Mars Global Surveyor (MGS), Mars Express (MEX), and Venus Express (VEX) experienced several superior solar conjunctions. These conjunctions cause severe degradations of radio signals when the line of sight between the Earth and the spacecraft passes near to the solar corona region. The primary objective of this work is to deduce a solar corona model from the spacecraft navigation data acquired at the time of solar conjunctions and to estimate its average electron density. The corrected or improved data are then used to fit the dynamical modeling of the planet motions, called planetary ephemerides. We analyzed the radio science raw data of the MGS spacecraft using the orbit determination software GINS. The range bias, obtained from GINS and provided by ESA for MEX and VEX, are then used to derive the electron density profile. These profiles are obtained for different intervals of solar distances: from 12  $R_{\odot}$  to 215  $R_{\odot}$  for MGS, 6  $R_{\odot}$  to 152  $R_{\odot}$  for MEX, and from 12  $R_{\odot}$  to 154  $R_{\odot}$  for VEX. They are acquired for each spacecraft individually, for ingress and egress phases separately and both phases together, for different types of solar winds (fast, slow), and for solar activity phases (minimum, maximum). We compared our results with the previous estimations that were based on in situ measurements, and on solar type III radio and radio science studies made at different phases of solar activity and at different solar wind states. Our results are consistent with estimations obtained by these different methods. Moreover, fitting the planetary ephemerides including complementary data that were corrected for the solar corona perturbations, noticeably improves the extrapolation capability of the planetary ephemerides and the estimation of the asteroids masses.

**Key words.** celestial mechanics – ephemerides – Sun: corona

## 1. Introduction

The solar corona and the solar wind contain primarily ionized hydrogen ions, helium ions, and electrons. These ionized particles are ejected radially from the Sun. The solar wind parameters, the velocity, and the electron density are changing with time, radial distances (outward from Sun), and the solar cycles (Schwenn & Marsch 1990, 1991). The strongly turbulent and ionized gases within the corona severely degrade the radio wave signals that propagate between spacecraft and Earth tracking stations. These degradations cause a delay and a greater dispersion of the radio signals. The group and phase delays induced by the Sun activity are directly proportional to the total electron contents along the **line of sight (LOS)** and inversely proportional with the square of carrier radio wave frequency.

By analyzing spacecraft radio waves facing a solar conjunction (when the Sun directly intercepts the radio signals between the spacecraft and the Earth), it is possible to study the electron content and to better understand the Sun. An accurate determination of the electron density profile in the solar corona and in the solar wind is indeed essential for understanding the energy transport in collision-less plasma, which is still an open question (Cranmer 2002). Nowadays, mainly radio scintillation and

**Table 1.** Previous models based on in situ and radio science measurements (see text for detailed descriptions).

Spacecraft	Data type	Author
Mariner 6 and 7	radio science	Muhleman et al. (1977)
Voyager 2	radio science	Anderson et al. (1987)
<i>Ulysses</i>	radio science	Bird et al. (1994)
Helios land 2	in situ	Bougeret et al. (1984)
<i>Ulysses</i>	in situ	Issautier et al. (1998)
Skylab	Coronagraph	Guhathakurta et al. (1996)
Wind	solar radio burst III	Leblanc et al. (1998)

white-light coronagraph measurements can provide an estimation of the electron density profile in the corona (Guhathakurta & Holzer 1994; Bird et al. 1994; Guhathakurta et al. 1996, 1999; Woo & Habbal 1999). However, the solar wind acceleration and the corona heating take place between 1 to 10  $R_{\odot}$  where in situ observations are not possible. Several density profiles of solar corona model based on different types of data are described in the literature (Table 1). The two viable methods that are generally used to derive these profiles are (Muhleman & Anderson 1981) (1) direct in situ measurements of the electron density, speed, and energies of the electron and photons, and (2) an

<sup>★</sup> Tables 5, 6 and Appendix A are available in electronic form at <http://www.aanda.org>

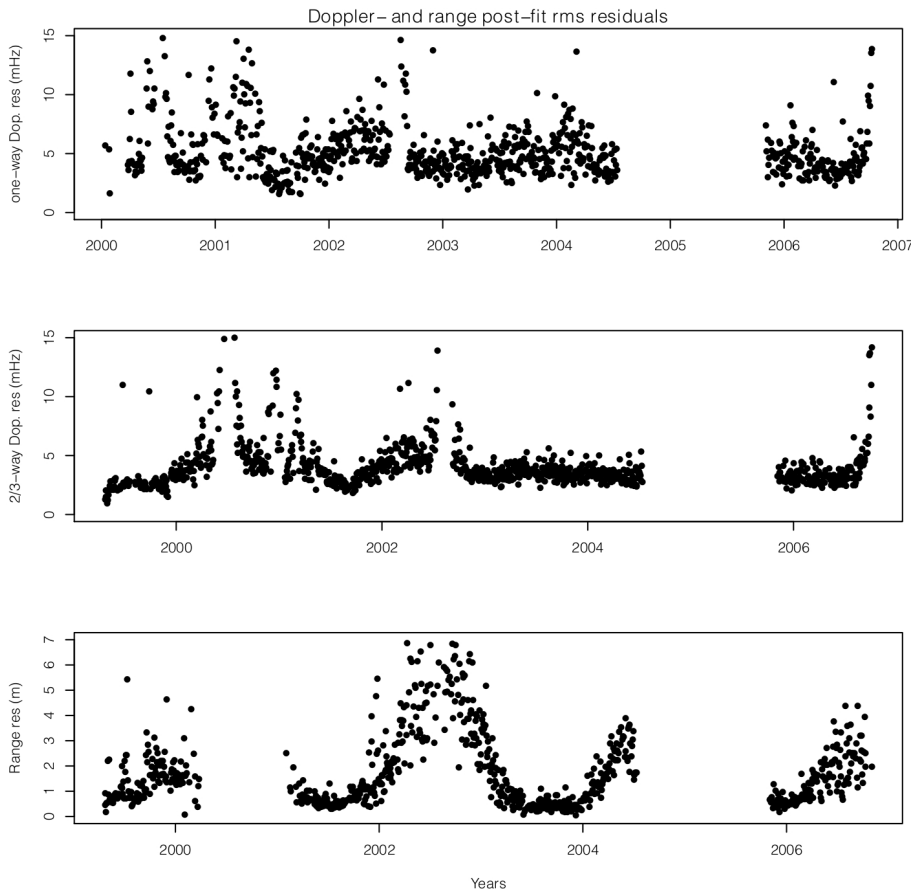


**Fig. 1.** Doppler- and range rms of post-fit residuals of MGS for each two day data-arc. The residuals show the accuracy of the orbit determinations. The peaks and gaps in residuals correspond to solar conjunction periods of MGS.

analysis of single- and dual-frequency time delay data acquired from interplanetary spacecraft.

We performed such estimations using [Mars Global Surveyor \(MGS\)](#), [Mars Express \(MEX\)](#), and [Venus Express \(VEX\)](#) navigation data obtained from 2002 to 2011. These spacecraft experienced several superior solar conjunctions. This happened for MGS in 2002 (solar activity maximum), for MEX in 2006, 2008, 2010, and 2011 (solar activity minimum), and for VEX in 2006, 2008 (solar activity minimum). The influences of these conjunctions on a spacecraft orbit are severely noticed in the post-fit range and can be seen in the Doppler residuals obtained from the orbit determination software (see Fig. 1).

In Sect. 2, we use Doppler- and range-tracking observations to compute the MGS orbits. From these orbit determinations, we obtained range systematic effects induced by the planetary ephemeris uncertainties, which is also called range bias. For the MEX and VEX spacecraft, these range biases are provided by the (ESA; [Fienga et al. 2009](#)). These range biases are used in the planetary ephemerides to fit the dynamical modeling of the planet motions. For the three spacecraft, solar corona corrections were not applied in the computation of the spacecraft orbits. Neither the conjunction periods included in the computation of the planetary orbits.

In Sect. 3, we introduce the solar corona modeling and the fitting techniques that were applied to the range bias data. In Sect. 4, the results are presented and discussed. In particular, we discuss the new fitted parameters, the obtained average electron density, and the comparisons with the estimations found in the literature. The impact of these results on planetary ephemerides and new estimates of the asteroid masses are also discussed in this section. The conclusions of this work are given in Sect. 5.

## 2. Data analysis of MGS, MEX, and VEX spacecraft

### 2.1. Overview of the MGS mission

The MGS began its Mars orbit insertion on 12 September 1997. After almost sixteen months of orbit insertion, the aerobraking event converted the elliptical orbit into an almost circular two-hour polar orbit with an average altitude of 378 km. The MGS started its mapping phase in March 1999 and lost communication with the ground station on 2 November 2006. The radio science data collected by the [Deep Space Network \(DSN\)](#) consist of one-way Doppler, 2/3 way ramped Doppler and two-way range observations. The radio science instrument used for these data sets consists of an ultra-stable oscillator and the normal MGS transmitter and receiver. The oscillator provides the reference frequency for the radio science experiments and operates on the X-band 7164.624 MHz uplink and 8416.368 MHz downlink frequency. Detailed information of observables and reference frequency are given in [Moyer \(2003\)](#).

#### 2.1.1. MGS data analysis with GINS

The radio science data used for MGS are available on the [National Aeronautics and Space Administration \(NASA\) planetary data system \(PDS\) Geoscience website](#)<sup>1</sup>. These observations were analyzed with the help of the [Géodésie par Intégrations Numériques Simultanées \(GINS\)](#) software provided by the [Centre National d'Études Spatiales \(CNES\)](#). GINS numerically integrates the equations of motion and the associated variational equations. It simultaneously retrieves the physical

<sup>1</sup> <http://geo.pds.nasa.gov/missions/mgs/rsraw.html>

parameters of the force model using an iterative least-squares technique. Gravitational and non-gravitational forces acting on the spacecraft are taken into account. The representation of the MGS spacecraft *macro-model* and the dynamic modeling of the orbit used in the GINS software are described in Marty et al. (2009).

For the orbit computation, the simulation was performed by choosing two day data-arcs with two hours (approx. one orbital period of MGS) of overlapping period. From the overlapping period, we were then able to estimate the quality of the spacecraft orbit determination by taking orbit overlap differences between two successive data-arcs. The least-squares fit was performed on the complete set of Doppler- and range-tracking data-arcs corresponding to the orbital phase of the mission using the DE405 ephemeris (Standish 1998). To initialize the iteration, the initial position and velocity vectors of MGS were taken from the SPICE Navigation and Ancillary Information Facility (NAIF) kernels<sup>2</sup>.

The parameters that were estimated during the orbit fitting are (1) the initial position and velocity state vectors of the spacecraft, (2) the scale factors  $F_D$  and  $F_S$  for drag acceleration and solar radiation pressure, (3) the Doppler- and range residuals per data-arc, (4) the DSN station bias per data arc, and (5) the overall range bias per data-arc to account the geometric positions error between the Earth and the Mars.

### 2.1.2. Results obtained during the orbit computation

In Fig. 1, we plot the root mean square (rms) values of the Doppler- and range post-fit residuals estimated for each data-arc. These post-fit residuals represent the accuracy of the orbit determination. To plot realistic points, we did not consider 19% of the data-arcs during which the rms value of the post-fit Doppler residuals are above 15 mHz, the range residuals are above 7 m, and the drag coefficients and solar radiation pressures have unrealistic values. In Fig. 1, the peaks and the gaps in the post-fit residuals correspond to solar conjunction periods. The average value of the post-fit Doppler- and two-way range residuals are less than 5 mHz and 1 m, which excludes the residuals at the time of solar conjunctions.

## 2.2. MEX and VEX data analysis

The MEX and VEX radiometric data were analyzed done by the European Space Agency (ESA) navigation team. These data consist of two-way Doppler- and range measurements. These data sets were used for the orbit computations of MEX and VEX. However, despite their insignificant contribution to the accuracy of the orbit computation, range measurements are mainly used for the purpose of analyzing errors in the planetary ephemerides. These computations are performed with the DE405 (Standish 1998) ephemeris. The range bias obtained from these computations is provided by ESA, and we compared them to light-time delays computed with the planetary ephemerides (Intégrateur Numérique Planétaire de l'Observatoire de Paris (INPOP)), version 10b, (Fienga et al. 2011b), and the DE421 (Folkner et al. 2008) ephemerides. For more details, see Fienga et al. (2009).

### 2.2.1. MEX: orbit and its accuracy

Mars Express is the first ESA planetary mission for Mars, launched on 2 June 2003. It was inserted into Mars orbit on 25 December 2003. The orbital period of MEX is roughly 6.72 h

<sup>2</sup> <http://naif.jpl.nasa.gov/naif/>

and the low polar orbit attitude ranges from 250 km (pericenter) to 11 500 km (apocenter).

The MEX orbit computations were made using 5–7-day track data-arcs with an overlapping period of two days between successive arcs. The differences in the range residuals computed from overlapping periods are less than 3 m, which represents the accuracy of the orbit determination. As described in Fienga et al. (2009), there are some factors that have limited the MEX orbit determination accuracy, such as the imperfect calibrations of thrusting and the off-loading of the accumulated angular momentum of the reaction wheels and the inaccurate modeling of solar radiation pressure forces.

### 2.2.2. VEX: orbit and its accuracy

Venus Express is the first ESA planetary mission for Venus, launched on 9 November 2005. It was inserted into Venus orbit on 11 April 2006. The average orbital period of VEX is roughly 24 h and its highly elliptical polar orbit attitude ranges from 185 km (pericenter) to 66 500 km (apocenter). However, data were almost never acquired during the descending leg of orbit, nor around periapsis (Fienga et al. 2009).

The orbit was computed in the same manner as the MEX. The computed orbit accuracy is more degraded than MEX (Fienga et al. 2009). This can be explained by the unfavorable patterns of tracking data-arcs, the imperfect calibration of the wheel off-loadings, the inaccurate modeling of solar radiation pressure forces, and the characteristics of the orbit itself. The differences in the range residuals computed from overlapping periods are from a few meters to ten meters, even away from the solar conjunction periods.

## 2.3. Solar conjunction: MGS, MEX, VEX

The MGS, MEX, and VEX experienced several superior solar conjunctions. In June 2002, when the solar activity was maximum, the MGS Sun Earth Probe (SEP) angle (see Fig. 3) remained below  $10^\circ$  for two months and went at minimum to  $3.325^\circ$  according to available data. For MEX, the SEP angle remained below  $10^\circ$  for two months and was at minimum three times: in October 2006, December 2008, and February 2011. Similarly, the VEX SEP angle remained below  $8^\circ$  for two months and was at minimum in October 2006 and June 2008. The MEX and VEX superior conjunctions happened during solar minima. The influences of the solar plasma on radio signals during solar conjunction periods have been noticed through post-fit range and Doppler residuals, obtained during the orbit computations. Owing to insufficient modeling of the solar corona perturbations within the orbit determination software, no correction was applied during the computations of the spacecraft orbit and range rate residuals. The peaks and gaps shown in Fig. 2 demonstrate the effect of the solar conjunction on the range bias. The effect of the solar plasma during the MEX and VEX conjunctions on the radiometric data are described in Fienga et al. (2009), and for the MGS it is shown in Fig. 1. The range bias (Fig. 2) during solar conjunctions is used for deriving the electron density profiles of a solar corona model. These profiles are derived separately from the orbit determination.

## 3. Solar corona model

### 3.1. Model profile

As described in Sect. 1, propagations of radio waves through the solar corona cause a travel-time delay between the Earth

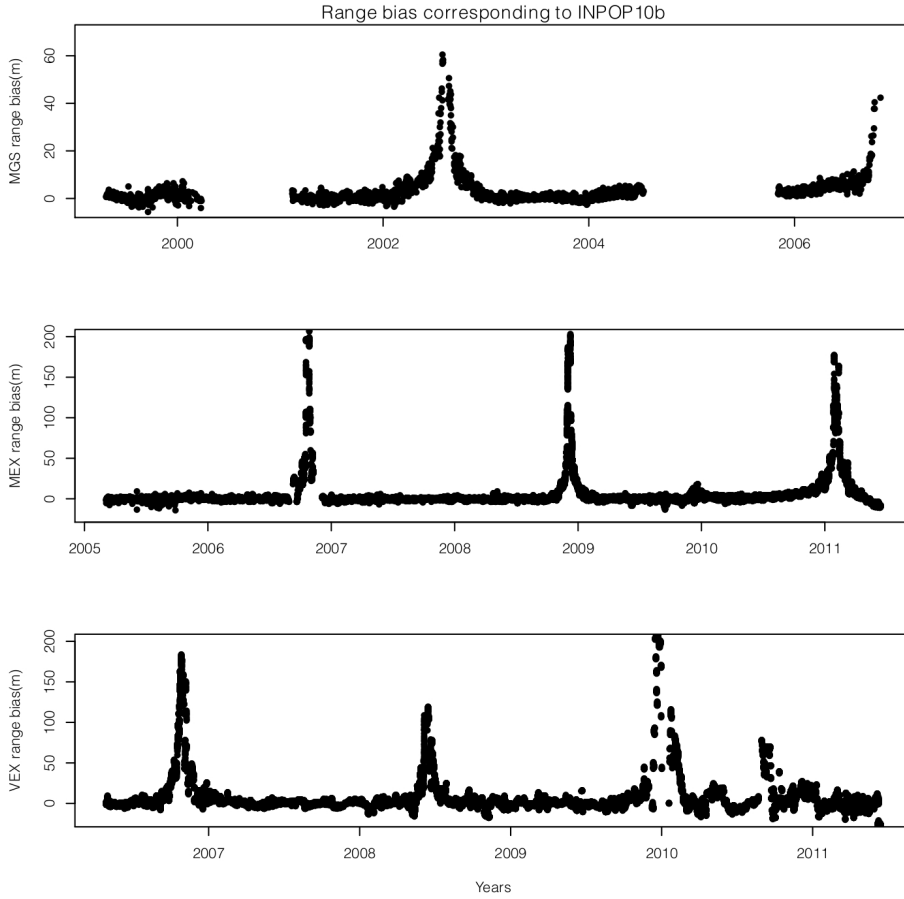


**Fig. 2.** Systematic error (range bias) in the Earth-Mars and the Earth-Venus distances obtained from the INPOP10b ephemeris: (*top panel*) range bias corresponding to the MGS obtained for each two day data-arc; (*middle and bottom panels*) range bias corresponding to the MEX and the VEX.

station and the spacecraft. These time delays can be modeled by integrating the entire ray path (Fig. 3) from the Earth station ( $L_{\text{Earth}/n}$ ) to the spacecraft ( $L_{\text{S}/c}$ ) at a given epoch. This model is defined as

$$\Delta\tau = \frac{1}{2cn_{\text{cri}}(f)} \times \int_{L_{\text{Earth}/n}}^{L_{\text{S}/c}} N_e(l) dl \quad (1)$$

$$n_{\text{cri}}(f) = 1.240 \times 10^4 \left( \frac{f}{1 \text{ MHz}} \right)^2 \text{ cm}^{-3},$$

where  $c$  is the speed of light,  $n_{\text{cri}}$  is the critical plasma density for the radio carrier frequency  $f$ , and  $N_e$  is an electron density in the unit of electrons per  $\text{cm}^3$  and is expressed as (Bird et al. 1996)

$$N_e(l, \theta) = B \left( \frac{l}{R_{\odot}} \right)^{-\epsilon} F(\theta) \text{ cm}^{-3}, \quad (2)$$

where  $B$  and  $\epsilon$  are the real positive parameters to be determined from the data.  $R_{\odot}$  and  $l$  are the solar radius and radial distance in AU.  $F(\theta)$  is the heliolatitude dependency of the electron density (Bird et al. 1996), where  $\theta$  represents the heliolatitude location of a point along the LOS at a given epoch. The maximum contribution in the electron density occurs when  $l$  equals the minimum distance of the line of sight (MDLOS),  $p$  (see Fig. 3), from the Sun. At a given epoch, MDLOS is estimated from the planetary and spacecraft ephemerides. The ratio of the MDLOS and the solar radii ( $R_{\odot}$ ) is given by  $r$ , which is also called the impact factor:

$$\left( \frac{p}{R_{\odot}} \right) = r.$$

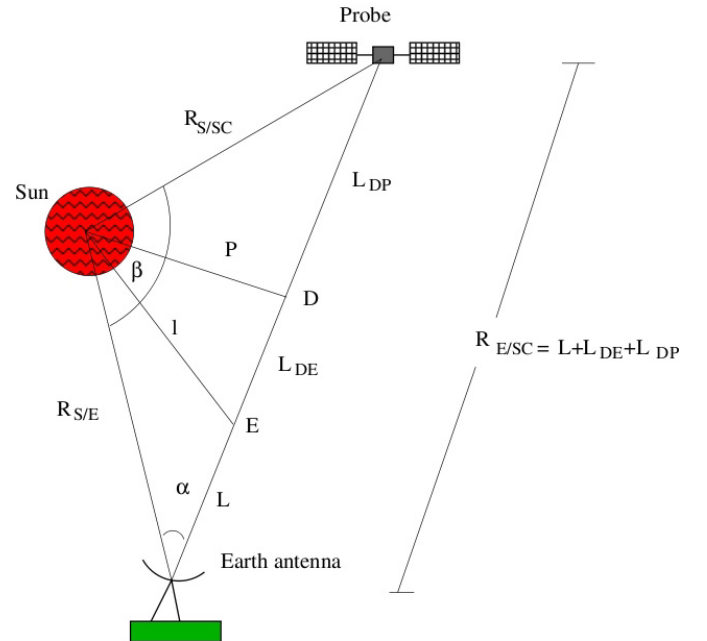


**Fig. 3.** Geometric relation between Earth-Sun-Probe. Where  $\beta$  is the Earth-Sun-Probe (ESP) angle and  $\alpha$  is the Sun-Earth-Probe (SEP) angle.

The electron density profile presented by Bird et al. (1996) is valid for MDLOS greater than  $4 R_{\odot}$ . Below this limit, turbulences and irregularities are very high and non-negligible. The solar plasma is therefore considered as inhomogeneous and additional terms (such  $r^{-6}$  and  $r^{-16}$ ) could be added to Eq. (2)

(Muhleman et al. 1977; Bird et al. 1994). However, because of the very high uncertainties in the spacecraft orbit and range bias measurements within these inner regions, we did not include these terms in our solar corona corrections.

At a given epoch, the MGS, MEX, and VEX MDLOS always remain in the ecliptic plane. The latitudinal variations in the coverage of data are hence negligible compared to the variation in the MDLOS. These data sets are thus less appropriate for the analysis of the electron density as a function of heliolatitude (Bird et al. 1996). Equation (2) can therefore be expressed as a function of the single-power-law ( $\epsilon$ ) of radial distance only and be reduced to

$$N_e(l) = B \left( \frac{l}{R_\odot} \right)^{-\epsilon} \text{ cm}^{-3}. \quad (3)$$

On the other hand, at a given interval of the MDLOS in the ecliptic plane, Guhathakurta et al. (1996) and Leblanc et al. (1998) added one or more terms to Eq. (3), that is

$$N_e(l) = A \left( \frac{l}{R_\odot} \right)^{-c} + B \left( \frac{l}{R_\odot} \right)^{-d} \text{ cm}^{-3} \quad (4)$$

with  $c \simeq 4$  and  $d = 2$ .

To estimate the travel-time delay, we analytically integrated the LOS (Eq. (1)) from the Earth station to the spacecraft, using Eq. (3) and Eq. (4) individually. The analytical solutions of these integrations are given in Appendix A.

In general, the parameters of the electron density profiles differ from one model to another. These parameters may vary with the type of observations, with the solar activity, or with the solar wind state. In contrast, the primary difference between the several models postulated for the electron density ( $r > 4$ ) is the parameter  $\epsilon$  (Eq. (3)), which can vary from 2.0 to 3.0.

For example, the density profile parameters obtained by Muhleman et al. (1977) using the Mariner-7 radio science data for the range of the MDLOS from  $5 R_\odot$  to  $100 R_\odot$  at the time of maximum solar cycle phase are

$$N_e = \frac{(1.3 \pm 0.9) \times 10^8}{r^6} + \frac{(0.66 \pm 0.53) \times 10^6}{r^{2.08 \pm 0.23}} \text{ cm}^{-3}.$$

The electron density profile derived by Leblanc et al. (1998) using the data obtained by the *Wind* radio and plasma wave investigation instrument, for the range of the MDLOS from about  $1.3 R_\odot$  to  $215 R_\odot$  at the solar cycle minimum is

$$N_e = \frac{0.8 \times 10^8}{r^6} + \frac{0.41 \times 10^7}{r^4} + \frac{0.33 \times 10^6}{r^2} \text{ cm}^{-3}.$$

Furthermore, based on in situ measurements, such as those obtained with the *Helios 1 and 2* spacecraft, Bougeret et al. (1984) gave an electronic profile as a function of the MDLOS from  $64.5 R_\odot$  to  $215 R_\odot$  as follows

$$N_e = \frac{6.14}{p^{2.10}} \text{ cm}^{-3}.$$

Similarly, Issautier et al. (1998) analyzed in situ measurements of the solar wind electron density as a function of heliolatitude during a solar minimum. The deduced electron density profile at high latitude ( $>40^\circ$ ) is given as

$$N_e = \frac{2.65}{p^{2.003 \pm 0.015}} \text{ cm}^{-3}.$$

This *Ulysses* high-latitude data set is a representative sample of the stationary high-speed wind. This offered the opportunity to

study the in situ solar wind structure during the minimal variations in the solar activity. As presented in Issautier et al. (1998), electronic profiles deduced from other observations in numerous studies were obtained either during different phases of solar activity (minimum or maximum), different solar wind states (fast or slow-wind), using data in the ecliptic plane (low latitudes). These conditions may introduce some bias in the estimation of electronic profiles of density.

Comparisons of the described profiles with the results obtained in this study are presented in Sect. 4.2 and are plotted in Fig. 9.

### 3.2. Solar wind identification of LOS and data fitting

As described in Schwenn (2006), the electronic profiles are very different in slow- and fast-wind regions. In slow-wind regions, one expects a higher electronic density close to the MNL of the solar corona magnetic field at low latitudes (You et al. 2007). It is then necessary to identify if the region of the LOS is either affected by the slow-wind or by the fast-wind. To investigate that question, we computed the projection of the MDLOS on the Sun surface. We then located the MDLOS heliographic longitudes and latitudes with the maps of the solar corona magnetic field as provided by the WSO<sup>3</sup>. This magnetic field is calculated from photospheric field observations with a potential field model<sup>4</sup>.

However, zones of slow-wind are variable and not precisely determined (Mancuso & Spangler 2000; Tokumaru et al. 2010). As proposed in You et al. (2007, 2012), we took limits of the slow solar wind regions as a belt of  $20^\circ$  above and below the MNL during the solar minima. For the 2002 solar maximum, this hypothesis is not valid, the slow-wind region being wider than during solar minima. Tokumaru et al. (2010) showed the dominating role of the slow-wind for this entire period and for latitudes lower than  $\pm 70^\circ$  degrees.

An example of the MDLOS projection on the Sun's surface with the maps of solar corona magnetic field is shown in Fig. 4. These magnetic field maps correspond to the mean epoch of the ingress and egress phases of the solar conjunction at  $20 R_\odot$ . The dark solid line represents the MNL and the belt of the slow-wind region is presented by dashed lines. The two marked points give the projected locations of the MDLOS, ingress ( $\blacktriangle$ ) and egress ( $\blacktriangledown$ ) at  $20 R_\odot$ . For the entire MDLOS, this distribution of the slow- or fast-wind regions in the ingress and egress phases of solar conjunctions are shown in Fig. 5. The black (white) bars in Fig. 5 present the count of data sets distributed in the slow- (fast-) wind region.

After separating the MDLOS into slow- and fast-wind regions as defined in Fig. 5, the parameters of Eqs. (3) and (4) are then calculated using least-squares techniques. These parameters are obtained for various ranges of the MDLOS, from  $12 R_\odot$  to  $215 R_\odot$  for MGS,  $6 R_\odot$  to  $152 R_\odot$  for MEX, and from  $12 R_\odot$  to  $154 R_\odot$  for VEX. The adjustments were performed, for all available data acquired at the time of the solar conjunctions, for each spacecraft individually, and separately for fast- and slow-wind regions (see Table 2).

To estimate the robustness of the electronic profile determinations, adjustments on ingress and egress phases were performed separately. The differences between these two estimations and the one obtained on the whole data set give the sensitivity of the profile fit to the distribution of the data, but also to the solar wind states. These differences are thus taken as

<sup>3</sup> <http://wso.stanford.edu/>

<sup>4</sup> <http://wso.stanford.edu/synsourcel.html>

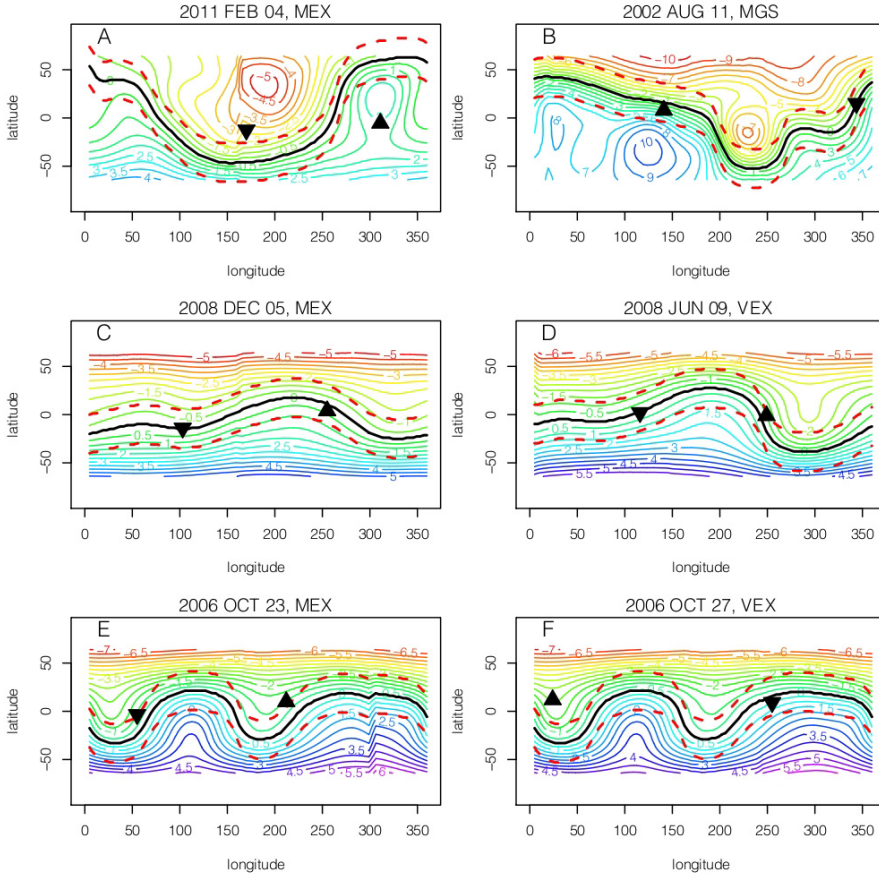


**Fig. 4.** Solar corona magnetic field maps extracted from Wilcox Solar Observatory (WSO) at the mean epoch of  $20 R_{\odot}$  ingress and egress. The dark solid line represents the magnetic neutral line. The dashed red lines correspond to the belt of the slow-wind region. The two marked points give the projected locations of the ingress (▲) and egress (▼) minimal distances at  $20 R_{\odot}$ . For the MGS 2002 solar conjunction, the hypothesis of a  $\pm 20^{\circ}$  belt is not relevant (see Sect. 4.1.1).

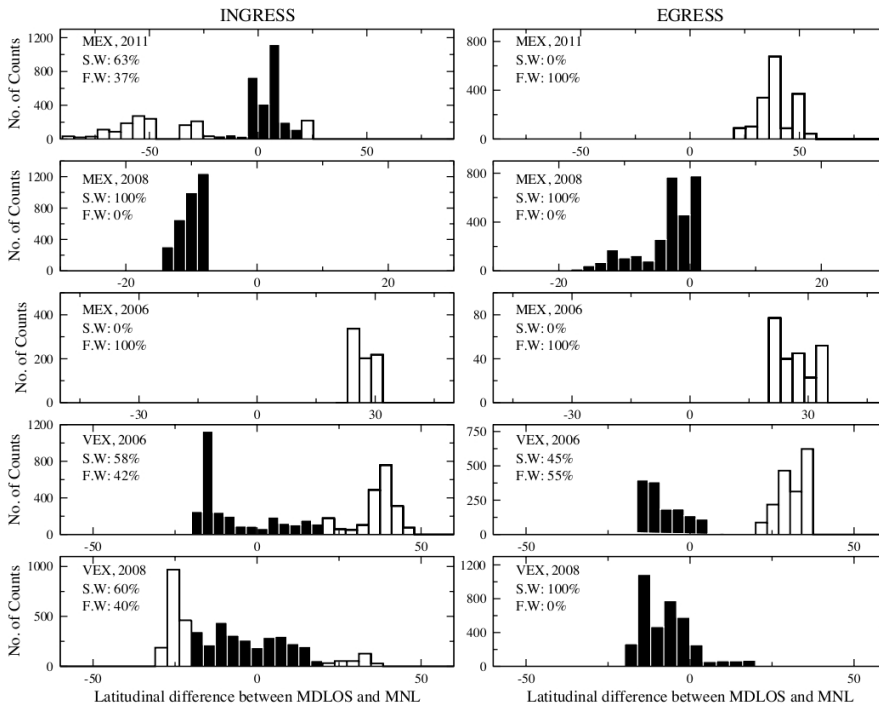


**Fig. 5.** Distribution of the latitudinal differences between MDLOS and magnetic neutral line (MNL) in the slow- and fast-wind regions during the ingress and egress phases of solar conjunctions. The black (white) bars present the slow-(fast-) wind regions as defined by  $\pm 20^{\circ}$  ( $> \pm 20^{\circ}$ ) along the MNL during solar minima.

the uncertainty in the estimations and are given as error bars in the Table 2.

## 4. Results and discussions

### 4.1. Estimated model parameters and electron density

As described in Sect. 3.2, we estimated the model parameters and the electron density separately for each conjunction of the

MGS, MEX, and VEX. A summary of these results is presented in Table 2. The MDLOS in the unit of solar radii ( $R_{\odot}$ ) mentioned in this table (Col. 5) represents the interval of available data used for calculating the electronic profiles of density. These profiles were then used for extrapolating the average electron density at  $215 R_{\odot}$  (1 AU). The period of the solar conjunctions, solar activities, and solar wind states are also given in Cols. 2–4. Table 2 also contains the estimated parameters of

**Table 2.** Solar corona model parameters and electron densities estimated from two different models using the MGS, MEX, and VEX range bias.

S/C	Year	S.C. <sup>1</sup>	S.W.S <sup>2</sup>	MDLOS <sup>3</sup>	$N_c = Br^{-\epsilon}$			$N_c = Ar^{-4} + Br^{-2}$				
					$B(\times 10^6)$	$\epsilon$	Ne@20 $R_\odot$	Ne@215 $R_\odot$ *	$A(\times 10^8)$	Ne@20 $R_\odot$	Ne@215 $R_\odot$ *	
MGS	Aug. 2002	Max	S.W	12–215	0.51 ± 0.06	2.00 ± 0.01	1275 ± 150	11 ± 1.5	0.52 ± 0.04	0	1300 ± 100	11 ± 1
			F.W	–	–	–	–	–	–	–	–	–
MEX	Oct. 2006	Min	S.W	6–40	1.90 ± 0.50	2.54 ± 0.07	942 ± 189	2.3 ± 0.9	0.30 ± 0.10	0.16 ± 0.02	850 ± 263	6 ± 1
			F.W	–	–	–	–	–	–	–	–	–
MEX	Dec. 2008	Min	S.W	6–71	0.89 ± 0.42	2.40 ± 0.16	673 ± 72	2.3 ± 1.3	0.22 ± 0.04	0.10 ± 0.02	615 ± 90	5 ± 1
			F.W	–	–	–	–	–	–	–	–	–
MEX	Feb. 2011	Min	S.W	40–152	0.52 ± 0.10	2**	1300 ± 25*	11 ± 1	0.52 ± 0.10	0	1300 ± 25*	11 ± 1
			F.W	6–60	1.70 ± 0.10	2.44 ± 0.01	1138 ± 31	3.5 ± 0.5	0.33 ± 0.02	0.24 ± 0.04	975 ± 60	7 ± 1
VEX	Oct. 2006	Min	S.W	12–154	0.52 ± 0.30	2.10 ± 0.10	964 ± 600	7 ± 4	0.40 ± 0.28	0	1000 ± 600	9 ± 6
			F.W	12–130	1.35 ± 1.10	2.33 ± 0.30	1256 ± 649	5 ± 2	0.44 ± 0.15	0	1087 ± 480	9 ± 4
VEX	Jun. 2008	Min	S.W	12–154	1.70 ± 1.50	2.50 ± 0.50	950 ± 625	3 ± 2	0.31 ± 0.20	0	775 ± 450	7 ± 4
			F.W	41–96	0.10 ± 0.01	2**	250 ± 25*	2 ± 1	0.10 ± 0.01	0	250 ± 25*	2 ± 1

**Notes.** The electron density out from the interval of the MDLOS is extrapolated from the given model parameters. <sup>(1)</sup> S.C: solar cycle; <sup>(2)</sup> S.W.S: solar wind state (F.W: fast-wind, S.W: slow-wind); <sup>(3)</sup> MDLOS: minimum distance of the line of sight in the unit of solar radii ( $R_\odot$ ); <sup>(\*)</sup> extrapolated value; <sup>(\*\*)</sup> fixed.

two different models: the first model from Bird et al. (1996) corresponds to Eq. (3), whereas the second model is based on Guhathakurta et al. (1996) and Leblanc et al. (1998) and follows Eq. (4) with  $c = 4$ . Estimated model parameters for the slow- and fast-wind regions are presented in Cols. 6 and 7.

#### 4.1.1. Mars superior conjunction

The MGS experienced its superior conjunction in 2002 when the solar activity was maximum and the slow-wind region was spread at about  $\pm 70^\circ$  of heliolatitude (Tokumaru et al. 2010). Figure 6 represents the projection of the MGS MDLOS on the solar surface (black dots) superimposed with the 2002 synoptic source surface map of solar wind speeds derived from STEL IPS observations extracted from Tokumaru et al. (2010). It suggests that, the MDLOS of the MGS exclusively remains in the slow-wind region. Respective estimates of the model parameters and of the electron densities are given in Table 2. From this table one can see that the estimates of the electron density from both models are very similar. Parameter  $\epsilon$  of Eq. (3) is then estimated as  $2.00 \pm 0.01$ , which represents a radially symmetrical behavior of the solar wind and hence validates the assumption of a spherically symmetrical behavior of the slow-wind during solar maxima (Guhathakurta et al. 1996). Whereas for Eq. (4), the contribution of the  $r^{-4}$  term at large heliocentric distances ( $r > 12 R_\odot$ ) is negligible compared to the  $r^{-2}$  term. Thus, the parameter  $A$  for these large heliocentric distances is fixed to zero and consequently gave similar results to Eq. (3), as shown in Table 2.

In contrast, MEX experienced its superior conjunctions in 2006, 2008, and 2011 during solar minima. The distribution of data during these conjunctions with respect to MDLOS are shown in Fig. 7. From this figure, one can see that the MEX 2006 (2008) conjunction corresponds to the fast- (slow-) wind region, whereas 2011 conjunction is a mixture of slow- and fast-winds. The estimated parameters of these conjunctions are given in Table 2. An example of the comparison between two models (Eqs. (3) and (4)) is shown in Fig. 8. This figure compares the electron density profiles obtained from the two models during the MEX 2008 conjunction. These profiles are extrapolated from  $1 R_\odot$  to  $6 R_\odot$  and from  $71 R_\odot$  to  $215 R_\odot$ . The upper triangles in Fig. 8 indicate electronic densities obtained at  $20 R_\odot$  and at the extrapolated distance of  $215 R_\odot$  (1 AU) with error bars obtained as described in Sect. 3.2. As one sees in that figure, electronic profiles are quite similar over the computation interval till  $71 R_\odot$  and become significantly different after this limit. This suggests that the estimated parameters for both models are valid for the range of MDLOS given in Table 2. Finally, for the MEX 2011 conjunction, as shown in Figs. 5 and 7, the data are mainly distributed in the slow-wind (63%) during ingress phase and in the fast-wind (100%) during egress phase. Owing to the unavailability of slow-wind data near the Sun (MDLOS  $< 40 R_\odot$ ), we fixed  $\epsilon$  to 2 for Eq. (3) (see Table 2). Moreover, the average electron density estimated for this conjunction is higher for the slow-wind than for the fast-wind and it is consistent with Tokumaru et al. (2010), which suggests that near the MNL, the electron content is higher than in the fast-wind regions.

#### 4.1.2. Venus superior conjunction

The VEX 2006 and 2008 conjunctions exhibit a mixture of slow- and fast-wind (Fig. 7). These conjunctions occurred approximately at the same time as the MEX superior conjunctions.

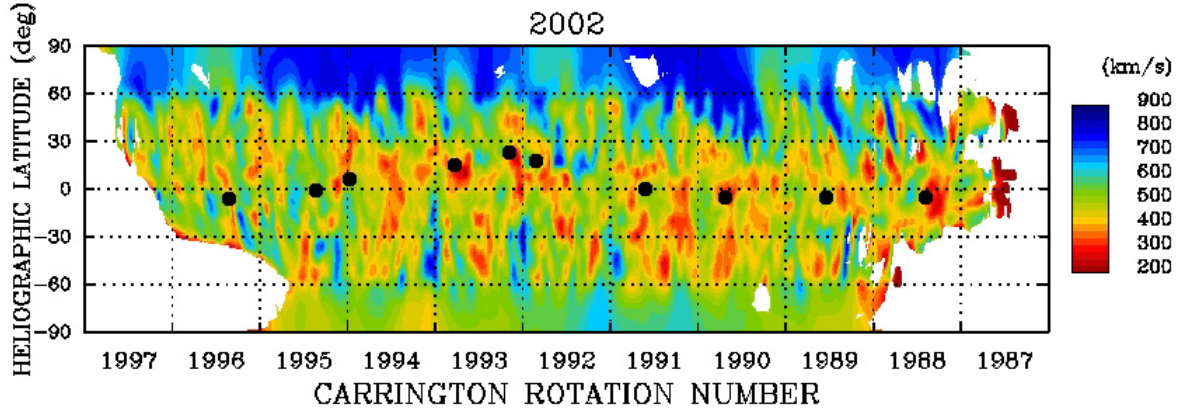


**Fig. 6.** 2002 synoptic source surface map of solar wind speeds derived from STEL IPS observations extracted from Tokumaru et al. (2010). The black dots represent the MGS MDLOS during the 2002 conjunction period for the range of  $12 R_{\odot}$  to  $120 R_{\odot}$ .

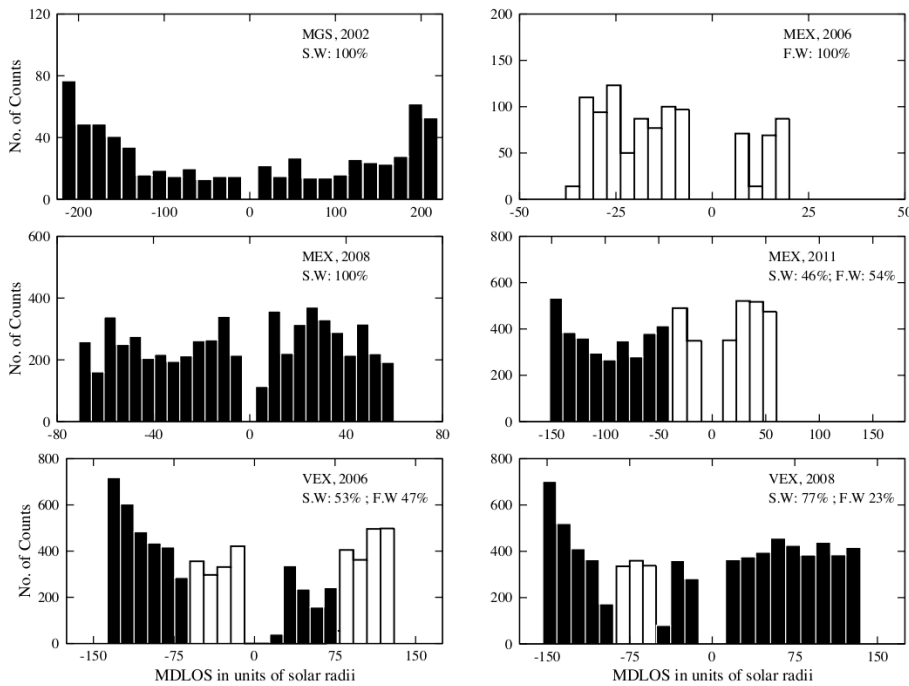


**Fig. 7.** Distribution of the MGS, MEX, and VEX data in the slow (black) and fast (white) wind with respect to MDLOS in units of solar radii ( $R_{\odot}$ ). Negative (positive) MDLOS represents the distribution in the ingress (egress) phase.

**Table 3.** Electron densities estimated from different models at  $20 R_{\odot}$  and at  $215 R_{\odot}$  (1 AU).

Authors	Spacecraft	Solar activity	MDLOS	$Ne$ @ $20 R_{\odot}$ (el. $\text{cm}^{-3}$ )	$Ne$ @ $215 R_{\odot}$ (el. $\text{cm}^{-3}$ )
Leblanc et al. (1998)	Wind	Min	1.3–215	847	7.2
Bougeret et al. (1984)	Helios 1 and 2	Min/Max	65–215	890	6.14
Issautier et al. (1998)	<i>Ulysses</i>	Min	327–497	307*	$2.65 \pm 0.5^*$
Muhleman et al. (1977)	Mariner 6 and 7	Max.	5–100	$1231 \pm 64$	$9 \pm 3$
Bird et al. (1994)	<i>Ulysses</i>	Max	5–42	$1700 \pm 100$	$4.7 \pm 0.415$
Anderson et al. (1987)	Voyager 2	Max	10–88	$6650 \pm 850$	$38 \pm 4$

**Notes.** (\*) Mean electron density corresponds to latitude  $\geq 40^{\circ}$ .

However, the limitations in the VEX orbit determination introduced bias in the estimation of the model parameters and the electron densities. This can be verified from the discrepancies presented in Table 2 for the VEX 2006 and 2008 conjunctions. Despite these high uncertainties, post-fit range bias corrected for the solar corona allows one to add complementary data in the construction of the planetary ephemerides (see Sect. 4.5).

#### 4.2. Comparison with other models

Table 3 represents the estimated electron densities at  $20 R_{\odot}$  and  $215 R_{\odot}$  (1 AU) from the various models. These models are representative of radio science measurements (Muhleman et al. 1977; Anderson et al. 1987; Bird et al. 1994, 1996), in situ measurements (Bougeret et al. 1984; Issautier et al. 1997), and



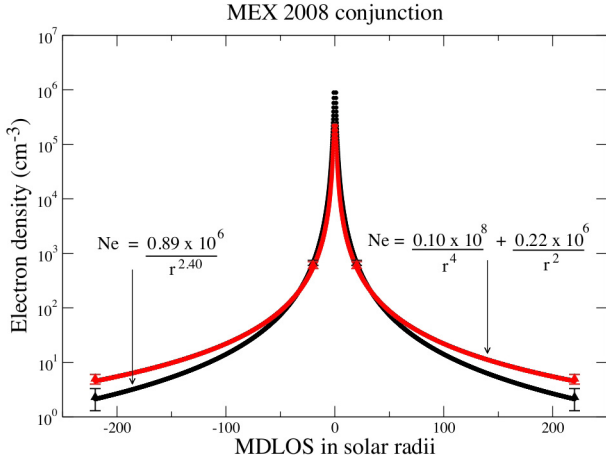


**Fig. 8.** Example of the comparison between electron density models given in Eqs. (3) and (4). The electron density profiles are plotted from  $1 R_{\odot}$  to  $215 R_{\odot}$  (1 AU) for the MEX 2008 conjunction using the model parameters given in Table 2. The error bars plotted in the figure correspond to the electron density obtained at  $20 R_{\odot}$  and  $215 R_{\odot}$  (see Table 2).

solar type III radio emission (Leblanc et al. 1998) measurements (Table 1). Table 3 and Fig. 9 allow us to compare the average electron density, obtained from different observations, made approximately during the same solar activity cycle.

Figure 9 illustrates the comparisons of different electron density profiles, extrapolated from  $1 R_{\odot}$  to  $215 R_{\odot}$ . From this figure it can be seen that approximately all electron density profiles follow similar trends ( $\propto r^{-\epsilon}$ ,  $\epsilon$  varying from 2 to 3) until  $10 R_{\odot}$  (panel B), whereas the dispersions in the profiles below  $10 R_{\odot}$  (panel A) are due to the contribution of higher order terms, such as  $r^{-4}$ ,  $r^{-6}$  or  $r^{-16}$ .

In Table 3, we also provide the average electron density at  $20 R_{\odot}$  and  $215 R_{\odot}$ , based on the corresponding models (if not given by the authors). The two individual electron density profiles for ingress and egress phases have been given by Anderson et al. (1987) and Bird et al. (1994). To compare their estimates with ours, we took the mean values of both phases. Similarly, Muhleman et al. (1977) gave the mean electron density at  $215 R_{\odot}$  estimated from round-trip propagation time delays of the Mariner 6 and 7 spacecraft.

Table 3 shows a wide range of the average electron densities, estimated at  $20 R_{\odot}$  and  $215 R_{\odot}$  during different phases of solar activity. Our estimates of the average electron density shown in Table 2 are very close to the previous estimates, especially during solar minimum. The widest variations between our results and the earlier estimates were found during solar maxima and can be explained from the high variability of the solar corona during these periods.

#### 4.3. Post-fit residuals

One of the objectives of this study is to minimize the effect of the solar corona on the range bias. These post-fit range biases can then be used to improve the planetary ephemeris (INPOP). The pre-fit range bias represents the systematic error in the planetary ephemerides during the solar conjunction periods. Figure 10 shows the pre-fit residuals over plotted with the simulated time delay (in units of distance), obtained from the solar corona model based on Eq. (3). In contrast, the post-fit range bias represents the error in the ephemerides after correction for solar corona perturbations.

**Table 4.** Statistics of the range bias before and after solar corona corrections.

S/C	Pre-fit		Post-fit	
	mean (m)	$\sigma$ (m)	mean (m)	$\sigma$ (m)
MGS, 2002	6.02	10.10	-0.16	2.89
MEX, 2006	42.03	39.30	0.85	9.06
MEX, 2008	16.00	20.35	-0.10	4.28
MEX, 2011	15.44	19.20	0.11	6.48
VEX, 2006	5.47	11.48	-0.74	6.72
VEX, 2008	3.48	11.48	-0.87	7.97

From Fig. 10 one can see that the systematic trend of the solar corona perturbations is almost removed from the range bias. The post-fit range bias of the VEX at low solar radii (especially during the egress phase) is not as good as the MGS and MEX. This can be explained by the degraded quality of the VEX orbit determination (see Sect. 2.2.2). The dispersion in the pre-fit and post-fit range bias is given in Table 4. The estimated dispersions in the post-fit range bias are one order of magnitude lower than the dispersions in the pre-fit range bias. It shows a good agreement between the model estimates and the radiometric data. The corrected range bias (post-fit) is then used to improve the planetary ephemerides (see Sect. 4.5).

#### 4.4. Model parameter dependency on the ephemerides

The range bias data are usually very important for constructing the planetary ephemerides (Folkner et al. 2008; Fienga et al. 2011b). These measurements correspond to at least 57% of the total amount of data used for the INPOP construction (Fienga et al. 2009). Range bias data at the time of the solar conjunctions are not taken into account due to very high uncertainties (see Fig. 2). Equation (3) and Fig. 3 show the dependency of the density profile over geometric positions of the spacecraft (orbiting a planet) relative to the Earth and the Sun. The range bias used for this study includes the error in the geometric distance of Mars and Venus relative to the Earth. These errors are varying from one ephemeris to another and impact directly on the estimates of the mean electron density.

Figure 11 illustrates the electron density estimated at  $20 R_{\odot}$  for MGS, MEX and VEX using DE421 and INPOP10b ephemerides. The dashed (DE421) and dotted-dashed (INPOP10b) lines present the time limit up to which these ephemerides are fitted over range bias data. The curve represents the differences between INPOP10b and DE421 estimations of Mars-Earth geometric distances.

In particular, the Mars orbit is affected by the belt of asteroids. The asteroid masses may cause a degradation in the estimates of the Mars orbit. Therefore, as one can see in Fig. 11, the geometric differences between the INPOP10b and DE421 estimates of the Mars-Earth geometric distances are magnified from the extrapolation period onward. Hence, the electron densities estimated using DE421 and INPOP10b are consistent with each other within the error bars before the extrapolation period, whereas after this period, the DE421 and INPOP10b estimates of the electron densities are quite different from each other. The sensitivity of the solar corona parameters and the electron densities, deduced from the analysis of the range bias, is then low as long as the computation is included in the time interval of the fit of the planetary ephemerides. However, out from the fitting time, the quality of these computations can be degraded by the extrapolation capability of the planetary ephemerides. Conversely, by

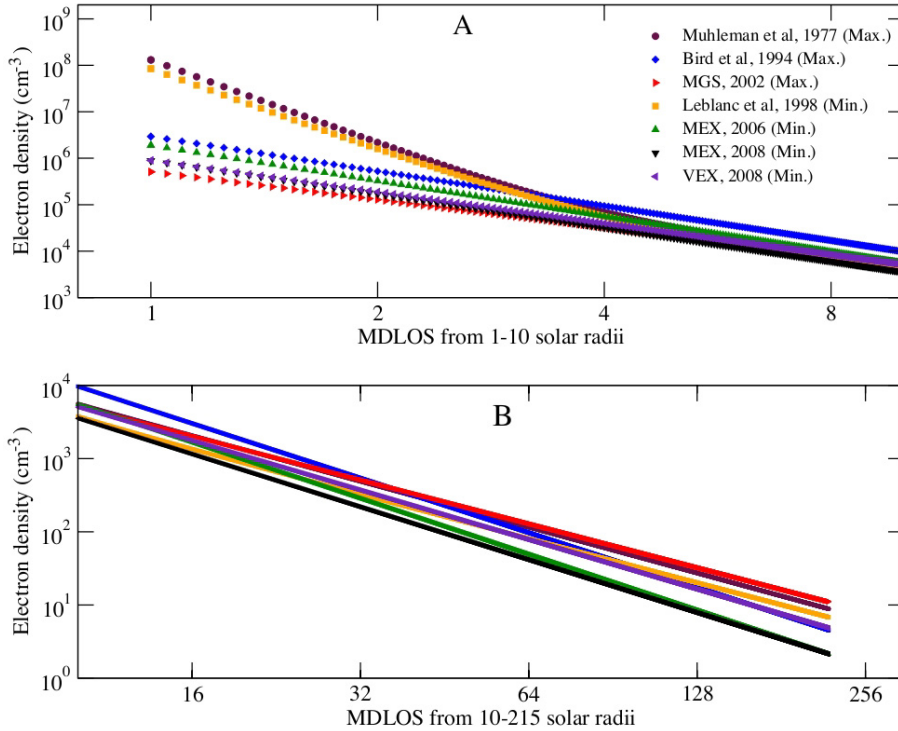


**Fig. 9.** Comparison of different electron density profiles at different phases of the solar cycle from  $1 R_{\odot}$  to  $215 R_{\odot}$  (1 AU).

fitting the planetary ephemerides (INPOP) including data corrected for the solar corona perturbations, some noticeable improvement can appear in the extrapolation capability of the planetary ephemerides and in the estimates of the asteroid masses (see Sect. 4.5).

#### 4.5. Impact on planetary ephemerides

As one can see in Fig. 10, correct the effects induced by the solar corona on the observed Mars-Earth distances is significant over some specific periods of time (during solar conjunctions). We aim to estimate the impact of this important but time-limited improvement of the measurements of interplanetary distances on the construction of the planetary ephemerides. To evaluate any possible improvement, we produced two ephemerides, INPOP10c and INPOP10d, both fitted over the same data set as was used for the construction of INPOP10b (Fienga et al. 2011b). This data set contains all planetary observations commonly used for INPOP (see Fienga et al. 2009, 2011a), including the MGS data obtained in section 2.1.1 and the MEX and VEX range bias provided by ESA. These newly built ephemerides are based on the same dynamical modeling as described in Fienga et al. (2009, 2011a). However, INPOP10c is estimated without any solar corona corrections on the MGS, MEX and VEX range bias, and INPOP10d includes the solar corona corrections evaluated in the previous sections. The selection of the fitted asteroid masses and the adjustment method (bounded value least-squares associated with a priori sigmas) are the same for the two cases. The weighting schema are also identical. The differences remain in the quality and the quantity of the range bias used for the fit (one corrected for solar plasma and one not) and in the procedure selecting the data actually used in the fit.

For INPOP10c, about 119901 observations were selected. Of these, 57% are MGS, MEX, and VEX range bias data that are not corrected for solar corona effects. Based on a very conservative procedure, observations obtained two months before and after the conjunctions were removed from the fitted data sample. This strategy leads to removal of about 7% of the whole

data set, which represents 14% of the MGS, MEX, and VEX observations. For INPOP10d, thanks to the solar corona corrections, only observations of SEP smaller than 1.8 degrees were removed from the data sample. This represents less than 1% of the whole data sample. The estimated accuracy of the measurements corrected for the solar plasma is 2.4 meters when observations not affected by the solar conjunctions have an accuracy of about 1.7 m. By keeping more observations during solar conjunction intervals, the number of data with a good accuracy is then significantly increased.

Adjustments of planet initial conditions, mass of the sun, sun oblateness, mass of an asteroid ring, and the masses of 289 asteroids were then performed in the same fitting conditions as INPOP10b.

No significant differences were noted for the evaluated parameters except for the asteroid masses.

For the masses estimated both in INPOP10c and INPOP10d, 20% induce perturbations bigger than 5 m on the Earth-Mars distances during the observation period. The masses of these 59 objects are presented in Table 5. Within the  $1\text{-}\sigma$  uncertainties deduced from the fit, we notice 10 (17%) significant differences in masses obtained with INPOP10c and INPOP10d, quoted with a “\*” in Col. 5 of the Table, 7 (12%) new estimates made with INPOP10d, noted N in Cols. 5, and 6 (10%) masses put to 0 in INPOP10d when estimated in INPOP10c, marked with 0 in the fifth column.

Table 6 lists masses found in the literature compared with the quoted values of Table 5. In this Table, 80% of the INPOP10d estimates have a better consistency with the values obtained by close encounters than the one obtained with INPOP10c. Of these, the new estimates obtained with INPOP10d for (20), (139) and (27) agree well with the values found in the literature. For (45) Eugenia, the INPOP10c value is closer to the mass deduced from the motion of its satellite (Marchis et al. 2008) even if the INPOP10d value is still compatible at  $2\text{-}\sigma$ . For (130) Elektra, the INPOP10c and INPOP10d estimated values are certainly under evaluated. Finally, one can note the systematic bigger

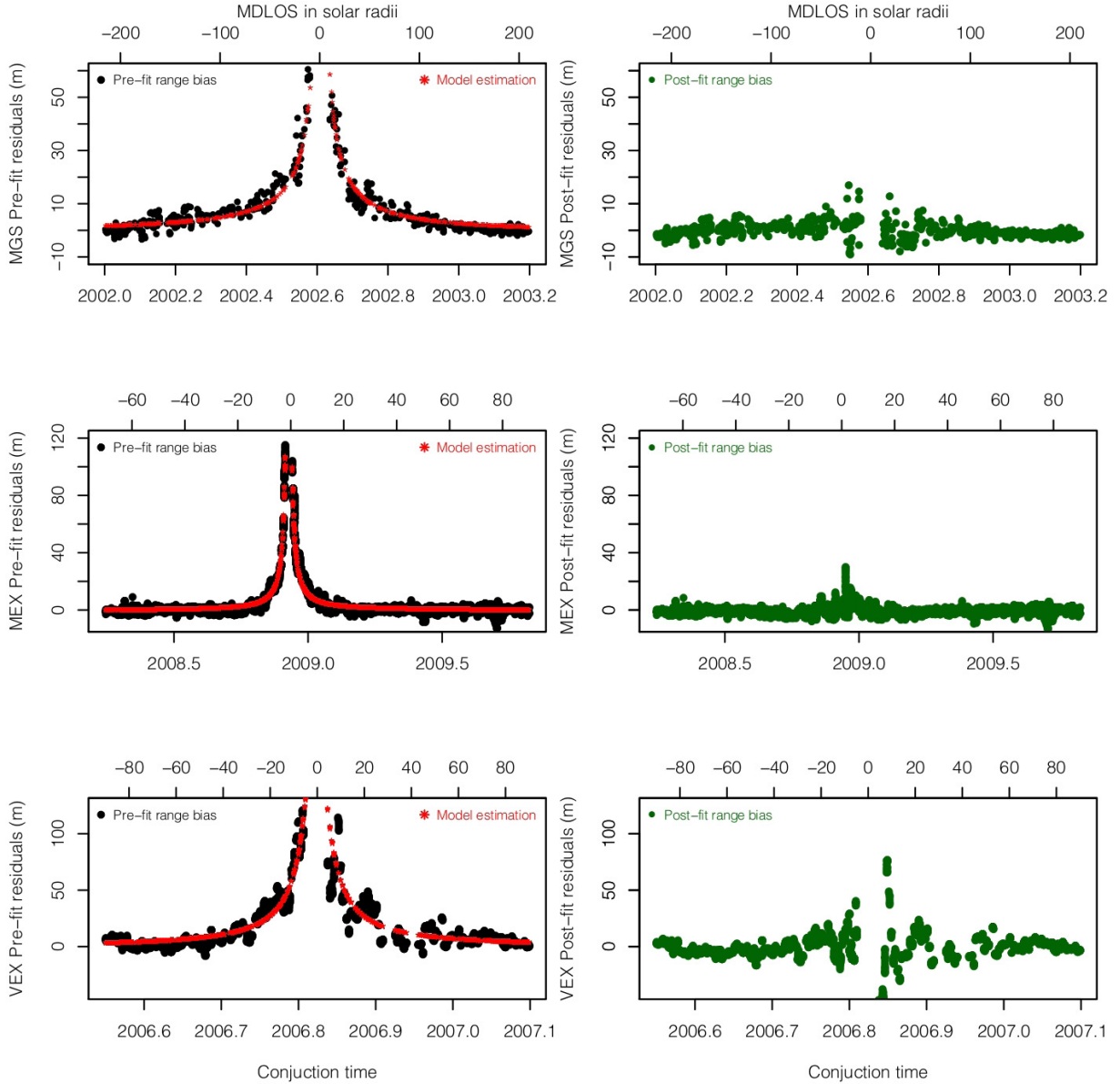


**Fig. 10.** *Left panel:* model-estimated solar corona over-plotted on the pre-fit residuals. *Right panel:* post-fit residuals after corona corrections. *Top, middle, and bottom panels* correspond to the MGS 2002, MEX 2008, and VEX 2006 conjunctions.

uncertainties of the INPOP10d estimates. The supplementary data sample collected during the solar conjunctions that has 30% more noise than the data collected beyond the conjunction can explain the degradation of the uncertainties for the INPOP10d determinations compared to INPOP10c.

By correcting the range bias for the solar corona effects, we added more informations related to the perturbations induced by the asteroids during the conjunction intervals.

In principal, during the least-squares estimation of the asteroid masses, the general trend of the gravitational perturbation induced by the asteroid on the planet orbits should be described the most completely by the observable (the Earth-Mars distances) without any lack of information. In particular, for an optimized estimation, the data sets used for the fit should include local maxima of the perturbation.

However, it could happen that some of the local maxima occur during the solar conjunction intervals. One can then expect a degradation of the least-squares estimation of the perturber mass if no solar corrections are applied or if these intervals are not

taken into account during the fit. To estimate which mass determination can be more degraded than another by this *window* effect, we estimated  $L$ , the percentage of local maxima rejected from the INPOP10c fit in comparison with the INPOP10d adjustment including all data sets corrected for solar plasma.  $L$  will give the loss of information induced by the rejection of the solar conjunction intervals in terms of highest perturbations.

The  $L$  criteria are given in Col. 7 of Table 5. As an example, for (24) Themis one notes in Table 6 the good agreement between the close encounter estimates and the INPOP10d mass determination compared with INPOP10c. On the other hand, based on the  $L$  criteria, 36% of the local maxima happen near solar conjunctions. By neglecting the solar conjunction intervals, more than a third of the biggest perturbations are missing in the adjustment. This can explain the more realistic INPOP10d estimates compared with INPOP10c.

We also indicate in Table 5 if important constraints were added in the fit (Col. 8). In these cases, even if new observations are added to the fit (during the solar conjunction periods),

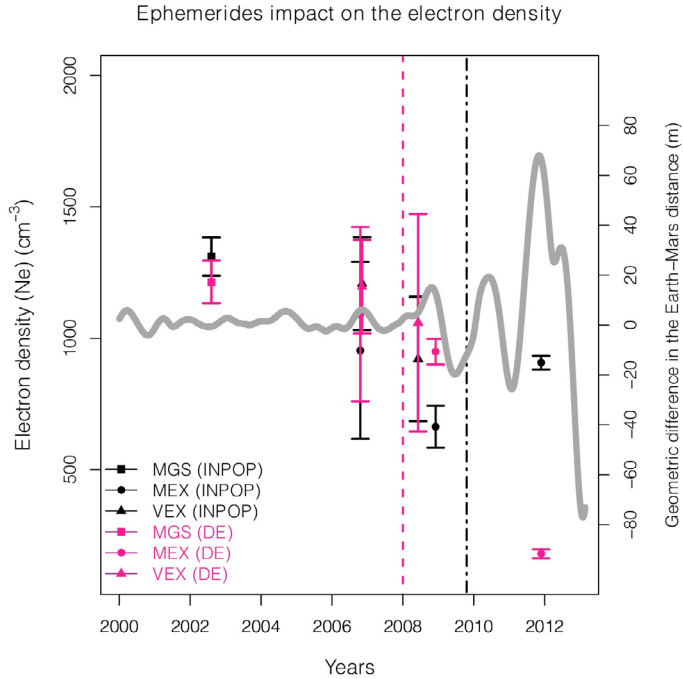


**Fig. 11.** Variation of the average electron density at  $20 R_{\odot}$  and  $215 R_{\odot}$  using the DE421 and INPOP10b ephemeris. The dotted-dashed (INPOP) and dashed (DE421) vertical lines present the starting time of extrapolation. The plain line shows the differences in the Mars-Earth geometric distances estimated with INPOP10b and DE421.

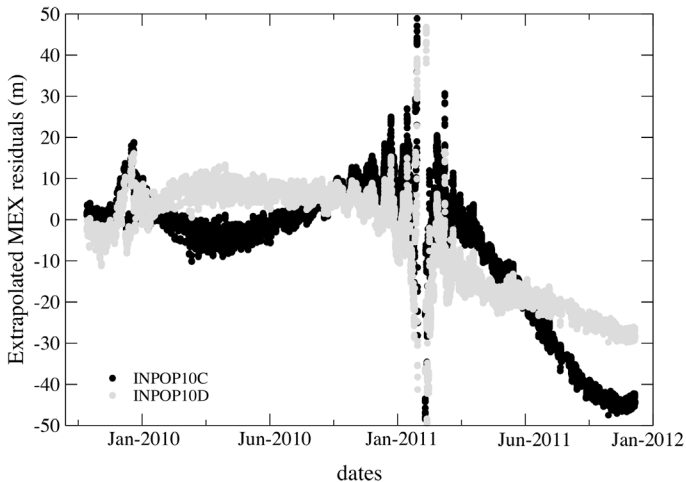


**Fig. 12.** MEX extrapolated residuals estimated with INPOP10d (light dots) and INPOP10c (dark dots).

there is a high probability to obtain a stable estimates of the constrained masses as for the biggest perturbers of Table 5. For the other mass determinations, one can note a consistency between high values of the  $L$  criteria and the non-negligible mass differences between INPOP10c and INPOP10d.

By improving the range bias residuals during the solar conjunction periods, we then slightly improved the asteroid mass determinations.

Estimates of residuals for data samples not used in the INPOP fit and dated after or before the end of the fitting interval are currently made to evaluate the real accuracy of the planetary ephemerides (Fienga et al. 2011a, 2009). To estimate if the use of the solar corona corrections induces a global improvement of the planetary ephemerides, the MEX extrapolated residuals

were computed with INPOP10c and INPOP10d. As one can see in Fig. 12, the INPOP10d MEX extrapolated residuals show a better long-term behavior compared with INPOP10c with 30% less degraded residuals after two years of extrapolation.

Supplementary data of the MEX and VEX obtained during the first six months of 2012 would confirm the long-term evolutions of the INPOP10d, INPOP10c and INPOP10b.

This improvement can be explained by the more realistic adjustment of the ephemerides with denser data sets (7%) and more consistent asteroid mass fitting.

## 5. Conclusion

We analyzed the navigation data of the MGS, MEX, and VEX spacecraft acquired during solar conjunction periods. We estimated new characteristics of solar corona models and electron densities at different phases of solar activity (maximum and minimum) and at different solar wind states (slow and fast). Good agreement was found between the solar corona model estimates and the radiometric data. We compared our estimates of electron densities with earlier results obtained with different methods. These estimates were found to be consistent during the same solar activities. During solar minima, the electron densities obtained by in situ measurements and solar radio burst III are within the error bars of the MEX and VEX estimates. However, during the solar maxima, electron densities obtained with different methods or different spacecraft show weaker consistencies. These discrepancies need to be investigated in more detail, which requires a deeper analysis of data acquired at the time of solar maxima.

The MGS, MEX, and VEX solar conjunctions data allow us to analyze the large-scale structure of the corona electron density. These analyses provide individual electron density profiles for slow- and fast-wind regions during solar maxima and minima activities.

In the future, planetary missions such as MESSENGER will also provide an opportunity to analyze the radio-science data, especially at the time of maximum solar cycle.

We tested the variability caused by the planetary ephemerides on the electron density parameters deduced from the analysis of the range bias. This variability is smaller than the  $1-\sigma$  uncertainties of the time-fitting interval of the planetary ephemerides but becomes wider beyond this interval. Furthermore, data corrected for solar corona perturbations were used for constructing the INPOP ephemerides. Thanks to these supplementary data, an improvement in the estimation of the asteroid masses and a better behavior of the ephemerides were achieved.

*Acknowledgements.* A.K. Verma is the research fellow of CNES and Region Franche-Comté and thanks CNES and Region Franche-Comté for financial support. Part of this work was made using the GINS software; we would like to acknowledge CNES, who provided us access to this software. We are also grateful to J.C. Marty (CNES) and P. Rosenbatt (Royal Observatory of Belgium) for their support in handling the GINS software. The Authors are grateful to the anonymous referee for helpful comments, which improved the manuscript.

## References

- Anderson, J. D., Krisher, T. P., Borutzki, S. E., et al. 1987, ApJ, 323, L141
- Baer, J., Chesley, S. R., & Matson, R. 2011, AJ, submitted
- Bird, M. K., Volland, H., Paetzold, M., et al. 1994, ApJ, 426, 373
- Bird, M. K., Paetzold, M., Edenhofer, P., Asmar, S. W., & McElrath, T. P. 1996, A&A, 316, 441

- Bougeret, J.-L., King, J. H., & Schwenn, R. 1984, *Sol. Phys.*, 90, 401
- Cranmer, S. R. 2002, *Space Sci. Rev.*, 101, 229
- Fienga, A., Laskar, J., Morley, T., et al. 2009, *A&A*, 507, 1675
- Fienga, A., Laskar, J., Manche, H., et al. 2011a, *Celestial Mechanics and Dynamical Astronomy*
- Fienga, A., Kuchynka, P., Laskar, J., et al. 2011b, in *EPSC-DPS Join Meeting 2011*, 1879
- Folkner, W. M., Williams, J. G., & Boggs, D. H. 2008, IOM 343R-08-003
- Guhathakurta, M., & Holzer, T. E. 1994, *ApJ*, 426, 782
- Guhathakurta, M., Holzer, T. E., & MacQueen, R. M. 1996, *ApJ*, 458, 817
- Guhathakurta, M., Fludra, A., Gibson, S. E., Biasecker, D., & Fisher, R. 1999, *J. Geophys. Res.*, 104, 9801
- Issautier, K., Meyer-Vernet, N., Moncuquet, M., & Hoang, S. 1997, *Sol. Phys.*, 172, 335
- Issautier, K., Meyer-Vernet, N., Moncuquet, M., & Hoang, S. 1998, *J. Geophys. Res.*, 103, 1969
- Kuchynka, P., Laskar, J., Fienga, A., & Manche, H. 2010, *A&A*, 514, A96
- Leblanc, Y., Dulk, G. A., & Bougeret, J.-L. 1998, *Sol. Phys.*, 183, 165
- Mancuso, S., & Spangler, S. R. 2000, *ApJ*, 539, 480
- Marchis, F., Descamps, P., Baek, M., et al. 2008, *Icarus*, 196, 97
- Marty, J. C., Balmino, G., Duron, J., et al. 2009, *Planet. Space Sci.*, 57, 350
- Moyer, T. D. 2003, *Formulation for Observed and Computed Values of Deep Space Network Data Types for Navigation* (John Wiley & Sons), 2
- Muhleman, D. O., & Anderson, J. D. 1981, *ApJ*, 247, 1093
- Muhleman, D. O., Esposito, P. B., & Anderson, J. D. 1977, *ApJ*, 211, 943
- Schwenn, R. 2006, *Space Sci. Rev.*, 124, 51
- Schwenn, R., & Marsch, E. 1990, *Physics of the Inner Heliosphere, I Large-Scale Phenomena* (Springer), *Phys. Chem. Space*, 20
- Schwenn, R., & Marsch, E. 1991, *Physics of the Inner Heliosphere, II Particles, Waves and Turbulence* (Springer), *Phys. Chem. Space*, 21
- Standish, E. M. 1998, IOM 312F-98-483
- Tokumaru, M., Kojima, M., & Fujiki, K. 2010, *J. Geophys. Res. (Space Physics)*, 115, 4102
- Woo, R., & Habbal, S. R. 1999, *Geophys. Res. Lett.*, 26, 1793
- You, X. P., Hobbs, G. B., Coles, W. A., Manchester, R. N., & Han, J. L. 2007, *ApJ*, 671, 907
- You, X. P., Coles, W. A., Hobbs, G. B., & Manchester, R. N. 2012, *MNRAS*, 422, 1160
- Zielenbach, W. 2011, *ApJ*, 142, 120

**Table 5.** Masses of the 59 asteroids that induce perturbations greater than 5 m on the Earth-Mars distances during the period of observations (Kuchynka et al. 2010).

IAU designation number	INPOP10c $10^{12} \times M_{\odot}$	INPOP10d $10^{12} \times M_{\odot}$	Diff $10^{12} \times M_{\odot}$	S	Impact m	$L$ %	
4	$130.109 \pm 0.716$	$130.109 \pm 0.983$	0.000		1198.953	20.5	S
1	$467.267 \pm 2.047$	$467.267 \pm 2.437$	0.000		793.741	17.3	S
2	$103.843 \pm 1.689$	$102.654 \pm 1.933$	1.189		146.270	11.8	S
324	$5.723 \pm 0.531$	$5.723 \pm 0.611$	0.000		93.536	1.0	S
10	$43.513 \pm 3.300$	$43.513 \pm 3.877$	0.000		77.003	15.9	S
19	$3.884 \pm 0.447$	$3.450 \pm 0.526$	0.435		59.069	13.8	N
3	$11.793 \pm 0.714$	$11.793 \pm 0.803$	0.000		55.639	0.6	S
704	$19.217 \pm 2.315$	$19.217 \pm 2.869$	0.000		34.492	7.4	S
532	$2.895 \pm 1.043$	$2.895 \pm 1.093$	0.000		32.714	2.3	S
9	$3.864 \pm 0.613$	$3.063 \pm 0.665$	0.801		29.606	20.6	N
7	$5.671 \pm 0.512$	$5.367 \pm 0.591$	0.305		27.822	13.9	S
29	$7.629 \pm 1.067$	$7.227 \pm 1.225$	0.402		26.673	2.9	S
24	$7.641 \pm 1.596$	$2.194 \pm 1.775$	5.447	*	26.131	36.0	N
31	$3.256 \pm 2.034$	$4.411 \pm 2.050$	1.155		23.466	24.1	S
15	$13.576 \pm 0.939$	$13.576 \pm 1.264$	0.000		21.555	20.6	S
6	$7.084 \pm 0.822$	$7.084 \pm 1.048$	0.000		21.150	7.4	S
11	$3.771 \pm 0.976$	$3.771 \pm 1.110$	0.000		17.301	31.9	S
139	$0.000 \pm 0.000$	$3.579 \pm 0.595$	3.579	N	16.687	32.0	N
747	$4.129 \pm 0.841$	$6.805 \pm 1.089$	2.676	*	15.937	31.6	N
105	$3.111 \pm 0.556$	$3.111 \pm 0.745$	0.000		15.196	4.5	N
20	$0.000 \pm 0.000$	$1.921 \pm 0.661$	1.921	N	14.763	39.9	N
372	$12.365 \pm 2.676$	$12.365 \pm 2.990$	0.000		13.796	19.0	S
8	$3.165 \pm 0.353$	$3.325 \pm 0.365$	0.159		12.664	17.7	S
45	$3.523 \pm 0.819$	$1.518 \pm 0.962$	2.005	*	11.790	21.0	N
41	$3.836 \pm 0.721$	$2.773 \pm 0.977$	1.063		11.568	15.2	N
405	$0.005 \pm 0.003$	$0.006 \pm 0.003$	0.001		11.378	21.2	N
511	$9.125 \pm 2.796$	$9.125 \pm 3.138$	0.000		10.248	20.5	S
52	$8.990 \pm 2.781$	$8.990 \pm 3.231$	0.000		9.841	3.0	S
16	$12.613 \pm 2.286$	$12.613 \pm 2.746$	0.000		9.701	8.9	S
419	$1.185 \pm 0.461$	$0.425 \pm 0.398$	0.760		9.585	10.2	N
78	$0.026 \pm 0.016$	$0.024 \pm 0.016$	0.002		9.389	9.8	N
259	$0.092 \pm 0.002$	$0.006 \pm 0.003$	0.086		9.222	31.4	N
27	$0.000 \pm 0.000$	$1.511 \pm 0.982$	1.511	N	9.146	29.5	N
23	$0.000 \pm 0.000$	$0.093 \pm 0.156$	0.093	N	9.067	31.1	N
488	$3.338 \pm 1.850$	$0.000 \pm 0.000$	3.338	0	8.614	2.8	N
230	$0.000 \pm 0.000$	$0.263 \pm 0.169$	0.263	N	7.620	27.0	N
409	$0.002 \pm 0.001$	$0.002 \pm 0.001$	0.000	0	7.574	2.2	N
94	$1.572 \pm 1.097$	$7.631 \pm 2.488$	6.058	*	7.466	28.5	N
344	$2.701 \pm 0.497$	$2.088 \pm 0.515$	0.613		7.465	15.3	N
130	$0.099 \pm 0.047$	$0.221 \pm 0.069$	0.122	*	7.054	31.7	N
111	$1.002 \pm 0.323$	$0.000 \pm 0.000$	1.002	0	6.985	11.4	N
109	$0.495 \pm 0.322$	$1.318 \pm 0.852$	0.823		6.865	18.7	N
42	$1.144 \pm 0.362$	$0.083 \pm 0.389$	1.061	*	6.829	0.6	N
63	$0.000 \pm 0.000$	$0.424 \pm 0.143$	0.424	N	6.451	17.4	N
12	$2.297 \pm 0.319$	$1.505 \pm 0.331$	0.792	*	6.159	21.7	N
469	$0.088 \pm 0.073$	$0.000 \pm 0.000$	0.088	0	6.107	18.1	N
144	$0.176 \pm 0.297$	$0.751 \pm 0.361$	0.575		6.087	22.8	N

**Notes.** Columns 2 and 3 give the values of the masses with the  $1\text{-}\sigma$  uncertainties obtained with INPOP10c and INPOP10d. The differences between INPOP10c and INPOP10d values are given in Col. 4. Column 5 indicates if the INPOP10d masses are newly determined (quoted N), set equal to 0 when estimated by INPOP10c (quoted 0), significantly different from INPOP10c determinations (\*). The maximum impacts of the perturbations are given in Col. 5. In Col. 7 is given the  $L$  criteria, the rate of local maxima rejected from the INPOP10c fit but included in the INPOP10d. In the last column we provide the status of the imposed constraints: S for strong and N for normal.

**Table 5.** continued.

IAU designation number	INPOP10c $10^{12} \times M_{\odot}$	INPOP10d $10^{12} \times M_{\odot}$	Diff $10^{12} \times M_{\odot}$	S	Impact m	L %	
356	$4.173 \pm 0.868$	$4.173 \pm 0.902$	0.000		5.759	2.2	N
712	$0.000 \pm 0.000$	$1.228 \pm 0.267$	1.228	N	5.745	2.2	N
88	$1.340 \pm 0.866$	$0.000 \pm 0.000$	1.340	0	5.742	1.4	N
60	$0.402 \pm 0.221$	$0.282 \pm 0.268$	0.120		5.733	3.8	N
50	$0.686 \pm 0.187$	$1.031 \pm 0.566$	0.345		5.702	2.0	N
128	$4.699 \pm 1.522$	$0.000 \pm 0.000$	4.677	0	5.624	3.0	N
5	$0.448 \pm 0.165$	$0.913 \pm 0.220$	0.466	*	5.533	15.8	N
59	$4.332 \pm 0.607$	$1.364 \pm 1.097$	2.968	*	5.325	12.1	N
98	$1.414 \pm 0.603$	$2.100 \pm 0.705$	0.686		5.195	15.1	N
194	$6.387 \pm 0.701$	$4.380 \pm 0.819$	2.007	*	5.145	2.9	N
51	$3.546 \pm 0.748$	$3.639 \pm 0.937$	0.093		5.109	15.6	N
156	$3.263 \pm 0.438$	$3.089 \pm 0.576$	0.174		5.103	19.3	N

**Table 6.** Asteroid masses found in the recent literature compared with the values estimated in INPOP10c and INPOP10d.

IAU designation number	INPOP10c $10^{12} \times M_{\odot}$	Close-encounters $10^{12} \times M_{\odot}$	Refs.	INPOP10d $10^{12} \times M_{\odot}$	%
5	$0.448 \pm 0.165$	$1.705 \pm 0.348$	Zielenbach (2011)	$0.913 \pm 0.220$	15.8
12	$2.297 \pm 0.319$	$2.256 \pm 1.910$	Zielenbach (2011)	$1.505 \pm 0.331$	21.7
20	$0.000 \pm 0.000$	$1.680 \pm 0.350$	Baer et al. (2011)	$1.921 \pm 0.661$	39.9
24	$7.6 \pm 1.6$	$2.639 \pm 1.117$	Zielenbach (2011)	$2.2 \pm 1.7$	36.0
27	$0.000 \pm 0.000$	$1.104 \pm 0.732$	Zielenbach (2011)	$1.511 \pm 0.982$	29.5
45	$3.523 \pm 0.819$	$2.860 \pm 0.060$	Marchis et al. (2008)	$1.518 \pm 0.962$	21.0
59	$4.332 \pm 0.607$	$1.448 \pm 0.0187$	Zielenbach (2011)	$1.364 \pm 1.097$	12.1
94	$1.572 \pm 1.097$	$7.878 \pm 4.016$	Zielenbach (2011)	$7.631 \pm 2.488$	28.5
130	$0.099 \pm 0.047$	$3.320 \pm 0.200$	Marchis et al. (2008)	$0.221 \pm 0.069$	31.7
139	$0.000 \pm 0.000$	$3.953 \pm 2.429$	Zielenbach (2011)	$3.579 \pm 0.595$	32.0

**Notes.** The uncertainties are given at 1 published sigma.

## Appendix A: Analytical solution

This section presents the analytical solutions of Eq. (1). Let,  $I_1$  and  $I_2$  be the integral solutions of Eq. (1) using Eqs. (3) and (4) i.e.,

$$I_1 = \int_{L_{\text{Earth}/\text{sn}}}^{L_{\text{s/c}}} B \left( \frac{l}{R_{\odot}} \right)^{-\epsilon} dL \quad (\text{A.1})$$

and

$$I_2 = \int_{L_{\text{Earth}/\text{sn}}}^{L_{\text{s/c}}} \left[ A \left( \frac{l}{R_{\odot}} \right)^{-4} + B \left( \frac{l}{R_{\odot}} \right)^{-2} \right] dL \quad (\text{A.2})$$

From the geometry (Fig. 3) we define

$$P = R_{\text{S}/\text{E}} \sin \alpha,$$

$$L_{\text{DC}} = R_{\text{E}/\text{SC}} - R_{\text{S}/\text{E}} \cos \alpha,$$

$$L_{\text{DE}}^2 = l^2 - P^2,$$

$$l^2 = L^2 + R_{\text{S}/\text{E}}^2 - 2 L R_{\text{S}/\text{E}} \cos \alpha,$$

where  $\alpha$  and  $\beta$  are the angle between the Sun-Earth-Probe (SEP) and the Earth-Sun-Probe (ESP).  $P$  is the MDLOS from the Sun. With these expressions,  $I_1$  can be written as

$$\begin{aligned} I_1 &= \int_{L_{\text{Earth}/\text{sn}}}^{L_{\text{s/c}}} B R_{\odot}^{\epsilon} \left( \frac{dL}{(L^2 + R_{\text{S}/\text{E}}^2 - 2 L R_{\text{S}/\text{E}} \cos \alpha)^{\epsilon/2}} \right) \\ &= B R_{\odot}^{\epsilon} \int_{L_{\text{Earth}/\text{sn}}}^{L_{\text{s/c}}} \left( \frac{dL}{([L - R_{\text{S}/\text{E}} \cos \alpha]^2 + R_{\text{S}/\text{E}}^2 \sin^2 \alpha)^{\epsilon/2}} \right). \end{aligned}$$

Assuming,

$$x = L - R_{\text{S}/\text{E}} \cos \alpha,$$

$$a = R_{\text{S}/\text{E}} \sin \alpha,$$

$$dx = dL,$$

with  $L = 0$  at the Earth station ( $L_{\text{Earth}/\text{sn}}$ ) and  $L = R_{\text{E}/\text{SC}}$  at the spacecraft ( $L_{\text{s/c}}$ ). Then the integral  $I_1$  can be written as

$$\begin{aligned} I_1 &= B R_{\odot}^{\epsilon} \int_{-R_{\text{S}/\text{E}} \cos \alpha}^{R_{\text{E}/\text{SC}} - R_{\text{S}/\text{E}} \cos \alpha} \frac{dx}{(x^2 + a^2)^{\epsilon/2}} \\ &= \frac{B R_{\odot}^{\epsilon}}{a^{\epsilon}} \int_{-R_{\text{S}/\text{E}} \cos \alpha}^{R_{\text{E}/\text{SC}} - R_{\text{S}/\text{E}} \cos \alpha} \frac{dx}{(1 + \frac{x^2}{a^2})^{\epsilon/2}}. \end{aligned}$$

Now let

$$\frac{x}{a} = \tan \theta,$$

and

$$dx = a \sec^2 \theta d\theta.$$

Therefore,

$$I_1 = \frac{B R_{\odot}^{\epsilon}}{a^{\epsilon}} \int_{\arctan\left(\frac{-R_{\text{S}/\text{E}} \cos \alpha}{a}\right)}^{\arctan\left(\frac{R_{\text{E}/\text{SC}} - R_{\text{S}/\text{E}} \cos \alpha}{a}\right)} \frac{a \sec^2 \theta}{(\tan^2 \theta + 1)^{\epsilon/2}} d\theta. \quad (\text{A.3})$$

From the geometry of Fig. 3, the lower limit of Eq. (A.3) can be written as

$$\arctan\left(\frac{-R_{\text{S}/\text{E}} \cos \alpha}{a}\right) = \arctan\left(\frac{-R_{\text{S}/\text{E}} \cos \alpha}{R_{\text{S}/\text{E}} \sin \alpha}\right),$$

with

$$\cot \alpha = \tan \left( \frac{\pi}{2} - \alpha \right).$$

Hence,

$$\arctan\left(\frac{-R_{\text{S}/\text{E}} \cos \alpha}{a}\right) = \alpha - \frac{\pi}{2}.$$

Similarly, the upper limit of Eq. (A.3) can be written as

$$\arctan\left(\frac{R_{\text{E}/\text{SC}} - R_{\text{S}/\text{E}} \cos \alpha}{a}\right) = \arctan\left(\frac{R_{\text{E}/\text{SC}} - R_{\text{S}/\text{E}} \cos \alpha}{R_{\text{S}/\text{E}} \sin \alpha}\right),$$

with

$$R_{\text{E}/\text{SC}} - R_{\text{S}/\text{E}} \cos \alpha = R_{\text{S}/\text{E}} \sin \alpha \left[ \tan \left( \beta - \left\{ \frac{\pi}{2} - \alpha \right\} \right) \right].$$

Hence,

$$\arctan\left(\frac{R_{\text{E}/\text{SC}} - R_{\text{S}/\text{E}} \cos \alpha}{a}\right) = \beta + \alpha - \frac{\pi}{2}.$$

Now Eq. (A.3) is given by

$$I_1 = \frac{B R_{\odot}^{\epsilon}}{a^{\epsilon}} \int_{\alpha - \frac{\pi}{2}}^{\beta + \alpha - \frac{\pi}{2}} \frac{a \sec^2 \theta}{(\tan^2 \theta + 1)^{\epsilon/2}} d\theta.$$

with

$$\sec^2 \theta = \tan^2 \theta + 1,$$

and

$$\cos \theta = \frac{1}{\sec \theta}.$$

Therefore, the integral  $I_1$  can be written as

$$I_1 = \frac{B R_{\odot}^{\epsilon}}{a^{\epsilon-1}} \int_{\alpha - \frac{\pi}{2}}^{\beta + \alpha - \frac{\pi}{2}} (\cos \theta)^{\epsilon-2} d\theta. \quad (\text{A.4})$$

The maximum contribution of the integral occurs at  $\theta = 0$ . To solve this integral, Taylor series expansion was used and for  $\theta$  near zero, it can be given as

$$\begin{aligned} f(\theta) &= f(0) + \theta \left( \frac{df}{d\theta} \right) + \frac{\theta^2}{2!} \left( \frac{d^2 f}{d\theta^2} \right) + \frac{\theta^3}{3!} \left( \frac{d^3 f}{d\theta^3} \right) \\ &\quad + \frac{\theta^4}{4!} \left( \frac{d^4 f}{d\theta^4} \right) \dots + \theta(\theta^n), \end{aligned} \quad (\text{A.5})$$

with

$$f(\theta) = (\cos \theta)^{\epsilon-2}.$$

Then

$$f(0) = 1$$

$$\left( \frac{df}{d\theta} \right) = -(\epsilon - 2) (\sin \theta) (\cos \theta)^{(\epsilon-3)},$$

$$\left( \frac{df}{d\theta} \right)_{\theta=0} = 0,$$

$$\begin{aligned} \left( \frac{d^2 f}{d\theta^2} \right) &= (\epsilon - 2) (\epsilon - 3) (\sin^2 \theta) (\cos \theta)^{(\epsilon-4)} \\ &\quad - (\epsilon - 2) (\cos \theta)^{(\epsilon-2)}, \end{aligned}$$



$$\left(\frac{d^2 f}{d\theta^2}\right)_{\theta=0} = -(\epsilon - 2),$$

$$\left(\frac{d^3 f}{d\theta^3}\right)_{\theta=0} = -(\epsilon - 2)(\epsilon - 3)(\epsilon - 4)(\sin^3 \theta)(\cos \theta)^{(\epsilon-5)} \\ + (\epsilon - 2)(3\epsilon - 8)(\sin \theta)(\cos \theta)^{(\epsilon-3)},$$

$$\left(\frac{d^3 f}{d\theta^3}\right)_{\theta=0} = 0,$$

$$\left(\frac{d^4 f}{d\theta^4}\right)_{\theta=0} = (\epsilon - 2)(\epsilon - 3)(\epsilon - 4)(\epsilon - 5)(\sin^4 \theta)(\cos \theta)^{(\epsilon-6)} \\ - (\epsilon - 2)(\epsilon - 3)(6\epsilon - 20)(\sin^2 \theta)(\cos \theta)^{(\epsilon-4)} \\ + (\epsilon - 2)(3\epsilon - 8)(\cos \theta)^{(\epsilon-2)},$$

$$\left(\frac{d^4 f}{d\theta^4}\right)_{\theta=0} = (\epsilon - 2)(3\epsilon - 8).$$

Now, Eq. (A.5) can be written as

$$(\cos \theta)^{(\epsilon-2)} = 1 - (\epsilon - 2) \frac{\theta^2}{2!} + (\epsilon - 2)(3\epsilon - 8) \frac{\theta^4}{4!} + \dots \theta (\theta^n) \\ = 1 - \frac{\epsilon - 2}{2} \theta^2 + \frac{3\epsilon^2 - 14\epsilon + 16}{24} \theta^4 + \dots \theta (\theta^n).$$

By neglecting the higher order terms, the integral (Eq. (A.4)) can be written as

$$I_1 = \frac{B R_{\odot}^{\epsilon}}{a^{\epsilon-1}} \int_{\alpha-\frac{\pi}{2}}^{\beta+\alpha-\frac{\pi}{2}} \left(1 - \frac{\epsilon - 2}{2} \theta^2 + \frac{3\epsilon^2 - 14\epsilon + 16}{24} \theta^4\right) d\theta \\ = \frac{B R_{\odot}^{\epsilon}}{a^{\epsilon-1}} \left[ \theta - \frac{\epsilon - 2}{6} \theta^3 + \frac{3\epsilon^2 - 14\epsilon + 16}{120} \theta^5 \right]_{\alpha-\frac{\pi}{2}}^{\beta+\alpha-\frac{\pi}{2}} \\ = \frac{B R_{\odot}^{\epsilon}}{a^{\epsilon-1}} \left[ \beta - \frac{\epsilon - 2}{6} \left( (\beta + \alpha - \pi/2)^3 - (\alpha - \pi/2)^3 \right) \right. \\ \left. + \frac{3\epsilon^2 - 14\epsilon + 16}{120} \left( (\beta + \alpha - \pi/2)^5 - (\alpha - \pi/2)^5 \right) \right].$$

By substituting the value of  $a$ , we can write the integral  $I_1$  as

$$I_1 = \frac{B R_{\odot}^{\epsilon}}{(R_{S/E} \sin \alpha)^{\epsilon-1}} \left[ \beta - \frac{\epsilon - 2}{6} \left( (\beta + \alpha - \pi/2)^3 - (\alpha - \pi/2)^3 \right) \right. \\ \left. + \frac{3\epsilon^2 - 14\epsilon + 16}{120} \left( (\beta + \alpha - \pi/2)^5 - (\alpha - \pi/2)^5 \right) \right]. \quad (\text{A.6})$$

Now, Eq. (A.2) can be written as  $I_2 = I_{2a} + I_{2b}$  where,

$$I_{2a} = \int_{L_{\text{Earth}/s/n}}^{L_{s/c}} A \left( \frac{l}{R_{\odot}} \right)^{-4} dL, \quad (\text{A.7})$$

and

$$I_{2b} = \int_{L_{\text{Earth}/s/n}}^{L_{s/c}} B \left( \frac{l}{R_{\odot}} \right)^{-2} dL. \quad (\text{A.8})$$

Using a similar approach to the previous integral, one can write

$$I_{2a} = \frac{A R_{\odot}^4}{a^3} \int_{\alpha-\frac{\pi}{2}}^{\beta+\alpha-\frac{\pi}{2}} \cos^2 \theta d\theta \\ = \frac{A R_{\odot}^4}{a^3} \left[ \frac{1}{4} (2\theta + \sin 2\theta) \right]_{\alpha-\frac{\pi}{2}}^{\beta+\alpha-\frac{\pi}{2}} \\ = \frac{A R_{\odot}^4}{4 a^3} \left[ (2\beta - \sin 2(\alpha + \beta) + \sin 2\alpha) \right] \\ = \frac{A R_{\odot}^4}{4 R_{S/E}^3 \sin^3 \alpha} \left[ (2\beta - \sin 2(\alpha + \beta) + \sin 2\alpha) \right].$$

Similarly, Eq. (A.8) can be written as

$$I_{2b} = \frac{B R_{\odot}^2}{a} \int_{\alpha-\frac{\pi}{2}}^{\beta+\alpha-\frac{\pi}{2}} d\theta \\ = \frac{B R_{\odot}^2}{a} \left[ \theta \right]_{\alpha-\frac{\pi}{2}}^{\beta+\alpha-\frac{\pi}{2}} \\ = \frac{B R_{\odot}^2}{R_{S/E} \sin \alpha} \beta.$$

Now by using  $I_{2a}$  and  $I_{2b}$ , expression  $I_2$  can be written as

$$I_2 = \frac{A R_{\odot}^4}{4 R_{S/E}^3 \sin^3 \alpha} \left[ (2\beta - \sin 2(\alpha + \beta) + \sin 2\alpha) \right] \\ + \frac{B R_{\odot}^2}{R_{S/E} \sin \alpha} \beta. \quad (\text{A.9})$$



## Chapter 5

# Improvement of the planetary ephemeris and test of general relativity with MESSENGER

### 5.1 Introduction

Mercury is the smallest and least explored terrestrial planet of the solar system. Mariner 10 was the first spacecraft which made three close encounters (two in 1974 and one in 1975) to this planet and provided most of our current knowledge of the planet until early 2008 ([Smith et al., 2010](#)). In addition to Mariner 10 flyby observations, ground based radar measurements were the only observations which were used to study the gravity field of Mercury and its physical structure (spherical body with slightly flattened at the poles and mildly elongated equator) ([Anderson et al., 1987a, 1996](#)). In 2004, NASA launched a dedicate mission, MESSENGER, to learn more about this planet. MESSENGER made three close encounters (two in 2008 and one in 2009) to Mercury and became the first spacecraft which observed Mercury from its orbit.

Till now, MESSENGER has completed more than two years on orbit at Mercury. During the orbital period, radio tracking of MESSENGER routinely measured the Doppler and range observables at DSN stations. These observables are important to estimate the spacecraft state vectors (position and velocity) and to improve the knowledge of Mercury's gravity field and its geophysical properties ([Srinivasan et al., 2007](#)). Using the first six months of radioscience data during the orbital period, [Smith et al. \(2012\)](#) computed the gravity field and gave better constraints on the internal structure (density distribution) of Mercury. This updated gravity field becomes crucial for the present computation of MESSENGER orbit and to perform precise relativistic tests.

The primary objectives of this work is to determine the precise orbit of the MESSENGER spacecraft around Mercury using radioscience data and then improve the planetary ephemeris

---

INPOP (see Chapter 1). The updated spacecraft and planetary ephemerides are then used to perform sensitive relativistic tests of the PPN parameters ( $\gamma$  and  $\beta$ ).

As described in Chapter 1, spacecraft range measurements are used for the construction of planetary ephemerides. These measurements approximately cover 56% of whole INPOP data and impose strong constraints on the planet orbits and on the other solar system parameters including asteroid masses. However, until now, only five flybys (two from Mariner 10 and three from MESSENGER) range measurements were available for imposing strong constraints to the Mercury's orbit (Fienga et al., 2011a). Therefore, range measurements obtained by MESSENGER spacecraft during its mapping period are important to improve our knowledge of the orbit of Mercury.

Moreover, high precision radioscience observations also gave an opportunity to perform sensitive relativistic tests by estimating possible violation of GR of the two relativistic parameters ( $\gamma$  and  $\beta$ ) of the PPN formalism of general relativity (Will, 1993). The previous estimations of these parameters, using different techniques and different data set, can be found in Bertotti et al. (2003); Müller et al. (2008); Pitjeva (2009); Williams et al. (2009); Manche et al. (2010); Konopliv et al. (2011); Fienga et al. (2011a). However, because of Mercury relatively large eccentricity and close proximity to the Sun, its orbital motion provides one of the best solar system tests of general relativity (Anderson et al., 1997). In addition, Fienga et al. (2010, 2011a) also demonstrated that, Mercury observations are far more sensitive to PPN modification of GR than other data used in the planetary ephemerides construction. We therefore, also performed such tests with the latest MESSENGER observations to obtain one of the best value for PPN parameters.

In this chapter, we introduce the updated planetary ephemeris INPOP13a and summarize the technique used for the estimation of the PPN parameters. The outline of the chapter is as follow: The section 5.2 gives an overview of the MESSENGER mission. The radioscience data analysis and the dynamical modeling of MESSENGER are also discussed in the same section. In section 5.3, we present the results obtained during the orbit determination. The evolution of INPOP with the accuracy of MESSENGER orbit, and the brief description of tests performed with the INPOP13a are also discussed in this section.

The results presented in this chapter are gathered in an article published in Astronomy & Astrophysics. The Section 5.4 is therefore stated as Verma et al. (2014). This section deals with the detailed analysis of the tests performed with the high precision Mercury ephemeris INPOP13a.

---

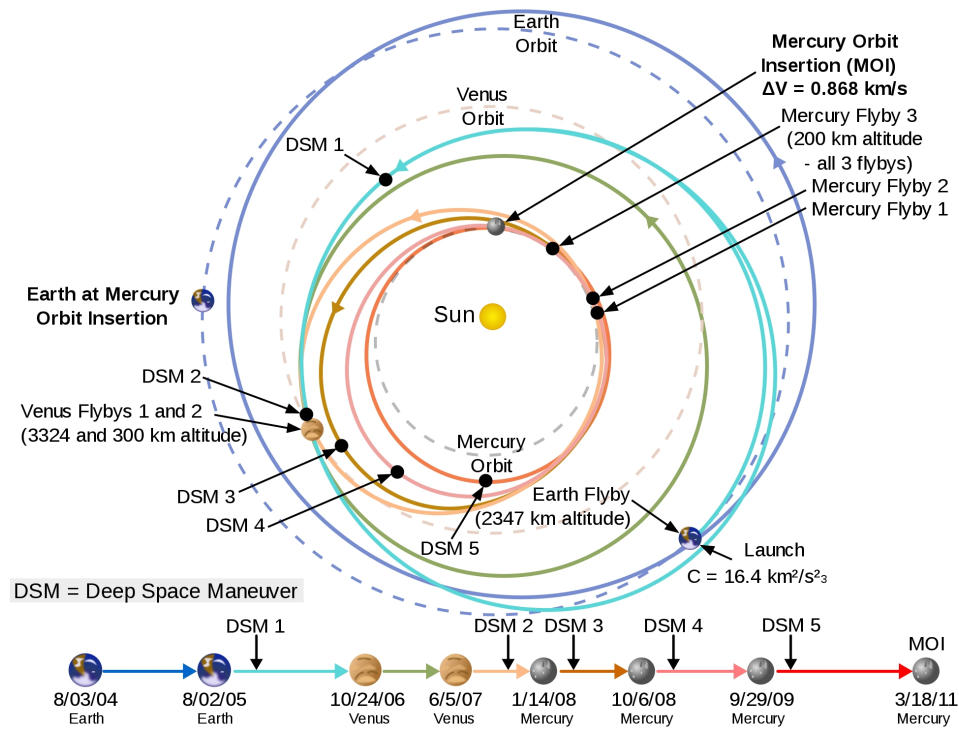


Figure 5.1: Summary of MESSENGER's entire trajectory from launch to mapping period (McAdams et al., 2007).

## 5.2 MESSENGER data analysis

### 5.2.1 Mission design

Under the NASA's Discovery program, the Mercury Surface, Space ENvironment, GEochemistry, and Ranging (MESSENGER) spacecraft is the first probe to orbit the planet Mercury. It launched in August 3, 2004, from Pad B of Space Launch Complex 17 at Cape Canaveral Air Force Station, Florida, aboard a three-stage Boeing Delta II rocket. On March 18, 2011, MESSENGER successfully entered Mercury's orbit after completing three flybys of Mercury following two flybys of Venus and one of Earth.

The 6.6-year trip from launch to Mercury orbit insertion is one of the longest interplanetary cruise phase options considered for MESSENGER. The spacecraft system design lifetime accounted for a seven-year journey to Mercury followed by a prime (one-year) and extended (one-or more-year) Mercury orbit phases. MESSENGER used gravity assists from Earth, Venus and Mercury to lower its speed relative to Mercury at orbit insertion. Several trajectory-correction maneuvers (TCMs), including five large deep-space maneuvers (DSMs) were also used to adjust its path to Mercury (McAdams et al., 2007). As a summary of the entire trajectory from launch to mapping period is shown in Fig. 5.1.

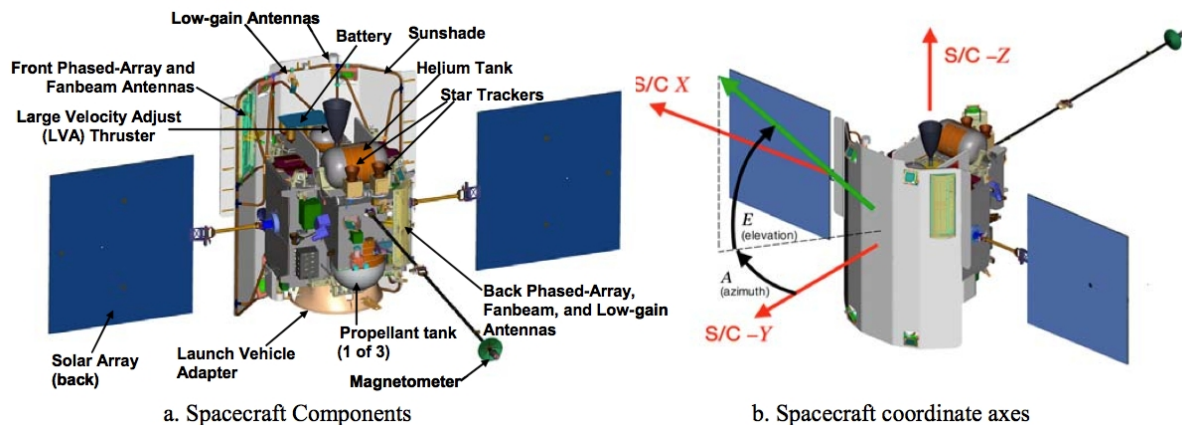


Figure 5.2: MESSENGER spacecraft geometry (Vaughan et al., 2006).

As shown in this figure, approximately one year after launch, MESSENGER made its first flyby of Earth on August 2, 2005 and then headed toward the Venus flybys using largest DSM. The MESSENGER made two Venus flybys, first occurred on October 24, 2006 and second on June 5, 2007. These flybys headed MESSENGER towards Mercury by additionally using the DSM performed after second flyby of Venus. In January 14, 2008 MESSENGER became first spacecraft which provided first close-up look of Mercury in more than 30 years. The Mercury flyby 1-to-Mercury orbit insertion transfer trajectory, shown in Fig. 5.1, includes three Mercury flyby-DSM segments that lower the spacecraft speed relative to Mercury and on March 18, 2011, MESSENGER successfully entered Mercury's orbit.

The MESSENGER spacecraft was initially inserted into a  $\sim 12$ -hour, near-polar orbit around Mercury, with an initial periapsis altitude of 200 km, initial periapsis longitude of  $60^\circ\text{N}$ , and apoapsis at  $\sim 15,200$  km altitude in the southern hemisphere. After successful first year flight in the orbit, mission was extended to one or more year which began on 18 March 2012. During first extended mission, two orbit-correction maneuvers were executed, four days apart, in April 2012 to reduce MESSENGER's orbital period from  $\sim 12$  to  $\sim 8$  hours (Flanigan et al., 2013)

### 5.2.2 Spacecraft geometry

The MESSENGER spacecraft was designed and constructed to withstand the harsh environments associated with achieving and operating in Mercury orbit. The spacecraft structure is constructed primarily of lightweight composite material housing a complex dual-mode propulsion system. Figure 5.2 shows the complex geometry of the MESSENGER spacecraft, where, panel (a) shows the spacecraft components, and panel (b) represents the coordinate system. Table 5.1 gives the approximated characteristics of the spacecraft components, extracted from the Vaughan et al. (2002).

The whole system of the MESSENGER spacecraft can be divided into eight subsystems. The briefly introduction of these subsystems is given below and detailed information can be found in [Leary et al. \(2007\)](#):

- **Structures and mechanisms:** the primary spacecraft structures are the core, the adapter ring, the sunshade, the solar panels, and the magnetometer boom. The core of the spacecraft tightly integrates support panels with the propulsion system. Three mechanical assemblies were deployed during operation, the two solar panels and the 3.6-m magnetometer boom. The solar array hinges are located at each end of the arms connecting the panels to the core structure. Whereas, the magnetometer boom is separated into two segments with one hinge between the spacecraft structure and the first segment and the other between the two segments.
  - **Propulsion:** the MESSENGER propulsion system is a pressurized bipropellant dual-mode system. As shown in Figure 5.2, they are three main propellant tanks, a refillable auxiliary fuel tank, and a helium pressurant tank provide propellant and pressurant storage. MESSENGER carries seventeen thrusters. Three thruster types, arranged in five different thruster module configurations, provide the required spacecraft forces and torques.
  - **Thermal:** the thermal design of the MESSENGER spacecraft relies upon a ceramic-cloth sunshade to protect the vehicle from the intense solar environment. Sunshade can experienced maximum temperature of 350°C at Mercury but creates a benign thermal environment for the main spacecraft bus, allowing the use of essentially standard electronics, components, and thermal blanketing materials.
  - **Power:** the power system is designed to support about 390 W of load power near Earth and 640 W during Mercury orbit. The power is primarily provided by two solar panels that are mounted on small booms extendable beyond the sunshade and rotating to track the Sun.
  - **Avionics:** MESSENGER is equipped with redundant integrated electronics modules (IEM). The IEM implements command and data handling, guidance and control, and fault protection functions. A primary driver of the IEM architecture was to simplify spacecraft fault protection.
  - **Software:** it provides the main processor-supported code that performs commanding, data handling, and spacecraft control.
  - **Guidance and control:** this subsystem maintains spacecraft attitude and executes propulsive maneuvers for spacecraft trajectory control. It also controls the solar panel orientation to maintain a Sun offset angle providing sufficient power at moderate panel temperatures. It is also responsible for keeping the sunshade pointed towards the Sun to protect the spacecraft bus from extreme heat and radiation.
  - **Radio frequency telecommunications:** this subsystem consists of small deep space transponders, solid-state power amplifiers, phased-array antennas, and medium- and low-gain antennas. The goals of this subsystem is, to provide the highest quality and quantity
-

of scientific data, and to provide highly accurate Doppler and range data for navigation and science.

Table 5.1: MESSENGER spacecraft *macro-model* characteristics (Vaughan et al., 2002).

S/C body	Components	App. area (m <sup>2</sup> )	Diffuse Ref.	Specular Ref.
Spacecraft Bus	±X side of sunshade	2.057	0.35	0.15
	Center of sunshade, along -Y	1.132	0.35	0.15
	+Y side of the spacecraft	4.933	0.35	0.15
Solar Arrays	Front side of ±X solar panel	2.5	0.07	0.52
	Back side of ±X solar panel	2.5	0.07	0.52

### 5.2.3 Radioscience data

The MESSENGER spacecraft was tracked by the NASA's DSN stations at X-band frequency, 7.2 GHz for uplink from the ground stations and 8.4 GHz for downlink from the spacecraft. Communications are accomplished via the 34-m and 70-m antennas of DSN stations in Goldstone, USA; Madrid, Spain; and Canberra, Australia. The MESSENGER X-band tracking consists in measuring the round-trip time delay (two-way range), and the two- and three-way ramped Doppler shift of the carrier frequency of the radio link between the spacecraft and the DSN stations on Earth. The precision of the Doppler measurement for the radio frequency subsystem is within  $\pm 0.1$  mm/s over 10s to several minutes of integration time (Srinivasan et al., 2007).

### 5.2.4 Dynamical modeling and orbit determination processes

We have analyzed one-and-half year of tracking data collected by the DSN during the MESSENGER orbital period. This data sample corresponds to one year of prime mission and six months of first extended mission. The complete data set that were used for the analysis are available on the Geoscience node<sup>1</sup> of the NASA's PDS. For precise orbit determination, all available observations were analyzed with the help of the GINS software (see Chapter 2).

The precise orbit determination is based on a full dynamical approach. The dynamical modeling includes gravitational (gravitational attraction of Mercury, Eq. 2.65, third-body gravity perturbations from the Sun and other planets, Eq. 2.71, and relativistic corrections, Eq. 2.72) and non-gravitational (solar radiation pressure, Eq. 2.74, Mercury radiation pressure, Eqs. 2.78

<sup>1</sup><http://pds-geosciences.wustl.edu/messenger/>



and 2.79) forces that are acting on the spacecraft. These forces have been taken into account in the force budget of MESSENGER. Because of the thin atmosphere of Mercury, we have assumed that MESSENGER experienced negligible resistance due to the atmosphere, hence atmospheric drag force was not included in the force budget. Moreover, MESSENGER fires small thrusters (nominally on each Tuesday) to perform Momentum Dump Maneuver (MDM)<sup>2</sup> for reducing the spacecraft angular momentum to a safe level. In addition to MDM, MESSENGER also performed Orbit Correction Maneuver (OCM)<sup>2</sup> typically once every Mercury year (~88 Earth days) to maintain minimum altitude below 500 kilometers. Due to insufficient information of these maneuvers, we therefore did not include the epoch of each maneuver during the orbit computation. Hence, empirical delta accelerations, radial, along-track, and cross-track, at the epoch of maneuvers were not included in the force budget.

The measurement (Doppler and range) models (see Sec. 2.4.3) and the light time corrections (see Sec. 2.4.2), that are modeled in GINS, are described in chapter 2. During the computations, DSN station coordinates were corrected from the Earth's polar motion, solid-Earth tides, and from the ocean loading, based on the formulation given in Moyer (2003). In addition to these corrections, radiometric data also have been corrected from tropospheric propagation through the meteorological data<sup>2</sup> (pressure, temperature and humidity) of the stations.

The complex geometry of the MESSENGER spacecraft was treated as a combination of flat plates arranged in the shape of box, with attached solar arrays, so called *Box-Wing* macro-model. The approximated characteristics of this macro-model, which includes cross-section area and specular and diffuse reflectivity coefficients of the components, extracted from Vaughan et al. (2002) and are given in Table 5.1. In addition to the macro-model characteristics, orientations of the spacecraft were also taken in account. The attitude of the spacecraft, and of its articulated panels in an inertial frame are usually defined in terms of quaternions. The approximate value of these quaternions were extracted from the SPICE NAIF software. The macro-model and its orientation have allowed to calculate the non-gravitational accelerations that are acting on the MESSENGER spacecraft due to the radiation pressure from the Sun and Mercury (albedo and thermal infra-red emission).

For orbit computations and for parameters estimations, a multi-arc approach was used to get an independent estimate of the MESSENGER accelerations. In this method, we integrated the equations of motion using the time-step of 50s and then, orbital fits were obtained from short data-arcs fitted over the observations span of one-day using an iterative process. The short data-arcs of one-day have been chosen to account for the model imperfections (see section 3.5 of Chapter 3).

An iterative least-square fit was performed on the complete set of Doppler- and range-tracking data-arcs corresponding to the orbital phase of the mission. The summary of these tracking data are given in Table 5.2. Several parameters have been estimated during the orbit computation. They are similar to the one estimated for MGS spacecraft (see Sec. 3.3.2 of Chapter 3) except scale factor for atmospheric drag and empirical delta accelerations.

---

<sup>2</sup>[http://pds-geosciences.wustl.edu/messenger/mess-v\\_h-rss-1-edr-rawdata-v1/messrs\\_0xxx/ancillary/](http://pds-geosciences.wustl.edu/messenger/mess-v_h-rss-1-edr-rawdata-v1/messrs_0xxx/ancillary/)

---

Table 5.2: Summary of the Doppler and range tracking data used for orbit determination.

Mission phase	Begin date dd-mm-yyyy	End date dd-mm-yyyy	Number of 2-way Doppler	Number of 3-way Doppler	Number of range
Prime	17-05-2011	18-03-2012	2108980	184138	11540
Extended	26-03-2012	18-09-2012	1142974	23211	5709

## 5.3 Orbit determination

### 5.3.1 Acceleration budget

As mentioned in the Chapter 3, the accurate orbit determination of a planetary spacecraft requires a good knowledge of gravitational and non-gravitational forces which are acting on the spacecraft. The model of these forces is described in the Chapter 2. The Figure 5.3 illustrates an average of various accelerations that are acting on the MESSENGER spacecraft during the prime and extended phases of the orbital periods. The comparison between MGS (see Chapter 3) and MESSENGER accelerations that are taken in account in the force budget is also shown in Figure 5.3.

Mercury and Mars have different positions in the solar system and have different physical properties (such as internal mass distribution). These physical properties of the planets, and the shape of the spacecraft orbit, largely affect the force budget of MESSENGER and MGS spacecraft, respectively. The comparison between MESSENGER and MGS accelerations based on Figure 5.3 can lead to the following comments:

- **Accelerations due to gravitational potential:** Mars and Mercury, both planets have very different mass distributions, and MGS and MESSENGER, both spacecraft have very different shapes of their orbits (MGS: low altitude near circular; MESSENGER: highly eccentric). As a consequence, the contribution of the mean and zonal coefficients ( $GM/r + J_2$ ) in the accelerations for MESSENGER spacecraft is  $\sim 8$  times smaller than for the MGS spacecraft. Similarly, the contribution of the tesseral ( $l \neq m$ ) and sectoral ( $l = m$ ) coefficients in the accelerations is  $\sim 90$  times smaller in MESSENGER spacecraft.
- **Accelerations due to third body attractions:** Mercury is the closest planet to the Sun and hence, experiences the largest gravitational attraction from the Sun as compared to other planets of the solar system. As a result, accelerations due to the Sun attraction on MESSENGER is  $\sim 172$  time greater than the one experienced by MGS spacecraft.
- **Accelerations due to general relativity** from Eq. 2.72 one can see that, the acceleration due to GR is a function of the gravitational constant ( $GM$ ) of the orbiting body and the

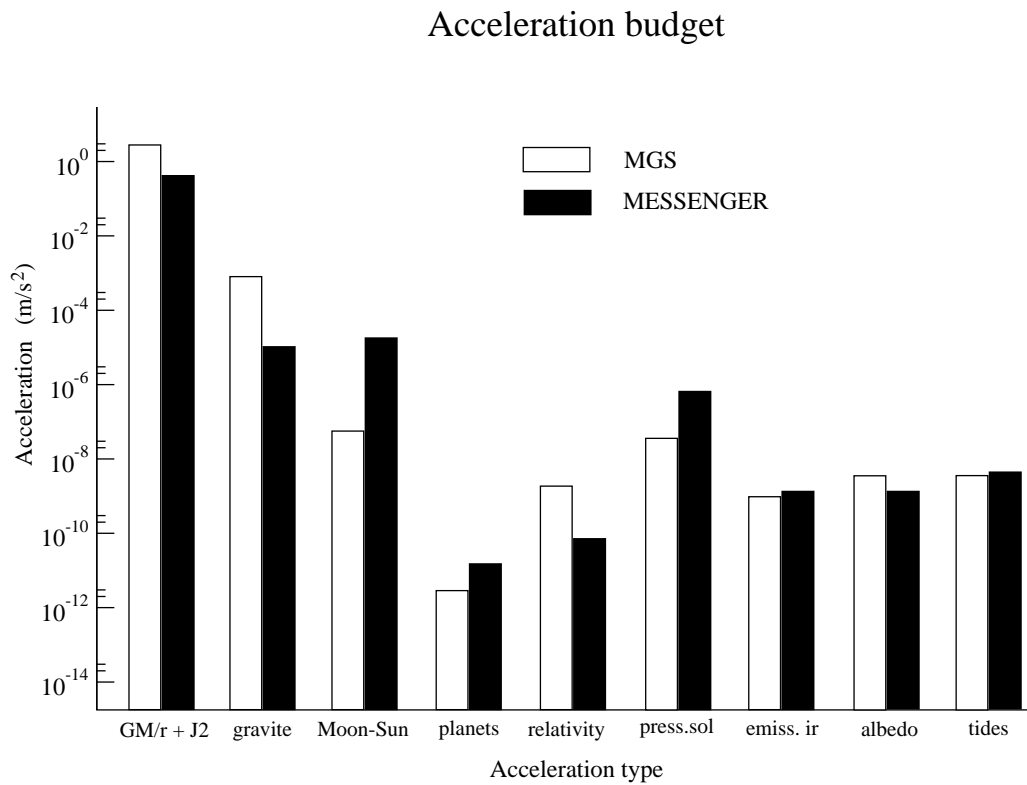


Figure 5.3: Gravitational and non-gravitational accelerations acting on the MESSENGER spacecraft. The empirical accelerations correspond to maneuvers and accelerations due to atmospheric drag were not computed for MESSENGER (see Section 5.2.4).

position and velocity vectors of the spacecraft relative to the center of orbiting body. Due to the smaller GM of the Mercury than the Mars one, and to the highly eccentric MESSENGER orbit, the acceleration due to GR experienced by MESSENGER is  $\sim 14$  time smaller than MGS. However, beside this situation, Mercury is the planet the most affected by GR as its advance of perihelia induced by the Sun gravity is about 30 times bigger than the advance of the Mars orbit (43 arcsecond/cy and 1.3 arcsecond/cy for Mars).

- **Accelerations due to the solar radiation pressure:** It is the largest non-gravitational acceleration acting on the both spacecraft. Due to the close proximity of MESSENGER to the Sun, it experienced  $\sim 13$  time more solar radiation pressure than MGS.
- **Accelerations due to planet radiation:** The Infra-Red radiation and the Albedo of the planets cause small accelerations in the spacecraft motion, respectively. These are the smallest non-gravitational accelerations that are acting on both spacecraft. An average value of these accelerations are relatively similar for both missions.
- **Accelerations due to solid planetary tides:** During prime mission of the MESSENGER spacecraft, an average value of computed accelerations due to solid planetary tides is similar for both spacecraft, while during extended mission, MESSENGER experienced relatively larger acceleration (see Table 5.3).

As stated previously, during the extended phase of the mission apoapsis altitude of MESSENGER was significantly tuned up to 5000km. Because of its relatively shorter orbit compared to the prime phase (for example, see Figure 5.4), one can expect a different distribution of the accelerations during both phases. A summary of an average magnitude of these accelerations are given on Table 5.3. As expected during the extended phase, MESSENGER experienced  $\sim 40\%$  greater accelerations due to the gravitational potential of Mercury and approximately the same percentage of increment has been estimated for the acceleration due to GR. These increments in the accelerations can be explained from the close approach of MESSENGER to Mercury, as shown in Figure 5.4. However, gravitational accelerations due to the third body (including the Moon and the Sun) attraction are relatively smaller during extended phase. In addition to gravitational accelerations, non-gravitational accelerations due to Mercury radiations, Infra-Red radiation and Albedo, were also enhanced by  $\sim 42\%$  and  $\sim 11\%$ , respectively, whereas solar radiation pressure remains approximately similar during both phases.

### 5.3.2 Significance of MESSENGER observation for INPOP

As discussed in Chapter 1, the INPOP planetary ephemerides are built on a regular basis and are provided to users through the IMCCE website [www.imcce.fr/inpop](http://www.imcce.fr/inpop). The INPOP10e ephemerides were the latest release (Fienga et al., 2013) and were delivered as the official Gaia mission planetary ephemerides used for the navigation of the satellite as well as for the analysis of the data. Specific developments and analysis were done for the Gaia release such as TCB time-scale version or an accurate estimation of the INPOP link to ICRF.

---

Table 5.3: An average magnitude of MESSENGER accelerations estimated during prime and extended phase of the mission.

Acceleration	Mission Phase	
	Prime (m/s <sup>2</sup> )	Extended (m/s <sup>2</sup> )
GM/r + J2	$3.25 \times 10^{-1}$	$4.62 \times 10^{-1}$
Gravity	$0.86 \times 10^{-5}$	$1.19 \times 10^{-5}$
Moon-Sun	$1.12 \times 10^{-5}$	$0.87 \times 10^{-5}$
Planets	$1.53 \times 10^{-11}$	$0.87 \times 10^{-11}$
Relativity	$6.78 \times 10^{-11}$	$9.44 \times 10^{-11}$
Solar rad. press.	$5.47 \times 10^{-7}$	$5.87 \times 10^{-7}$
IR emissi.	$1.24 \times 10^{-9}$	$1.77 \times 10^{-9}$
Albedo	$1.03 \times 10^{-9}$	$1.15 \times 10^{-9}$
Solid tides	$4.32 \times 10^{-9}$	$6.31 \times 10^{-9}$

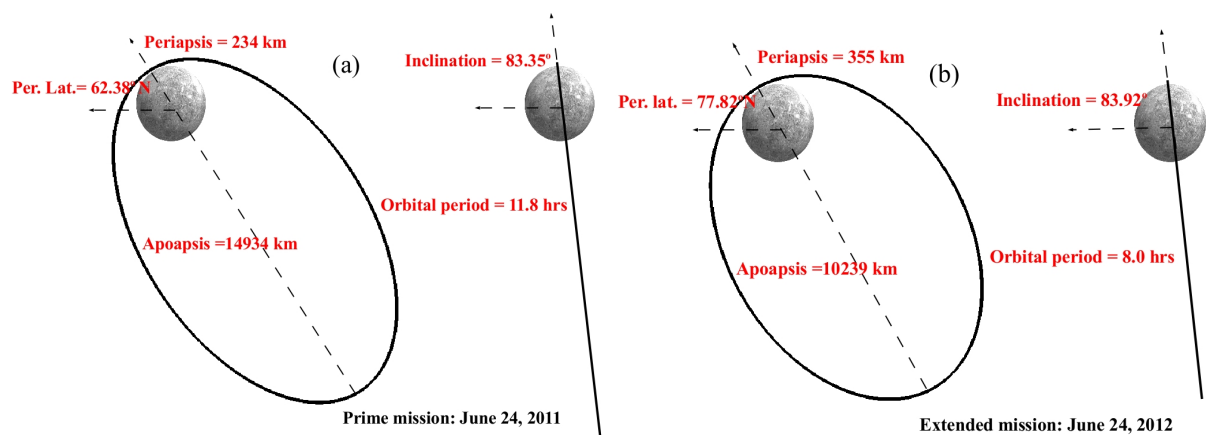


Figure 5.4: MESSENGER orbit: (a) prime phase (June 24, 2011) (b) extended phase (June 24, 2012).

With the delivery of the MESSENGER radio science data, a new opportunity was offered to improve drastically our knowledge of the Mercury orbit and to perform tests of gravity at a close distance from the Sun. In order to perform such tests with a decisive accuracy, one should first reduce the uncertainty of the Mercury orbit. Indeed, as it was stated previously, only five positions of Mercury were deduced from spacecraft flybys over 40 years: 2 positions in the 70's from the Mariner flybys and 3 in 2008 and 2009 from the MESSENGER flybys. These positions gave very accurate positions of Mercury of about several tens of meters compared to direct radar observations of the surface of planet obtained with an accuracy of about 1 kilometer from the 70's to the late 90's. Using the 1.5 year range measurements (see Section 5.3.3.5) is then a crucial chance for obtaining a better tangle over the  $\sim 0.3$  year Mercury orbit. The few

meter accuracy of the MESSENGER range data will give big constraints over short period perturbations on the Mercury orbit when the 5 flyby positions obtained with Mariner and the MESSENGER flybys will still be significant for the measurements of long term perturbations.

### 5.3.3 Evolution of INPOP with the accuracy of MESSENGER orbit

The rms values of the postfit Doppler and range residuals give some indications about the quality of the orbit fit and the quality of the estimated parameters. Moreover, the quality of the used parameters associated with the physical model can also be estimated from these residuals. However, Mercury is the least explored terrestrial planet and the poor knowledge of the parameters associated with the Mercury physical model highly influenced the MESSENGER orbit. Therefore, numbers of tests have been performed to compute precise orbit of MESSENGER with a gradual improvement of Mercury physical model, such as: spherical harmonic model of the gravity field, rotational model, and the Mercury ephemeris.

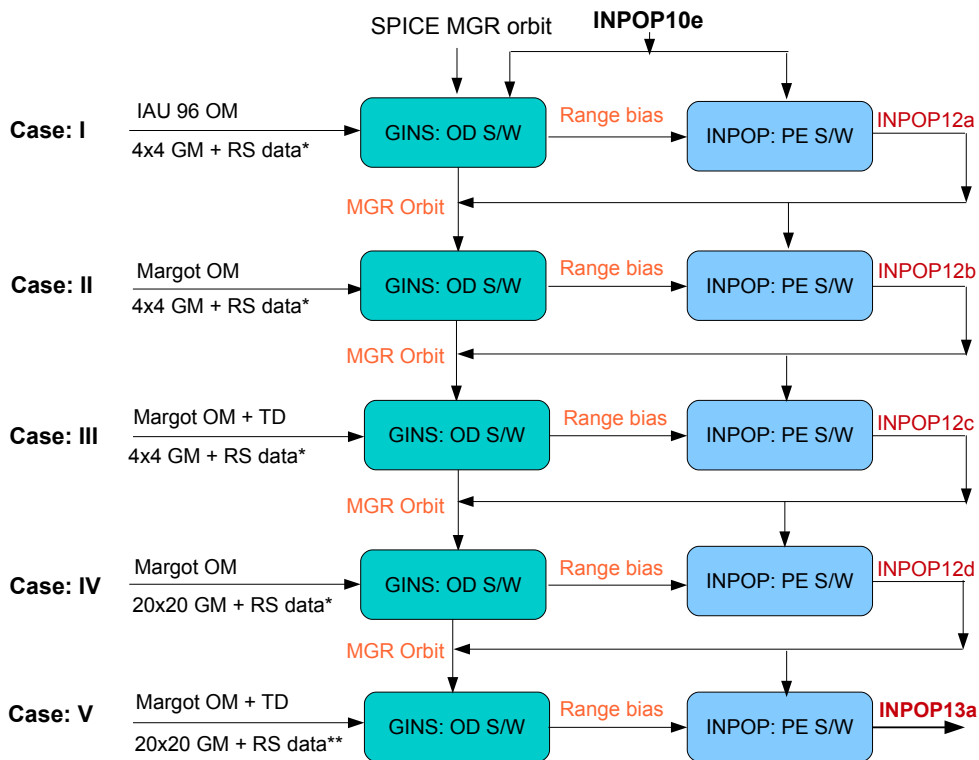


Figure 5.5: Schematic diagram of the evolution of planetary ephemeris from INPOP10e to INPOP13a with the improvement of MESSENGER orbit.

OM: Orientation Model; GM: Gravity Model; TD : Transponder Delay; RS : Radioscience  
 OD S/W : Orbit Determination software; PE S/W : Planetary Ephemeris software  
 (\*) Prime mission; (\*\*) prime+extended mission.

The evolution of planetary ephemeris from INPOP10e to INPOP13a with these gradual

improvements is shown in Figure 5.5. From this figure one can see that, improved inputs have been implemented to GINS software in the subsequent tests. Using these inputs and the one described in Sections 5.2.4, GINS constructs the MESSENGER orbit precisely. The estimated range bias from GINS are then used to build the new planetary ephemeris. The constants and dynamical modeling used for the construction of the new ephemerides are similar to INPOP10e (see Chapter 1). A global adjustment of the planet initial conditions including Pluto, the mass of the Sun, the oblateness of the Sun, the ratio between the mass of the Moon and 140 asteroid masses. The improved ephemeris and the MESSENGER orbit are then used as a input for subsequent tests to reconstruct the MESSENGER orbit and planetary ephemeris. The detailed analysis of these tests are given in the following sections:

### 5.3.3.1 Case I: First guess orbit for Messenger and INPOP12a

#### 5.3.3.1.1 Description

Before the MESSENGER mission, Mariner 10 flybys observations and ground based radar measurements were the only observations which were used to study the gravity field of Mercury and its physical structure (spherical body with slightly flattened at the poles and mildly elongated equator) (Anderson et al., 1987a, 1996). Later, using the altimetric and radio tracking observations from MESSENGER first two flybys of Mercury Smith et al. (2010) derived the spherical harmonic model of Mercury gravity field HgM001 developed up to degree and order 4. In this test, we have analyzed radioscience data of the MESSENGER spacecraft acquired at the time of prime phase of the mission (see Table 5.2) using HgM001 gravity model. The MESSENGER orbital fits were obtained from one-day data-arcs using an iterative process (see Section 5.2.4 for more details). To initialize the iteration, initial position and velocity vectors of MESSENGER were taken from the SPICE NAIF kernels<sup>3</sup>. The positions and velocities of the planets were accessed through the latest INPOP10e planetary ephemeris. Moreover, the orientation of Mercury was defined as recommended by the IAU<sup>4</sup> (see Table 5.4).

Table 5.4: Recommended values for the direction of the north pole of rotation and the prime meridian of the Mercury, 1996 (Davies et al., 1996).

Parameter	value	
$\alpha_0 =$	281.01 - 0.033T	$\alpha_0, \delta_0$ : are right ascension and declination respectively, which define the spin axis with equinox J2000 at epoch J2000. $W$ : is the rotational phase $T$ : is the interval in Julian centuries (of 36525 days) from the standard epoch $d$ : is the interval in days (of 86400 SI seconds) from the standard epoch, with epochs defined in TDB
$\delta_0 =$	61.45 - 0.005T	
$W =$	329.68 + 6.1385025d	

<sup>3</sup>[ftp://naif.jpl.nasa.gov/pub/naif/pds/data/mess-e\\_v\\_h-spice-6-v1.0/](ftp://naif.jpl.nasa.gov/pub/naif/pds/data/mess-e_v_h-spice-6-v1.0/)

<sup>4</sup>It is a default orientation of Mercury defined in the GINS software

### 5.3.3.1.2 Results

As stated before, rms values of the postfit Doppler and range residuals give some indications about the quality of the orbit fit and the quality of the estimated parameters. On panel *a* of Figure 5.6, are plotted the rms values of two- and three-way Doppler residuals, obtained for each data-arc and expressed in millihertz (mHz). The range measurements were also used to assist in fitting the Doppler data for a precise orbit determination. The panel *b* of Figure 5.6 presents the rms values of two-way range residuals, obtained for each data-arc. On panel *c*, are plotted the range bias (error in the Earth-Mercury distances) estimated with INPOP10e. These range bias are then used to fit the planetary ephemeris software (see Figure 5.5). The postfit range bias of newly fitted INPOP12a ephemeris are plotted in panel *d*. The differences in the Earth-Mercury distances over 50 years between these two ephemeris are plotted in panel *e* of the same figure.

The statistics of these results are given in Table 5.5 and are compared with the required accuracy. From this table and Figure 5.6 one can see that, the rms values of the postfit Doppler and range residuals are widely dispersed, and experienced  $\sim 3$  times more dispersion compared to required accuracy with a mean value of about  $\sim -0.3$ mHz and  $\sim 0.89$ m, respectively. Such high discrepancies in the residuals are likely due to insufficient spherical harmonic coefficients of the gravity model, that are not able to capture small spatial scales. Moreover, Mercury has shorter orbit than other planets and hence, it experiences several (approximately three) superior conjunctions in one Earth year. During the conjunction period, one can expect severe degradations in the signals (see Chapter 4). However, because of the high dispersion in the residuals, the corona impact on the residuals is not clearly visible.

Nevertheless, it is worth to note that computed range bias (one per arc for ranging measurements) for INPOP10e were still useful for improving the planetary ephemeris. As one can see on Figure 5.6 and Table 5.5, the ephemeris INPOP12a newly fitted over these observations, improved the Earth-Mercury distance by a factor 2 during the observational period. However, the dispersion in the range bias is still 10 times greater than the required accuracy. The differences between INPOP10e and INPOP12a ephemerides in terms of Earth-Mercury distances are plotted on panel *e* of the same figure. One can see that, MESSENGER observations (which is the only difference between these two ephemerides construction) can cause up to 4km differences in the Earth-Mercury distances over the time period of  $\sim 50$  years.

### 5.3.3.2 Case II: New Mercury orientation model and INPOP12b

#### 5.3.3.2.1 Description

In this case, to reconstruct the MESSENGER orbit and to initialize the iteration, initial position and velocity vectors of MESSENGER were deduced from the previous solution and the positions and velocities of the planets were accessed through the newly fitted ephemeris INPOP12a (see Figure 5.5). In addition to these changes, a new model of Mercury orientation (Margot, 2009) has been implemented in the GINS. The previous orientation model for Mer-

---



Table 5.5: Statistics of the residuals obtained for Case I, i) postfit Doppler and range residuals, ii) prefit (INPOP10e) and postfit (INPOP12a) range bias.

Residuals type	Value **	Required accuracy (Srinivasan et al., 2007)
2-, and 3-way Doppler	$-0.3 \pm 16.3$ mHz	$< 0.1$ mm/s ( $\sim 5.7$ mHz*)
2-way Range	$-0.002 \pm 8$ m	$< 3$ m
1-way range bias, INPOP10e	$161 \pm 249$ m	$< 10$ m
1-way range bias, INPOP12a	$181 \pm 102$ m	$< 10$ m

\* 2/3-way:  $1 \text{ mHz} = 0.0178 \text{ mm/s} = 0.5 \times \text{speed of light} / \text{X-band frequency}$ .

\*\*  $\text{mean} \pm 1\text{-}\sigma$  dispersion of the rms values

Table 5.6: Recommended model for the orientation of Mercury (Margot, 2009).

Parameter	value	
$\alpha_0 =$	$281.0097 - 0.0328T$	
$\delta_0 =$	$61.4143 - 0.0049T$	
$W =$	$329.75 + 6.1385025d$ $+ 0.00993822 \sin(M1)$ $-0.00104581 \sin(M2)$ $-0.00010280 \sin(M3)$ $-0.00002364 \sin(M4)$ $-0.00000532 \sin(M5)$	Angles are expressed in degrees, and T and d are defined as in Table 5.4.
where	$M1 = 174.791086 + 4.092335d$ $M2 = 349.582171 + 8.184670d$ $M3 = 164.373257 + 12.277005d$ $M4 = 339.164343 + 16.369340d$ $M5 = 153.955429 + 20.461675d$	

cury was inadequate because it uses an obsolete spin orientation, neglects oscillations in the spin rate called longitude librations, and relies on a prime meridian that no longer reflects its intended dynamical significance (Margot, 2009). These effects induce positional errors on the surface of  $\sim 2.5$  km in latitude and up to several km in longitude (e.g, see Figure 5.7). The Margot (2009) updated orientation model incorporates modern values of the spin orientation, includes non-zero obliquity and librations, and restores the dynamical significance to the prime meridian. The characteristics of this model is given in Table 5.6. The gravity model used for this computations is the one used for previous solution (i.e, HgM001).

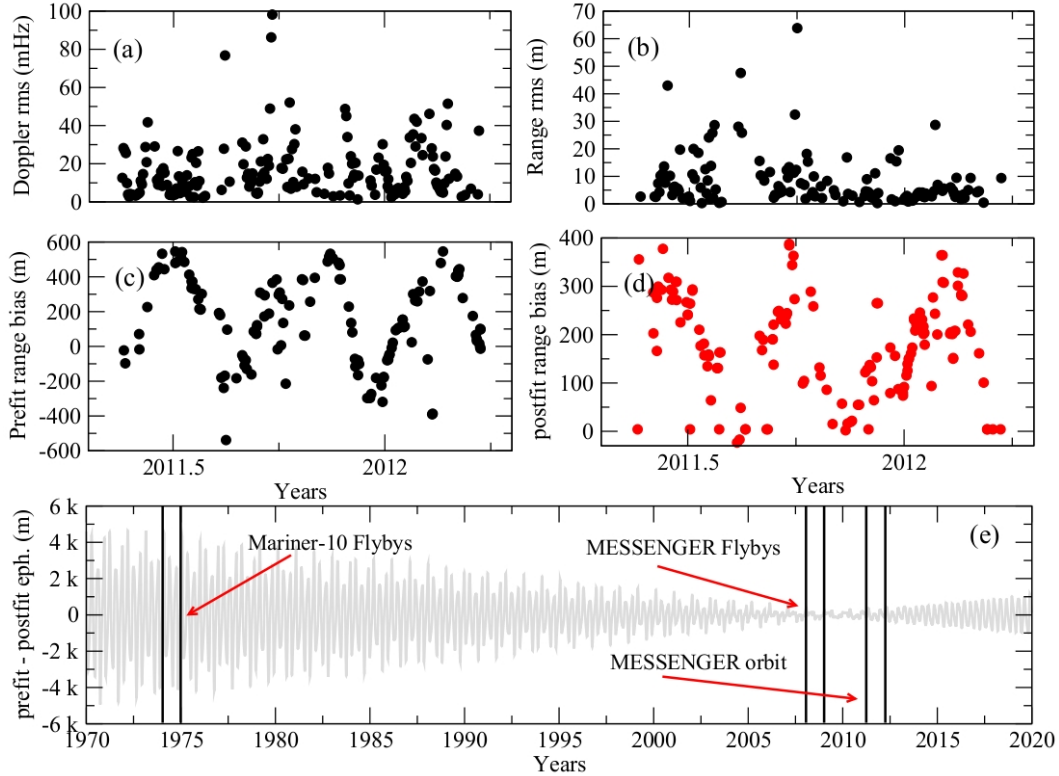


Figure 5.6: Case 1: (a) rms values of the postfit two- and three-way Doppler residuals for each one-day data-arc, (b) rms values of the postfit two-way range residuals for each one-day data-arc, (c) range bias (prefit) correspond to INPOP10e, (d) range bias (postfit) correspond to newly fitted INPOP12a ephemeris, and (e) difference in the Mercury-Earth geometric distances between INPOP10e and INPOP12a ephemerides. The indicated area are intervals of time corresponding to Mariner 10 and MESSENGER observations.

### 5.3.3.2.2 Results

On Table 5.7, statistics and comparison of the obtained results are given. From this table and the Figure 5.8 (similar to 5.6) one can see that, because of the same gravity model, discrepancies in the residuals are similar to the Case I. These discrepancies are about  $\sim 3$ ,  $\sim 2.5$ , and  $\sim 6$  times larger compared to the required values of Doppler, range, and range bias residuals, respectively. However, [Margot \(2009\)](#) orientation model of Mercury removed the systematic trend in the range bias (see Figure 5.6) and reduced the dispersion up to 29 m in the INPOP12a range bias.

Moreover, on panel *d* of Figure 5.8, one can noticed that, the newly fitted ephemeris INPOP12b shows a clear offset of about 190 m with a dispersion of about 56 m. This offset can be explained from the transponder delay, which was not taken in account during the orbit construction of MESSENGER. This offset with  $1\sigma$  of dispersion is however compatible with the transponder delay that was measured on the ground (see Section 5.4 for more detailed analy-

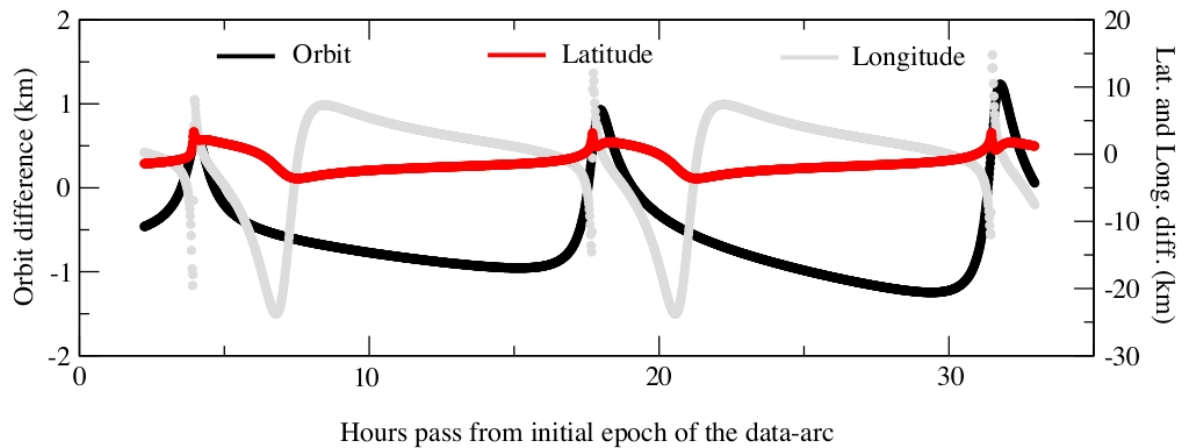


Figure 5.7: An example for the change of MESSENGER orbit characteristics due to [Margot \(2009\)](#) Mercury orientation model. The differences are plotted with respect to IAU 1996 Mercury orientation model.

sis), calibrated from 1,356.89 ns ( $\sim 407$  m) to 1,383.74 ns ( $\sim 415$  m) depending on the radio frequency configuration (transponder, solid-state power amplifiers, and antenna configuration) ([Srinivasan et al., 2007](#)). Thus, such compatibility of the ephemeris offset with the measured transponder delay suggests that, there is not a large error included in the spacecraft and in the planetary orbit fit procedure. Moreover, on panel *e* of Figure 5.8, are plotted the Earth-Mercury distance differences between INPOP12a and INPOP12b. The change in the Mercury orientation model brought up to 2km of differences in the Earth-Mercury distances over the time period of  $\sim 50$  years.

Table 5.7: Statistics of the residuals obtained for Case II, i) postfit Doppler and range residuals, ii) prefit (INPOP12a) and postfit (INPOP12b) range bias.

Residuals type	Value** (mean $\pm$ rms)	Required accuracy ( <a href="#">Srinivasan et al., 2007</a> )
2-, and 3-way Doppler	$-0.01 \pm 15.6$ mHz	$< 0.1$ mm/s ( $\sim 5.7$ mHz*)
2-way Range	$-0.04 \pm 7.6$ m	$< 3$ m
1-way range bias, INPOP12a	$195 \pm 73$ m	$< 10$ m
1-way range bias, INPOP12b	$189 \pm 56$ m	$< 10$ m

\* 2/3-way:  $1 \text{ mHz} = 0.0178 \text{ mm/s} = 0.5 \times \text{speed of light} / \text{X-band frequency}$ .

\*\* mean $\pm 1\text{-}\sigma$  dispersion of the rms values

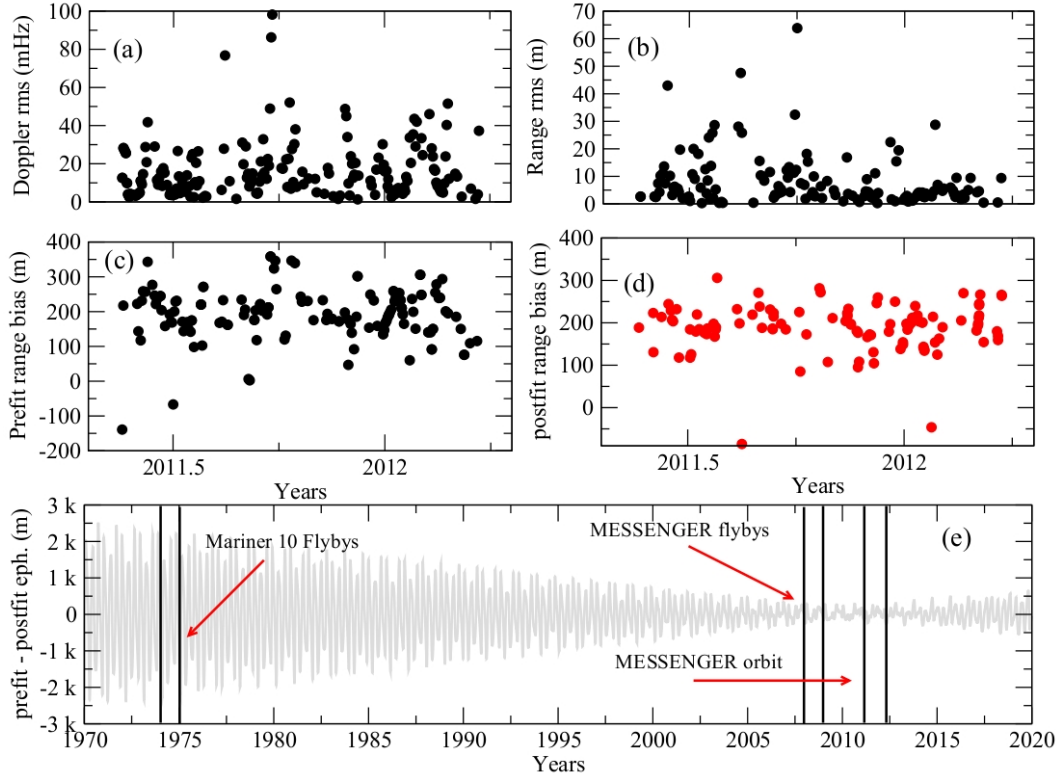


Figure 5.8: Case II: (a) rms values of the postfit two- and three-way Doppler residuals for each one-day data-arc, (b) rms values of the postfit two-way range residuals for each one-day data-arc, (c) range bias (prefit) correspond to INPOP12a, (d) range bias (postfit) correspond to newly fitted INPOP12b ephemeris, and (e) difference in the Mercury-Earth geometric distances between INPOP12a and INPOP12b ephemerides. The indicated area are intervals of time corresponding to Mariner 10 and MESSENGER observations.

### 5.3.3.3 Case III: Group delay and INPOP12c

#### 5.3.3.3.1 Description

Similarly to the previous case, to reconstruct the MESSENGER orbit and to initialize the iteration, initial position and velocity vectors of MESSENGER were deduced from the old solution (Case II) and the positions and velocities of the planets were accessed through the newly fitted ephemeris INPOP12b (see Figure 5.5). The gravity model and the Mercury orientation model used for this computation are the one used for the previous solution. However, a mean value of 1,371 ns (Srinivasan et al., 2007) has been implemented in GINS as a transponder delay for range measurements.

### 5.3.3.3.2 Results

Table 5.8: Statistics of the residuals obtained for Case III, i) postfit Doppler and range residuals, ii) prefit (INPOP12b) and postfit (INPOP12c) range bias.

Residuals type	Value <sup>**</sup> (mean±rms)	Required accuracy (Srinivasan et al., 2007)
2-, and 3-way Doppler	-0.01±16 mHz	< 0.1 mm/s (~5.7 mHz <sup>*</sup> )
2-way Range	0.02±6.9 m	< 3 m
1-way range bias, INPOP12b	8±50 m	< 10 m
1-way range bias, INPOP12c	9±48 m	< 10 m

<sup>\*</sup> 2/3-way: 1 mHz = 0.0178 mm/s = 0.5×speed of light / X-band frequency.

<sup>\*\*</sup> mean±1- $\sigma$  dispersion of the rms values

MESSENGER orbit is mainly constrained by the Doppler observations which describing the range rate between the spacecraft and the ground station. Therefore, as expected, a constant transponder delay did not affect the MESSENGER orbit, thus there is no significant change in the Doppler postfit residuals as compared to Case II (see Table 5.8). In contrast, the time delay due to the ranging transponder directly affects the light time and adds additional bias in the range observables.

The range bias estimation relies on all the range observations of the data-arc. This range bias is related to the onboard range devices themselves (transponder in this case) and to the expected error of ephemerides. Therefore, one can noticed that on Figure 5.9 and on Table 5.8, new estimations of range bias are dramatically different from the Case II. The offset in the range bias of about 190 m found for INPOP12b (see Section 5.3.3.2) is thus almost removed in the new estimation of range bias. Forthwith, the new ephemeris INPOP12c fitted over these range bias has an offset of about 9 m with the dispersion of about 50 m. Moreover, on panel *e* of Figure 5.9, are plotted the Earth-Mercury distance differences between INPOP12b and INPOP12c. The implementation of the transponder delay brought up to 300 m of differences in the Earth-Mercury distances over the time period of ~50 years.

### 5.3.3.4 Case IV: New gravity field HgM002 and INPOP12d

#### 5.3.3.4.1 Description

The radioscience data are significantly important to improve our knowledge of Mercury gravity

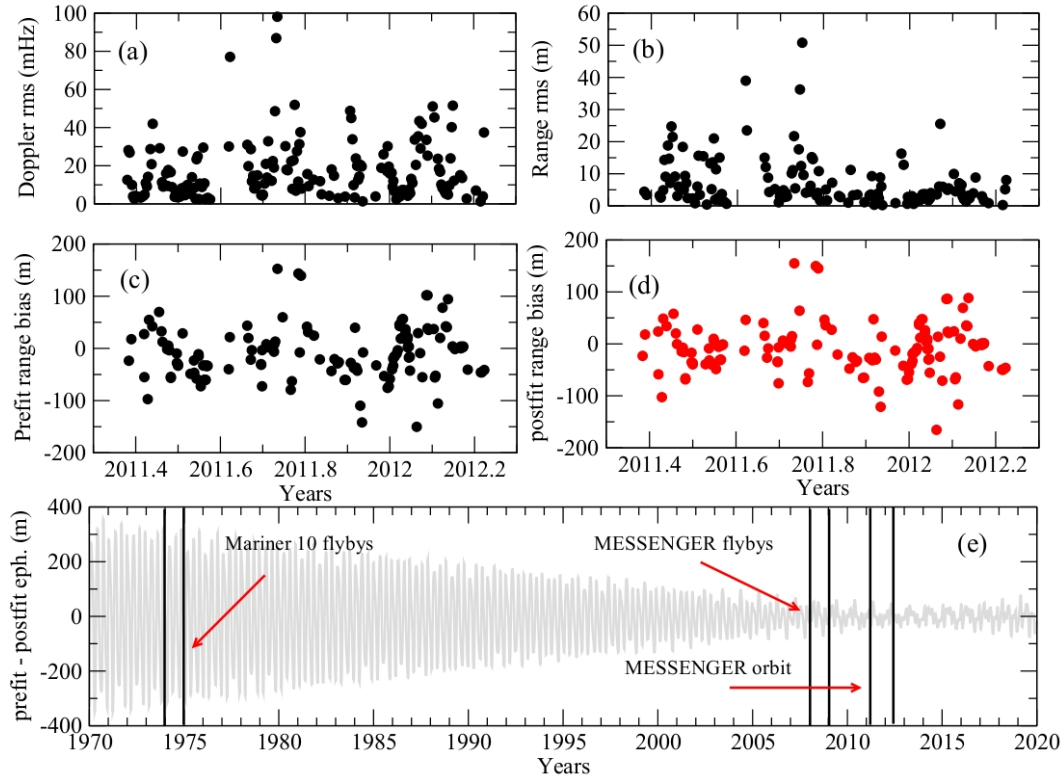


Figure 5.9: Case III: (a) rms values of the postfit two- and three-way Doppler residuals for each one-day data-arc, (b) rms values of the postfit two-way range residuals for each one-day data-arc, (c) range bias (prefit) correspond to INPOP12b, (d) range bias (postfit) correspond to newly fitted INPOP12c ephemeris, and (e) difference in the Mercury-Earth geometric distances between INPOP12b and INPOP12c ephemerides. The indicated area are intervals of time corresponding to Mariner 10 and MESSENGER observations.

field and its geophysical properties. Using the first six months of radioscience data of the orbital period, (Smith et al., 2012) computed the gravity field and the internal structure (density distribution) of Mercury. This updated gravity field solution is crucial for the precise computation of MESSENGER orbit and also to perform precise relativistic tests. In this case, the spherical harmonic model (Smith et al., 2012) of Mercury gravity field HgM002<sup>5</sup> developed up to degree and order 20 has been implemented in GINS. The initial conditions for MESSENGER, and the positions and velocities of the planets were taken from the case III (see Figure 5.5).

### 5.3.3.4.2 Results

The spherical harmonic model HgM002 of degree and order 20, gave a strong constraint to the MESSENGER orbit. Thanks to HgM002 model, we are then able to construct a very pre-

<sup>5</sup><http://pds-geosciences.wustl.edu/missions/messenger/rs.htm>

Table 5.9: Statistics of the residuals obtained for Case IV, i) postfit Doppler and range residuals, ii) prefit (INPOP12c) and postfit (INPOP12d) range bias.

Residuals type	Value <sup>**</sup> (mean±rms)	Required accuracy (Srinivasan et al., 2007)
2-, and 3-way Doppler	-0.002±5.0 mHz	< 0.1 mm/s (~5.7 mHz <sup>*</sup> )
2-way Range	-0.002±1.7 m	< 3 m
1-way range bias, INPOP12c	1.8±17 m	< 10 m
1-way range bias, INPOP12d	0.7±7.5 m	< 10 m

<sup>\*</sup> 2/3-way: 1 mHz = 0.0178 mm/s = 0.5×speed of light / X-band frequency.

<sup>\*\*</sup> mean±1- $\sigma$  dispersion of the rms values, excluding solar corona

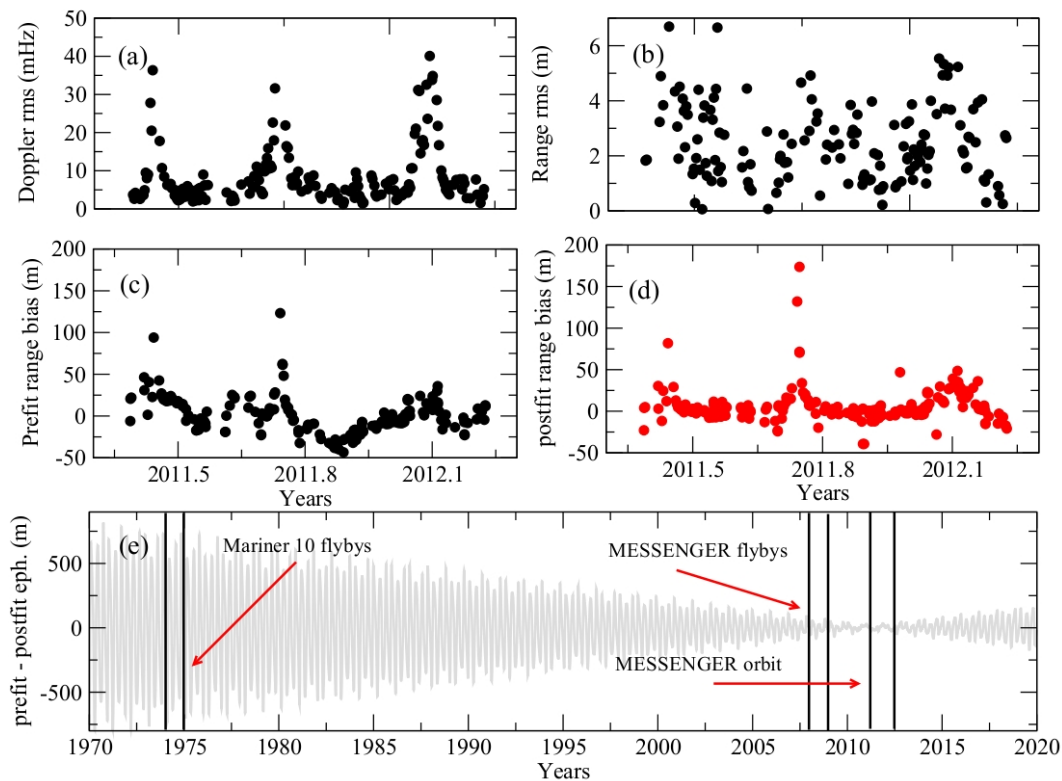


Figure 5.10: Case IV: (a) rms values of the postfit two- and three-way Doppler residuals for each one-day data-arc, (b) rms values of the postfit two-way range residuals for each one-day data-arc, (c) range bias (prefit) correspond to INPOP12c, (d) range bias (postfit) correspond to newly fitted INPOP12d ephemeris, and (e) difference in the Mercury-Earth geometric distances between INPOP12c and INPOP12d ephemerides. The indicated area are intervals of time corresponding to Mariner 10 and MESSENGER observations.

cise orbit of MESSENGER and then of Mercury. As one can see on Figure 5.10 and Table 5.9, the rms values of postfit Doppler and range residuals are  $\sim 3$  times smaller with almost zero mean values compared to the one found with HgM001 gravity model. Because of such accuracy in the orbit computation, one can easily disentangle the impact of the solar corona on the observations (peaks on Figure 5.10). As one can noticed from Table 5.9, the estimated rms values of the Doppler and range residuals, excluding superior solar conjunction periods, are compatible with the required accuracy of about 0.1 mm/s and 3 m, respectively (Srinivasan et al., 2007). Moreover, we have also adjusted Doppler offsets per arc and per DSN station (participating in the data-arc) accounting for the systematic errors generated by the devices at each tracking station. As expected, the fitted values for each DSN station tracking pass is of the order of a few tenths of mHz, which is lower than the Doppler postfit residuals for each data-arc. No large offset was then detected in the modeling of the Doppler shift measurements at each tracking station.

As a consequence of the precise MESSENGER orbit, the dispersion in the range bias estimated for INPOP12c is almost 30 m less than the one found with previous estimations (see Figure 5.10 and Table 5.9). The new ephemeris INPOP12d fitted over these range bias has an offset of about 7.5 m with a mean value less than meter. Such accuracy in the range bias also shows the compatibility with the required accuracy of about 10 m. Further improvements in the range bias however may be limited by the uncalibrated transponder time delays due to either temperature variations or electronic perturbations from other devices. On panel *e* of Figure 5.10, are plotted the Earth-Mercury distance differences between INPOP12c and INPOP12d. The improvement of the MESSENGER orbit can lead up to 500 m of changes in the Earth-Mercury distances. The accuracy of Mercury orbit depends then upon the quality of the range bias.

### 5.3.3.5 Case V: Extension of the mission and INPOP13a

#### 5.3.3.5.1 Description

As stated before, on March 2012, the MESSENGER mission was extended to one or more years. Therefore, in the construction of the latest INPOP13a ephemeris, we have analyzed all available MESSENGER radioscience data, including one year of prime phase and six months of extended phase. The analysis was performed in the same manner as for previous cases.

#### 5.3.3.5.2 Results

During the extended phase of the mission, MESSENGER was placed in an  $\sim 8$ -hour orbit to conduct further scans of Mercury by significantly tuned the apoapsis altitude of MESSENGER (e.g, see Figure 5.4). As described in Section 5.3.1, this change in the orbit significantly altered the acceleration budget of the MESSENGER spacecraft (see Table 5.3). On figure 5.11, are plotted the rms values of the postfit Doppler and range residuals for both phases. Statistics of

---



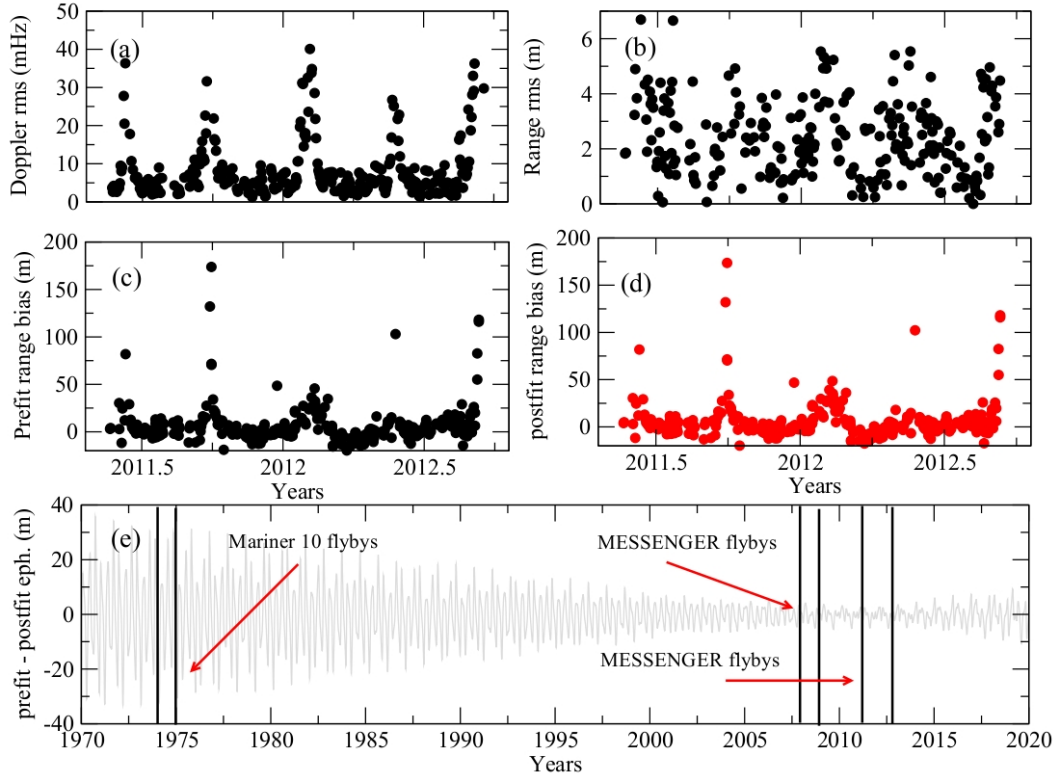


Figure 5.11: Case V: (a) rms values of the postfit two- and three-way Doppler residuals for each one-day data-arc, (b) rms values of the postfit two-way range residuals for each one-day data-arc, (c) range bias (prefit) correspond to INPOP12d, (d) range bias (postfit) correspond to newly fitted INPOP13a ephemeris, and (e) difference in the Mercury-Earth geometric distances between INPOP12d and INPOP13a ephemerides. The indicated area are intervals of time corresponding to Mariner 10 and MESSENGER observations.

Table 5.10: Statistics of the residuals obtained for Case V , i) postfit Doppler and range residuals, ii) prefit (INPOP12d) and postfit (INPOP13a) range bias.

Residuals type	Value** (mean±rms)	Required accuracy (Srinivasan et al., 2007)
2-, and 3-way Doppler	-0.00063±4.8 mHz	< 0.1 mm/s (~5.7 mHz*)
2-way Range	-0.003±1.5 m	< 3 m
1-way range bias, INPOP12d	0.6±8.0 m	< 10 m
1-way range bias, INPOP13a	-0.4±8.4 m	< 10 m

\* 2/3-way: 1 mHz = 0.0178 mm/s = 0.5×speed of light / X-band frequency.

\*\* mean±1-σ dispersion of the rms values, excluding solar corona

these residuals are similar to the Case IV and given on Table 5.10. These residuals and estimated range bias are comparable with the required accuracy for MESSENGER, hence confirmed that there is no large error included in the spacecraft dynamical modeling, and in the planetary orbit fit procedure.

### 5.3.3.5.3 Comparisons

To check the quality of MESSENGER orbit in terms of postfit Doppler and range residuals, we compared our estimation with the ones found in the literature (Genova et al., 2013; Smith et al., 2012). On Figure 5.12, are plotted the estimated mean and 1-sigma values of postfit residuals for each measurement types. These values are obtained separately for each data arc. Typical mean and rms values of the postfit Doppler, and two-way range residuals are estimated of about  $-0.00063 \pm 4.8$  mHz<sup>6</sup>, and  $-0.003 \pm 1.5$  m, respectively.

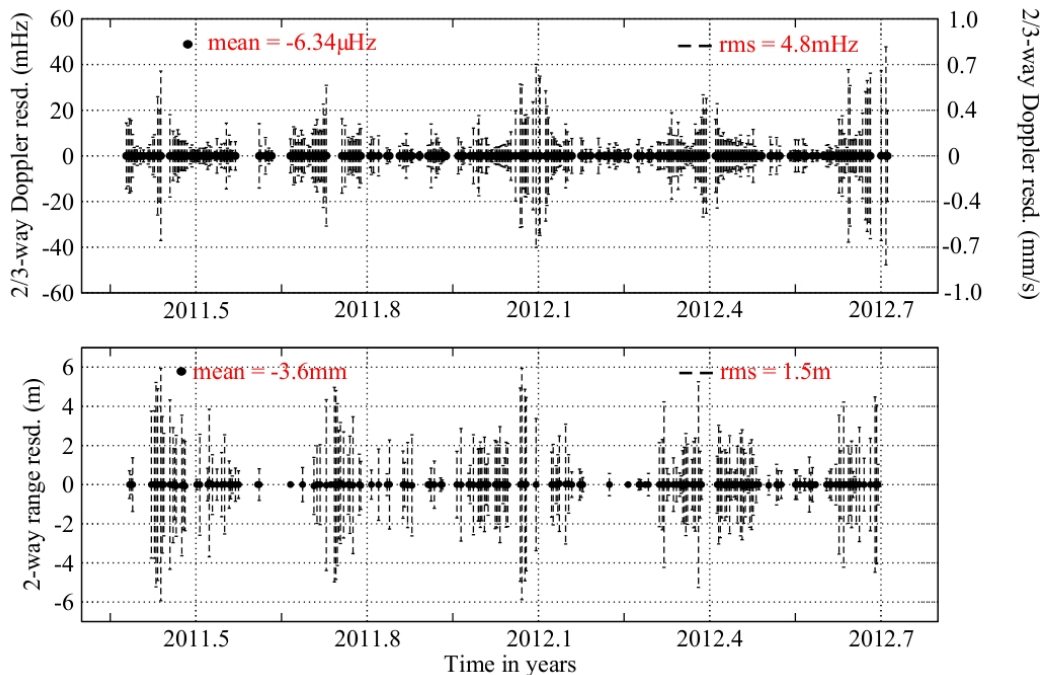


Figure 5.12: Mean and rms values of the postfit Doppler and range residuals, estimated for each data-arc.

On Table 5.11, are presented the comparisons. Our estimations are comparable with Smith et al. (2012) and Genova et al. (2013). These authors, however only used the first six months of orbital data for their computations. Our estimations are very close to the one found by Genova et al. (2013). However, comparatively high uncertainties in our Doppler residuals (of about 1.2 mHz) can be explained from the adjusted parameters. In addition to our adjustment, Genova

<sup>6</sup>2/3-way: 1 mHz = 0.0178 mm/s = 0.5×speed of light / X-band frequency

Table 5.11: Comparisons of postfit residuals between different authors.

Author	Doppler	Range
This chapter	$-0.00063 \pm 4.8$ mHz	$-0.003 \pm 1.5$ m
<a href="#">Genova et al. (2013)</a>	$-0.00088 \pm 3.6$ mHz	$-0.06 \pm 1.87$ m
<a href="#">Smith et al. (2012)</a>	$0.4 \pm 2.0^*$ mm/s	-

\* 2/3-way:  $1 \text{ mHz} = 0.0178 \text{ mm/s} = 0.5 \times \text{speed of light} / \text{X-band frequency}$ .

[et al. \(2013\)](#) also adjusted the Mercury gravity field up to degree 20, scale factors for albedo and infrared radiation pressure, and empirical delta accelerations for accounting the OCM. Such improved dynamical model could explain the better uncertainties in the [Genova et al. \(2013\)](#) residuals.

#### 5.3.3.5.4 INPOP13a ephemeris

One of the main objective of this work is to improve the planetary ephemerides. Range bias

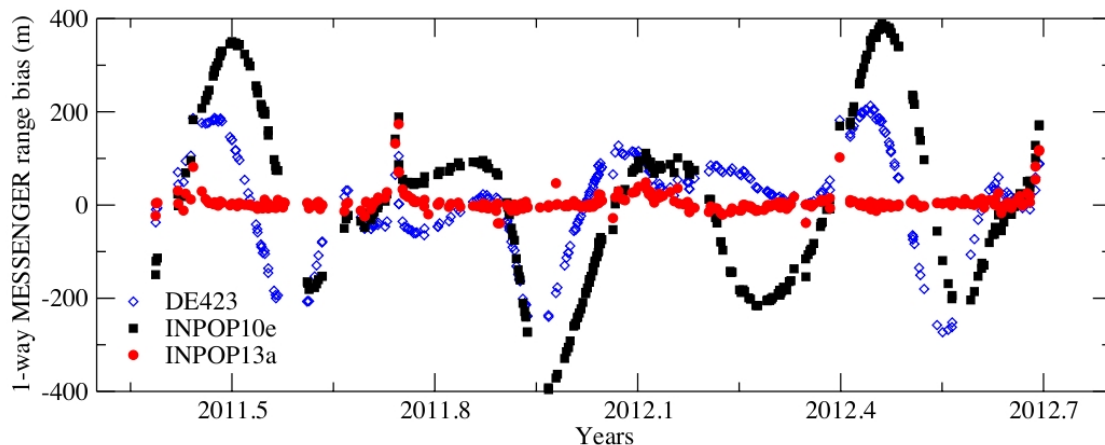


Figure 5.13: MESSENGER one-way range residuals obtained with INPOP13a, INPOP10a and DE423.

computed during the Case V are then used to further refinement of planetary ephemeris, especially of the Mercury orbit. The newly fitted planetary ephemeris INPOP13a showed postfit residuals in the Earth-Mercury distances of  $-0.4 \pm 8.4$  m excluding solar corona period, which is two order of improvement than any recent planetary ephemerides (e.g INPOP10e ( $21 \pm 187$  m) and DE423 ( $15 \pm 105$  m), see Figure 5.13 and Section 5.4). Moreover, as discussed in Section 5.4, over longer intervals of time, INPOP13a is consistent with the DE423 ephemerides and

improved the internal accuracy of INPOP by a factor two on the geocentric distances. Furthermore, to understand the impact of six months complementary data of the extended phase over the Mercury orbit, on panel *e* of Figure 5.11, are plotted the Earth-Mercury distance differences between INPOP12d and INPOP13a ephemerides. The additional data of the extended phase indeed gave small constraints to  $\sim 0.3$  Earth year of Mercury orbit, and brought up to 20 m of differences in the Earth-Mercury distances over the time period of  $\sim 50$  years.

As a scientific exploitation of these results, such high precision planetary ephemeris INPOP13a allowed us to perform several tests. The detailed analysis of these tests are described in the Section 5.4. An example of such tests are: (a) Impact of planetary ephemeris over the MESSENGER orbit, and (b) GR tests of PPN-formalism and its impact over the MESSENGER orbit.

- (a) The geometric distances between the Earth and Mercury are  $\sim 16$  times ameliorated in INPOP13a compared to INPOP10e. To analyze the impact of the improvement of the planetary ephemeris over the spacecraft orbit, we reanalyzed the entire one and half year of radioscience data using INPOP10e ephemeris. The dynamical modeling and the orbit determination process accounted for performing this analysis are the same as used for Case V. The improvement in the Mercury ephemeris however brought negligible variations in the MESSENGER orbit. The differences between the two solutions, one obtained with INPOP10e and other with INPOP13a, in the rms postfit Doppler and range residuals were estimated as  $0.008 \pm 0.04$  mHz, and  $0.05 \pm 0.3$  m, respectively. These values are however far below compared to the estimated accuracy of 4.8 mHz, and 1.5 m respectively.
- (b) GR tests of PPN-formalism were also performed with INPOP13a. Because of the high precision Mercury ephemeris, our estimations of the PPN parameters are most stringent than previous results. We considered the 5, 10 and 25% of changes in the postfit residuals compared to INPOP13a. These changes in the postfit residuals are then used to estimate the possible violation of two relativistic parameters ( $\gamma$  and  $\beta$ ) of the PPN formalism of GR. This analysis shows ten times smaller uncertainty in the estimation of  $\beta$  and  $\gamma$  than our previous results with INPOP10a or INPOP08. Moreover, one of the best estimation of the parameter  $\gamma$  by Bertotti et al. (2003) is compatible with our 25% of estimation.

## 5.4 Verma et al. (2014)

# Use of MESSENGER radioscience data to improve planetary ephemeris and to test general relativity

A. K. Verma<sup>1,2</sup>, A. Fienga<sup>3,4</sup>, J. Laskar<sup>4</sup>, H. Manche<sup>4</sup>, and M. Gastineau<sup>4</sup>

<sup>1</sup> Observatoire de Besançon, UTINAM-CNRS UMR6213, 41bis avenue de l'Observatoire, 25000 Besançon, France  
e-mail: ashok@obs-besancon.fr

<sup>2</sup> Centre National d'Études Spatiales, 18 avenue Édouard Belin, 31400 Toulouse, France

<sup>3</sup> Observatoire de la Côte d'Azur, GéoAzur-CNRS UMR7329, 250 avenue Albert Einstein, 06560 Valbonne, France

<sup>4</sup> Astronomie et Systèmes Dynamiques, IMCCE-CNRS UMR8028, 77 Av. Denfert-Rochereau, 75014 Paris, France

Received 24 June 2013 / Accepted 7 November 2013

## ABSTRACT

The current knowledge of Mercury's orbit has mainly been gained by direct radar ranging obtained from the 60s to 1998 and by five Mercury flybys made with Mariner 10 in the 70s, and with MESSENGER made in 2008 and 2009. On March 18, 2011, MESSENGER became the first spacecraft to orbit Mercury. The radioscience observations acquired during the orbital phase of MESSENGER drastically improved our knowledge of the orbit of Mercury. An accurate MESSENGER orbit is obtained by fitting one-and-half years of tracking data using GINS orbit determination software. The systematic error in the Earth-Mercury geometric positions, also called range bias, obtained from GINS are then used to fit the INPOP dynamical modeling of the planet motions. An improved ephemeris of the planets is then obtained, INPOP13a, and used to perform general relativity tests of the parametrized post-Newtonian (PPN) formalism. Our estimations of PPN parameters ( $\gamma$  and  $\beta$ ) are more stringent than previous results.

**Key words.** ephemerides – celestial mechanics

## 1. Introduction

Mercury is the smallest and least explored terrestrial planet of the solar system. Mariner 10 was the first spacecraft to make three close encounters (two in 1974 and one in 1975) to this mysterious planet, and it provided most of our current knowledge of the planet until early 2008 (Smith et al. 2010). In addition to Mariner 10 flyby observations, ground-based radar measurements were the only observations to be used to study Mercury's gravity field and its physical structure (spherical body with slight flattening at the poles and a mildly elongated equator) (Anderson et al. 1987, 1996). In 2004, the National Aeronautics and Space Administration (NASA) launched a dedicated mission, Mercury Surface, Space ENvironment, GEOchemistry, and Ranging (MESSENGER), to learn more about this planet. MESSENGER made three close encounters (two in 2008 and one in 2009) to Mercury and became the first spacecraft to observe Mercury from its orbit.

Until now, MESSENGER has completed more than two years on orbit at Mercury. During the orbital period, radio tracking of MESSENGER routinely measured the Doppler and range observables at Deep Space Network (DSN) stations. These observables are important for estimating the spacecraft state vectors (position and velocity) and improving the knowledge of Mercury's gravity field and its geophysical properties (Srinivasan et al. 2007). Using the first six months of radioscience data during the orbital period, Smith et al. (2012) computed the gravity field and gave better constraints on the internal structure (density distribution) of Mercury. This updated gravity field becomes crucial for the present computation of MESSENGER orbit and for performing precise relativistic tests.

The primary objectives of this work are to determine the precise orbit of the MESSENGER spacecraft around Mercury using radioscience data and then to improve the planetary ephemeris INPOP (Fienga et al. 2008, 2009, 2011). The updated spacecraft and planetary ephemerides are then used to perform sensitive relativistic tests of the parametrized post-Newtonian (PPN) formalism (Will 1993, 2001, 2006).

Nowadays, spacecraft range measurements are the most accurate measurements used for constructing planetary ephemerides. These measurements cover approximately 56% of all INPOP data (Fienga et al. 2011) and impose strong constraints on the planet orbits and on the other solar system parameters, including asteroid masses. However, until now, only five flybys (two from Mariner 10 and three from MESSENGER) range measurements have been available for imposing strong constraints to Mercury's orbit (Fienga et al. 2011). Therefore, range measurements obtained by MESSENGER spacecraft during its mapping period are important for improving our knowledge of Mercury's orbit.

Moreover, high-precision radioscience observations also offered an opportunity to perform sensitive relativistic tests by estimating possible violation of the two relativistic parameters ( $\gamma$  and  $\beta$ ) of the Parametrized Post Newtonian (PPN) formalism of general relativity (GR) (Will 1993). The previous estimations of these parameters using different techniques and a different data set, can be found in (Bertotti et al. 2003; Müller et al. 2008; Pitjeva 2009; Williams et al. 2009; Manche et al. 2010; Konopliv et al. 2011; Fienga et al. 2011). However, because of Mercury's relatively high eccentricity and its close proximity to the Sun, its orbital motion provides one of the best solar system tests of GR (Anderson et al. 1997). In addition, Fienga et al. (2010, 2011)

**Table 1.** Summary of the Doppler and range tracking data used for orbit determination.

Mission phase	Begin date dd-mm-yyyy	End date dd-mm-yyyy	Number of 2-way Doppler	Number of 3-way Doppler	Number of range
Prime	17-05-2011	18-03-2012	2108980	184138	11540
Extended	26-03-2012	18-09-2012	1142974	23211	5709

also demonstrated, Mercury observations are far more sensitive to PPN modification of GR than other data used in the planetary ephemerides. We, therefore, also performed the test of GR with the latest MESSENGER observations to obtain one of the most precise value for PPN parameters.

In this paper, we introduce the updated planetary ephemeris INPOP13a and summarize the technique used for estimating the PPN parameters. The outline of the paper is as follows Sect. 2 discusses the radioscience data analysis of the MESSENGER spacecraft. The dynamic modeling of MESSENGER and the results obtained during orbit computation are also discussed in the same section. In Sect. 3, we discuss the construction of INPOP13a using the results obtained in Sect. 2. In Sect. 4, we discuss the gravitational tests using updated MESSENGER and Mercury ephemerides. Section 5 follows with conclusions and perspectives.

## 2. MESSENGER data analysis

Under NASA's Discovery program, the MESSENGER spacecraft is the first probe to orbit the planet Mercury. It was launched in August 3, 2004, from Pad B of Space Launch Complex 17 at Cape Canaveral Air Force Station, Florida, aboard a three-stage Boeing Delta II rocket. On March 18, 2011, MESSENGER successfully entered Mercury's orbit after completing three flybys of Mercury following two flybys of Venus and one of Earth (Solomon et al. 2007).

The MESSENGER spacecraft was initially inserted into a  $\sim 12$  h, near-polar orbit around Mercury, with an initial periastron altitude of 200 km, initial periastron latitude of  $60^\circ\text{N}$ , and apoapsis at  $\sim 15\,200$  km altitude in the southern hemisphere. After a successful first-year flight in this orbit, the mission was extended to one or more years which began on March 18 2012. During first extended mission, two orbit-correction maneuvers were executed, four days apart, in April 2012 to reduce MESSENGER's orbital period from  $\sim 12$  to  $\sim 8$  h (Flanigan et al. 2013).

The MESSENGER spacecraft was tracked by NASA's DSN stations at X-band frequency, 7.2 GHz for an uplink from the ground stations and 8.4 GHz for a downlink from the spacecraft. Communications were accomplished via the 34 m and 70 m antennas of DSN stations in Goldstone, CA; Madrid, Spain; and Canberra, Australia. MESSENGER's X-band tracking consists in measuring the round-trip time delay (two-way range) and the two- and three-way ramped Doppler shift of the carrier frequency of the radio link between the spacecraft and the DSN stations on Earth. The precision of the Doppler measurement for the radio frequency subsystem is within  $\pm 0.1$  mm/s over 10 s to several minutes of integration time (Srinivasan et al. 2007).

### 2.1. Data analysis and dynamic modeling

We have analyzed one-and-half years of tracking data collected by the DSN during the MESSENGER orbital period. These data belong to one year of the prime mission and six months of the first extended mission (see Table 1). The complete data set

that was used for the analysis is available on the Geoscience node<sup>1</sup> of the NASA's Planetary Data System (PDS). For precise orbit determination, all available observations were analyzed with the help of the Géodésie par Intégrations Numériques Simultanées (GINS) software, which was developed by the Centre National d'Études Spatiales (CNES) in collaboration with Royal Observatory of Belgium (ROB). GINS numerically integrates the equations of motion and the associated variational equations. It simultaneously retrieves the physical parameters of the force model using an iterative least-squares technique.

#### 2.1.1. Dynamic modeling and orbit determination processes

The precise orbit determination is based on a full dynamical approach. The dynamic modeling includes gravitational (gravitational attraction of Mercury, third-body gravity perturbations from the Sun and other planets, and relativistic corrections) and nongravitational (solar radiation pressure; Mercury radiation pressure) forces that are acting on the spacecraft. These forces have been taken into account in the force budget of MESSENGER. The latest spherical harmonic model (Smith et al. 2012) of Mercury's gravity field, HgM002<sup>2</sup> developed up to degree and order 20, and the associated Mercury's orientation model (Margot 2009) have been considered for precise computation.

The measurement (Doppler and range) models and the light time corrections that are modeled in GINS correspond to the formulation given by Moyer (2003). During computations, DSN station coordinates were corrected from the Earth's polar motion, from solid-Earth tides, and from the ocean loading. In addition to these corrections, radiometric data have also been corrected from tropospheric propagation through the meteorological data<sup>3</sup> (pressure, temperature, and humidity) of the stations.

The complex geometry of the MESSENGER spacecraft was treated as a combination of flat plates arranged in the shape of a box, with attached solar arrays, the so-called *Box-Wing* macro-model. The approximated characteristics of this macro-model, which includes cross-sectional area and specular and diffuse reflectivity coefficients of the components, were taken from (Vaughan et al. 2002). In addition to the macro-model characteristics, orientations of the spacecraft were also taken into account. The attitude of the spacecraft and of its articulated panels in inertial space were defined in terms of quaternions. The approximate value of these quaternions was extracted from the C-kernel<sup>4</sup> system of the SPICE Navigation and Ancillary Information Facility (NAIF) software. The macro-model and its orientation allowed calculation of the nongravitational accelerations that are acting

<sup>1</sup> <http://pds-geosciences.wustl.edu/messenger/>

<sup>2</sup> <http://pds-geosciences.wustl.edu/missions/messenger/rs.htm>

<sup>3</sup> [http://pds-geosciences.wustl.edu/messenger/mess-v\\_h-rss-1-edr-rawdata-v1/messrs\\_0xxx/ancillary/wea/](http://pds-geosciences.wustl.edu/messenger/mess-v_h-rss-1-edr-rawdata-v1/messrs_0xxx/ancillary/wea/)

<sup>4</sup> [ftp://naif.jpl.nasa.gov/pub/naif/pds/data/mess-e\\_v\\_h-spice-6-v1.0/messsp\\_1000/data/ck/](ftp://naif.jpl.nasa.gov/pub/naif/pds/data/mess-e_v_h-spice-6-v1.0/messsp_1000/data/ck/)

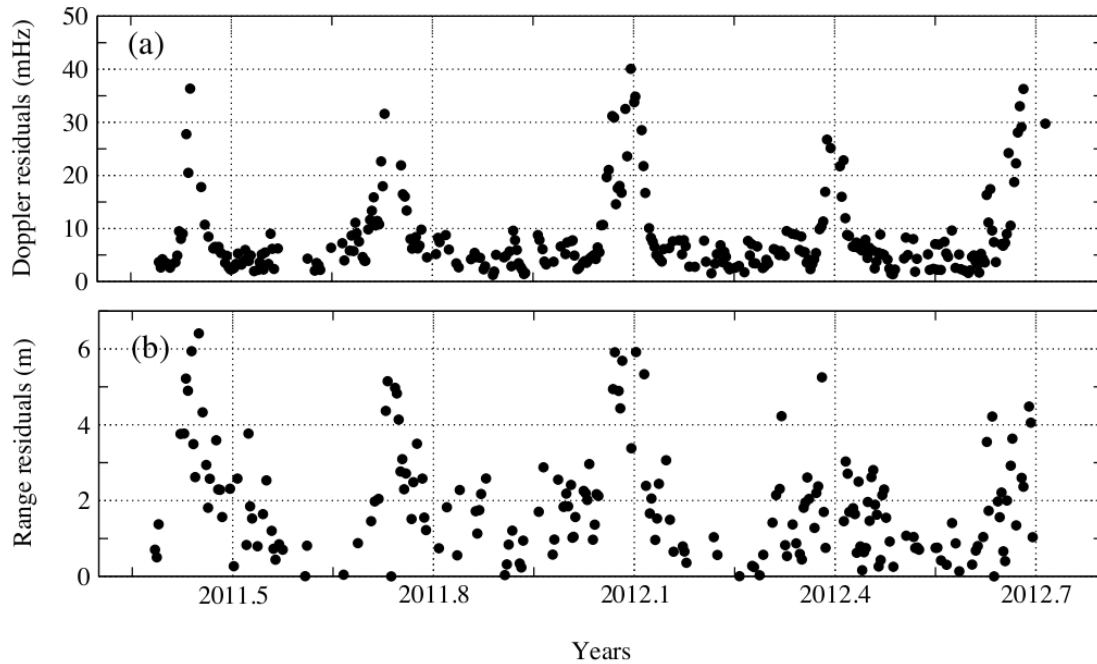


**Fig. 1.** Quality of the MESSENGER orbit in terms of rms values of the post-fit residuals for each one-day data arc: (a) two- and three-way Doppler given in millihertz (multiply by 0.0178 to obtain residuals in mm/s), and (b) two-way range given in meters.

on the MESSENGER spacecraft due to the radiation pressure from Sun and Mercury (albedo and thermal infrared emission).

For orbit computation and parameters estimation, a multi-arc approach was used to get independent estimates of the MESSENGER accelerations. In this method, we integrated the equations of motion using the time-step of 50 s then, and orbital fits were obtained from short data arcs fitted over the observations span of one day using an iterative process. The short data arcs of one day were chosen to account for the model imperfections. To initialize the iteration, the initial position and velocity vectors of MESSENGER were taken from the SPICE NAIF spk-kernels<sup>5</sup>.

### 2.1.2. Solve-for parameters

An iterative least-squares fit was performed on the complete set of Doppler- and range-tracking data arcs that correspond to the orbital phase of the mission using an INPOP10e (Fienga et al. 2013) planetary ephemeris<sup>6</sup>. We have processed data from May 17 2011 to September 18 2012 excluding the periods of the maneuvers. A summary of these tracking data is given in Table 1. MESSENGER fires small thrusters to perform momentum dump maneuver (MDM) for reducing the spacecraft angular momentum to a safe level. Normal operations (during orbital periods) includes only one commanded momentum dump every two weeks. In addition, orbit correction maneuvers (OCM) were also performed (typically once every Mercury year, 88 Earth days) to maintain the minimum altitude below 500 kilometers. Such large intervals between the MESSENGER maneuvers facilitate the orbit determination. The data arcs that correspond to the maneuver epochs are thus not included in the analysis. The total 440 one-day data arcs were then used for the analysis.

<sup>5</sup> [ftp://naif.jpl.nasa.gov/pub/naif/pds/data/mess-e\\_v\\_h-spice-6-v1.0/messsp\\_1000/data/spk/](ftp://naif.jpl.nasa.gov/pub/naif/pds/data/mess-e_v_h-spice-6-v1.0/messsp_1000/data/spk/)

<sup>6</sup> <http://www.imcce.fr/inpop/>

Several parameters were estimated during orbit computation: spacecraft state vectors at the start epoch of each data arc, for a total of  $440 \times 6 = 2640$  parameters; one scale factor per data arc for taking into account the mismodeling of the solar radiation force (total of 440 parameters); one Doppler bias per arc for each DSN station to account for the systematic errors generated by the devices at each tracking station (total of  $\sum_1^{440} 1 \times n$  parameters, where  $n$  is the number of stations participating in the data arc); one station bias per arc for each DSN station to account for the uncertainties on the DSN antenna center position or the instrumental delays (total of  $\sum_1^{440} 1 \times n$  parameters); and one range bias per arc for ranging measurements to account for the systematic geometric positions error (ephemerides bias) between the Earth and the Mercury (total of 440 parameters).

## 2.2. Orbit determination

### 2.2.1. Postfit residuals

The root mean square (rms) values of the post-fitted Doppler and range residuals give some indication about the quality of the orbit fit and the estimated parameters. Moreover, the quality of the used parameters associated to the physical model can also be judged from these residuals. Figure 1 illustrates the time history of the residuals estimated for each measurement type. In this figure, panel a represents the rms values of the two- and three-way Doppler residuals that were obtained for each data arc and are expressed in millihertz (mHz). As Mercury has shorter orbit than other planets, it experiences five superior conjunctions (when the Earth, the Sun and the spacecraft lie on the same line, with the spacecraft located on the opposite side of the Sun with respect to Earth) during the time interval covered by the analysis. Because of a lack of modelisation of the solar corona perturbations within the GINS software, no model of solar plasma was applied during the computations of the MESSENGER orbit. The peaks shown in Fig. 1, therefore, demonstrate the clear effect of

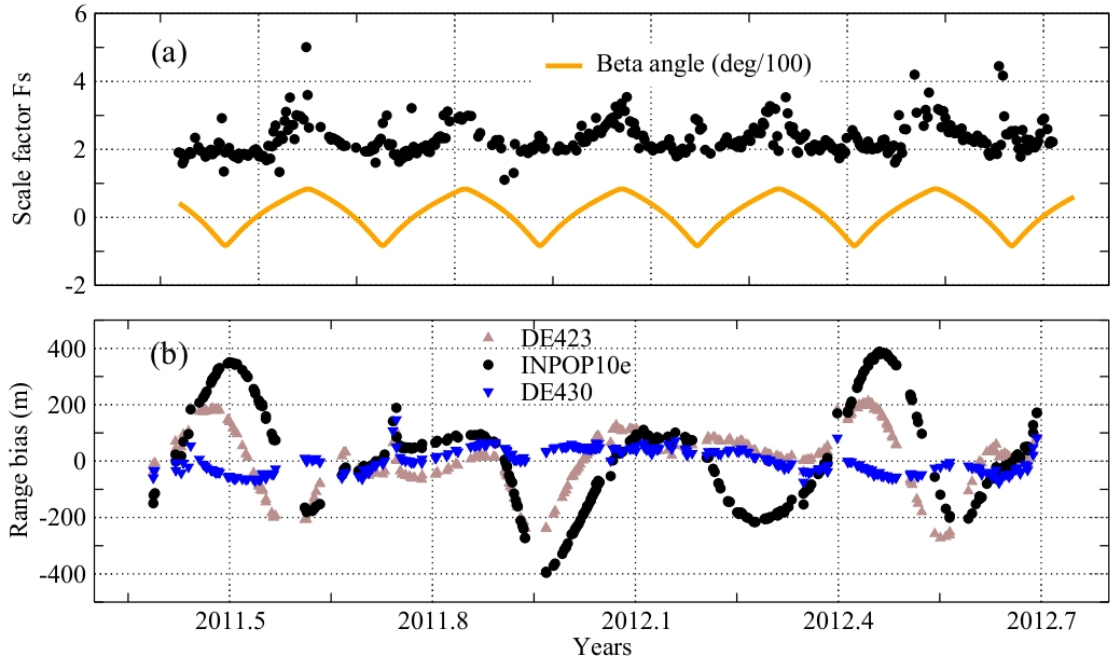


**Fig. 2.** History of the fitted scale factor and estimated range bias: **a)** scale factor (for solar radiation acceleration) fitted over each one-day data arc to account inaccuracy in the force model, and **b)** one-way range bias, represent the systematic error in the Earth-Mercury positions, estimated for each one-day arc using INPOP10e ( $\bullet$ ), DE423 ( $\blacktriangle$ ), and DE430 ( $\blacktriangledown$ ) planetary ephemerides.

the solar conjunctions on the typical fit to the Doppler and range data residuals.

Excluding the solar conjunction periods (about 100 data arcs), when Sun-Earth-Probe angle remained below  $10^\circ$ , an average value of Doppler residuals has been found to be approximately  $4.8 \pm 2.2$  mHz ( $\sim 0.09 \pm 0.04$  mm/s), which is comparable with values given by (Smith et al. 2012; Stanbridge et al. 2011; Srinivasan et al. 2007). The mean value of the estimated Doppler bias for each DSN station tracking pass was found to be very small (a few tenths of mHz), which is lower than the Doppler post-fit residuals for each data arc. It demonstrated that we have no large bias in the modeling of the Doppler shift measurements at each tracking station.

The range measurements were also used to assist in fitting the Doppler data for a precise orbit determination. Panel b of Fig. 1 represents the rms values of two-way range residuals that were obtained for each data arc. An average value of these range residuals is  $1.9 \pm 1.4$  m, which is comparable with the values given in Srinivasan et al. (2007).

### 2.2.2. Scale factor and range bias

We fitted one scale factor per data arc for the solar radiation force to account the inaccuracy in the force model. Panel a of Fig. 2 represents the time history of these scale factors. These scale factors are overplotted with the *beta angle*, which is the angle between MESSENGER orbital plane and the vector from the Sun direction. The variation in the MESSENGER orbital plane (beta angle) relative to the Sun occurs as Mercury moves around the Sun. For example, at  $10^\circ$ ,  $100^\circ$ , and  $180^\circ$  of Mercury's true anomaly, the corresponding beta angles are  $83^\circ$ ,  $0^\circ$ , and  $-78^\circ$ , respectively (Ercol et al. 2012). At  $0^\circ$  beta angle, the spacecraft travels directly between the Sun and the planet, while at  $90^\circ$ , the spacecraft is in sunlight 100% of the time. As one can see from

panel a of Fig. 2, the solar pressure coefficients have variations that approximately follow those of the beta angle. This implies that, whenever MESSENGER orbital plane approaches the maximum beta angle, it is fully illuminated by direct sunlight (no shadow affect). To protect the spacecraft from the direct sunlight, the automatic orientation of the solar panels therefore balances the need for power and the temperature of the surface of the panel. Thus, imperfection in the modeling of these orientations is then taken care of by the scale factor to reduce the error in the computation of solar radiation pressure (see Fig. 2). The fitted scale factor for solar radiation pressure is, therefore, typically in the range of about  $2.1 \pm 0.5$ . This value is nearly twice the a priori value and it reflects the imperfection in the force model due to the approximate representation of the macro-model.

Panel b of Fig. 2 illustrates the one-way range bias estimated for the ranging measurements for each data arc. These biases represent the systematic uncertainties in the Earth-Mercury geometric positions. The black ( $\bullet$ ), brown ( $\blacktriangle$ ) and blue ( $\blacktriangledown$ ) bullets in this figure correspond to INPOP10e (Fienga et al. 2013), DE423 (Folkner 2010), and DE430 (Williams et al. 2013), respectively. An average value of these range bias for INPOP10e, DE423 and DE430 is  $21 \pm 187$  m,  $15 \pm 105$  m, and  $-0.5 \pm 42$  m, respectively. This range bias is then used in the planetary ephemerides to fit the dynamical modeling of the planet motions (see Sect. 3). Thus, MESSENGER ranging measurements were used to reconstruct the orbit of Mercury around the Sun. The improved planetary ephemeris, INPOP13a (see Sect. 3.1) was then used to re-analyze the MESSENGER radiometric data to study the impact of planetary ephemeris over the computation of MESSENGER orbit and associated parameters (see Sect. 3.2).

### 2.2.3. Spacecraft transponder group delay calibration

Planetary ephemerides are a good tool for testing the gravity model and GR (Fienga et al. 2011) and performing solar corona



**Table 2.** Values of parameters obtained in the fit of INPOP13a and INPOP10e to observations including comparisons to DE423 and DE430.

	INPOP13a $\pm 1\sigma$	INPOP10e $\pm 1\sigma$	DE423 $\pm 1\sigma$	DE430 $\pm 1\sigma$
$(\text{EMRAT}-81.3000) \times 10^{-4}$	$(5.770 \pm 0.020)$	$(5.700 \pm 0.020)$	$(5.694 \pm 0.015)$	$(5.691 \pm 0.024)$
$J_2^\circ \times 10^{-7}$	$(2.40 \pm 0.20)$	$(1.80 \pm 0.25)$	1.80	$(2.1 \pm 0.7)$
$GM_\odot - 132712440000 \text{ [km}^3 \text{ s}^{-2}\text{]}$	$(48.063 \pm 0.4)$	$(50.16 \pm 1.3)$	40.944	41.94
$\text{AU} - 1.49597870700 \times 10^{11} \text{ [m]}$	9.0	9.0	$(-0.3738 \pm 3)$	0

studies (Verma et al. 2013). Moreover, it is also possible to calibrate the transponder group delay from the planetary ephemeris. The spacecraft receives and transmits the signal to the Earth station through the on-board transponder, which causes the time delay in the range measurements. This delay varies from one spacecraft to another depending on the radio frequency configuration. Usually an average value for this delay is measured at different occasions on the ground before launch. However, the group delay is not perfectly stable and can fluctuate by a few ns, depending upon variations in a number of parameters such as temperature and signal strength.

For MESSENGER, we estimated this group delay with the planetary ephemeris. This procedure becomes an alternate method of testing the procedure and quality of the orbit fit by comparing estimated group delay with the delay tested on the ground. Since the transponder delay does not affect the Doppler measurements we were therefore, able to compute the precise orbit of the spacecraft without considering the transponder delay in the range measurements. With this configuration, we then reanalyzed the entire radio tracking data (see Table 1). To check the precision on the knowledge of the spacecraft orbit, we compared the radial, along-track, and cross-track components of the orbit for each data arc with the solution obtained in Sect. 2.2.1. An average rms value of radial, along-track, and cross-track difference is 0.015 m, 0.16 m, and 0.19 m, respectively. Less than a meter level of differences in the orbit implies that the transponder delay has negligible impact on the orbit, since the spacecraft orbit is mostly constrained by the Doppler tracking data. However, there is a dramatic change in the estimation of range bias, which now includes ephemeris bias plus the bias due to the transponder delay. Using these range biases to fit the planetary ephemeris, we found a clear off-set in the Earth-Mercury geocentric distances of about  $410 \pm 20$  m (two-way) during the orbital period of the MESSENGER. This estimation of transponder delay is compatible with the one found during ground testing, which ranged from 1,356.89 ns ( $\sim 407$  m) to 1,383.74 ns ( $\sim 415$  m) (Srinivasan et al. 2007). Thus these results also suggested that there is not a large error in the spacecraft and the planetary orbit fit procedure.

### 3. Improvement of planetary ephemeris, INPOP

Since 2003, INPOP planetary ephemerides have been built on a regular basis and provided to users through the IMCCE website<sup>7</sup>. The INPOP10e ephemeris was the latest release (Fienga et al. 2013) that was delivered as the official Gaia mission planetary ephemerides used for the navigation of the satellite as well as for the analysis of the data. Specific developments and analysis were done for the Gaia release such as the TCB time-scale version or an accurate estimation of the INPOP link to ICRF. With the delivery of the MESSENGER radio science data, a new opportunity was offered to improve drastically our knowledge of

the orbit of Mercury and to perform tests of gravity at a close distance from the Sun.

The use of the 1.5 year range measurements deduced from the previous analysis (see Sect. 2) is then a crucial chance to obtain better knowledge over the  $\sim 0.3$  year Mercury orbit. The accuracy of a few meter for the MESSENGER range data will give big constraints over short period perturbations on Mercury's orbit. The five flyby positions obtained with Mariner and the MESSENGER flybys will still be significant for the measurements of long period (10 or more years) perturbations (see Fig. 8). Only the addition of the Bepi-Colombo range data will be able to disentangle such long period effects.

#### 3.1. INPOP13a

The constants and dynamical modeling used for constructing the new ephemerides, INPOP13a, are similar to INPOP10e. A complete adjustment of the planet initial conditions (including Pluto and the Moon), the mass of the Sun, the oblateness of the Sun, the ratio between the mass of the Earth and the Moon, and 62 asteroid masses is operated. Values of the obtained parameters are given in Tables 2 and 3. Even if Mercury is not directly affected by the main belt asteroids, the use of the range measurements between MESSENGER and the Earth does have an impact on the Earth's orbit and then could bring some information on asteroid masses perturbing the Earth orbit. On Table 3, we only gave the masses that are significantly different from those obtained with INPOP10e and inducing detectable signatures below five meters. These masses are also compared with the Konopliv et al. (2011) on the same table. The masses of the biggest objects differ from the two ephemerides inside their two-sigma error bars, and one can notice the new determination of the mass of (51) Nemausa inducing slightly bigger perturbations on Mercury (7 m) and Venus (8 m) geocentric distances than on Mars (5 m).

Table 4 gives the postfit residuals obtained with INPOP13a and compared with those obtained with INPOP10e. One can see a noticeable improvement in Mercury's orbit over all the periods of the fit including direct radar observations. The result is of course more striking for MESSENGER range measurements that were deduced from Sect. 2, and not used for the fit of INPOP10e. In this particular case, the improvement reaches a factor of almost 16 on the estimation of the distance between Mercury and the Earth (see Fig. 3). The extrapolated residuals given in Table 4 are not really significant since INPOP10e was fitted over a very similar interval of time ending at about 2010.4 when INPOP13a was fitted up to 2011.4.

Figure 4 plots the differences between INPOP13a, INPOP10e and DE423 for Mercury geocentric right ascension, declination, and distance, and the Earth-Moon barycenter longitudes, latitudes, and distances in the BCRS. These differences give estimations of the internal accuracy of INPOP13a. By comparison, the same differences between INPOP10a and DE421 are also plotted. They present the improvements

<sup>7</sup> [www.imcce.fr/inpop](http://www.imcce.fr/inpop)

**Table 3.** Asteroid masses obtained with INPOP13a, significantly different from values found in INPOP10e, and inducing a change in the Earth-planets distances smaller than 5 meters over the fitting interval.

IAU designation number	INPOP13a $10^{12} \times M_{\odot}$	INPOP10e $10^{12} \times M_{\odot}$	Konopliv et al. (2011) $10^{12} \times M_{\odot}$
1	$468.430 \pm 1.184$	$467.267 \pm 1.855$	$467.90 \pm 3.25$
2	$103.843 \pm 0.982$	$102.654 \pm 1.600$	$103.44 \pm 2.55$
9	$3.637 \pm 0.400$	$4.202 \pm 0.670$	$3.28 \pm 1.08$
15	$14.163 \pm 0.555$	$15.839 \pm 0.950$	$14.18 \pm 1.49$
16	$11.212 \pm 1.373$	$12.613 \pm 2.208$	$12.41 \pm 3.44$
19	$5.182 \pm 0.342$	$4.892 \pm 0.513$	$3.20 \pm 0.53$
46	$3.076 \pm 0.446$	$3.525 \pm 0.743$	–
51	$3.287 \pm 0.485$	$0.009 \pm 0.004$	–
65	$8.789 \pm 2.266$	$4.210 \pm 0.863$	–
78	$1.486 \pm 0.504$	$2.562 \pm 0.574$	–
105	$2.070 \pm 0.365$	$3.046 \pm 0.635$	–
106	$3.369 \pm 0.408$	$3.870 \pm 0.411$	–
134	$3.451 \pm 0.595$	$1.014 \pm 0.368$	–
194	$4.872 \pm 0.452$	$5.601 \pm 0.636$	–
324	$5.087 \pm 0.189$	$4.769 \pm 0.435$	$5.34 \pm 0.99$

**Notes.** The uncertainties are given at 1 published sigma and compared with Konopliv et al. (2011).

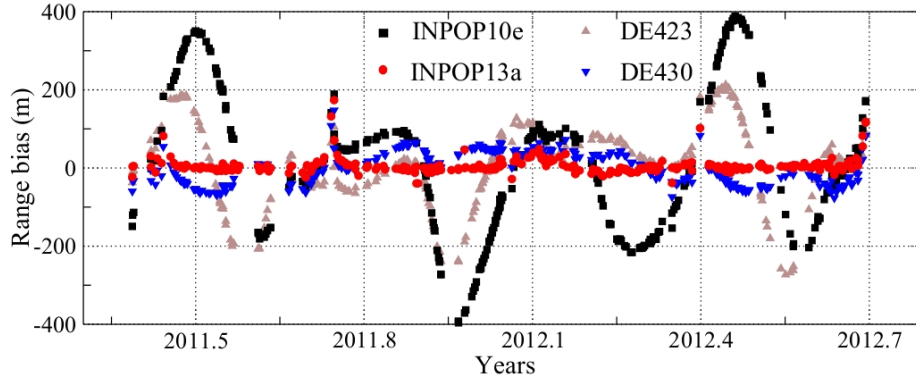


**Fig. 3.** MESSENGER one-way range residuals obtained with INPOP13a, INPOP10a, DE423, and DE430.

reached since INPOP10a, clearly noticeable for the Mercury geocentric distances (a factor two between INPOP13a-DE423 and INPOP10a-DE421). They are less impressive for the EMB; however, one can notice that the clear systematic trend in the INPOP10a-DE423 barycentric distances of the EMB is removed in INPOP13a-DE423. The fact that the differences between INPOP13a and INPOP10e are smaller than the differences to DE ephemerides is mainly discussed in Fienga et al. (2011) and Fienga et al. (2013) by a different method of computing the orbit of the Sun relative to the solar system barycenter, as well as a different distribution of planetary and asteroid masses.

In conclusion, INPOP13a shows an important improvement in the Mercury orbit especially during the MESSENGER orbital and flyby phases of the mission. The improvement over the EMB orbit in the BCRS is less important but still a systematic trend noticeable in the EMB barycentric distance differences between INPOP10a and DE421 seems to be removed in the new comparisons.

### 3.2. Reconstruction of MESSENGER orbit with INPOP13a

As given in Table 4, geometric distances between Earth and Mercury are  $\sim 16$  times better in INPOP13a than the INPOP10e. To analyze the impact of the improvement of the planetary ephemeris on the spacecraft orbit, we reanalyzed the entire

one and half years of radioscience data (see Table 1) using INPOP13a ephemeris. The dynamical modeling and orbit determination process for this analysis are the same as discussed in Sect. 2.1. To compare the results of this analysis with the one obtained from INPOP10e (see Sect. 2.2.1), the differences in the Doppler and range postfit residuals along with the changes that occurred in the periapsis and apoapsis altitudes of MESSENGER are plotted in Fig. 5.

An average value of these differences and its  $1\sigma$  mean dispersion for Doppler, and range postfit residuals was estimated as  $0.008 \pm 0.04$  mHz and  $0.05 \pm 0.3$  m, respectively. These values are far below the estimated accuracy of  $4.8 \pm 2.2$  mHz and  $1.9 \pm 1.4$  m (see Sect. 2.2.1) for Doppler and range postfit residuals, respectively. In addition to these residuals, we also compared the orbit of MESSENGER computed with INPOP13a and INPOP10e ephemerides. The differences in the periapsis  $\delta p$  and apoapsis  $\delta a$  altitudes of MESSENGER due to the change in planetary ephemeris are plotted in panels c and d of Fig. 5. An average and  $1\sigma$  dispersion of  $\delta p$  and  $\delta a$  was found as  $0.05 \pm 1.2$  m and  $0.03 \pm 1.2$  m, respectively. These values are also far below the required accuracy of 10 m (Srinivasan et al. 2007) for the MESSENGER orbit. This analysis is therefore consistent with the fact that change in the planetary ephemeris during the construction of the spacecraft orbit does not alter the radioscience analysis significantly.

**Table 4.** Statistics of the residuals obtained after the INPOP13a fit.

Type of data		Nbr	Time interval	INPOP13a		INPOP10e	
				mean	1 $\sigma$	mean	1 $\sigma$
Mercury	range [m]	462	1971.29–1997.60	−108	866	−45	872
Mercury Messenger	GINS range [m]	314	2011.39–2012.69	2.8	12.0	15.4	191.8
Out from SC*	GINS range [m]	267	2011.39–2012.66	−0.4	8.4	6.2	205.2
Mercury Mariner	range [m]	2	1974.24–1976.21	−124	56	−52.5	113
Mercury flybys Mess	ra [mas]	3	2008.03–2009.74	0.85	1.35	0.73	1.48
Mercury flybys Mess	de [mas]	3	2008.03–2009.74	2.4	2.4	2.4	2.5
Mercury flybys Mess	range [m]	3	2008.03–2009.74	−1.9	7.7	−5.05	5.8
Venus	VLBI [mas]	46	1990.70–2010.86	1.6	2.6	1.6	2.6
Venus	range [m]	489	1965.96–1990.07	502	2236	500	2235
Venus Vex	range [m]	24970	2006.32–2011.45	1.3	11.9	1.1	11.9
Mars	VLBI [mas]	96	1989.13–2007.97	−0.02	0.41	−0.00	0.41
Mars Mex	range [m]	21 482	2005.17–2011.45	−2.1	20.6	−1.3	21.5
Mars MGS	GINS range [m]	13 091	1999.31–2006.83	−0.6	3.3	−0.3	3.9
Mars Ody	range [m]	5664	2006.95–2010.00	1.6	2.3	0.3	4.1
Mars Path	range [m]	90	1997.51–1997.73	6.1	14.1	−6.3	13.7
Mars Vkg	range [m]	1257	1976.55–1982.87	−0.4	36.1	−1.4	39.7
Jupiter	VLBI [mas]	24	1996.54–1997.94	−0.5	11.0	−0.3	11.0
Jupiter Optical	ra [mas]	6532	1914.54–2008.49	−40	297	−39	297
Jupiter Optical	de [mas]	6394	1914.54–2008.49	−48	301	−48	301
Jupiter flybys	ra [mas]	5	1974.92–2001.00	2.6	2.9	2.4	3.2
Jupiter flybys	de [mas]	5	1974.92–2001.00	−11.0	11.5	−10.8	11.5
Jupiter flybys	range [m]	5	1974.92–2001.00	−1065	1862	−907	1646
Saturne Optical	ra [mas]	7971	1913.87–2008.34	−6	293	−6	293
Saturne Optical	de [mas]	7945	1913.87–2008.34	−12	266	−2	266
Saturne VLBI Cass	ra [mas]	10	2004.69–2009.31	0.19	0.63	0.21	0.64
Saturne VLBI Cass	de [mas]	10	2004.69–2009.31	0.27	0.34	0.28	0.33
Saturne Cassini	ra [mas]	31	2004.50–2007.00	0.8	3.4	0.8	3.9
Saturne Cassini	de [mas]	31	2004.50–2007.00	6.5	7.2	6.5	7.2
Saturne Cassini	range [m]	31	2004.50–2007.00	−0.010	18.44	−0.013	18.84
Uranus Optical	ra [mas]	13 016	1914.52–2011.74	7	205	7	205
Uranus Optical	de [mas]	13 008	1914.52–2011.74	−6	234	−6	234
Uranus flybys	ra [mas]	1	1986.07–1986.07	−21		−21	
Uranus flybys	de [mas]	1	1986.07–1986.07	−28		−28	
Uranus flybys	range [m]	1	1986.07–1986.07	20.7		19.7	
Neptune Optical	ra [mas]	5395	1913.99–2007.88	2	258	0.0	258
Neptune Optical	de [mas]	5375	1913.99–2007.88	−1	299	−0.0	299
Neptune flybys	ra [mas]	1	1989.65–1989.65	−12		−12	
Neptune flybys	de [mas]	1	1989.65–1989.65	−5		−5	
Neptune flybys	range [m]	1	1989.65–1989.65	66.8		69.6	
Pluto Optical	ra [mas]	2438	1914.06–2008.49	−186	664	34	654
Pluto Optical	de [mas]	2461	1914.06–2008.49	11	536	7	539
Pluto Occ	ra [mas]	13	2005.44–2009.64	6	49	3	47
Pluto Occ	de [mas]	13	2005.44–2009.64	−7	18	−6	18
Pluto HST	ra [mas]	5	1998.19–1998.20	−42	43	33	43
Pluto HST	de [mas]	5	1998.19–1998.20	31	48	28	48
Venus Vex**	range [m]	2827	2011.45–2013.00	51	124	52	125
Mars Mex**	range [m]	4628	2011.45–2013.00	−3.0	11.5	4.2	27.5

**Notes.** For comparison, means and standard deviations of residuals obtained with INPOP10e are given. The label GINS range indicates that the corresponding data set was obtained after orbit reconstruction of the spacecraft in using the GINS software. For MGS, see Verma et al. (2013). (\*) Solar corona period. (\*\*) Extrapolation period.

## 4. Test of general relativity

### 4.1. General presentation

INPOP13a was built in the framework of GR in using the PPN formalism. A detailed description of the modeling used for the INPOP ephemerides is given in (Fienga et al. 2011). Specific relativistic timescales have been set up and integrated in INPOP (TCB, TDB) and mainly two parameters characterized the relativistic formalism in modern planetary ephemerides: the

parameter  $\beta$  that measures the nonlinearity of gravity and  $\gamma$ , measuring the deflexion of light. In GR, both are supposed to be equal to 1 and were fixed to 1 for the INPOP13a construction. The GINS software used for the analysis of the radio science data and the reconstruction of the MESSENGER orbit is also coded in the PPN framework, including both  $\beta$  and  $\gamma$  PPN parameters.

Up to now, general relativity theory (GRT) has successfully described all available observations, and no clear observational evidence against GR has been identified. However, the discovery of Dark Energy which challenges GRT as a complete

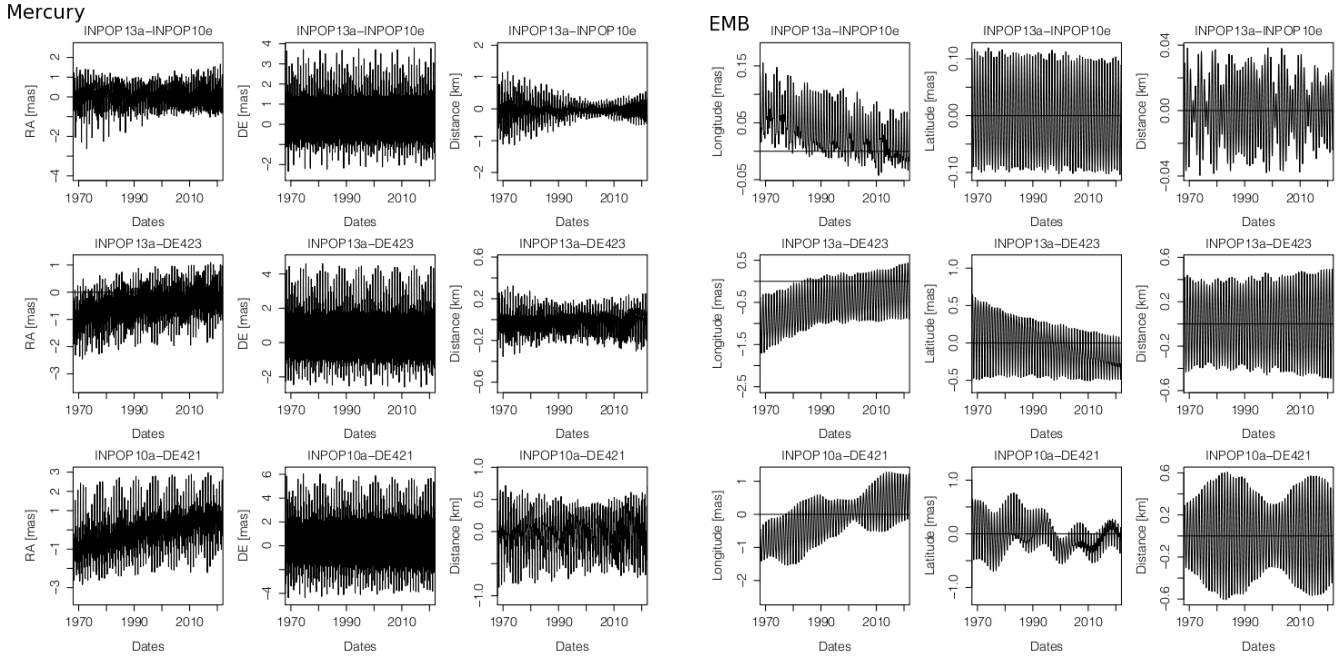


**Fig. 4.** In *Mercury* panel, differences in geocentric Mercury right ascension (RA), declination (DE) and distances between INPOP13a, INPOP10e and DE423. In *EMB* panel, differences in BCRF longitudes, latitudes and distances of the EMB between INPOP13a, INPOP10e and DE423. Differences between INPOP10a and DE421 are also given.

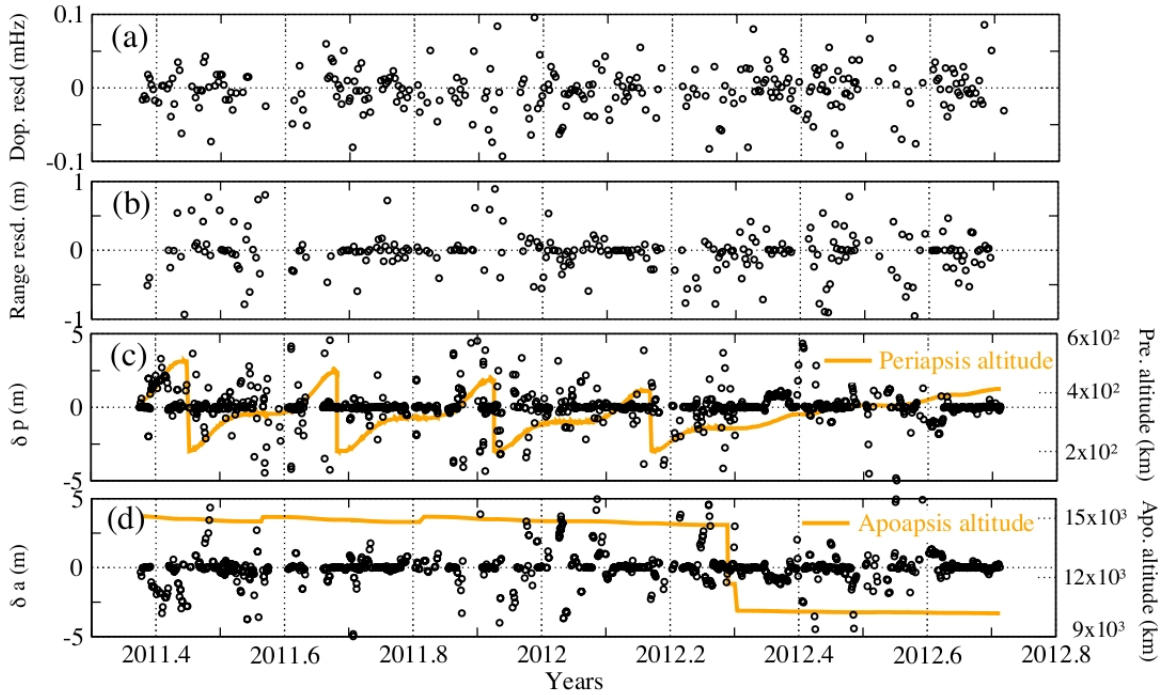


**Fig. 5.** Comparison between INPOP13a and INPOP10e estimations of MESSENGER orbit: **a)** differences in the postfit Doppler residuals; **b)** differences in the postfit range residuals; **c)** differences in the periapsis altitude  $\delta p$ ; **d)** differences in the apoapsis altitude  $\delta a$ .

model for the macroscopic universe, and the continuing failure to merge GRT and quantum physics indicate that new physical ideas should be sought. To streamline this search it is indispensable to test GRT in all accessible regimes and to the highest possible accuracy.

Among all possibilities for testing GRT, the tests of the motion and light propagation in the solar system were historically the first ones, and they are still very important since

they give highest accuracy since the dynamics of the solar system is well understood and supported by a long history of observational data. Concerning the Einstein field equations, the most important framework used for the tests in the solar system is the PPN formalism (such as Will 1993). The PPN formalism is a phenomenological scheme with ten dimensionless parameters covering certain class of metric theories of gravity, among them the  $\beta$  and  $\gamma$  parameters parts of the INPOP and

**Table 5.** Intervals of violation for PPN parameters  $\beta$  and  $\gamma$  deduced from Fig. 7 panel **a**) labelled INPOP13a and Fig. 7 panel **b**) labelled INPOP13aWF.

Ref.	$(\beta - 1) \times (\gamma - 1) \times 10^5$	INPOP13a	Limit [%]	$(\beta - 1) \times (\gamma - 1) \times 10^5$
INPOP10a	$(\beta - 1) = (-6.2 \pm 8.1)$ $(\gamma - 1) = (4.5 \pm 7.5)$	All data	25	$(\beta - 1) = (0.2 \pm 2.5)$ $(\gamma - 1) = (-0.3 \pm 2.5)$
			10	$(\beta - 1) = (-0.15 \pm 0.70)$ $(\gamma - 1) = (0.0 \pm 1.1)$
K11	$(\beta - 1) = (4 \pm 24)$ $(\gamma - 1) = (18 \pm 26)$	All data	5	$(\beta - 1) = (0.02 \pm 0.12)$ $(\gamma - 1) = (0.0 \pm 0.18)$
			Least squares	
M08-LLR-SEP*	$(\beta - 1) = (15 \pm 18)$	Least squares		
W09-LLR-SEP*	$(\beta - 1) = (12 \pm 11)$			
B03-CASS L11-VLB	$(\gamma - 1) = (2.1 \pm 2.3)$ $(\gamma - 1) = (-8 \pm 12)$	No flyby	25	$(\beta - 1) = (-0.5 \pm 4.5)$ $(\gamma - 1) = (12.5 \pm 17.5)$
			10	$(\beta - 1) = (0.0 \pm 2.0)$ $(\gamma - 1) = (0.5 \pm 3.5)$
P13	$(\beta - 1) = (-2 \pm 3)$ $(\gamma - 1) = (4 \pm 6)$	No flyby	5	$(\beta - 1) = (-0.25 \pm 1.25)$ $(\gamma - 1) = (-0.1 \pm 2.6)$

**Notes.** Values from INPOP10a are extracted from [Fienga et al. \(2010, 2011\)](#) with a threshold for the variations of the postfit residuals of 5% given in Col. 4. K11 stands for [Konopliv et al. \(2011\)](#), M08 for [Müller et al. \(2008\)](#), W09 for [Williams et al. \(2009\)](#), B03 for [Bertotti et al. \(2003\)](#), P13 for [Pitjeva & Pitjev \(2013\)](#) and L11 for [Lambert & Le Poncin-Lafitte \(2011\)](#). The least squares section gives the fitted values of  $\beta$  and  $\gamma$  at  $1\sigma$  as obtained by a global fit of INPOP presented in Sect. 4.2.1. (\*) values obtained for  $(\gamma - 1)_{B03-CASS}$ ; (\*\*) least square results given at  $1\sigma$ .

AINS modelings. The tracking data of space missions give a good possibility to test GRT since the data is very sensitive to the GRT-effects in both dynamics of the spacecraft and signal propagation. However, some factors, such as navigation unknowns (AMDs, solar panel calibrations), planet unknowns (potential, rotation, etc.), effect of the solar plasma, or the correlation with planetary ephemerides limit this sort of gravity test. Dynamics of the solar system are, however, less affected by poorly modeled accelerations and technical unknowns. Up to now, the best constraints for  $\beta$  come from the planetary data in INPOP ([Fienga et al. 2011](#)). Constraints on other PPN parameters can be found in [Will \(2006\)](#). A number of theoretical models predict deviations of PPN parameters that are smaller than current constraints. Typical examples here are certain types of tensor-scalar theories where cosmological evolution exhibits an attractor mechanism towards GRT ([Damour & Nordtvedt 1993](#)) or string-inspired scalar-tensor theories where the scalar field can decouple from matter ([Damour & Polyakov 1994](#)).

Another phenomenological test concerns the constancy of the Newtonian gravitational constant  $G$  in time. A variable  $G$  is produced say by alternative theories of gravity such tensor-scalar theory (see e.g. [Damour et al. 1990](#) and [Uzan 2003](#)) or some models of dark energy ([Steinhardt & Wesley 2009](#); [Alimi & Füzfa 2010](#)). The ratio is now constrained at the level of  $10^{-13}$  with LLR analysis ([Williams et al. 2004](#)).

#### 4.2. Estimation of PPN parameters, $\gamma$ and $\beta$

In this section, we propose to use the improvement of Mercury's orbit as an efficient tool for testing the consistency between planetary ephemerides built with MESSENGER radio science data and non-unity PPN parameters.

##### 4.2.1. Method

A first estimation of PPN  $\beta$  and  $\gamma$  is possible by least square methods during the adjustment of the INPOP planetary ephemerides, and the results are given in Table 5. Figure 6 gives the correlations between the first 71 over the 343 parameters

estimated in the adjustments. As one can see in Fig. 6 no correlation greater than 0.3 affects the determination of the PPN parameters  $\beta$  and  $\gamma$ , as well as the fit of the Sun oblateness, when the gravitational mass of the Sun is highly related to the Mercury and to the Earth orbits.

However to go further in the analysis of the uncertainties and the construction of acceptable intervals of violation of GR through the PPN  $\beta$  and  $\gamma$ , we also considered the same method as the one that was used and described in [Fienga et al. \(2011\)](#) for determining acceptable intervals of violation of GR when the PPN formalism. Small variations in these two parameters near unity are imposed when constructing alternative planetary ephemerides that are fit over the whole data sets presented in Table 4 and with the same parameters and hypothesis as INPOP13a. A minimum of three iterations in the adjustment process is required for building new ephemerides, and comparisons between these ephemerides and INPOP13a are done to scale up what variations to GR are acceptable at the level of uncertainty of the present planetary ephemerides.

The improvement of Mercury's orbit in INPOP13a justifies these new estimations. Indeed, Mercury played a historical role in testing gravity and GR in 1912 (Einstein 1912) and it is still the planet the most influenced by the gravitational potential of the Sun. Its orbit can then lead to the most efficient constraints on  $\beta$ , hence on  $\gamma$  in the PPN formalism. Before the recent input of MESSENGER flyby and orbital radio science data in the INPOP construction, Mars was the most constraining planet for the PPN parameters ([Fienga et al. 2010](#)). The reason was the long range of high accurate observations on Mars. The implementation of the first MESSENGER flyby data reduces the interval of violation of  $\beta$  to 50%. The first estimation of the  $\gamma$  interval of violation was made possible thanks to the gain in uncertainty on the Mercury orbit. With INPOP13a, even better improvement is achieved.

##### 4.2.2. Results

The results obtained by direct least squares fit are presented in Table 5. As expected, the estimated uncertainties are very

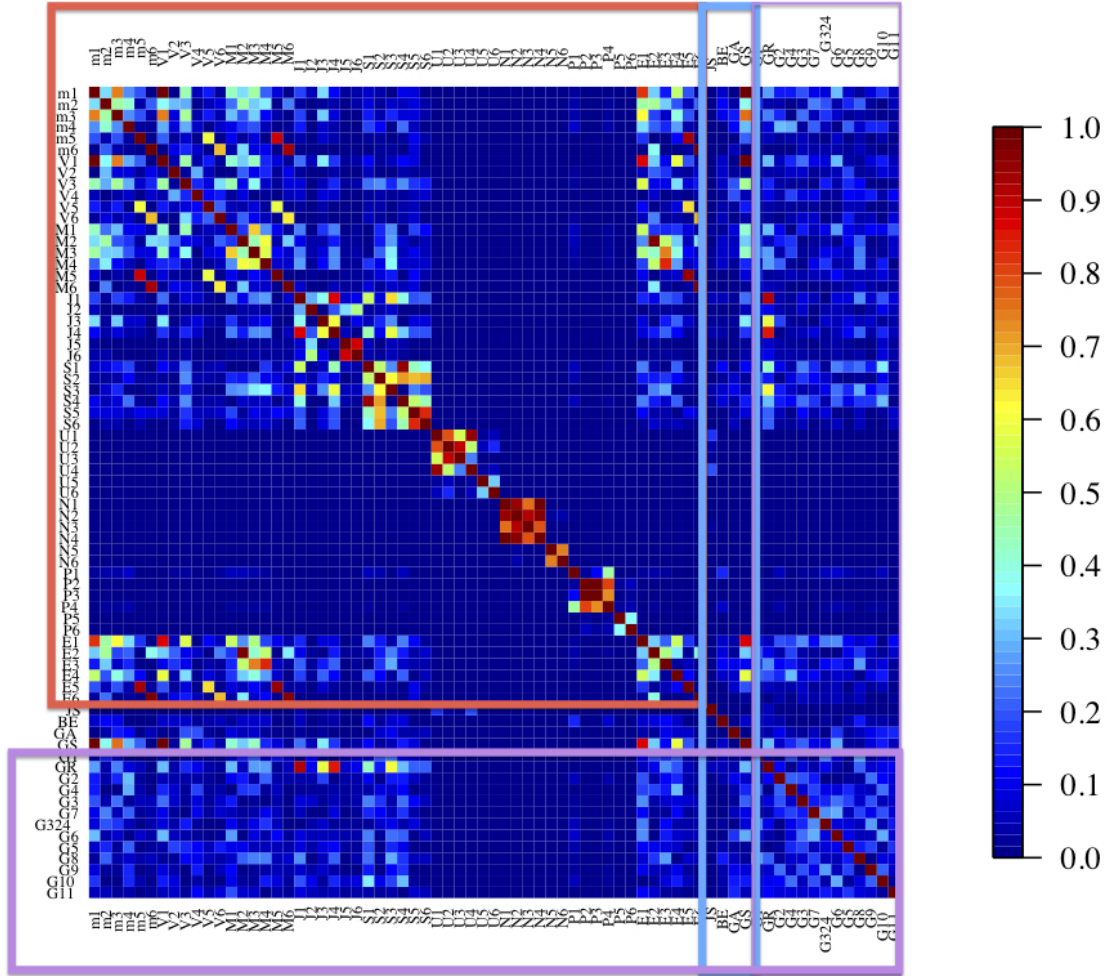


**Fig. 6.** Correlation between the first 71 (over 343) parameters estimated during the fit of the planetary ephemerides. The red frame frames the correlations related to the initial conditions of planet orbits and the blue rectangle frames the correlations related to the Sun  $J_2$  ( $JS$ ), the PPN parameters  $\beta$  ( $BE$ ) and  $\gamma$  ( $GA$ ) and the gravitational mass of the Sun ( $GS$ ). The magenta rectangle frames the correlations related to the gravitational mass of the first most perturbing asteroids including the gravitational mass of the asteroid ring ( $GR$ ).  $m_1, \dots, m_6$  expresses the initial conditions of the Mercury orbit in equinoctial coordinates: semi-major axis, mean motion,  $k$ ,  $h$ ,  $q$ , and  $p$  respectively. The other planet initial conditions are indicated by the first letter of the planet ( $V$  for Venus,  $M$  for Mars etc...) and by the figures of the corresponding initial conditions as given for Mercury.

optimistic and a more detailed analysis is done based on the method proposed by [Fienga et al. \(2011\)](#).

Results obtained in terms of percentages of the variations in postfit residuals between a planetary ephemeris fitted and built up with PPN parameters different from one and INPOP13a are given in Fig. 7. Panel a in Fig. 7 gives the map of the variations in percent of the full dataset postfit residuals. Panel b in Fig. 7 gives the same map but without taking the variations of the Mercury flyby data into account. For panel b, the Mercury flyby data are indeed used in the ephemerides fit but not in the analysis of the postfit residuals for testing GR. The map of panels a and b is then dramatically different: where the limits for  $\beta$  and  $\gamma$  are stringent for the map including the Mariner data, the constraints are greatly enlarged for these two parameters. These phenomena were expected since the variations in PPN parameters induce long-term perturbations in the geocentric distances of Mercury as one can see in Fig. 8. Panels c and d are similar to a and b, but they are obtained with ephemeris INPOP10a. In this ephemeris, MESSENGER flyby data were included in its fits but not in the orbital data. By comparing panels a and c, one can see that the use of the MESSENGER orbital data significantly

reduce the intervals of violation for both PPN parameters by a factor 10. The same manner, in the most pessimistic case and without considering the Mercury flybys in analysing of the variations in the postfit residual, one can see in panels b and d that the improvement of Mercury's orbit is again crucial for reducing the violation intervals of PPN parameters.

Table 5 collects the acceptable violation intervals obtained from INPOP10a and INPOP13a. Values extracted from INPOP10a were obtained at 5% of postfit residual variations ([Fienga et al. 2011](#)). With INPOP13a, we extracted values from i) panel a of Fig. 7 obtained at 5%, but also at 10% and 25%; and ii) from panel b of Fig. 7 obtained at 5%, which is consistent with the 25% of intervals extracted from panel a.

All given intervals are compatible with GR with an uncertainty at least ten times smaller than our previous results with INPOP10a. In Table 5, comparisons to least squares estimations of other planetary ephemerides or Moon ephemerides like [Pitjeva & Pitjev \(2013\)](#), [Konopliv et al. \(2011\)](#), [Müller et al. \(2008\)](#), and [Williams et al. \(2009\)](#), as well as estimations deduced from VLBI observations [Lambert & Le Poncin-Lafitte \(2011\)](#), are also given. The most stringent published constraint

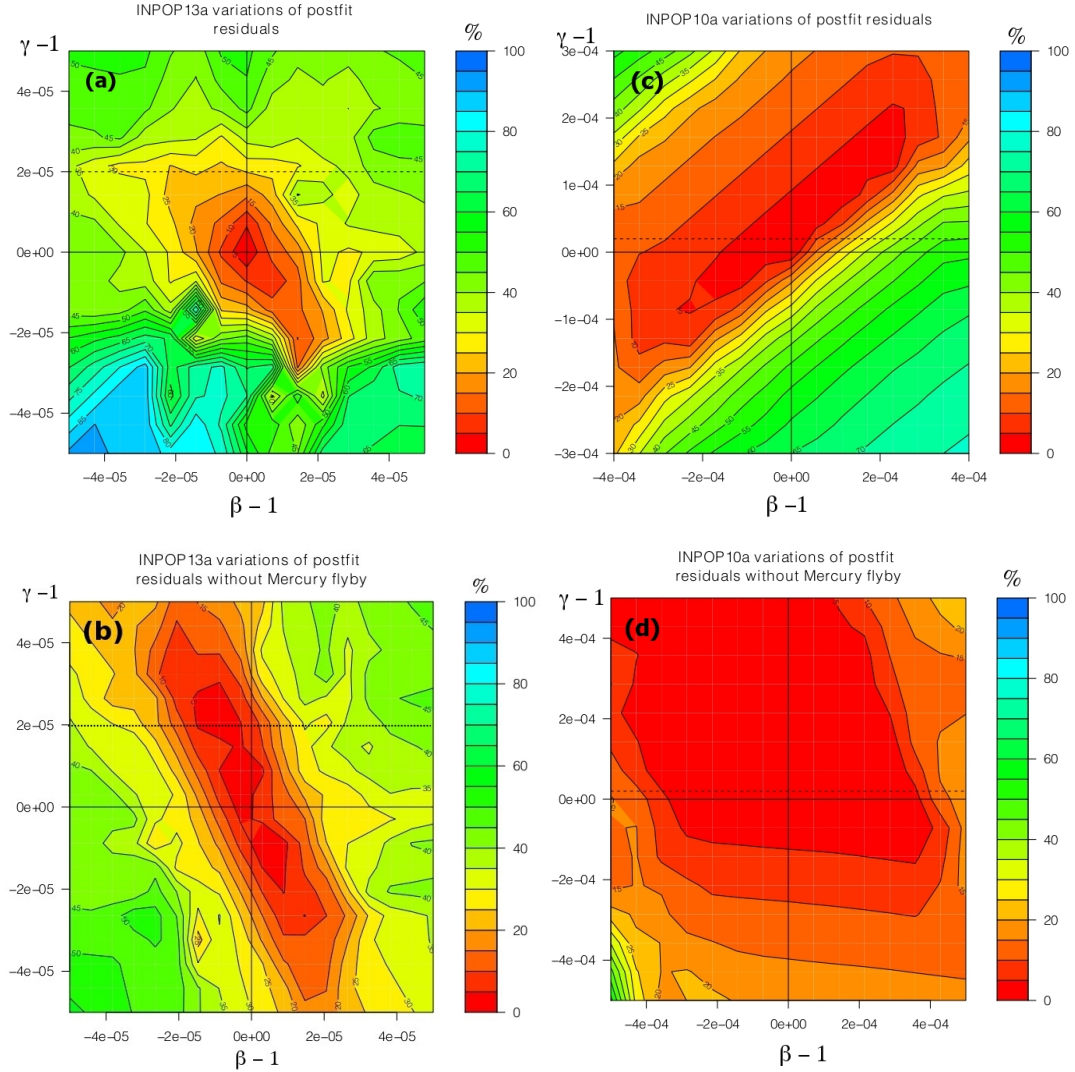


**Fig. 7.** Variations in postfit residuals obtained for different values of PPN  $\beta$  ( $x$ -axis) and  $\gamma$  ( $y$ -axis). Panels **a**) and **c**) are obtained by considering the variations in the whole data sets when for panels **b**) and **d**), variations in the Mercury flyby data (from Mariner and MESSENGER missions) are excluded from the analysis. The dashed line indicates the limit in  $\gamma$  given by Bertotti et al. (2003).

for the PPN parameter  $\gamma$  has been obtained so far during a dedicated phase of the Cassini mission by Bertotti et al. (2003). This value is compatible with our 25% estimation when our 5% and 10% estimations give more restrictive intervals of GR violations.

Confirmations of the results presented in Table 5 will be obtained by the use of the radioscience data obtained during the future Bepi-Colombo mission. In addition, the recovery of the Mariner flyby data would also be a great help for such confirmations. Unfortunately, the Mariner data seem to have been lost, and access to these data seems to be unrealistic. Indeed as one can see in Fig. 8, perturbations induced by a slight change in the PPN parameters ( $\beta - 1$ ) =  $1.5 \times 10^{-5}$  and ( $\gamma - 1$ ) =  $-2.2 \times 10^{-5}$  inducing an effect of about six meters on the Mariner range data (12%) will induce a signature of about the same level at the Bepi-Colombo epoch. With the improved Bepi-Colombo radio science tracking, the expected accuracy in the range measurement is planned to be about 50 centimeters. With such accuracy, detecting the perturbations induced by the same modification of the PPN parameters should be done at 1200%! Two orders of magnitude are expected as a gain in the uncertainty for the  $\beta$  and  $\gamma$  estimations.

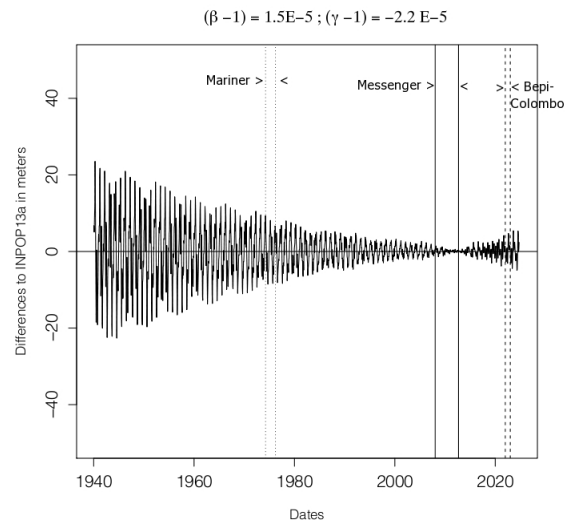


**Fig. 8.** Differences in geocentric Mercury distances between INPOP13a and a planetary ephemeris built with PPN  $\beta$  and  $\gamma$  different from 1. The indicated area shows intervals of time corresponding to Mariner observations, MESSENGER and the future Bepi-Colombo.

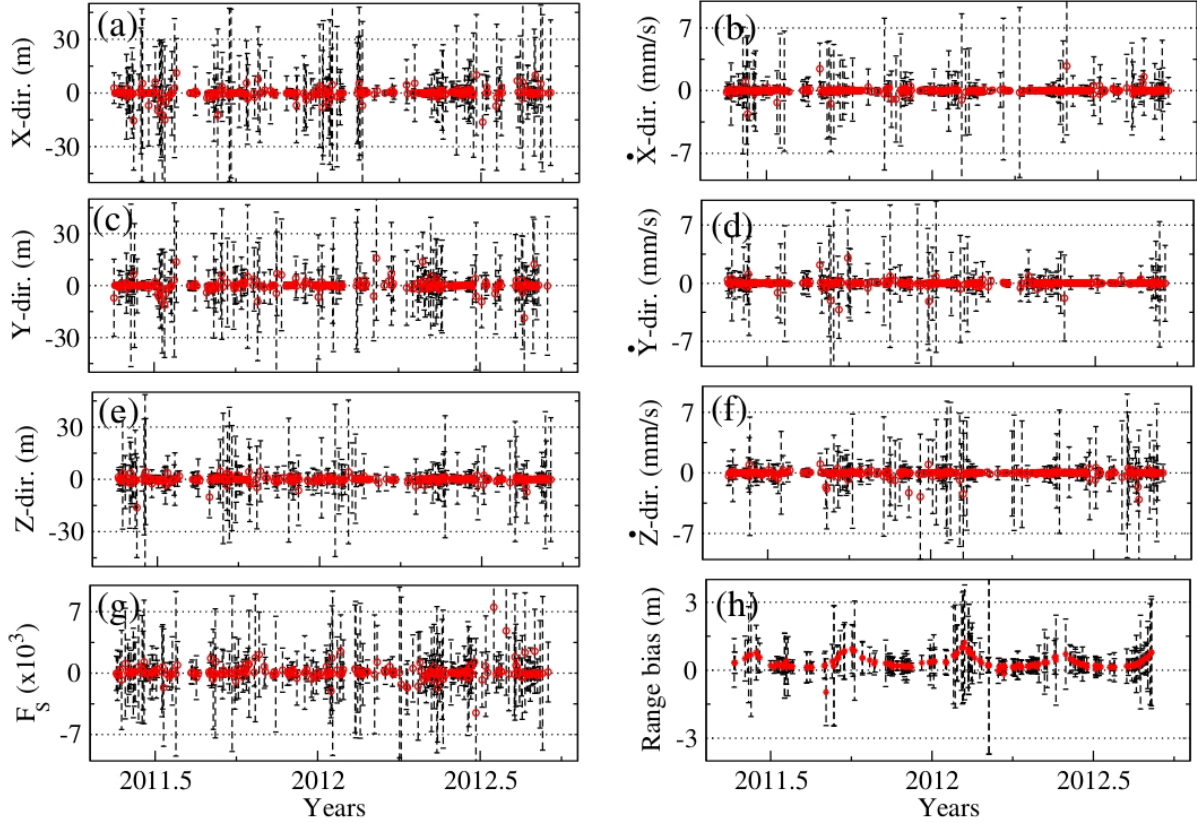


**Fig. 9.** Differences between solve-for parameters obtained from the solutions  $SOL_{Ref}$  and  $SOL_{\beta\gamma \neq 1}$  (see text): panels **a**–**f**) represent the changes in the initial state vectors, panel **g**) represents the changes in the scale factors estimated for solar radiation pressure, panel **h**) represents the changes in the estimated range bias. The error bars represent the  $1\sigma$  uncertainties in the estimation of solve-for parameters obtained with the reference solution  $SOL_{Ref}$ .

#### 4.2.3. Impact on MESSENGER orbit

As stated previously, the GINS software was modeled in the framework of the PPN formalism which includes  $\beta$  and  $\gamma$  parameters. To analyze the combined impact of PPN parameters over the MESSENGER orbit and the planetary ephemerides construction, we analyzed the entire one and half years of radio-science data again using the PPN parameters that are different from unity. The same procedure as described in Sect. 2.1 has been used for reconstructing the MESSENGER orbit. Two sets of MESSENGER orbits were then built, one with  $\beta$  and  $\gamma$  equal to unity and the other with  $\beta$  and  $\gamma$  different from unity (in this case,  $\beta - 1 = \gamma - 1 = 1 \times 10^{-4}$ ). Hereafter, the solution obtained from  $\beta$  and  $\gamma$  equal to unity is referred to as  $SOL_{Ref}$  (for the reference solution), and the solution corresponds to  $\beta$  and  $\gamma$  different from unity referred to as  $SOL_{\beta\gamma \neq 1}$ .

To maintain consistency in constructing the MESSENGER orbit, we used corresponding planetary ephemerides that were built with the same configurations of PPN parameters as used for  $SOL_{Ref}$  and  $SOL_{\beta\gamma \neq 1}$ . In Fig. 9, we plotted the differences between solve-for parameters obtained for  $SOL_{Ref}$  and  $SOL_{\beta\gamma \neq 1}$ . The error bars shown in the same figure represent the  $1\sigma$  uncertainties in the estimation of solve-for parameters corresponding to  $SOL_{Ref}$ . From this figure, one can notice the differences in the parameters are always below the  $1\sigma$  uncertainties. The estimated solve-for parameters for  $SOL_{\beta\gamma \neq 1}$  are analogous to  $SOL_{Ref}$ , and there is no significant change in the MESSENGER orbit due to

the change in PPN parameters. In contrast, as shown in Fig. 7, this configuration of PPN parameters ( $\beta - 1 = \gamma - 1 = 1 \times 10^{-4}$ ) in the construction of planetary ephemerides led to  $\sim 65\%$  of change in the postfit residuals, which shows that, the planetary ephemerides are more sensitive to GR effects. This can be explained from the fitting intervals of the data set. Usually planetary ephemerides are fitted over long intervals of times (see Table 4) to exhibit long-term effects, while a spacecraft orbit is usually constructed over much shorter intervals (usually one day to a few days) of data arcs to account for the model's imperfections. The short fitting interval of the spacecraft orbit would absorb such effects.

Moreover, it is worth noticing that, unlike state vectors and scale factor  $F_S$  (see panels a–g of Fig. 9), the range bias differences between  $SOL_{Ref}$  and  $SOL_{\beta\gamma \neq 1}$  solutions (see panel h) shows systematic behavior. This trend in the range bias can be explained from the contribution of the relativistic deflection of light by the Sun (a function of PPN parameter  $\gamma$ , Shapiro 1964) in the light time computations. Explicitly this effect was not absorbed during the computation of range bias and it becomes important to examine this effect when constructing planetary ephemerides.

We, therefore, reconstruct the planetary ephemerides using the range bias obtained from  $SOL_{\beta\gamma \neq 1}$  and the PPN parameters  $\beta - 1 = \gamma - 1 = 1 \times 10^{-4}$ . The newly estimated postfit range bias is then compared with the range bias (prefit) corresponding to  $SOL_{\beta\gamma \neq 1}$ . This investigation shows that, the postfit residuals are modified by  $\sim 6\%$  for MESSENGER and  $\sim 1\%$  for Mariner 10



with respect to prefit residuals. This modification in the residuals is negligible compared to a  $\sim 65\%$  of change with respect to reference residuals obtained from INPOP13a. As a result, the supplementary contributions in the range bias due to the relativistic deflection between DSN station and MESSENGER did not bring any significant change in the planetary ephemerides construction.

## 5. Conclusions

We analyzed one and half years of radioscience data of the MESSENGER spacecraft using orbit determination software GINS. An accurate orbit of MESSENGER was then constructed with the typical range of Doppler, and two-way range residuals of about  $4.8 \pm 2.2$  mHz ( $\sim 0.09 \pm 0.04$  mm/s), and  $1.9 \pm 1.4$  m. Such accuracies are comparable to those in [Smith et al. \(2012\)](#); [Stanbridge et al. \(2011\)](#); [Srinivasan et al. \(2007\)](#). Range measurements obtained by the MESSENGER spacecraft during its mapping period were then used to construct improved planetary ephemerides called INPOP13a. This ephemeris showed an accuracy of about  $-0.4 \pm 8.4$  m in the Mercury-Earth geometric distances, which is two orders of improvement compared to DE423 and INPOP10e, and one order compared to the latest DE430.

Such high precision Mercury ephemeris allowed us to perform one of the best GR tests of PPN-formalism. To determine the acceptable intervals of the violation of GR through the PPN parameters ( $\beta$ ,  $\gamma$ ), small variations of these two parameters near unity were imposed in the construction of alternative planetary ephemerides fitted over the whole data sets. The percentage difference between these ephemerides to INPOP13a are then used to defined the interval of PPN parameters  $\beta$  and  $\gamma$ .

As expected, our estimations of PPN parameters are more stringent than previous results. We considered the 5%, 10% and 25% of changes in the postfit residuals. That the PPN intervals correspond to these changes is compatible with GR with an uncertainty at least ten times smaller than our previous results with INPOP10a. Moreover, one of the best estimation of parameter  $\gamma$  has so far been estimated from the Cassini observations by [Bertotti et al. \(2003\)](#), which is compatible with our 25% estimation.

To further the accuracy of the PPN parameters improve, and to confirm the results given in Table 5, one needs to analysis the radioscience data of the future Bepi-Colombo mission.

*Acknowledgements.* We are very thankful to the CNES and Région Franche-Comté, who gave us financial support. Part of this work uses GINS software, so we would like to acknowledge the CNES for providing access to this software. A. K. Verma is thankful to P. Rosenbatt and S. Le Maistre for fruitful discussions. We are also thankful to G.Esposito-Farese for his constructive remarks and comments.

## References

- Alimi, J.-M., & Füzfa, A. 2010, in AIP Conf. Ser., 1241, 690
- Anderson, J. D., Colombo, G., Espitio, P. B., Lau, E. L., & Trager, G. B. 1987, *Icarus*, 71, 337
- Anderson, J. D., Jurgens, R. F., Lau, E. L., Slade, III, M. A., & Schubert, G. 1996, *Icarus*, 124, 690
- Anderson, J. D., Turyshv, S. G., Asmar, S. W., et al. 1997, *Planet. Space Sci.*, 45, 21
- Bertotti, B., Iess, L., & Tortora, P. 2003, *Nature*, 425, 374
- Damour, T., & Nordtvedt, K. 1993, *Phys. Rev. D*, 48, 3436
- Damour, T., & Polyakov, A. M. 1994, *Gen. Relativ. Gravit.*, 26, 1171
- Damour, T., Gibbons, G. W., & Gundlach, C. 1990, *Phys. Rev. Lett.*, 64, 123
- Ercol, C. J., M., B. S., & Holtzman, G. A. 2012, in Thermal and Fluids Analysis Workshop, TFAWS2012-PT-03
- Fienga, A., Manche, H., Laskar, J., & Gastineau, M. 2008, *A&A*, 477, 315
- Fienga, A., Laskar, J., Morley, T., et al. 2009, *A&A*, 507, 1675
- Fienga, A., Laskar, J., Kuchynka, P., et al. 2010, in IAU Symp. 261, eds. S. A. Klioner, P. K. Seidelmann, & M. H. Soffel, 159
- Fienga, A., Laskar, J., Kuchynka, P., et al. 2011, *Celest. Mech. Dyn. Astron.*, 111, 363
- Fienga, A., Manche, H., Laskar, J., Gastineau, M., & Verma, A. 2013 [[arXiv:1301.1510](#)]
- Flanigan, S. H., OShaughnessy, D. J., Wilson, M. N., & Hill, T. A. 2013, in 23rd Space Flight Mechanics Meeting, AAS, 13
- Folkner, W. M. 2010, JPL, interoffice memorandum, IOM 343R-10-001
- Konopliv, A. S., Asmar, S. W., Folkner, W. M., et al. 2011, *Icarus*, 211, 401
- Lambert, S. B., & Le Poncin-Lafitte, C. 2011, *A&A*, 529, A70
- Manche, H., Fienga, A., Laskar, J., et al. 2010, in Journées 2010 Systèmes de Référence Spatio-temporels
- Margot, J.-L. 2009, *Celest. Mech. Dyn. Astron.*, 105, 329
- Moyer, T. D. 2003, in Formulation for Observed and Computed Values of Deep Space Network Data Types for Navigation (John Wiley & Sons), Vol. 2
- Müller, J., Soffel, M., & Klioner, S. A. 2008, *J. Geodesy*, 82, 133
- Pitjeva, E. V. 2009, in IAU Symp. (AAS), 261, 603
- Pitjeva, E. V., & Pitjev, N. P. 2013, *MNRAS*, 432, 3431
- Shapiro, I. I. 1964, *Phys. Rev. Lett.*, 13, 789
- Smith, D. E., Zuber, M. T., Phillips, R. J., et al. 2010, *Icarus*, 209, 88
- Smith, D. E., Zuber, M. T., Phillips, R. J., et al. 2012, *Science*, 336, 214
- Solomon, S. C., McNutt, R. L., Gold, R. E., & Domingue, D. L. 2007, *Space Sci. Rev.*, 131, 3
- Srinivasan, D. K., Perry, M. E., Fielhauer, K. B., Smith, D. E., & Zuber, M. T. 2007, *Space Sci. Rev.*, 131, 557
- Stanbridge, D. R., Williams, K. E., Taylor, A. H., et al. 2011, in AAS/AIAA Astrodynamics Specialist Conference, AAS 11-548
- Steinhardt, P. J., & Wesley, D. 2009, *Phys. Rev. D*, 79, 104026
- Uzan, J.-P. 2003, *Annales Henri Poincaré*, 4, 347
- Vaughan, R. M., Haley, D. R., OShaughnessy, D. J., & Shapiro, H. S. 2002, *Adv. Astronau. Sci.*, 109, 1139
- Verma, A. K., Fienga, A., Laskar, J., et al. 2013, *A&A*, 550, A124
- Will, C. 2001, *Liv. Rev. Rel.*, 4, 4
- Will, C. M. 1993, *Theory and Experiment in Gravitational Physics* (Cambridge University Press)
- Will, C. M. 2006, *Liv. Rev. Rel.*, 9, 3
- Williams, J. G., Turyshv, S. G., & Boggs, D. H. 2004, *Phys. Rev. Lett.*, 93, 261101
- Williams, J. G., Turyshv, S. G., & Boggs, D. H. 2009, *Int. J. Mod. Phys. D*, 18, 1129
- Williams, J. G., Boggs, D. H., & Folkner, W. M. 2013, IOM 335-JW, DB, WF-20080314-001



## Chapter 6

### General conclusions

This thesis has been essentially motivated by the independent analysis of the past and present space mission radiometric data, and to provide data analysis tools for the improvement of the planetary ephemerides INPOP, as well as to use improved ephemerides to perform tests of physics such as general relativity, solar corona studies, etc.

The thesis has presented the research results obtained from the direct analysis of the MGS and MESSENGER radiometric raw data. To start the analysis, we have first developed an independent software to extract the contents of the Orbit Data Files (ODFs). These contents are then used to reconstruct the precise orbits of the MGS and MESSENGER spacecraft using GINS software developed by CNES. In addition, based on the algorithms given in Chapter 2, we have also developed an independent light time solution software in order to treat the JPL light time data.

The first part of the thesis deals with the analysis of the MGS radiometric data as an academic case to test our understanding of the raw radiometric data and their analysis with GINS by comparing our results with the literature. We have analyzed the entire radioscience data of MGS since 1999 to 2006 using *Box-Wing* macro-model consisting ten-plate and a parabolic high gain antenna. On average, an estimated root mean square (rms) value of the post-fit Doppler- and two-way range residuals are less than 5 mHz and 1 m respectively, excluding the residuals at the time of solar conjunctions. Such accuracy of the orbit and of the estimated parameters (see Chapter 3) are consistent with the results found in the literature (Yuan et al. (2001); Lemoine et al. (2001); Konopliv et al. (2006); Marty et al. (2009), see Table 3.3). Moreover, we also compared range bias that were computed from GINS with the reduced light time data provided by JPL. These range bias are consistent with each other, and hence confirm the validity of our analysis with respect to JPL ODP software.

Furthermore, the study has been also performed to understand the impact of the macro-model over the orbit perturbations and the estimated parameters. Instead to a *Box-Wing* macro-model, a *Spherical* macro-model was used for a new analysis of the entire radiometric data. By

---

comparing the outcomes of these models (see Chapter 3), we confirmed that, in the absence of precise knowledge of the spacecraft characteristics, short data-arc can be preferable to account for the mis-modeling in the spacecraft model without costing the orbit accuracy. However, this analysis may be not preferable for extracting an accurate geophysical signals from the Doppler measurements, such as the estimation of gravity field coefficients.

As a supplementary exploitation of MGS, we also performed solar physic studies for the first time using range bias data acquired at the time of solar conjunction periods. In addition to MGS, range bias data of MEX and VEX missions were also used and allowed us to analyze the large-scale structure of the electron density of the solar corona since 2001 to 2011. The parameters of the solar corona models, estimated separately for each spacecraft at different phases of solar activity (maximum and minimum) and at different solar wind states (slow and fast), are then deduced from these data using least square techniques. We compared our estimates with earlier results obtained with different methods. These estimates were found to be consistent during the same solar activities, especially during solar minima. However, during the solar maxima, electron densities obtained with different methods or different spacecraft show weaker consistencies.

We have also demonstrated the impact of solar corona correction on the construction of planetary ephemerides. Data acquired during the period of solar conjunctions show a severe degradation in the radio signals and consequently in the range bias. The observations obtained two months before and after the conjunctions were therefore usually removed from the fitted data sample of planetary ephemerides. The supplementary data, corrected from the solar corona perturbations, allowed us to gain  $\sim 8\%$  of whole data set. Such corrected data are then used for the first time in the construction of INPOP and induce a noticeable improvement in the estimation of the asteroid masses and a better long-term behavior of the ephemerides. These results are published in the *Astronomy & Astrophysics* journal, [Verma et al. \(2013\)](#).

After the successful analysis of the MGS radiometric data, the second part of the thesis deals with the complete analysis of the MESSENGER tracking data. MESSENGER is the first spacecraft orbiting Mercury. It therefore gives an ample opportunity to improve our knowledge of the Mercury orbit and also to perform one of the most sensitive GR tests of PPN-formalism. We analyzed one and half year of radioscience data using GINS software. The *Box-Wing* macro-model of the MESSENGER spacecraft was seen as a combination of flat plates arranged in the shape of a box, with attached solar arrays. For orbit computation and for parameters estimation, a multi-arc approach was used to get an independent estimate of the MESSENGER accelerations. In this method, we integrated the equations of motion using the time step of 50s and then, orbital fits were obtained from short data-arcs fitted over the observation span of one-day using an iterative process. Excluding solar corona period, the estimated typical mean and rms value of postfit Doppler, and two-way range residuals of about  $-0.00063 \pm 4.8$  mHz, and  $-0.003 \pm 1.5$  m respectively. Such accuracies are comparable with [Genova et al. \(2013\)](#); [Smith et al. \(2012\)](#); [Stanbridge et al. \(2011\)](#); [Srinivasan et al. \(2007\)](#).

The range bias computed from the GINS are then used for further refinement in the Mercury ephemeris. Using these range bias, we built the planetary ephemerides INPOP13a. This

---

ephemeris showed an accuracy of  $-0.4 \pm 8.4$  m in the geocentric Mercury residuals excluding solar corona period, which is two order of improvement than any latest planetary ephemerides (*e.g* INPOP10e ( $21 \pm 187$  m) and DE423 ( $15 \pm 105$  m)). The GR tests of PPN-formalism were then performed with such high precision Mercury ephemerides. To determine the acceptable intervals of the violation of GR thought the PPN parameters ( $\beta$ ,  $\gamma$ ), small variations of these two parameters near unity were imposed in the construction of alternative planetary ephemerides fitted over the whole data sets. The percentage difference between these ephemerides to INPOP13a are then used to define the intervals of PPN parameters  $\beta$  and  $\gamma$ .

As expected, our estimations of PPN parameters are most stringent than previous results. We considered 5, 10 and 25% of changes in the postfit residuals. The PPN intervals corresponding to these changes are compatible with GR with an uncertainty at least ten times smaller than our previous results with INPOP10a or INPOP08. Moreover, so far one of the best estimation of parameter  $\gamma$  has been estimated from the Cassini observations by Bertotti *et al.* (2003), which is compatible with our 25% of estimation. Furthermore, our 5 and 10% estimations give no indication of possible asymmetry. We also demonstrated that, despite the less quantity and quality of the Mariner 10 data, these latest are very important to consider for long term effects of the PPN parameters. The results of this study are published in *Astronomy & Astrophysics*, Verma *et al.* (2014).

In 2015, the BepiColombo mission, a joint mission of the European Space Agency (ESA) and the Japan Aerospace and eXploration Agency (JAXA) to the planet Mercury, will be launch. The main future work will be therefore to analyze the radioscience data obtained from this mission to further improvement in the accuracy of the PPN parameters. Moreover, the tools developed during these thesis will also be useful for the analysis of past, present, and future space missions, such as Odyssey, MRO etc..., and to deliver most up-to-date high accurate ephemerides to the users. This will definitely propel INPOP at the forefront of planetary ephemerides and will make team INPOP independent from the navigation team of the space agencies.

---



## Publications

- Verma, A. K., Fienga, A., Laskar, J., Manche, H., Gastineau, M., 2013b. Use of MESSENGER radioscience data to improve planetary ephemeris and to test general relativity. *Astronomy & Astrophysics*, submitted.
  - Verma, A. K., Fienga, A., Laskar, J., Issautier, K., Manche, H., Gastineau, M., Feb. 2013a. Electron density distribution and solar plasma correction of radio signals using MGS, MEX, and VEX spacecraft navigation data and its application to planetary ephemerides. *Astronomy & Astrophysics* 550, A124.
  - Fienga, A.; Manche, H.; Laskar, J.; Gastineau, M.; Verma, A. INPOP new release: INPOP10e. eprint arXiv:1301.1510, 2013.
  - Fienga, A.; Laskar, J.; Verma, A.; Manche, H.; Gastineau, M. INPOP: Evolution, applications, and perspective. SF2A-2012: Proceedings of the Annual meeting of the French Society of Astronomy and Astrophysics. Eds.: S. Boissier, P. de Laverny, N. Nardetto, R. Samadi, D. Valls-Gabaud and H. Wozniak, pp.25-33, 2012.
  - Verma, A.K., Fienga, A. New developments in spacecraft raw data direct analysis for the INPOP planetary ephemerides. IAU Joint Discussion 7: Space-Time Reference Systems for Future Research at IAU General Assembly-Beijing, id.39, August 2012.
  - Verma, A.K., Fienga. INPOP: The planetary ephemerides and its applications. 39th COSPAR Scientific Assembly, 14-22 July 2012, Mysore, India. Abstract C5.1- 15-12, p.2082.
  - Verma, A.K., Fienga, A. Electron density distribution and solar plasma correction of radio signals using MGS, MEX and VEX spacecraft navigation data and its application to planetary ephemerides. 39th COSPAR Scientific Assembly, 14-22 July 2012, Mysore, India. Abstract D3.5-5-12, p.2081.
  - Verma, A.K., Fienga, A. Re-Estimation of Solar Corona Coefficients (a, b, c) by Using MGS & Mex Spacecraft Data. EPSC-DPS Joint Meeting 2011, 2-7 October 2011, Nantes, France, 2011epsc.conf.1828V.
-





---

## Bibliography

- Afonso, G., Barlier, F., Mignard, F., Carpino, M., Farinella, P., Oct. 1989. Orbital effects of LAGEOS seasons and eclipses. *Annales Geophysicae* 7, 501–514.
- Albee, A. L., Arvidson, R. E., Palluconi, F., Thorpe, T., Oct. 2001. Overview of the Mars Global Surveyor mission. *Journal of Geophysical Research* 106, 23291–23316.
- Anderson, J. D., Colombo, G., Espitio, P. B., Lau, E. L., Trager, G. B., Sep. 1987a. The mass, gravity field, and ephemeris of Mercury. *Icarus* 71, 337–349.
- Anderson, J. D., Jurgens, R. F., Lau, E. L., Slade, III, M. A., Schubert, G., Dec. 1996. Shape and Orientation of Mercury from Radar Ranging Data. *Icarus* 124, 690–697.
- Anderson, J. D., Keesey, M. S. W., Lau, E. L., Standish, Jr., E. M., Newhall, X. X., 1978. Tests of general relativity using astrometric and radio metric observations of the planets. *Acta Astronautica* 5, 43.
- Anderson, J. D., Keesey, M. S. W., Lau, E. L., Standish, Jr., E. M., Newhall, X. X., V. N. Novikov & D. N. Cheverov (Eds.), Oct. 1976. Tests of general relativity using astrometric and radiometric observations of the planets.
- Anderson, J. D., Krisher, T. P., Borutzki, S. E., Connally, M. J., Eshe, P. M., Hotz, H. B., Kinslow, S., Kursinski, E. R., Light, L. B., Matousek, S. E., Moyd, K. I., Roth, D. C., Sweetnam, D. N., Taylor, A. H., Tyler, G. L., Gresh, D. L., Rosen, P. A., Dec. 1987b. Radio range measurements of coronal electron densities at 13 and 3.6 centimeter wavelengths during the 1985 solar conjunction of Voyager 2. *The Astrophysical Journal* 323, L141–L143.
- Anderson, J. D., Turyshv, S. G., Asmar, S. W., Bird, M. K., Konopliv, A. S., Krisher, T. P., Lau, E. L., Schubert, G., Sjogren, W. L., Jan. 1997. Radio-science investigation on a Mercury Orbiter mission. *Planet. Space Sci.* 45, 21–29.
- Ash, M. E., Shapiro, I. I., Smith, W. B., Apr. 1967. Astronomical constants and planetary ephemerides deduced from radar and optical observations. *AJ* 72, 338–+.
- Barlier, F., Berger, C., Falin, J. L., Kockarts, G., Thuillier, G., Mar. 1978. A thermospheric model based on satellite drag data. *Annales de Geophysique* 34, 9–24.
- Bertotti, B., Ciufolini, I., Bender, P. L., Mar. 1987. New test of general relativity - Measurement of de Sitter geodetic precession rate for lunar perigee. *Physical Review Letters* 58, 1062–1065.
-

- 
- Bertotti, B., Iess, L., Tortora, P., Sep. 2003. A test of general relativity using radio links with the Cassini spacecraft. *Nature* 425, 374–376.
- Bird, M. K., Paetzold, M., Edenhofer, P., Asmar, S. W., McElrath, T. P., Dec. 1996. Coronal radio sounding with Ulysses: solar wind electron density near 0.1AU during the 1995 conjunction. *Astronomy & Astrophysics* 316, 441–448.
- Bird, M. K., Volland, H., Paetzold, M., Edenhofer, P., Asmar, S. W., Brenkle, J. P., May 1994. The coronal electron density distribution determined from dual-frequency ranging measurements during the 1991 solar conjunction of the ULYSSES spacecraft. *The Astrophysical Journal* 426, 373–381.
- Bougeret, J.-L., King, J. H., Schwenn, R., Feb. 1984. Solar radio burst and in situ determination of interplanetary electron density. *Solar Physics* 90, 401–412.
- Bravo, S., Stewart, G. A., Nov. 1997. Fast and Slow Wind from Solar Coronal Holes. *ApJ* 489, 992.
- Cash, P., Emmons, D., Welgemoed, J., Dec. 2008. Ultra-stable oscillators for space application. In: 40th Annual Precise Time and Time Interval (PTTI) Meeting. pp. 51–56.
- Chao, C. C., Oct. 1971. New Tropospheric Range Corrections with Seasonal Adjustment. *New Tropospheric Range Corrections with Seasonal Adjustment, Deep Space Network Progress Report*, 31-1526, VI, 67-82 31.
- Ciufolini, I., Jan. 1986. Measurement of the Lense-Thirring drag on high-altitude, laser-ranged artificial satellites. *Physical Review Letters* 56, 278–281.
- Davies, M. E., Abalakin, V. K., Bursa, M., Lieske, J. H., Morando, B., Morrison, D., Seidelmann, P. K., Sinclair, A. T., Yallop, B., Tjuflin, Y. S., Jan. 1996. Report of the IAU/IAG/COSPAR Working Group on Cartographic Coordinates and Rotational Elements of the Planets and Satellites: 1994. *Celestial Mechanics and Dynamical Astronomy* 63, 127–148.
- Dow, J. M., 1988. An improved tidal model for high accuracy satellite orbit determination. In: 16th International Symposium on Space Technology and Science, Vol. 1. Vol. 1. pp. 701–705.
- Eshleman, V. R., Tyler, G. L., Anderson, J. D., Fjeldbo, G., Levy, G. S., Wood, G. E., Croft, T. A., Nov. 1977. Radio science investigations with Voyager. *Space Science Reviews* 21, 207–232.
- Feldman, U., Landi, E., Schwadron, N. A., Jul. 2005. On the sources of fast and slow solar wind. *Journal of Geophysical Research (Space Physics)* 110, 7109.
- Fienga, A., May 2011. Ephemerides planetaires et systemes de reference. Habilitation a Diriger des Recherches, Universite de Franche-Comte - Observatoire de Besancon, in French.
- Fienga, A., Kuchynka, P., Laskar, J., Manche, H., Gastineau, M., Oct. 2011b. Asteroid mass determinations with the inpop planetary ephemerides. EPSC-DPS Joint Meeting 2011. p. 1879.
-

- Fienga, A., Laskar, J., Kuchynka, P., Le Poncin-Lafitte, C., Manche, H., Gastineau, M., Jan. 2010. Gravity tests with INPOP planetary ephemerides. In: Klioner, S. A., Seidelmann, P. K., Soffel, M. H. (Eds.), IAU Symposium. Vol. 261 of IAU Symposium. pp. 159–169.
- Fienga, A., Laskar, J., Manche, H., Kuchynka, P., Desvignes, G., Gastineau, M., , Cognard, I., a. G., 2011a. The planetary ephemerides inpop10a and its applications in fundamental physics. *Celestial Mechanics and Dynamical Astronomy*.
- Fienga, A., Laskar, J., Morley, T., Manche, H., Kuchynka, P., Le Poncin-Lafitte, C., Budnik, F., Gastineau, M., Somenzi, L., Dec. 2009. INPOP08, a 4-D planetary ephemeris: from asteroid and time-scale computations to ESA Mars Express and Venus Express contributions. *Astronomy & Astrophysics* 507, 1675–1686.
- Fienga, A., Manche, H., a. L. J., Gastineau, M., 2008. Inpop06: a new numerical planetary ephemeris. *Astronomy & Astrophysics* 477, 315–327.
- Fienga, A., Manche, H., Laskar, J., Gastineau, M., Verma, A., Jan. 2013. INPOP new release: INPOP10e. ArXiv e-prints.
- Fjeldbo, G., Kliore, A. J., Eshleman, V. R., Mar. 1971. The Neutral Atmosphere of Venus as Studied with the Mariner V Radio Occultation Experiments. *Astronomical Journal* 76, 123.
- Flanigan, S. H., OShaughnessy, D. J., Wilson, M. N., Hill, T. A., 2013. MESSENGER maneuvers to reduce orbital period during the extended mission: Ensuring maximum use of the bi-propellant propulsion system. In: 23rd Space Flight Mechanics Meeting, American Astronomical Society. pp. 13–382.
- Folkner, W. M., Feb. 2010. Planetary ephemeris DE423 fit to Messenger encounters with Mercury. JPL, interoffice memorandum IOM 343R-10-001.
- Folkner, W. M., Williams, J. G., Boggs, D. H., Mar. 2008. JPL planetary and lunar ephemerides DE421, IOM 343R-08-003.
- Genova, A., Iess, L., Marabucci, M., Jun. 2013. Mercury’s gravity field from the first six months of MESSENGER data. *Planet. Space Sci.* 81, 55–64.
- Guhathakurta, M., Holzer, T. E., May 1994. Density structure inside a polar coronal hole. *The Astrophysical Journal* 426, 782–786.
- Guhathakurta, M., Holzer, T. E., MacQueen, R. M., Feb. 1996. The Large-Scale Density Structure of the Solar Corona and the Heliospheric Current Sheet. *The Astrophysical Journal* 458, 817.
- Hairer, E., Norsett, S. P., Wanner, G. (Eds.), 1987. *Solving Ordinary Differential Equations I: Nonstiff Problems*. Springer series in Computational Mathematics. Springer.
- Hassler, D. M., Dammasch, I. E., Lemaire, P., Brekke, P., Curdt, W., Mason, H. E., Vial, J.-C., Wilhelm, K., Feb. 1999. Solar Wind Outflow and the Chromospheric Magnetic Network. *Science* 283, 810.
-

- Hedin, A. E., Fleming, E. L., Manson, A. H., Schmidlin, F. J., Avery, S. K., Clark, R. R., Franke, S. J., Fraser, G. J., Tsuda, T., Vial, F., Vincent, R. A., Sep. 1996. Empirical wind model for the upper, middle and lower atmosphere. *Journal of Atmospheric and Terrestrial Physics* 58, 1421–1447.
- Howard, H. T., Tyler, G. L., Fjeldbo, G., Kliore, A. J., Levy, G. S., Brunn, D. L., Dickinson, R., Edelson, R. E., Martin, W. L., Postal, R. B., Seidel, B., Sesplaukis, T. T., Shirley, D. L., Stelzried, C. T., Sweetnam, D. N., Zygielbaum, A. I., Esposito, P. B., Anderson, J. D., Shapiro, I. I., Reasenberg, R. D., Mar. 1974. Venus: Mass, Gravity Field, Atmosphere, and Ionosphere as Measured by the Mariner 10 Dual-Frequency Radio System. *Science* 183, 1297–1301.
- Huang, C., Ries, J. C., Tapley, B. D., Watkins, M. M., Jun. 1990. Relativistic effects for near-earth satellite orbit determination. *Celestial Mechanics and Dynamical Astronomy* 48, 167–185.
- Hudson, H., Haisch, B., Strong, K. T., Mar. 1995. Comment on 'The solar flare myth' by J. T. Gosling. *J. Geophys. Res.* 100, 3473–3477.
- Issautier, K., Meyer-Vernet, N., Moncuquet, M., Hoang, S., Feb. 1998. Solar wind radial and latitudinal structure - Electron density and core temperature from ULYSSES thermal noise spectroscopy. *Journal of Geophysical Research* 103, 1969.
- Jacchia, L. G., Mar. 1977. Thermospheric Temperature, Density, and Composition: New Models. *SAO Special Report* 375.
- Kallenrode, M.-B., 2004. *Space physics : an introduction to plasmas and particles in the heliosphere and magnetospheres.*
- Kaula, W. M. (Ed.), 1966. *Theory of satellite geodesy: Applications of satellites to geodesy.* Dover Publications.
- Klioner, S. A., Feb. 2008. Relativistic scaling of astronomical quantities and the system of astronomical units. *A&A* 478, 951–958.
- Kojima, M., Kakinuma, T., Aug. 1990. Solar cycle dependence of global distribution of solar wind speed. *Space Sci Rev*, 53, 173–222.
- Konopliv, A. S., Asmar, S. W., Folkner, W. M., Karatekin, Ö., Nunes, D. C., Smrekar, S. E., Yoder, C. F., Zuber, M. T., Jan. 2011. Mars high resolution gravity fields from MRO, Mars seasonal gravity, and other dynamical parameters. *icarus* 211, 401–428.
- Konopliv, A. S., Yoder, C. F., Standish, E. M., Yuan, D.-N., Sjogren, W. L., May 2006. A global solution for the Mars static and seasonal gravity, Mars orientation, Phobos and Deimos masses, and Mars ephemeris. *Icarus* 182, 23–50.
- Kuchynka, P., 2010. *Etude des perturbations induites par les asteroides sur les mouvements des planetes et des sondes spatiales autour du point de lagrange l2.* PhD in astronomy, Observatoire de Paris.
-

- Kwok, A., 2000. TRK-2-18 Tracking System Interfaces Orbit Data File Interface. TRK-2-18 Tracking System Interfaces Orbit Data File Interface, Deep Space Mission System, JPL D-16765, 820-013.
- Lainey, V., Dehant, V., Pätzold, M., Apr. 2007. First numerical ephemerides of the Martian moons. *Astronomy and Astrophysics* 465, 1075–1084.
- Lang, K. R., Sep. 2000. The Sun From Space. *Ap&SS*273, 1–6.
- Lawson, C. L., Hanson, R. J., 1995. *Solving Least Squares Problems*. SIAM, Philadelphia, PA.
- Leary, J. C., Conde, R. F., Dakermanji, G., Engelbrecht, C. S., Ercol, C. J., Fielhauer, K. B., Grant, D. G., Hartka, T. J., Hill, T. A., Jaskulek, S. E., Mirantes, M. A., Mosher, L. E., Paul, M. V., Persons, D. F., Rodberg, E. H., Srinivasan, D. K., Vaughan, R. M., Wiley, S. R., Aug. 2007. The MESSENGER Spacecraft. *Space Sci Rev*, 131, 187–217.
- Leblanc, Y., Dulk, G. A., Bougeret, J.-L., Nov. 1998. Tracing the Electron Density from the Corona to 1au. *Solar Physics* 183, 165–180.
- Lemoine, F. G., Rowlands, D. D., Smith, D. E., Chinn, D. S., Pavlis, D. E., Luthcke, S. B., Neumann, G. A., Zuber, M. T., Aug. 1999. Orbit determination for Mars Global Surveyor during mapping. In: *AAS/AIAA Astrodynamics Specialist Conference*, 16-19 August. pp. 99–328.
- Lemoine, F. G., Smith, D. E., Rowlands, D. D., Zuber, M. T., Neumann, G. A., Chinn, D. S., Pavlis, D. E., Oct. 2001. An improved solution of the gravity field of Mars (GMM-2B) from Mars Global Surveyor. *J. Geophys. Res.*106, 23359–23376.
- Leon, G., Jay, M. P., 2010. *The solar corona*; 2nd ed. Cambridge Univ. Press.
- Manche, H., 2011. *Elaboration des ephemeride inpop : modele dynamique et ajustements aux donnees de telemetrie laser lune*. Ph.D. thesis, in french, Observatoire de Paris.
- Manche, H., Fienga, A., Laskar, J., Gastineau, M., Bouquillon, S., Francou, G., Kuchynka, P., Nov. 2010. LLR residuals of the latest INPOP solution and constraints on post-Newtonian parameters. In: *Journées Systèmes de Référence Spatio-temporels 2010*. Journées Systemes de references.
- Margot, J.-L., Dec. 2009. A Mercury orientation model including non-zero obliquity and librations. *Celestial Mechanics and Dynamical Astronomy* 105, 329–336.
- Marshall, J. A., 1992. Modeling radiation forces acting on TOPEX/Poseidon for precision orbit determination.
- Marty, J. C., 2011. Characteristics of the MGS macro-model. Private communication.
- Marty, J. C., Balmino, G., Duron, J., Rosenblatt, P., Le Maistre, S., Rivoldini, A., Dehant, V., van Hoolst, T., Mar. 2009. Martian gravity field model and its time variations from MGS and Odyssey data. *Planetary and Space Science* 57, 350–363.
-

- 
- McAdams, J. V., Farquhar, R. W., Taylor, A. H., Williams, B. G., Aug. 2007. MESSENGER Mission Design and Navigation. *Space Sci Rev*, 131, 219–246.
- McCarthy, D. D., Petit, G., 2003. IERS technical note no 32. Tech. rep., IERS Convention Centre, <http://www.iers.org/iers/publications/tn/tn32/>.  
URL <http://www.iers.org/iers/publications/tn/tn32/>
- McCarthy, D. D., Petit, G., 2004. IERS Conventions (2003). IERS Technical Note 32, 1.
- Milani, A., Nobili, A. M., Farinella, P., 1987. Non-gravitational perturbations and satellite geodesy.
- Moyer, T., 1971. Dpodp manual. IOM 3215-37, JPL.
- Moyer, T. D., 2003. Formulation for Observed and Computed Values of Deep Space Network Data Types for Navigation. Vol. 2. John Wiley & Sons.
- Muhleman, D. O., Anderson, J. D., Aug. 1981. Solar wind electron densities from Viking dual-frequency radio measurements. *The Astrophysical Journal* 247, 1093–1101.
- Muhleman, D. O., Esposito, P. B., Anderson, J. D., Feb. 1977. The electron density profile of the outer corona and the interplanetary medium from Mariner-6 and Mariner-7 time-delay measurements. *Astrophysics Journal* 211, 943–957.
- Müller, J., Soffel, M., Klioner, S. A., Mar. 2008. Geodesy and relativity. *Journal of Geodesy* 82, 133–145.
- Newhall, X. X., 1989. Numerical Representation of Planetary Ephemerides. *Celestial Mechanics* 45, 305.
- Newhall, X. X., Standish, E. M., Williams, J. G., Aug. 1983. DE 102 - A numerically integrated ephemeris of the moon and planets spanning forty-four centuries. *Astronomy & Astrophysics* 125, 150–167.
- Parker, E. N., Jul. 1963. The Solar-Flare Phenomenon and the Theory of Reconnection and Annihilation of Magnetic Fields. *ApJS*8, 177.
- Pätzold, M., Bird, M. K., Edenhofer, P., Asmar, S. W., McElrath, T. P., 1995. Dual-frequency radio sounding of the solar corona during the 1995 conjunction of the Ulysses spacecraft. *Geographical research letters* 22, 3313–3316.
- Pätzold, M., Neubauer, F. M., Carone, L., Hagermann, A., Stanzel, C., Häusler, B., Remus, S., Selle, J., Hagl, D., Hinson, D. P., Simpson, R. A., Tyler, G. L., Asmar, S. W., Axford, W. I., Hagfors, T., Barriot, J.-P., Cerisier, J.-C., Imamura, T., Oyama, K.-I., Janle, P., Kirchengast, G., Dehant, V., Aug. 2004. MaRS: Mars Express Orbiter Radio Science. In: Wilson, A., Chicarro, A. (Eds.), *Mars Express: the Scientific Payload*. Vol. 1240 of ESA Special Publication. pp. 141–163.
- Petrie, G. J. D., May 2013. Solar Magnetic Activity Cycles, Coronal Potential Field Models and Eruption Rates. *ApJ*768, 162.
-

- Pitjeva, E. V., May 2005. High-Precision Ephemerides of Planets-EPM and Determination of Some Astronomical Constants. *Solar System Research* 39, 176–186.
- Pitjeva, E. V., May 2009. EPM Ephemerides and Relativity. In: IAU Symposium, American Astronomical Society. Vol. 261. p. 603.
- Pitjeva, E. V., Jan. 2010. EPM ephemerides and relativity. In: Klioner, S. A., Seidelmann, P. K., Soffel, M. H. (Eds.), IAU Symposium. Vol. 261 of IAU Symposium. pp. 170–178.
- Pitjeva, E. V., Pitjev, N. P., Jul. 2013. Relativistic effects and dark matter in the Solar system from observations of planets and spacecraft. *MNRAS* 432, 3431–3437.
- Ringnes, T. S., 1964. On the lifetime of sunspot groups. *Astrophysica Norvegica* 9, 95.
- Schwenn, R., Nov. 1983. The average solar wind in the inner heliosphere: Structures and slow variations. In: NASA Conference Publication. Vol. 228 of NASA Conference Publication. pp. 489–507.
- Schwenn, R., Jun. 2006. Solar Wind Sources and Their Variations Over the Solar Cycle. *Space Science Reviews* 124, 51–76.
- Schwenn, R., Marsch, E. (Eds.), 1990. *Physics of the Inner Heliosphere, Vol. I: Large-Scale Phenomena*. Vol. 20 of *Physics and Chemistry in Space*. Springer.
- Schwenn, R., Marsch, E. (Eds.), 1991. *Physics of the Inner Heliosphere, Vol. II: Particles, Waves and Turbulence*. Vol. 21 of *Physics and Chemistry in Space*. Springer.
- Shapiro, I. I., Dec. 1964. Fourth Test of General Relativity. *Physical Review Letters* 13, 789–791.
- Smith, D. E., Zuber, M. T., Phillips, R. J., Solomon, S. C., Hauck, S. A., Lemoine, F. G., Mazarico, E., Neumann, G. A., Peale, S. J., Margot, J.-L., Johnson, C. L., Torrence, M. H., Perry, M. E., Rowlands, D. D., Goossens, S., Head, J. W., Taylor, A. H., Apr. 2012. Gravity Field and Internal Structure of Mercury from MESSENGER. *Science* 336, 214–.
- Smith, D. E., Zuber, M. T., Phillips, R. J., Solomon, S. C., Neumann, G. A., Lemoine, F. G., Peale, S. J., Margot, J., Torrence, M. H., Talpe, M. J., Head, J. W., Hauck, S. A., Johnson, C. L., Perry, M. E., Barnouin, O. S., McNutt, R. L., Oberst, J., Sep. 2010. The equatorial shape and gravity field of Mercury from MESSENGER flybys 1 and 2. *icarus* 209, 88–100.
- Srinivasan, D. K., Perry, M. E., Fielhauer, K. B., Smith, D. E., Zuber, M. T., Aug. 2007. The Radio Frequency Subsystem and Radio Science on the MESSENGER Mission. *Space Science Reviews* 131, 557–571.
- Stanbridge, D. R., Williams, K. E., Taylor, A. H., Page, B. R., Bryan, C. G., Dunham, D. W., Wolff, P., Williams, B. G., Aug. 2011. Achievable force model accuracies for messenger in mercury orbit. In: AAS/AIAA Astrodynamics Specialist Conference. AAS 11-548.
- Standish, E. M., Aug. 1998. JPL planetary and lunar ephemerides, DE405/LE405, IOM 312F-98-483.
-

- 
- Standish, Jr., E. M., Keesey, M. S. W., Newhall, X. X., Feb. 1976. JPL Development Ephemeris number 96.
- Standish, E. M., J., Jul. 1990. The observational basis for JPL's DE 200, the planetary ephemerides of the *Astronomical Almanac*. *Astronomy & Astrophysics* 233, 252–271.
- Stark, P., Parker, R., 1995. Bounded-variable least-squares: an algorithm and applications. *Computational Statistics* 10, 1292013141.
- Tokumaru, M., Kojima, M., Fujiki, K., Apr. 2010. Solar cycle evolution of the solar wind speed distribution from 1985 to 2008. *Journal of Geophysical Research (Space Physics)* 115, 4102.
- Tyler, G. L., Balmino, G., Hinson, D. P., Sjogren, W. L., Smith, D. E., Simpson, R. A., Asmar, S. W., Priest, P., Twicken, J. D., Oct. 2001. Radio science observations with Mars Global Surveyor: Orbit insertion through one Mars year in mapping orbit. *Journal of geophysical research* 106, 23327–23348.
- Tyler, G. L., Eshleman, V. R., Anderson, J. D., Levy, G. S., Lindal, G. F., Wood, G. E., Croft, T. A., Apr. 1981. Radio science investigations of the Saturn system with Voyager 1 - Preliminary results. *Science* 212, 201–206.
- Tyler, G. L., Eshleman, V. R., Hinson, D. P., Marouf, E. A., Simpson, R. A., Sweetnam, D. N., Anderson, J. D., Campbell, J. K., Levy, G. S., Lindal, G. F., Jul. 1986. Voyager 2 radio science observations of the Uranian system Atmosphere, rings, and satellites. *Science* 233, 79–84.
- van der Ha, J. C., Modi, V. J., Dec. 1977. Analytical evaluation of solar radiation induced orbital perturbations of space structures. *Journal of the Astronautical Sciences* 25, 283–306.
- Vaughan, R. M., Haley, D. R., OShaughnessy, D. J., Shapiro, H. S., 2002. Momentum management for the MESSENGER mission. *Advances in the Astronautical Sciences* 109, 1139–1158.
- Vaughan, R. M., Leary, J. C., Conde, R. F., Dakermanji, G., Ercol, C. J., Fielhauer, K. B., Grant, D. G., Hartka, T. J., Hill, T. A., Jaskulek, S. E., McAdams, J. V., Mirantes, M. A., Persons, D. F., Srinivasan, D. K., Jan. 2006. Return to Mercury: The MESSENGER spacecraft and mission. In: *Institute of Electrical and Electronics Engineers (IEEE) Aerospace Conference*. IEEEAC paper 1562, 15 pp., 2006.
- Verma, A. K., Fienga, A., Laskar, J., Issautier, K., Manche, H., Gastineau, M., Feb. 2013. Electron density distribution and solar plasma correction of radio signals using MGS, MEX, and VEX spacecraft navigation data and its application to planetary ephemerides. *Astronomy & Astrophysics* 550, A124.
- Verma, A. K., Fienga, A., Laskar, J., Manche, H., Gastineau, M., Jan. 2014. Use of MESSENGER radioscience data to improve planetary ephemeris and to test general relativity. *A&A* 561, A115.
-



- 
- Wahr, J. M., Mar. 1981. Body tides on an elliptical, rotating, elastic and oceanless earth. *Geophysical Journal International* 64, 677–703.
- Will, C. M. (Ed.), 1993. pp. 396. ISBN 0521439736. *Theory and Experiment in Gravitational Physics*. Cambridge University Press.
- Williams, J. G., Turyshev, S. G., Boggs, D. H., 2009. Lunar Laser Ranging Tests of the Equivalence Principle with the Earth and Moon. *International Journal of Modern Physics D* 18, 1129–1175.
- You, X. P., Coles, W. A., Hobbs, G. B., Manchester, R. N., May 2012. Measurement of the electron density and magnetic field of the solar wind using millisecond pulsars. *MNRAS* 422, 1160–1165.
- You, X. P., Hobbs, G. B., Coles, W. A., Manchester, R. N., Han, J. L., Dec. 2007. An Improved Solar Wind Electron Density Model for Pulsar Timing. *The Astrophysical Journal* 671, 907–911.
- Yuan, D.-N., Sjogren, W. L., Konopliv, A. S., Kucinskas, A. B., Oct. 2001. Gravity field of Mars: A 75th Degree and Order Model. *J. Geophys. Res.* 106, 23377–23402.
- Zirker, J. B., Aug. 1977. Coronal holes and high-speed wind streams. *Reviews of Geophysics and Space Physics* 15, 257–269.
-

